UNIVERSITY OF CALIFORNIA

Los Angeles

Mid-Rapidity π^0 Production in *d*+*Au* Collions at $\sqrt{s_{nn}}$ = 200 GeV

A dissertation submitted in partial satisfaction

of the requirements for the degree

Doctor of Philosophy in Physics

by

Steven Michael Guertin

2008

The dissertation of Steven Michael Guertin is approved.

Yuanxun Wang

Ernest S. Abers

Charles A. Whitten Jr.

Huan Z. Huang, Committee Chair

University of California, Los Angeles

2008

To my family and friends…

for helping me keep my bearings and for your unyielding support

Through you I found the reflection of nature in humanity

and the reflection of humanity in nature.

Especially to my mother

TABLE OF CONTENTS

LIST OF FIGURES

LIST OF TABLES

ACKNOWLEDGEMENTS

This work would not have come to completion without the patient and knowledgeable guidance of my advisors. I am also very thankful for the daily interactions I have had with the members of the UCLA relativistic heavy ion group, many of whom have come or gone during my time with the group. The environment created by the group, past and present, helped me understand that we are a community working together on individual and group goals, and by standing together we can accomplish them all efficiently.

I also must thank the STAR collaboration and the high-p_T working group in particular. The work in this dissertation reflects many discussions with the working group and individual members over a span of several years.

During the time spent working on this dissertation I also relied on a strong network through my contacts, personal and professional, within the radiation effects group at the Jet Propulsion Laboratory. They provided me with support during this research. I am in debt to them for insights, technical discussions, and personal support.

Last, I would like to acknowledge the sacrifices made by my family. Through the whole process they were there to help me even when things were not looking good. There are so many to thank that I consider it a blessing to have all of you to call upon.

VITA

6 August 1973	Born, Honolulu, Hawaii, USA
1997-1999	Academic Part Time Radiation Effects Group, Jet Propulsion Laboratory Pasadena, CA
1998	B. S. in Mathematics and Physics California State Polytechnic University Pomona, CA
1999 – Present	Radiation Effects Test Engineer Radiation Effects Group, Jet Propulsion Laboratory Pasadena, CA
2001	Teaching Assistant Department of Physics, University of California Los Angeles, CA
2001	M. S. in Physics University of California Los Angeles, CA
2002-2008	Graduate Research Assistant Department of Physics, University of California Los Angeles, CA

PUBLICATIONS

S.M. Guertin, "Proton Dosimetry Using a Commercial Scanner", *Project Report*, NSF REU Program at IUCF (1997).

S.M. Guertin, G.M. Swift, D. Nguyen, "Single-event upset test results for the Xilinx XQ1701L PROM", *IEEE Radiation Effects Data Workshop*, (1999).

S.M. Guertin, L.D. Edmonds, G.M. Swift, "Angular dependence of DRAM upset susceptibility and implications for testing and analysis", *IEEE TNS*, **47**:2380-2385 (2000)

L.Z. Scheick, S.M. Guertin, G.M. Swift, "Analysis of radiation effects on individual DRAM cells", *IEEE TNS*, **47**:2534-2538 (2000)

G.M. Swift, F.F. Farmanesh, S.M. Guertin, F. Irom, D.G. Millward, "Single-event upset in the PowerPC750 microprocessor", *IEEE TNS*, **48**:1822-1827 (2001)

S.M. Guertin, J.D. Patterson, D.N. Nguyen, "Dynamic SDRAM SEFI detection and recovery test results", *IEEE Radiation Effects Data Workshop*, 62-67, (2004)

S.M. Guertin, D.N. Nguyen, J.D. Patterson, "Microdose Induced Data Loss on Floating Gate Memories", *IEEE TNS*, **53**:3118-3524 (2006)

J. Adams, et al. (STAR Collaboration), "Strange anti-particle to particle ratios at mid-rapidity in $\sqrt{s_{nn}}$ = 130 GeV *Au+Au* Collisions", *Phys Lett.* **B567**:157 (2003).

J. Adams, et al. (STAR Collaboration), "Narrowing of the Balance Function with Centrality in *Au+Au* Collisions at $\sqrt{s_{nn}}$ = 130 GeV", *Phys. Rev. Lett.* **90**:172301 (2003).

J. Adams, et al. (STAR Collaboration), "Transverse momentum and collision energy dependence of high-p_T hadron suppression in *Au+Au* collisions at ultrarelativistic energies", *Phys. Rev. Lett.* **91**:172302 (2003).

J. Adams, et al. (STAR Collaboration), "Particle-type dependence of azimuthal anisotropy and nuclear modification of particle production in *Au+Au* collisions at $\sqrt{s_{nn}}$ = 200 GeV", *Phys. Rev. Lett.* **92**:052302 (2004).

J. Adams, et al. (STAR Collaboration), "Evidence from *d+Au* measurements for final-state suppression of high-p_T hadrons in *Au+Au* collisions at RHIC", *Phys. Rev. Lett.* **91**:072304 (2003).

J. Adams, et al. (STAR Collaboration), "Three-Pion Hanbury Brown-Twiss Correlations in Relativistic Heavy-Ion Collisions from the STAR Experiment", *Phys. Rev. Lett.* **91**:262301 (2003).

J. Adams, et al. (STAR Collaboration), "Rapidity and Centrality Dependence of Proton and Anti-proton from *Au+Au* Collisions at $\sqrt{s_{nn}}$ = 130 GeV", *Phys. Rev.* **C70**:041901 (2004).

J. Adams, et al. (STAR Collaboration), "Net charge fluctuations in *Au+Au* collisions at $\sqrt{s_{nn}}$ = 130 GeV", *Phys. Rev.* **C68**:044905 (2003).

J. Adams, et al. (STAR Collaboration), "rho-0 Production and Possible Modification in *Au+Au* and *p+p* Collisions at $\sqrt{s_{nn}}$ = 200 GeV", *Phys. Rev. Lett.* **92**:092301 (2004).

J. Adams, et al. (STAR Collaboration), "Multi-strange baryon production in *Au-Au* collisions at $\sqrt{s_{nn}}$ = 130 GeV", *Phys. Rev. Lett.* **92**:182301 (2004).

J. Adams, et al. (STAR Collaboration), "Pion-Kaon Correlations in Central *Au+Au* Collisions at $\sqrt{s_{nn}}$ = 130 Gev", *Phys. Rev. Lett.* **91**:262302 (2003).

J. Adams, et al. (STAR Collaboration), "Event-wise mean-p_T fluctuations in *Au-Au* collisions at $\sqrt{s_{nn}}$ = 130 GeV", *Phys Rev.* **C71**:064906 (2005).

J. Adams, et al. (STAR Collaboration), "Pion, kaon, proton and anti-proton transverse momentum distributions from *p+p* and *d+Au* collisions at $\sqrt{s_{nn}}$ = 200 GeV", *Phys. Lett.* **B616**:8 (2005)s

J. Adams, et al. (STAR Collaboration), "Identified particle distributions in *p+p* and *Au+Au* collisions at $\sqrt{s_{nn}}$ = 200 GeV", *Phys. Rev. Lett.* **92**:112301 (2004)

J. Adams, et al. (STAR Collaboration), "Cross Sections and Transverse Single-Spin Asymmetries in Forward Neutral Pion Production from Proton Collisions at $\sqrt{s_{nn}}$ = 200 GeV", *Phys. Rev. Lett.* **92**:171801 (2004)

J. Adams, et al. (STAR Collaboration), "Azimuthal anisotropy at the Relativistic Heavy Ion Collider: the first and fourth harmonics", *Phys. Rev. Lett.* **92**:062301 (2004)

J. Adams, et al. (STAR Collaboration), "Azimuthally sensitive HBT in *Au+Au* collisions at $\sqrt{s_{nn}}$ = 200 GeV", *Phys. Rev. Lett.* **93**:012301 (2004)

J. Adams, et al. (STAR Collaboration), "Photon and neutral pion production in *Au+Au* collisions at $\sqrt{s_{nn}}$ = 130 GeV", *Phys. Rev.* **C70**:044902 (2004)

J. Adams, et al. (STAR Collaboration), "Production of e^+e^- Pairs Accompanied by Nuclear Dissociation in Ultra-Peripheral Heavy Ion Collision", *Phys. Rev.* **C70**:031902 (2004)

J. Adams, et al. (STAR Collaboration), "Centrality and pseudorapidity dependence of charged hadron production at intermediate p_T in *Au+Au* collisions at $\sqrt{s_{nn}}$ = 130 GeV", *Phys. Rev.* **C70**:044901 (2004)

J. Adams, et al. (STAR Collaboration), "Phi meson production in *Au+Au* and *p+p* collisions at $\sqrt{s_{nn}}$ = 200 GeV", *Phys. Lett.* **B612**:181 (2005)

J. Adams, et al. (STAR Collaboration), "Hadronization geometry and net-charge angular correlations on momentum subspace (eta,phi) in *Au-Au* collisions at $\sqrt{s_{nn}}$ = 130 GeV", *Phys. Lett.* **B634**:347 (2006)

J. Adams, et al. (STAR Collaboration), "Transverse-momentum dependent modification of dynamic texture in central *Au+Au* collisions at $\sqrt{s_{nn}}$ = 200 GeV", *Phys. Rev.* **C71**:031901 (2005)

J. Adams, et al. (STAR Collaboration), "Measurements of transverse energy distributions in *Au+Au* collisions at $\sqrt{s_{nn}}$ = 200 GeV", *Phys. Rev.* **C70**:054907 (2004)

J. Adams, et al. (STAR Collaboration), "Open charm yields in *d+Au* collisions at $\sqrt{s_{nn}}$ = 200 GeV", *Phys. Rev. Lett.* **94**:062301 (2005)

J. Adams, et al. (STAR Collaboration), "Azimuthal anisotropy and correlations at large transverse momenta in *p+p* and *Au+Au* collisions at $\sqrt{s_{nn}}$ = 200 GeV", *Phys. Rev. Lett.* **93**:252301 (2004)

J. Adams, et al. (STAR Collaboration), "Transverse momentum correlations and minijet dissipation in *Au-Au* collisions at $\sqrt{s_{nn}}$ = 130 GeV", *J. Phys.* **G34**:799 (2007)

J. Adams, et al. (STAR Collaboration), "Pseudorapidity Asymmetry and Centrality Dependence of Charged Hadron Spectra in *d*+*Au* Collisions at $\sqrt{s_{nn}}$ = 200 GeV", *Phys. Rev.* **C70**:064907 (2004)

J. Adams, et al. (STAR Collaboration), "Azimuthal Anisotropy in *Au*+*Au* Collisions at $\sqrt{s_{nn}}$ = 200 GeV", *Phys. Rev.* **C72**:014904 (2005)

J. Adams, et al. (STAR Collaboration), "Minijet deformation and charge-independent angular correlations on momentum subspace (eta,phi) in *Au*-*Au* collisions at $\sqrt{s_{nn}}$ = 130 GeV", *Phys. Rev.* **C73**:064907 (2006)

J. Adams, et al. (STAR Collaboration), "Pion interferometry in *Au*+*Au* collisions at $\sqrt{s_{nn}}$ = 200 GeV", *Phys. Rev.* **C71**:044906 (2005)

J. Adams, et al. (STAR Collaboration), "K(892)* Resonance Production in *Au*+*Au* and *p*+*p* Collisions at $\sqrt{s_{nn}}$ = 200 GeV at STAR", *Phys. Rev.* **C71**:064902 (2005)

J. Adams, et al. (STAR Collaboration), "Experimental and Theoretical Challenges in the Search for the Quark Gluon Plasma: The STAR Collaboration's Critical Assessment of the Evidence from RHIC Collisions", *Nucl. Phys.* **A757**:102 (2005)

J. Adams, et al. (STAR Collaboration), "Distributions of Charged Hadrons Associated with High Transverse Momentum Particles in *p*+*p* and *Au*+*Au* Collisions at $\sqrt{s_{nn}}$ = 200 GeV", *Phys. Rev. Lett.* **95**:152301 (2005)

J. Adams, et al. (STAR Collaboration), "Multiplicity and Pseudorapidty Distributions of Photons in *Au*+*Au* Collisions at $\sqrt{s_{nn}}$ = 62.4 GeV", *Phys. Rev. Lett.* **95**:062301 (2005)

J. Adams, et al. (STAR Collaboration), "Multi-strange baryon elliptic flow in *Au+Au* collisions at $\sqrt{s_{nn}}$ = 200 GeV", *Phys. Rev. Lett.* **95**:122301 (2005)

J. Adams, et al. (STAR Collaboration), "Incident Energy Dependence of p_T Correlations at RHIC", *Phys. Rev.* **C72**:044902 (2005)

J. Adams, et al. (STAR Collaboration), "Transverse-momentum p_T correlations on (eta,phi) from mean-p_T fluctuations in *Au-Au* collisions at $\sqrt{s_{nn}}$ = 200 GeV", *J. Phys.* **G32**:L37 (2006)

J. Adams, et al. (STAR Collaboration), "Directed flow in *Au+Au* collisions at $\sqrt{s_{nn}}$ = 62 GeV", *Phys. Rev.* **C73**:034903 (2006)

J. Adams, et al. (STAR Collaboration), "Proton-lambda correlations in central *Au+Au* collisions at $\sqrt{s_{nn}}$ = 200 GeV", *Phys Rev.* **C74**:064906 (2007)

J. Adams, et al. (STAR Collaboration), "Multiplicity and Pseudorapidity Distributions of Charged Particles and Photons at Forward Pseudorapidity in *Au+Au* Collisions at $\sqrt{s_{nn}}$ = 62.4 GeV", *Phys. Rev.* **C73**:034906 (2006)

B.I. Abelev, et al. (STAR Collaboration), "Strangelet Search in *Au+Au* collisions at 200 GeV", *Phys. Rev.* **C76**:011901 (2007)

J. Adams, et al. (STAR Collaboration), "Identified hadron spectra at large transverse momentum in *p+p* and *d+Au* collisions at $\sqrt{s_{nn}}$ = 200 GeV", *Phys. Rev.* **B637**:161 (2006)

J. Adams, et al. (STAR Collaboration), "Forward Neutral Pion Production in *p+p* and *d+Au* Collisions at $\sqrt{s_{nn}}$ = 200 GeV", *Phys. Rev. Lett.* **97**:152302 (2006)

J. Adams, et al. (STAR Collaboration), "Direct observation of dijets in central *Au+Au* collisions at $\sqrt{s_{nn}}$ = 200 GeV", *Phys. Rev. Lett.* **97**:162301 (2006)

B.I. Abelev, et al. (STAR Collaboration), "Strange baryuon resonance production in $\sqrt{s_{nn}}$ = 200 GeV *p+p* and *Au+Au* collisions", *Phys. Rev. Lett.* **97**:132301 (2006)

B.I. Abelev, et al. (STAR Collaboration), "Identified baryon and meson distributions at large transverse momenta from *Au+Au* collisions at $\sqrt{s_{nn}}$ = 200 GeV", *Phys. Rev. Lett.* **97**:152301 (2006)

J. Adams, et al. (STAR Collaboration), "Scaling properties of hyperon production in *Au+Au* collisions at $\sqrt{s_{nn}}$ = 200 GeV", *Phys. Rev. Lett.* **98**:062301 (2007)

J. Adams, et al. (STAR Collaboration), "The multiplicity dependenc of inclusive p_T spectra from *p+p* collisions at $\sqrt{s_{nn}}$ = 200 GeV", *Phys. Rev.* **D74**:032006 (2006)

J. Adams, et al. (STAR Collaboration), "$\Delta\phi\Delta\eta$ Correlations in Central *Au+Au* Collisions at $\sqrt{s_{nn}}$ = 200 GeV", *Phys. Rev.* **C75**:034901 (2007)

B.I. Abelev, et al. (STAR Collaboration), "Transverse momentum and centrality dependence of high-p_T non-photonic electron suppression in *Au+Au* collisions at $\sqrt{s_{nn}}$ = 200 GeV", *Phys. Rev. Lett.* **98**:192301 (2007)

B.I. Abelev, et al. (STAR Collaboration), "Strange particle production in *p+p* collisions at $\sqrt{s_{nn}}$ = 200 GeV", *Phys. Rev.* **C75**:064901 (2007)

B.I. Abelev, et al. (STAR Collaboration), "Neutral Kaon Interferometry in *Au+Au* collisions at $\sqrt{s_{nn}}$ = 200 GeV", *Phys. Rev.* **C74**:54902 (2006)

J. Adams, et al. (STAR Collaboration), "Longitudinal Double-Spin Asymmetry and Cross Section for Inclusive Jet Production in Polarized Proton Collisions at $\sqrt{s_{nn}}$ = 200 GeV", *Phys. Rev. Lett.* **97**:252001 (2006)

B.I. Abelev, et al. (STAR Collaboration), "Rapidity and species dependence of particle production at large transverse momentum for *d+Au* collisions at $\sqrt{s_{nn}}$ = 200 GeV", *Phys. Rev.* **C76**:54903 (2007)

B.I. Abelev, et al. (STAR Collaboration), "The energy dependence of p_T angular correlations inferred from mean-p_T fluctuation scale dependence in heavy ion collisions at the SPS and RHIC", *J. Phys.* **G34**:451 (2007)

B.I. Abelev, et al. (STAR Collaboration), "Mass, quark-number, and $\sqrt{s_{nn}}$ dependence of the second and fourth flow harmonics in ultra-relativistic nucleus-nucleus collisions", *Phys. Rev.* **C75**:54906 (2007)

B.I. Abelev, et al. (STAR Collaboration), "Partonic flow and ϕ-meson production in *Au+Au* collisions at $\sqrt{s_{nn}}$ = 200 GeV", *Phys. Rev. Lett.* **99**:112301 (2007)

B.I. Abelev, et al. (STAR Collaboration), "Energy dependence of $\pi^{\pm}$, *p* and *p*-bar transverse momentum spectra for *Au+Au* collisions at $\sqrt{s_{nn}}$ = 62.4 and 200 GeV", *Phys. Lett.* **B655**:104 (2007)

B.I. Abelev, et al. (STAR Collaboration), "Global polarization measurement in *Au+Au* collisions",*Phys. Rev.* **C76**:024915 (2007)

B.I. Abelev, et al. (STAR Collaboration), "Measurement of Transverse Single-Spin Asymmetries for Di-Jet Production in Proton-Proton Collisions at $\sqrt{s_{nn}}$ = 200 GeV", *Phys. Rev. Lett.* **99**:142003 (2007)

B.I. Abelev, et al. (STAR Collaboration), "Forward Lambda Production and Nuclear Stopping Power in *d+Au* Collisions at $\sqrt{s_{nn}}$ = 200 GeV", *Phys. Rev.* **C76**:64904 (2007)

A.H. Johnston, G.M. Swift, T. Miyahira, S. Guertin, L.D. Edmonds, "Single-event upset effects in optocouplers", *IEEE TNS*, **45**:2867-2875 (1998)

P.B. Seigel, S. Guertin, "Dynamical Formation of s-wave Baryon Resonances: How Many Could There Be?", *Proceedings of the Eighth International Symposium on Meson-Nucleon Physics and the Structure of the Nucleon*, *Pi-N Newsletter* No. **15**:246-249 (1999)

A.H. Johnston, T. Miyahira, G.M. Swift, S.M. Guertin, L.D. Edmonds, "Angular and energy dependence of proton upset in optocouplers", *IEEE TNS*. **46**:1335-1341 (1999)

D.N. Nguyen, S.M. Guertin, G.M. Swift, A.H. Johnston, "Radiation effects on advanced flash memories", *IEEE TNS*, **46**:1744-1750 (1999)

G.M. Swift, S.M. Guertin "In-flight observations of multiple-bit upset in DRAMs", *IEEE TNS*, **47**: 2386-2391 (2000)

A.H. Johnston, S.M. Guertin "The effects of space radiation on linear integrated circuits", *IEEE Aerospace Conference Proceedings*, 363-369, (2000).

L.Z. Scheick, S.M. Guertin, "SEU evaluation of SRAM memories for space applications", *IEEE Radiation Effects Data Workshop*, (2000)

L.D. Edmonds, S.M. Guertin, L.Z. Scheick, D.N. Nguyen, G.M. Swift, "Ion-induced stuck bits in 1T/1C SDRAM cells", *IEEE TNS*, **48**:1925-1930 (2001).

S.M. Guertin, L.Z. Scheick, D.N. Nguyen "Endurance Cycling in Extreme Environments", *Non-Volatile Memory Technology Symposium*, San Diego, (2003).

Y. Chen, D. Nguyen, S. Guertin, J. Bernstein, M. White, R. Menke, S. Kayali, "A reliability evaluation methodology of rmemory chips for space applications when sample size is small", *IEEE International Integrated Reliability Workshop*, (2003).

L.E. Selva, L.Z. Scheick, S. McClure, T. Miyahira, S.M. Guertin, S.K. Shah, L.D. Edmonds, J.D. Patterson, "Catastrophic SEE in high-voltage power MOSFETs", *IEEE Radiation Effects Data Workshop*, (2003).

J. George, G. Swift, S. Guertin, C. Carmichael, S. Rezgui, R. Koga, "Heavy ion SEE testing of Xilinx one-time programmable configuration PROMs", *IEEE Radiation Effects Data Workshop*, (2004)

D.N. Nguyen, S.M. Guertin, J.D. Patterson, "The Effect of Total Ionizing Dose Degradation on Laptop Hard Disks", *RADECS* (2005).

J. Patterson, S. Guertin, D. Nguyen, "Emerging SEFI modes and SEE testing strategies for highly scaled NAND flash devices", *Non-Volatile Memory Technology Symposium*, (2005).

D.N. Nguyen, S.M. Guertin, J.D. Patterson, "Radiation Tests on 2Gb NAND Flash Memories", *IEEE Radiation Effects Data Workshop*, 121-125 (2006).

P. Layton, S. Kniffin, S. Guertin, G. Swift, S. Buchner, "SEL Induced Latent Damage, Testing, and Evaluation", *IEEE TNS*, **53**:3153-3157 (2006).

ABSTRACT OF THE DISSERTATION

Mid-Rapidity π^0 Production in *d+Au* Collions at $\sqrt{s_{nn}}$ = 200 GeV

by

Steven Michael Guertin

Doctor of Philosophy in Physics

University of California, Los Angeles, 2008

Professor Huan Z. Huang, Chair

The spectrum of π^0 production in *d+Au* collisions at $\sqrt{s_{nn}}$ = 200 GeV is measured to provide constraints on the initial-state influence on observed particle suppression in *Au+Au* collisions. Nucleus-nucleus collisions have provided evidence of deconfined matter at high energy densities. The STAR detector collaboration has collected this evidence in *Au+Au* collisions. This deconfined matter is called Quark-Gluon Plasma (QGP). Quantum Chromodynamics (QCD), the fundamental theory of the strong interaction predicts the existence of QGP matter. QCD does not guarantee the conditions in nucleus-nucleus collisions under which the QGP will form, so the experimental evidence must be established for the formation of the QGP.

Signatures of QGP are observed in particle spectra produced during collisions. Produced particles are influenced by initial-state, collision, and final-state effects that

all require theoretical and experimental insight to disentangle. *d+Au* collisions provide a control case for disentangling the effect the Au-nucleus has on the initial-state. π^0 production in *d+Au* collisions provides a unique channel for observation of hadron production in nucleus-nucleus collisions.

The π^0 transverse momentum (p_T) spectrum at mid-rapidity in *d+Au* collisions at $\sqrt{s_{nn}}$ = 200 GeV is measured in the 2003 STAR dataset. Analysis of systematic effects and their impact on data quality at high p_T indicate the spectrum is determined for the range $1.25 < p_T < 9$ GeV/c with point-to-point systematic uncertainty ranging from 10% to 25% and scale uncertainty of about 15%. The spectrum is limited by systematics for most p_Ts. Measurements extend to 14 GeV/c with significantly increased uncertainty.

Comparison to *d+Au*, *p+p*, and *Au+Au* results for charged hadrons and π^0s are made. In reference to *p+p* and *d+Au*, the measured scaling of these results is in agreement with STAR's charged hadron measurements and PHENIX's π^0 measurements. The nuclear modification factor, $R_{dAu}(p_T)$, determined by our results are compared to the nuclear modification factor of π^0s observed in *Au+Au*.

The absence of high-p_T suppression in R_{dAu} compared to R_{AA} shows that particle suppression in *Au+Au* is due to medium effects produced by the high energy density matter created in *Au+Au* collisions. This result is in agreement with charged hadron and π^0 results reported by the STAR and PHENIX collaborations. The lack of suppression in *d+Au* indicates the Au nuclear structure is not the cause of observed particle suppression at mid-rapidity in central *Au+Au* collisions. Instead, the suppression is due to interactions between scattered partons and the medium created in central *Au+Au* collisions.

CHAPTER 1

Introduction

π^0s are one of the most abundantly produced particles in nuclear collisions. The angular and momentum distributions of π^0s, along with those of other produced particles, are probes of the conditions of the collisions in which they were produced. This dissertation studies π^0 production in deuteron-on-Au (*d+Au*) collisions. Previous studies have suggested the possibility that high-energy nucleus-nucleus collisions have produced a dense and strongly interacting medium. In such a medium, quarks and gluons, the fundamental building blocks of nuclei, are no longer confined within color-singlet entities, such as hadrons. This medium where the fundamental degrees of freedom are carried by quarks and gluons is referred to as the quark gluon plasma (QGP). Earlier results, however, could also be explained in theoretical calculations that do not require the production of the QGP in collisions. Our study of *d+Au* collisions and the π^0 spectra will provide new insight on the previous experimental observations and further constrain the alternate theoretical explanations.

Quantum ChromoDynamics (QCD) is believed to be the fundamental underlying theory that provides a basis for understanding the structure of hadrons and properties of hadronic matter. Quarks and gluons carry color charges and the interactions among quarks and gluons are mediated by gluons. QCD has two salient features: quark confinement and asymptotic freedom. Quark confinement states that quarks and

gluons must be confined to color-neutral singlet states of hadrons and there are no isolated free quarks or gluons. Asymptotic freedom describes the strength of coupling among quarks and gluons. The coupling constant, α_s, depends on the momentum transfer of the physical process. Asymptotic freedom means α_s decreases for large momentum transfer processes. It also means α_s, and hence the interaction strength among quarks and gluons, is not very strong at short distance. This running of the coupling constant provides the framework for perturbative QCD (pQCD) treatment of high transverse momentum processes where partons scatter off each other with large momentum transfer.

The properties of quarks and gluons are of great interest for experimental physics. The QGP would allow us to investigate the collective properties of bulk quarks and gluons. Lattice QCD (LQCD) provides a computational framework for solving the equations of QCD for steady-state systems with numerical methods. LQCD calculations predict that there is a transition from hadronic matter to QGP. The transition may be a smooth crossover as a function of energy density at very low net baryon density (total number of three-quark hadrons in the system), while it may be a first order phase transition at moderate-to-high baryon density. A critical point may exist at moderate baryon density. The exact location of the critical point has not been determined and is a subject of recent experimental investigations. The QGP, once formed in high-energy nucleus-nucleus collisions only exists for several to approximately ten Fermis and rapidly cools when quarks and gluons re-condense into hadrons. Application of QCD to cosmology suggests that the universe was in a QGP state during the epoch around 1 microsecond after the Big Bang. The continued expansion of the universe led to hadronization as it does in collisions at RHIC.

In order to search for and study the QGP in a laboratory experiment, the Relativistic Heavy Ion Collider (RHIC) was built at Brookhaven National Laboratory (BNL). This facility provides roughly a factor of 10 increase in the center of mass collision energy for nucleus-nucleus collisions compared to previous, fixed target, experiments. RHIC provides Au-on-Au (*Au*+*Au*) collisions to create energy densities over the extended volume necessary for the production of QGP.

Two important observations were made in early RHIC operation: the suppression of high transverse momentum particles with respect to the number predicted by binary scaling of proton-on-proton (*p*+*p*) collisions, and the disappearance of back-to-back high transverse momentum particles. These results observed in central *Au*+*Au* collisions were inconsistent with the expectation that high transverse momentum processes in central *Au*+*Au* collisions are the sum of processes in individual *p*+*p* collisions. Accounting for the experimental observations required either the presence of a dense medium causing significant amount of energy loss for traversing partons or modifications to the parton structure function of the Au nucleus leading to reduced numbers of parton scatterings in the relevant high transverse momentum range.

Starting with the RHIC operating period in 2003, an alternate collision system was used to test the dependence of Au nuclear effects on the results of *Au*+*Au* collisions. The collision system used employed deuterons in place of Au nuclei as one of the collision species. Using the *d*+*Au* collisions, further testing of the effect of modification of the parton structure functions in Au nuclei on the measurements of suppression of high transverse momentum particles from central *Au*+*Au* collisions could be made. The *d*+*Au* results can be compared with predictions from theoretical models and would then be used to test possible theoretical scenarios. It is the goal of

this dissertation to provide additional data to strengthen such arguments. It is a secondary goal here to provide information about analysis techniques that enable the use of the STAR (Solenoidal Tracker at RHIC) Barrel Electromagnetic Calorimeter (BEMC) detector subsystem, which was partially built by UCLA's Relativistic Heavy Ion group.

This dissertation is laid out as follows. Chapters 2 and 3 will provide background and introductory information for the physics involved in this work. Chapter 4 will describe the RHIC facility and the STAR detector. Chapter 5 provides details about the dataset used in the work. Chapter 6 covers analysis of detector data and measurement of particle production. Chapters 7 and 8 show the results and compare them to appropriate results from other collision species and the results of similar analyses.

CHAPTER 2

Brief Overview of Heavy Ion Collision Physics

2.1 Introduction

This chapter is an overview of the heavy ion collision physics relevant to the rest of the dissertation. This dissertation is based on nuclear collision data collected at the Relativistic Heavy Ion Collider (RHIC) at Brookhaven National Laboratory, so we will explain what that entails in these collisions. Theoretical calculations that predict the outcome of such collisions are of great interest and we will give a brief description next. In relativistic heavy ion collisions, quarks and gluons (partons) interact violently in the initial stage and create a high energy density matter and the system evolves eventually turning into hadrons through hadronization processes. The nature of produced hadrons measured in our detector depends on various nuclear effects and evolution dynamics that will be discussed. Along the way we will cover specific concepts and terminology used in the field of relativistic heavy ion physics.

2.2 Features of QCD and the Strong Interaction

The interactions among matter in the Universe manifest in microscopic scale as gravity, electromagnetism, the weak force and strong force. In the domain of nuclei, the length-scale is on the order of the Fermi (10^{-15} m) where the strong force

dominates most interactions. However, the electromagnetic and the weak interactions both play an important role in nuclear collisions through which many particles decay before they reach experimental detectors.

One goal of modern nuclear physics is to understand the properties of the strong force better. The theoretical framework that governs the behavior of the strong force is Quantum Chromodynamics (QCD). QCD is a gauge field theory that predicts the "color" charge of the quarks and gluons that make up the nucleons that constitute nuclei. It is a group theory-based framework that states quarks are found with one of 3 colors, anti-quarks are found with one of 3 corresponding anti-colors. Further, gluons, the gauge bosons of the strong force are combinations of quarks and anti-quarks, and form a color octet. Finally, QCD predicts that hadrons are made of color-singlet combinations of quarks, anti-quarks, and gluons [WN02].

The calculations in QCD are usually based on the emission or absorption of gluons between color charge carriers.[1] Each such exchange carries two weighting factor multiples, $\sqrt{\alpha_S}$, the strong coupling constant, one for each time a gluon is absorbed or emitted. For example, a quark may emit a gluon that is absorbed by another quark. The total number of gluon emissions or absorptions is two, so the weighting factor is α_S. This type of calculation is complicated by the fact that the strong coupling constant, α_S, is a running coupling constant that gets smaller as the energy scale of the gluon exchange increases. It is furthermore complicated by the fact that gluons can absorb or emit gluons just as quarks do. At low energy, the coupling constant is so large that more complex, convoluted, gluon exchanges are

[1] $qg \rightarrow q\gamma$ is an alternate strong interaction where a photon is emitted rather than a gluon. Also, quark/anti-quark formation or annihilation may occur through particles other than gluons.

more important for calculations than simple single gluon exchanges. This is in contrast to Quantum ElectroDynamics (QED) where, at low energies, the coupling constant $\alpha \approx 1/137$, so that the process of a single gauge boson exchange dominates calculations and perturbative calculations converge and are reliable.

Asymptotic freedom in QCD leads to another interesting aspect of the strong interaction among quarks and gluons. Here the interaction strength experienced between two color charges depends on the distance between them. The strong force becomes negligible at very short distances, this property of asymptotic freedom is opposite of the distance dependences in gravity and electromagnetism. Asymptotic freedom is directly related to the running of α_S in that high-energy collisions between hadrons may occur with large energy exchange in which the effective coupling constant is actually low enough that the interaction is calculable using an α_S expansion.

Lattice QCD provides another unique approach to solve QCD field equations precisely on discrete space-time [CGS86]. In this framework the field of interest is laid out as a space-time lattice and a computer algorithm iterates over the lattice points for a converged solution. The calculations of lattice QCD (LQCD) require large computing resources and fast processing, carrying them out pushes the limits of computational capacity. Recent results of lattice QCD suggest that although the transition to QGP should occur at RHIC, the baryon chemical potential may be such that the phase transition is smooth, rather than abrupt. Figure 2.1 shows the phase-diagram for QCD indicating possible existence of a critical point at finite baryon chemical potential [Bla06].

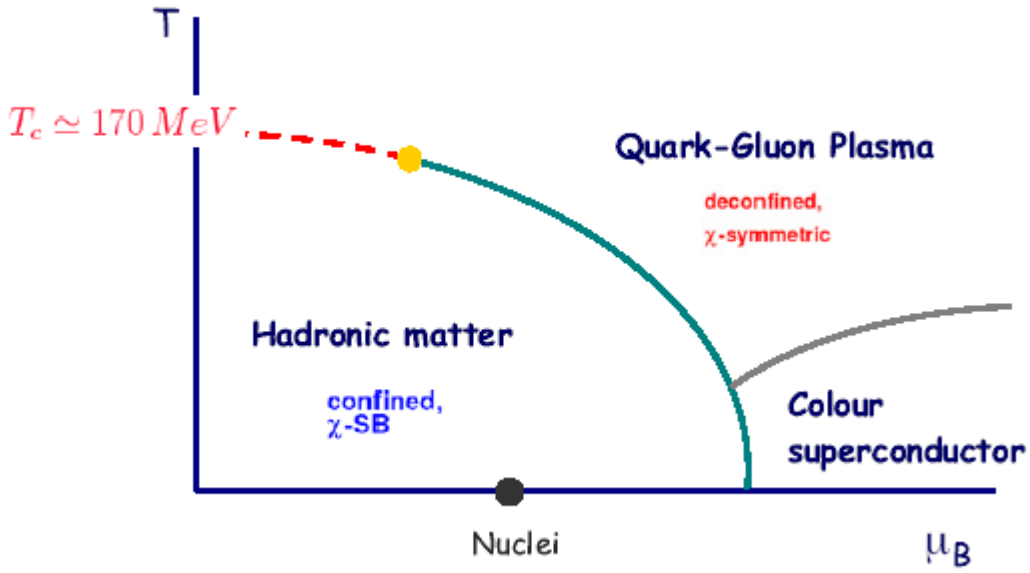

Figure 2.1: Schematic phase-diagram of QCD matter in temperature and baryon chemical potential showing the where the transition from hadronic matter to QGP occurs.

Lattice QCD has also been employed to show that even in the QGP phase, the entropy density present is below that of a non-interacting gas of particles. This is shown in Figure 2.2, which displays the temperature dependence of the pressure divided by the entropy density for several possible numbers of dynamical quarks [Ada05b]. LQCD predicts that the QGP state will result in lower pressure, and therefore entropy density, than a non-interacting plasma would have. This means that there are still interactions in the QGP phase even when the temperature reaches a few times the critical temperature.

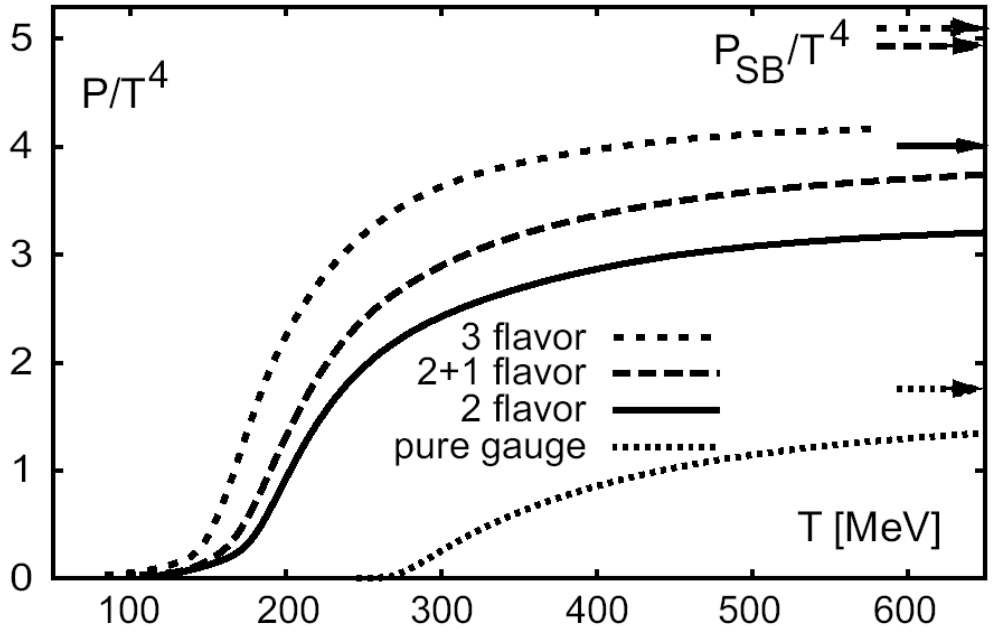

Figure 2.2: LQCD calculation result from [Kar02], as discussed in [Ada05b]. Pressure divided by T^4 is given for strongly interacting matter, for possibilities for the number of dynamical quarks. The arrows on the right correspond to the Stefan-Boltzmann pressures. This shows that some interactions must remain in the QGP.

Although LQCD provides interesting information about thermodynamics quantities and where to look for QGP, pQCD is the framework of choice for calculating most experimental observables. For this work, the applicability of pQCD at high energy is of primary importance. The energy we are talking about here is the scale involved, typically the momentum exchanged, when quarks and gluons scatter off each other. That is, we are interested in determining the cross-section for production of some particle (*C*) when two particles (*A* and *B*) collide.

The cross-section for particle production is given by equation (1.1)[Col84].

$$E_C \frac{d\sigma}{d^3 p_C}(AB \to CX) = \sum_{abcd} \int_0^1 dx_a \int_0^1 dx_b f_A^a(x_a) f_B^b(x_b) \frac{1}{\pi z_c} \frac{d\sigma}{dt}(ab \to cd) D_c^C(z_c) \tag{1.1}$$

Here A and B are incoming particles, C is the particle being studied, a,b,c and d are partons that are summed over, t is the momentum transfer (this will be covered again shortly), and z_c is the momentum fraction c contains in C.

The cross section above is dependent on knowledge of the structure function, $f_A^a(x_a)$, and the fragmentation functions, $D_c^C(z_c)$. The structure functions give the probability that parton a will be found with a fraction x of the momentum of the particle A in the light-cone frame. This x is called Bjorken x. The fragmentation functions give the probability that parton c will produce a hadron C at a given momentum fraction z. The structure functions and fragmentation functions are measured in other experiments. Armed with these functions, the pQCD framework allows us to calculate the desired cross section.

It should be noted that the calculation described above is only a general outline, and the full formalism necessary for these calculations depends on the particular incoming and outgoing particles, as well as any additional QCD fields present. Generally, however, calculations in pQCD are complicated by the fact that the energy scale of the interaction between partons a and b above determines the strength of the strong coupling constant α_S and the evolution of the structure functions follows the DGLAP equations [WN02, GL72, Lip75, AP77, Dok77]. Thus, in interactions at low energy-scale, more complicated interactions dominate. These interactions have four or more verticies and carry over coupling strengths of α_S^2 or greater. As stated in

[WN02] (where NLO and NNLO stand for "next to leading-order" and "next to next to leading-order" pQCD, respectively):

> The precision of the contemporary experimental data demand that NLO (or even NNLO) DGLAP evolution be used in comparisons between QCD theory and experiment.

The formalism above applies to elementary particle collisions. For larger systems of particles, such as nucleus-nucleus collisions, a medium is produced as the nuclei collide. In such collisions, particle formation and transmission are effected by the medium. Medium effects must be taken into account when considering scenarios for explaining particle production in nucleus-nucleus collisions. Thus, the most commonly observed medium effects are discussed in the next section.

2.3 Nucleus-Nucleus Collisions

When possible, particles are studied by isolating them and observing them. Early work on quarks and gluons started in this way.[2] It was also clear, from early experimental results, that $p+p$ collisions did not produce free quarks or gluons. Theorists, therefore, considered different scenarios for studying these particles [Kok69, IK65, Pac66, BDG66, It070, ILL74]. From lattice calculations, quarks and gluons will be deconfined, no longer associated with a color neutral hadron, if the temperature is over 150 MeV [MS81, MS81b, KPS81, Eng81, Ch074]. It is also

[2] The introduction in this paragraph closely follows that in [CGS86]

clear that this temperature has to be present in a semi-thermodynamically meaningful system. That is, some reasonably large number of particles must be present so that the system has a meaningful temperature and the deconfinement could exist over a distance scale larger than that of a hadron. This temperature can be reached in nucleus-nucleus collisions, as described in the following.

The predicted temperature corresponds to roughly 1.0 GeV/fm^3. The energy density in collisions can be calculated using the formula below.

$$\varepsilon = \left(\frac{dN_h}{dy} \right)_{y=0} \frac{w_h}{\pi R_A^2 \tau_0} \tag{1.2}$$

where dN_h/dy is the rapidity density of hadrons produced in the collision, w_h is the average energy of the hadrons, R_A is the nuclear radius, and τ_0 is the formation time of the medium. For *Au*+*Au* collisions at RHIC ($\sqrt{s_{nn}}$ = 200 GeV) the energy density is 5.0 GeV/fm^3 [Ent03].

In this section we will present a brief discussion of the ideology and terminology of nucleus-nucleus collisions. The primary goal here is to provide description of variables and their use in relativistic heavy-ion collisions. Some of this material is also covered in Appendix C.

The most prominent set of variables used in particle physics are the Mandlestam variables. Figure 2.3 shows the standard labeling of particle momenta in two particle interactions that produce two outgoing particles.

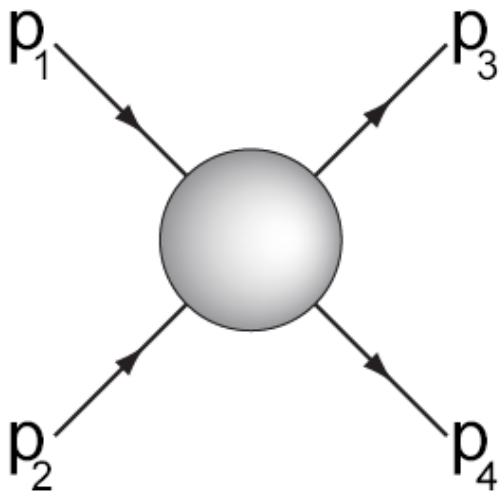

Figure 2.3: Diagram showing four particles (two entering, two exiting) defining the four momentum vectors involved in the Mandelstam variables.

For these trajectories, there are three Mandlestam variables: *s*, *t*, and *u* defined as follows:

$$\begin{aligned} s &= (p_1 + p_2)^2 = (p_3 + p_4)^2, \\ t &= (p_1 - p_3)^2 = (p_2 - p_4)^2, \\ u &= (p_1 - p_4)^2 = (p_2 - p_3)^2 \end{aligned} \tag{1.3}$$

Here, $\sqrt{s}$ is the energy contained in the collision system of p_1 and p_2, while $\sqrt{t}$ is the energy transferred from particle 1 to particle 3 during the interaction.

In collider experiments, the laboratory is usually placed in the center of mass frame. When the collisions are between two asymmetric nuclei, the center of mass does not correspond with the laboratory frame. In these collisions, however, the interactions are between nucleons, not nuclei. Thus, the laboratory remains very nearly in the center of mass of the individual nucleon collisions.

Particles originating from relativistic heavy ion collisions are characterized by the following parameters: (A) their particle type, (B) transverse momentum, p_T, of the

particle, and (C) rapidity, y. Definitions of some of these parameters are now given; additional parameter definitions can be found in Appendix C. The azimuthal angle ϕ is defined as:

$$\phi = \tan^{-1}\left(\frac{p_y}{p_x}\right). \tag{1.4}$$

(where p_x, p_y, p_z are the components of the momentum p, with p_z being along the beam direction). The rapidity is defined by the equation:

$$y = \frac{1}{2}\ln\left(\frac{E + p_z}{E - p_z}\right). \tag{1.5}$$

In practice, however, the pseudorapidity η is sometimes used since it does not require particle idenfication, whereas the rapidity depends on the mass of the particle. The pseudorapidity is defined by

$$\eta = -\ln\left(\tan\left(\frac{\theta}{2}\right)\right). \tag{1.6}$$

The relationship between pseudorapidity and rapidity is discussed in detail in Appendix F.

Relativistic nucleus-nucleus collisions occur in highly distorted space-time. The most common way to discuss the physics of the situation is to look at the individual nucleons. In this work the energy in a nucleon-nucleon collision is $\sqrt{s_{nn}}$ = 200 GeV. The energies that we are looking at here (100 GeV per nucleon in the laboratory) correspond to a relativistic gamma $\gamma \sim 100$. The resulting length contraction and time dilation give rise to the collision evolution shown in Figure 2.4. Figure 2.4 shows the evolution of a relativistic nucleus-nucleus collision starting with the approaching nuclei on the left, and developing into hadrons on the right.

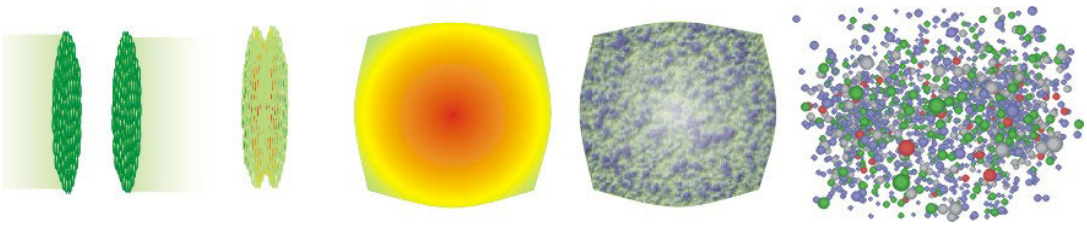

Figure 2.4: The evolution of a nucleus-nucleus collision, such as *Au+Au*, is shown from left to right. First the nuclei approach each other as flattened discs. The initial collision produces a dense, high-energy state that quickly equilibrates. Ultimately the partonic medium coalesces to form hadrons as the particles fly apart. Figure from [Bas04].

The stages of nucleus-nucleus collisions are important for discussion of effects observed. That is, there are many theoretical descriptions of the effects that occur in nucleus-nucleus collisions, and they often depend on the state of the system at a various points during the collisions. First, the colliding nuclei approach and begin to overlap, this is the initial state. Immediately following the collision, the system contains the colliding material at high energy and density. The system then equilibrates with an energy density high enough that the individual partons are deconfined. As the system expands and cools the deconfined matter hadronizes, but the hadrons continue to interact. Finally the hadrons separate enough that they are able to freely stream through the detector [Sor03]. QGP occurs during the deconfined phase, and the hadrons detected carry information about the deconfined phase.

2.4 Nuclear Effects

The search for QGP requires careful consideration of all aspects of the collisions in which it may be produced. After early observations in *Au+Au* collisions, much discussion was put into strengthening the evidence for QGP. It was determined that some of the observations in *Au+Au* might be due to the Au wavefunction itself, and a

control experiment, deuterons-on-Au (d+Au) was adopted to disentangle some complications [VG02].

Due to the various stages of nucleus-nucleus collisions and the complexity of the wavefunction of each nucleus, calculating production cross-sections can require many theoretical considerations. In this section we will cover the most important nuclear effects relevant to this work. This will proceed in the following order. First we will discuss some basic theoretical tools that are used to explain observations. Then we will discuss some of the physical processes that are observed when the theoretical tools are employed.

2.4.1 Glauber Model

High-p_T particle production in heavy ion collisions is due to parton interactions and is expected to scale with the number of parton-parton, and therefore nucleon-nucleon binary collisions in each event. The number of nucleon-nucleon collisions in an event is referred to as N_{bin}, which is also used to refer to the average number of binary collisions over an ensemble of collisions.

The method employed to determine N_{bin} is generally referred to as the Glauber model. It is based on the application of multiple-diffraction theory to the nucleus [2]. The Glauber Model is a geometrical description of the overlapping regions of colliding nuclei. It allows nucleons to interact multiple times as the nuclei cross each other.

The exact value determined for N_{bin} depends not only on the collision system, but also on the biases in the experimental setup. N_{bin} is only fixed for a certain impact parameter for a collision, so an average value of N_{bin} taken across all collision

configurations sampled by the detector. Thus, the value of N_{bin} depends on a statistical average across various impact parameters as well as being a statistical description for a fixed impact parameter. Specifically, if the experiment preferentially collects data when an event has more than some number of outgoing hadrons, then the collected data will be biased towards events with more interactions, and therefore, events with smaller impact parameter.

The Glauber model is thus employed to determine N_{bin}. It must be determined for each trigger mechanism in any experiment it is used for calculations. The determined N_{bin} is then used to compare measured quantities across different data sets. For example, to compare *d+Au* collisions to *p+p*, the nuclear modification factor may be employed:

$$R_{dAu}(p_T) = \frac{d^2N_{AA}/dp_T d\eta}{N_{bin} d^2N_{pp}/dp_T d\eta} \tag{1.7}$$

If the Glauber model were the only interesting physics going on in nucleus-nucleus collisions, Equation 1.7 would be sufficient for predicting cross sections. Instead, additional effects must be taken into account. These additional effects are usually taken as empirical effects that describe the shape of production distributions. In some cases theoretical explanations have been suggested but their numerical details are still being developed and argued.

2.4.2 Cronin Effect

Analysis of the nuclear modification factor in p-on-Au (*p+Au*) collisions led to the parametrization of R_{pAu} due to the Cronin effect [Arn90]. This effect predicts that R_{pA} will start below unity at low p_T and rise above unity at intermediate p_T.

An earlier description of the Cronin effect can be found in [Che03]:

> [T]he Cronin effect originates from initial state multiple parton scattering and a similar behavior is expected in high energy collisions although the effect could become smaller when the original jet spectra become much flatter.

Calculations based on this interpretation of the Cronin effect are usually based on considering the p_T distribution of the partons in the colliding nuclei [Che03].

For the collisions under consideration, this explanation does not provide acceptable results. However, even though there is not an-encompassing explanation for the effect, the rise in low to intermediate-p_T particle production is still a feature of particle production distributions.

2.4.3 Shadowing and Saturation

In the initial-state configuration of a nucleus-nucleus collision, shadowing and saturation contribute to modify the distributions of partons available for collision.

Shadowing refers to the deviation from the Glauber model. That is, the nucleons cannot be treated as independent collisions. However, the effects of additional nucleons contribute to both shadowing and anti-shadowing effects.

Gluon saturation refers to a condition in nuclei where low fractional momentum gluon states may be depleted due to the lower momentum gluons merging to higher

momentum. A similar depletion occurs in quark structure functions [Arn90]. This initial state effect

Gluons are important, however, for high-p_T jet production in heavy ion collisions. In these collisions a large portion of the high-p_T hadron production comes from fragmentation of a gluon jet.

Figure 2.5 shows a comparison of R_{pAu} for two possible models incorporating shadowing and saturation effects. The EKS98 shadowing refers to a parametrization using a global fit of data [EKS99]. The HIJING [GGX03] result showed highlights the results from the standard high-energy collision simulator. HIJING does not take into account the momentum scale of the interactions needed for determination of $R_{pAu.}$.

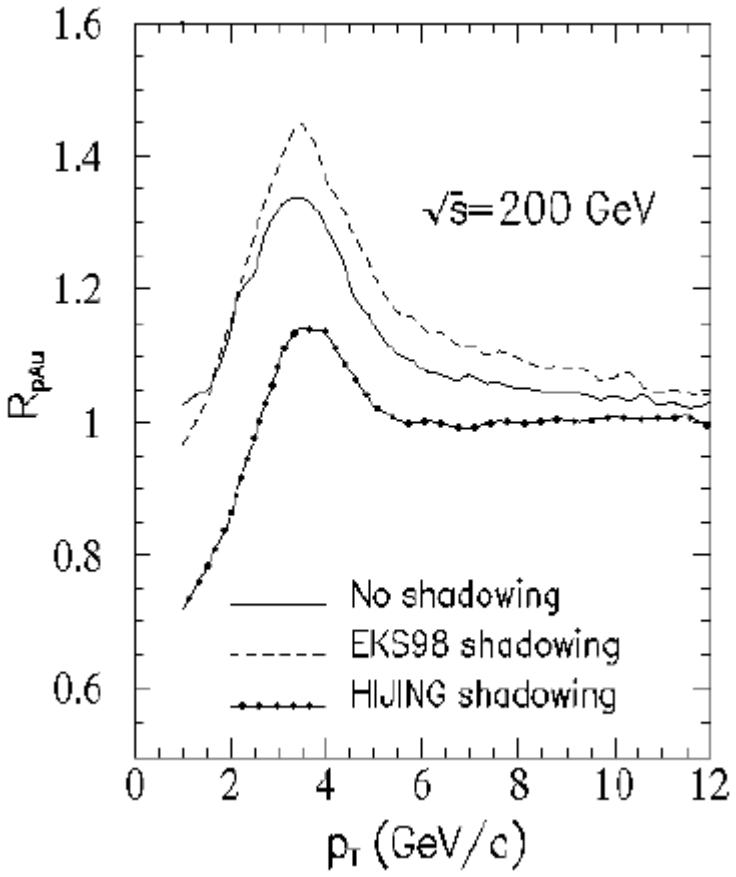

Figure 2.5: Figure is from [32]. Comparison of R_{pAu} for charged particles at RHIC energies is made. Three parametrizations of gluon shadowing, or low momentum fraction saturation, are compared. This figure shows the volatility of R_{pAu}, but it also shows the general structure of the distributions.

2.4.4 Final-State Hadronic Scattering

High-p_T hadrons formed in nucleus-nucleus collisions are also affected by the material created in the collisions. The formation time for a hadron fragmenting from a high-p_T parton after a large momentum transfer process is very short. Typically the

formation time is on the order of 1fm, and partons have well-established wavefunctions by the time they have traversed 10 fm [GGX03].

The fireball produced in RHIC *Au+Au* collisions has a size of $R(\tau) = 8\text{fm} + 0.5\tau$ fm [GGX03]. Where τ denotes local proper time. Thus, the hadrons produced at large momentum transfer, must do so within the collision fireball, where they are generally melted if there is a QGP. In the absence of medium events, or after traversing the fireball, hadrons emerge from the collision. Produced hadrons are then subject to final-state interactions with the other hadrons produced during the collision.

Qualitative examination of this situation was carried out in [GGX03]. A simple model was used, where dependences of cross sections (both coherent and incoherent) are ignored. The goal of the investigation was to determine whether or not the final-state interactions could produce effects on the order of those seen with *Au+Au* collisions, without invoking the QGP. Their result was that only one or two hadronic interactions between high-p_T fragmentation products and hadronic material in the expanding fireball were required to reduce the effective R_{AA} by a factor of more than two. Such interactions would depend on the cross-sections for interaction of the different particle species. No significant dependence on species is seen at high p_T. Thus final state hadronic scattering is not able to predict the observed particle distributions [Ada06].

2.5 High-p_T Hadron Production and pQCD

One source of motivation for studying high-p_T hadrons is the early results at RHIC. Figure 2.6 shows the early STAR results for charged hadrons in *Au+Au* collisions [Adl02]. The most central collisions (0-5%) are compared to two bins of

peripheral collisions (40-60% and 60-80%). The results are normalized using $<N_{bin}>$ determined from Monte Carlo Glauber calculations.

Due to the various model implications, high-p_T particle production is of great interest, and another source of motivation for study. At sufficiently high p_T, the soft processes, and final-state hadronic interactions will have less effect. Also, for RHIC energies, high-p_T suppression may be explained by the formation of QGP during the early stages of *Au*+*Au* collisions.

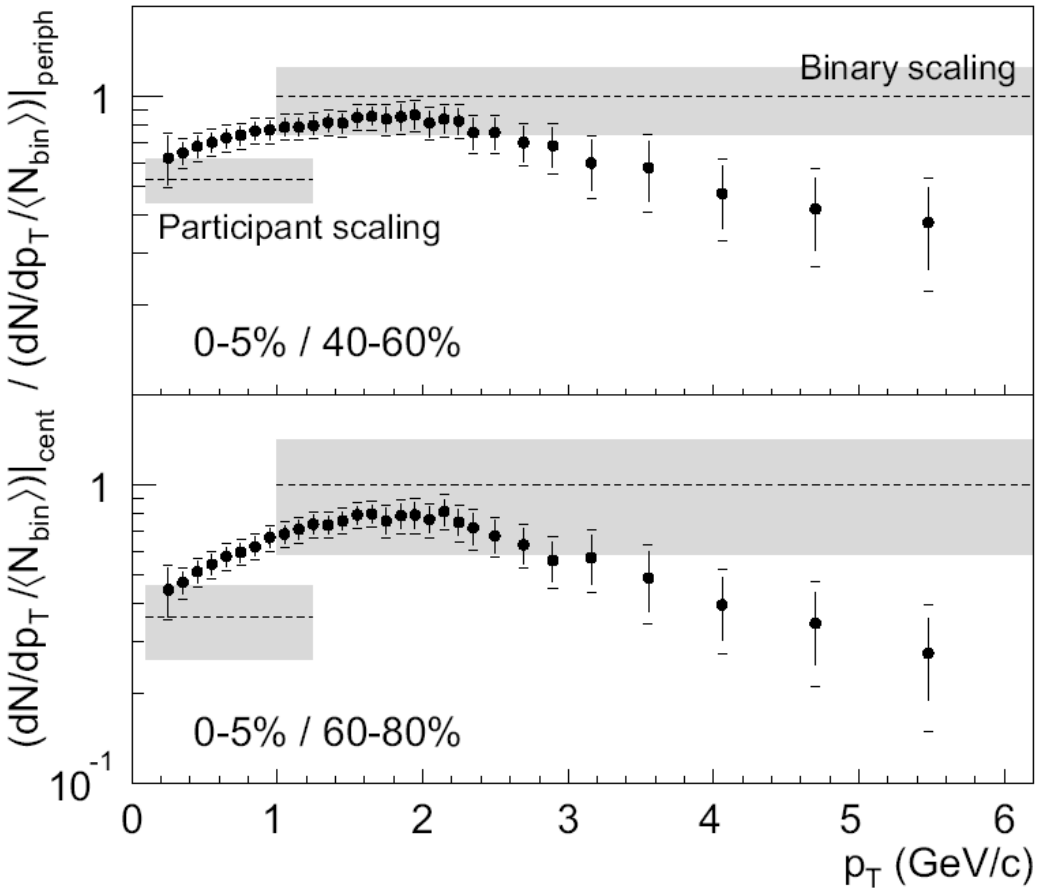

Figure 2.6: STAR results for *Au+Au* collisions [Adl02] showing a suppression in high-p_T hadron production in *Au+Au* collisions at $\sqrt{s_{nn}}$ = 130 GeV/c. The result is given by comparing the production rates, normalized to $<N_{bin}>$ calculations for the collision centralities compared. (0% central means fully overlapping nuclei.)

Hard scattering processes, as discussed earlier, are calculated in pQCD formalism. The calculations require the knowledge of the quark and gluon structure functions of the proton and the fragmentation functions for the production of the desired hadron by all out-going quarks and gluons.

pQCD provides a framework for calculation of cross sections in *p+p* collisions at intermediate to high-p_T. In *Au+Au* collisions, however, simple binary scaling is not

sufficient to describe results. Several conceptual effects described above, beyond binary-scaled pQCD, allow pQCD to predict qualitatively similar results to those seen in *Au*+*Au* collisions. One goal of relativistic heavy ion physics is make measurements accurate enough to enable quantitative comparisons to models used to explain the observed effects. For example, accurate measurements may suggest that k_T-broadening is not sufficient to explain the Cronin effect.

d+*Au* collisions provide an alternative to *Au*+*Au* collisions that shares some of the qualities of *Au*+*Au* collisions, but not all of them. These collisions will not eliminate all possible explanations for the *Au*+*Au* suppression, but the results definitely limit the possible models for the gluon densities in the Au nucleus.

pQCD can be applied in general collision systems for high-p_T hadron production. These production channels exclude the soft processes outside the domain of pQCD. High-p_T particle production in nucleus-nucleus collisions also exhibits modification due to some nuclear and final-state effects. These effects lead to suppression in *Au*+*Au* collisions. At sufficiently high p_T, Cronin enhancement is eliminated. The appropriate gluon densities in the Au nucleus could then be determined by the high-p_T dependence of hadron production in *d*+*Au* collisions. Any such results are, however, model dependent and require careful consideration before incorporation in updated models for high-p_T production.

This dissertation is concerned with the measurement of π^0s at relatively high p_T in *d*+*Au* collisions. In these collisions it is important to determine how the gluon densities in the Au nucleus, the Cronin effect, and possible final-state effects may apply. The degree of accuracy found in the application of scaled *p*+*p*-based pQCD

results to the π^0 production in these collisions will help understand these effects, and limit the uncertainty due to gluon saturation in the Au nucleus.

2.6 Application to π^0

A large momentum transfer interaction producing an inelastic scattering will produce partons with large transverse momentum (p_T). Each parton has an associated fragmentation function $D_c^{\pi}(z_c)$ for the production of π^0s. They may also produce other hardons, but neutral mesons such as the π^0 provide a unique opportunity compared to other hadrons. π^0s are the lightest mesons and should be produced in abundance, relative to other mesons.

Once produced, π^0s decay electromagnetically with a lifetime of about $10^{-17} s$. This means they cannot be directly measured in a detector, and that they do not usually decay within the collision fireball (which only survives about $10^{-21} s$). The former condition means that the decay products of the π^0, photons, make up the bulk of any simulation analysis of the detector. The latter, however, means that π^0s, like other hadrons, are susceptible to final-state interactions.

CHAPTER 3

Selection and Reference Data

3.1 Introduction

The physics of relativistic heavy ion collisions and possible QGP formation was discussed in the last chapter. The observations of low R_{AA} and high-p_T suppression in *Au+Au* collisions led to the need to collect data in *d+Au* collisions at RHIC. The detectors at RHIC thus have been used to collect data from such collisions at $\sqrt{s_{nn}}$ = 200 GeV. For this work, we chose to analyze this data to measure π^0 production cross sections. It remains, for this chapter, to give the background measurements and production details driving these choices, and to show how this work fits into the general scheme of available data.

This chapter will showcase the data from *Au+Au* and *p+p* collisions that suggest the formation of QGP. It will further provide the reference data necessary for the calculations that are made later in the dissertation. Finally, it will describe the direct benefit of the measurements presented in this dissertation.

3.2 QCD Model Calculations

In this chapter earlier results are presented. These results are generally presented relative to a theoretical description. Thus it is necessary to discuss the theoretical curves that will be used in this chapter. The theory curves used depend on the dataset being considered.

Three pQCD calculations will be used for comparison. The three calculations are the following. One is from Wang, and is used for evaluation of SPS results (with emphasis on k_T) [Wan98]. The two other calculations are the "Kretzer" [Kre00], and the "Kniehl-Kramer-Pötter" , KKP [KKP00]. The largest differences between these calculations are their fragmentation functions and parton structure functions.

The calculation used by Wang is the single-inclusive spectra for π^0 and is calculated as follows:

$$\frac{d\sigma_h^{AA}}{dyd^2p_T} = K\sum_{abcd}\int d^2b\int d^2r t_A(r)t_A(|\mathbf{b}-\mathbf{r}|)\int dx_a dx_b \\ d^2k_{aT}d^2k_{bT}g_A(k_{aT},Q^2,r)g_A(k_{aT},Q^2,|\mathbf{b}-\mathbf{r}|) \\ f_{a/A}(x_a,Q^2,r)f_{b/A}(x_b,Q^2,|\mathbf{b}-\mathbf{r}|)\frac{D^0_{h/c}(z_c,Q^2)}{\pi z_c}\frac{d\sigma}{d\hat{t}}(ab\to cd) \tag{3-1}$$

In this case, $f_{a/A}$ is based on the HIJING parametrization [WG91, WG94], and g_A is the initial k_T distribution.

The remaining two pQCD models for hadron production, Kretzer and KKP, will be used in section 3.4 for comparison with PHENIX data. They can be contrasted as stated in [Adl03d]:

These two sets differ mainly in that the gluon-to-pion fragmentation function, D_g^{π}, is greater in the KKP set. This difference is exhibited primarily at low p_T because of the dominance of gluon-gluon and gluon-quark interactions for p_T below ~10 GeV/c.

3.3 Background Data

The CERN SPS experiments measured π^0 production in *Pb*+*Pb* collisions at $\sqrt{s_{NN}} = 17.4\,\text{GeV}$ [Agg98]. Figure 3.1 shows their results, along with theoretical fits, for this collisions species as well as SPS *S*+*S* data. In this figure, the π^0 production at SPS in central collisions was used to test basic theoretical implications where a dense medium may shift the high-k_T portion of the spectrum towards lower k_T [Wan98].

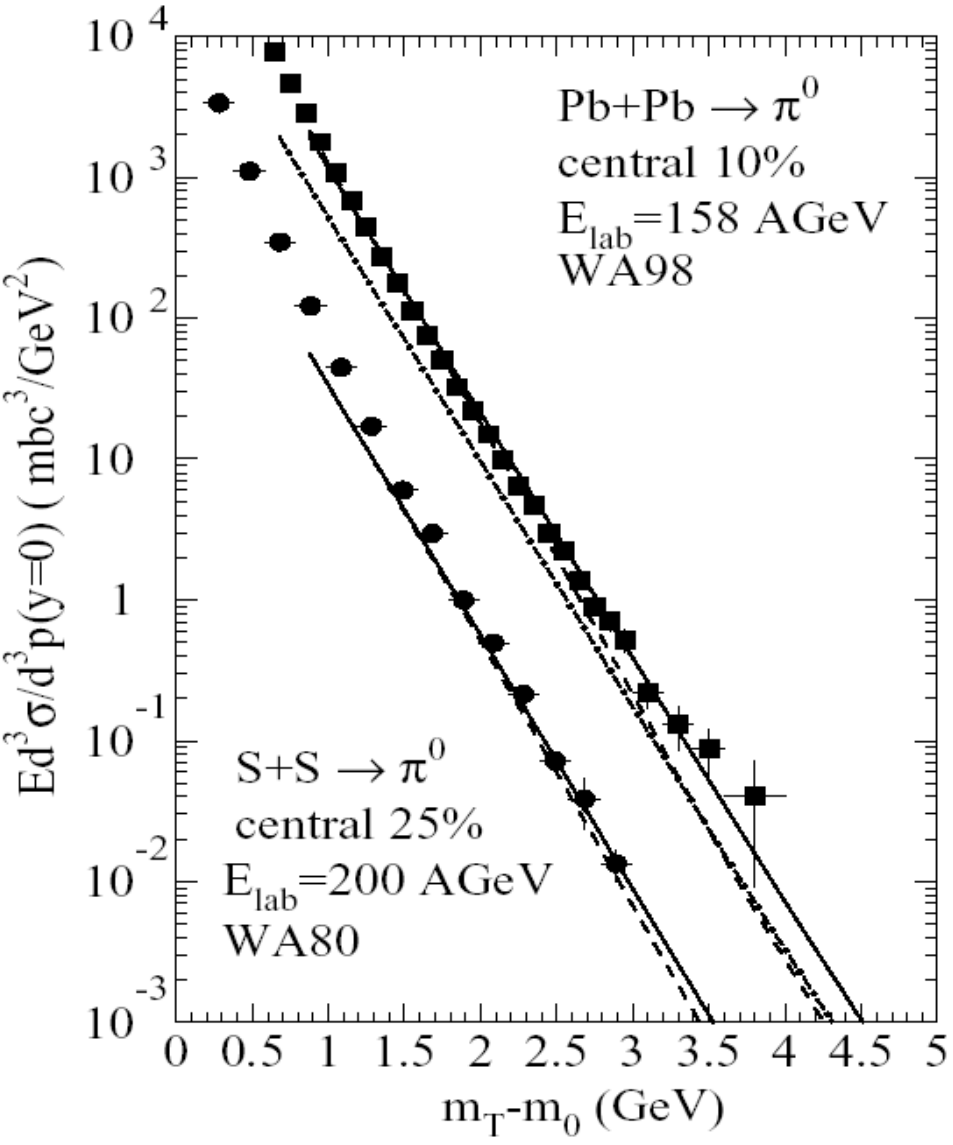

Figure 3.1: Hadron production in earlier nucleus-nucleus collisions [Wan98]. This figure shows the results from WA80 and WA98 [Alb98, Wan98], along with pQCD calculations for single-inclusive π^0 production. This π^0 production data shows very little deviation from binary-scaled p+p results.[1]

[1] This figure uses transverse energy, $k_T = m_T - m_0 = \sqrt{p_T^2 + m_0^2} - m_0$, which is a more appropriate variable in cases where a thermal distribution is expected.

There are several theory curves drawn on Figure 3.1. The solid lines show pQCD calculations with initial-k_T broadening. The dashed lines do not include this broadening. For these investigations, the primary reason for plotting k_T ($m_T - m_0$) is because a thermal distribution is expected. If the energy of the outgoing particles is reduced by interactions with a dense medium, the reduction was expected to be an overall decrease in k_T. However, the partons in a nucleus have an internal k_T before the collision, and this may influence the k_T of any outgoing particles. Another curve, where the transverse energy is reduced by 0.2 GeV is shown with a dot-dashed line. From this curve it is clear that the data is too high to be consistent with even that relatively small energy loss.

Given the data shown above, *Au+Au* collisions at RHIC provide a medium that is interacting with high-p_T hadron production. There are many possible reasons why the RHIC observations were qualitatively different than those made at the SPS. To strengthen the case for formation of a dense medium, additional measurements at RHIC energy were made.

d+Au collisions were selected to provide an alternate collision system at RHIC. In such collisions the wavefunction of the Au nucleus still participates in the collisions, but there is no high-energy medium through which high-p_T particles must pass. Figure 3.2 shows a drawing of the two collisions systems, *Au+Au* and *d+Au*. In that figure the upper panel shows how a hard scattering in a *Au+Au* collision must traverse the high-energy-density medium created by the interacting nuclei, while the lower panel shows that similar particles ejected from a *d+Au* would not have to traverse such a medium. The decision to run this collision type came from the observation, shown in Figure 3.3, of high-p_T particle suppression in *Au+Au* in central

collisions, and also from disappearance of the away-side jet observed as a missing peak at $\Delta\phi = \pi$.

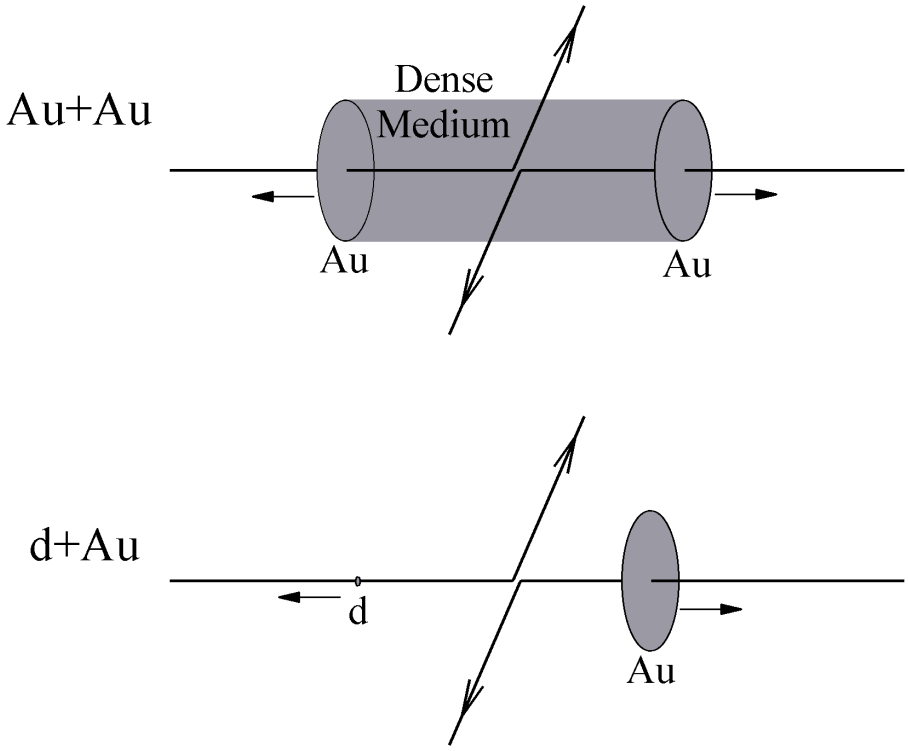

Figure 3.2: *Au+Au* and *d+Au* collisions are show in the diagram above. Lines representing parton collisions are shown the same in each panel. The upper panel shows that particles produced in *Au+Au* collisions must traverse the dense medium. The lower panel indicates that no such dense medium must be traversed in *d+Au* collisions.

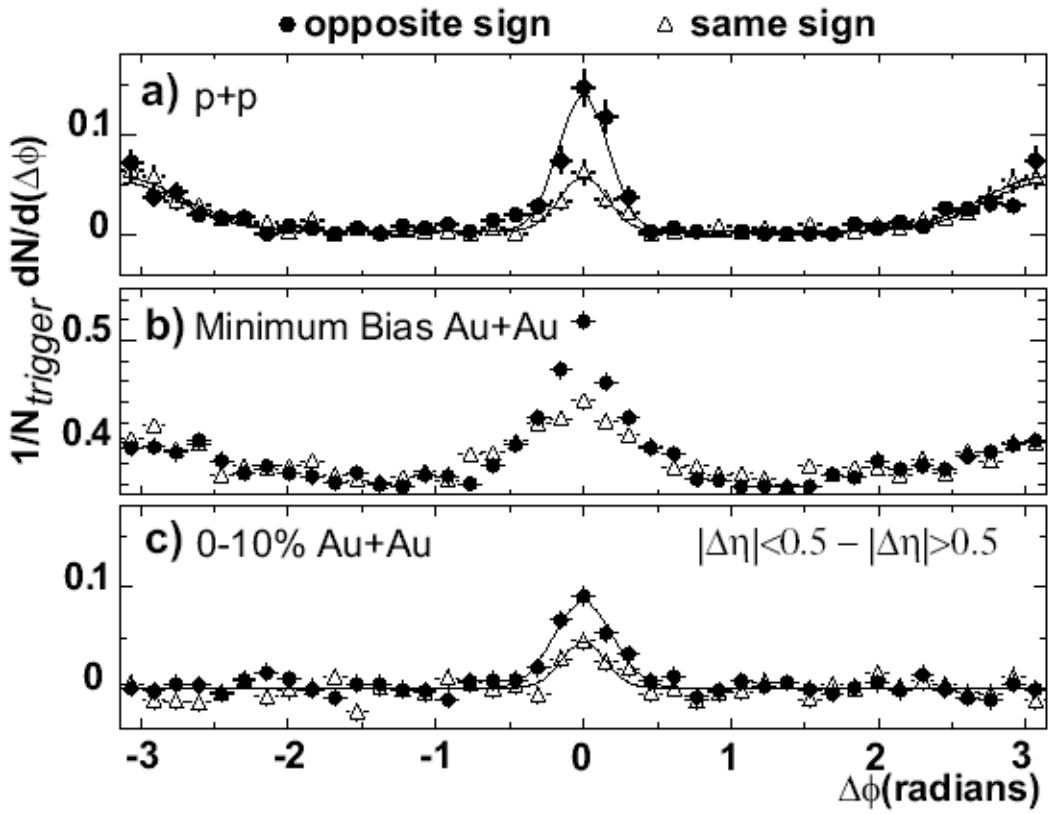

Figure 3.3: Figure take from [Adl03]. The azimuthal correlation of hadrons is shown. The distributions shown are for *p*+*p*, and binary-scaled *Au*+*Au*. The *Au*+*Au* collision data is separated into minimum bias and central (0-10%) collisions. The *Au*+*Au* central data shows no enhancement near π, where the away-side jet is expected.

3.4 Reference Data

In order to compare *d*+*Au* collisions to *p*+*p* and *Au*+*Au* collisions, appropriate reference data from those collisions is needed. In this section several reference data sets will be shown. The datasets come from STAR and PHENIX p+p, Au+Au, and other *d*+*Au* analyses.

Figure 3.4 shows cross-section results from the PHENIX experiment for π^0 production in 200 GeV *p*+*p* collisions. This data forms the basis for comparison to

p+p measurements. The raw data is also given in Table 3.1. The figure shows the data together with the Kretzer and KKP pQCD NLO calculations in the first panel. The second panel shows the uncertainty. The final panel provides a quantitative comparison of the theoretical results. Note that the KKP fragmentation function results agree better than the Kretzer results.

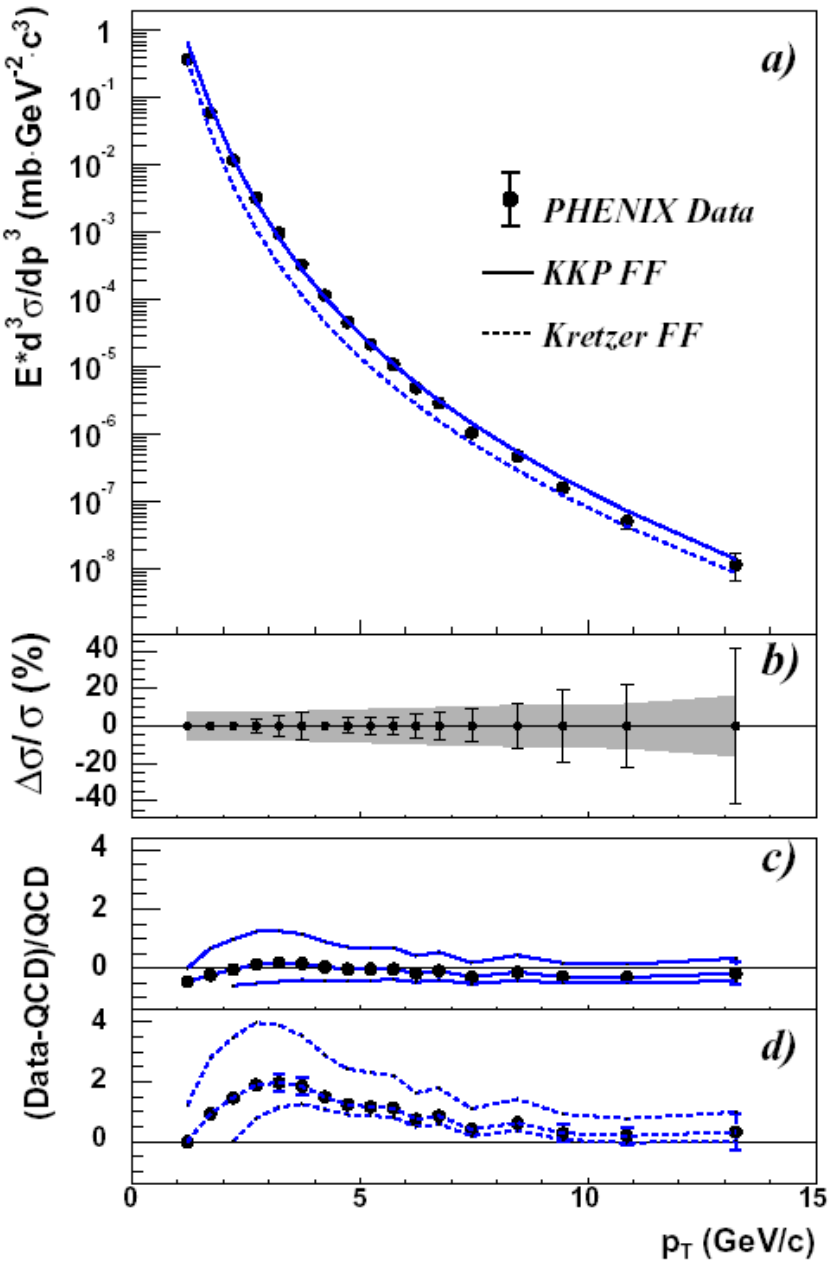

Figure 3.4: π^0 production in p+p collisions at PHENIX [Adl03d]. The upper panel shows the inclusive cross section. The middle panel shows the statistical and systematic uncertainties. The lower panel compares the observed data with the Kretzer and KKP versions of the pQCD NLO calculation.

The PHENIX results are well described by a power-law representation, based on the standard format [Alb90].

$$\frac{d^3n}{dp^3} \sim C\left(1+\frac{p_T}{p_0}\right)^{-\alpha} \qquad (3\text{-}2)$$

For the PHENIX data, the fit parameters are C = 393 mb GeV^{-2} c^3, p_0 = 1.212 GeV/c, and α = 9.97. Using this equation, we will compare the results developed in this work to this standard p+p π^0 result.

Table 3.1: Results for π^0 production at PHENIX in p+p collisions at $\sqrt{s_{nn}}$ = 200 GeV [Adl03d].

P_T bin	p_T* (GeV)	Cross Section (mb GeV^{-2} c^3)	Stat. Error		Syst. Error	
1.0-1.5	1.215	3.73E-01	6.12E-03	(1.6%)	0.02731	(7.3%)
1.5-2.0	1.719	6.05E-02	1.08E-03	(1.8%)	0.004284	(7.1%)
2.0-2.5	2.223	1.22E-02	3.01E-04	(2.5%)	0.000864	(7.1%)
2.5-3.0	2.726	3.31E-03	1.18E-04	(3.6%)	0.000238	(7.2%)
3.0-3.5	3.228	9.98E-04	5.65E-05	(5.7%)	7.28E-05	(7.3%)
3.5-4.0	3.73	3.39E-04	2.46E-05	(7.3%)	2.59E-05	(7.7%)
4.0-4.5	4.232	1.19E-04	2.91E-06	(2.4%)	9.89E-06	(8.3%)
4.5-5.0	4.733	4.73E-05	1.99E-06	(4.2%)	4E-06	(8.5%)
5.0-5.5	5.234	2.21E-05	1.10E-06	(5.0%)	1.93E-06	(8.7%)
5.5-6.0	5.735	1.11E-05	5.01E-07	(4.5%)	1.03E-06	(9.2%)
6.0-6.5	6.236	5.00E-06	3.17E-07	(6.3%)	4.76E-07	(9.5%)
6.5-7.0	6.737	3.00E-06	2.30E-07	(7.7%)	2.95E-07	(9.8%)
7.0-8.0	7.452	1.08E-06	9.53E-08	(8.8%)	1.09E-07	(10.10%)
8.0-9.0	8.457	4.85E-07	5.83E-08	(12.00%)	5.25E-08	(10.80%)
9.0-10.0	9.46	1.64E-07	3.17E-08	(19.30%)	1.81E-08	(11.00%)
10.0-12.0	10.861	5.23E-08	1.17E-08	(22.40%)	6.14E-09	(11.70%)
12.0-15.0	13.25	1.19E-08	4.91E-09	(41.30%)	1.89E-09	(15.90%)

The π^0 production measurements are one of many hadronic channels for observing high-p_T hadron suppression. Thus far STAR has limited data on π^0 production at mid-rapidity. STAR has measured other channels readily, due to the

strength of its charged particle detection system. Some of these results were shown in Chapter 2, and more will be shown in Chapter 8. For that reason the data is not shown here. However, we do state that STAR measurements in *Au+Au* collisions show a significant suppression of high-p_T hadrons. In Figure 3.5 Results from the RHIC collider are compared to those from the SPS and theoretical predictions for R_{AA} from the Large Hadron Collider (LHC). Those results are compared to pQCD calculations for these collisions including shadowing, the Cronin effect, and jet quenching. The bands show the possible impact from different shadowing configurations.

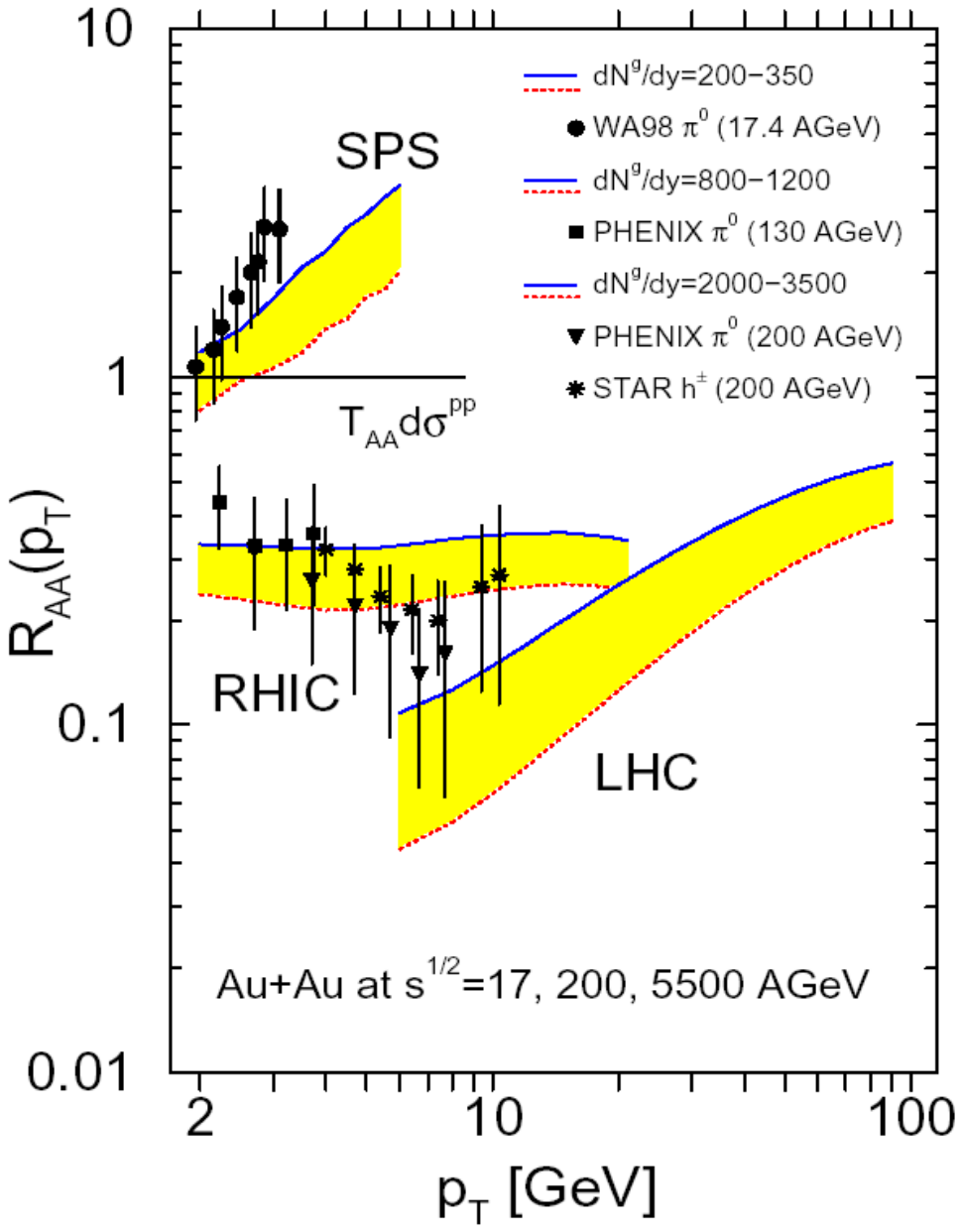

Figure 3.5: Figure from [VG02]. This figure shows SPS [Agg98], RHIC [Adc02, Adl02, Ent03b, Mio03, Kun03], and projected LHC results. The theory bands refer to smaller (larger) initial gluon density for the solid (dotted) lines. π^0s from WA98 and PHENIX, and charged hadrons from STAR, are shown. (Note, AGeV in figure is actually $\sqrt{s_{nn}}$.)

3.5 π^0 from *d+Au*

We have discussed the measurement of π^0 cross-sections from other experiments. We wish to measure these cross-sections for the STAR detector utilizing data from the STAR Barrel Electromagnetic Calorimeter (BEMC). This data comes from a clean channel relative to charged hadron measurements. Charged hadron spectra are complicated by contamination of other particle types due to poor particle identification. This mixture of charged hadrons is particularly difficult to separate at high p_T where particle identification capability is limited. This will be discussed shortly. For π^0 measurement, the STAR BEMC measures photons produced during the *d+Au* collisions and has relatively low occupancy, and therefore low backgrounds. It is worth mentioning that STAR is presently building a Time of Flight (TOF) system to improve charged hadron identification at moderate p_T.

STAR's primary benefit, relative to other detectors measuring relativistic heavy ion collisions, is the ability to measure and partially identify particle tracks over a very large solid angle. However, these measurements are made by a constellation of detectors, which must all work together. Thus it is important that STAR be able to measure many different types of particles across its detectors simultaneously.

STAR identifies and measures charged hadrons by two primary means. The first is the ionization trail a charged hadron leaves in a gas. The second is by observing the bending of the charged particle track within a large magnetic field. The net effect of these two measurements is that particles are identified by their energy loss (dE/dx) and their momentum. Figures 3.6 and 3.7 show examples of how this type of identification can be made [And03][WX07]. Figure 3.6 shows a density plot of dE/dx

versus momentum, where the densities begin to overlap. Figure 3.7 contains a similar plot, showing that particle velocities approach 1 at momentum around 3 GeV/c. This overlap reduces STAR's ability to distinguish particles based on ionization energy loss. Based on these figures it is apparent that the upper bound for separating charged particle species is roughly 3 GeV/c. Figure 3.6, however, indicates the degree of overlap, and therefore uncertainty, involved in distinguishing particles below 3 GeV/c.

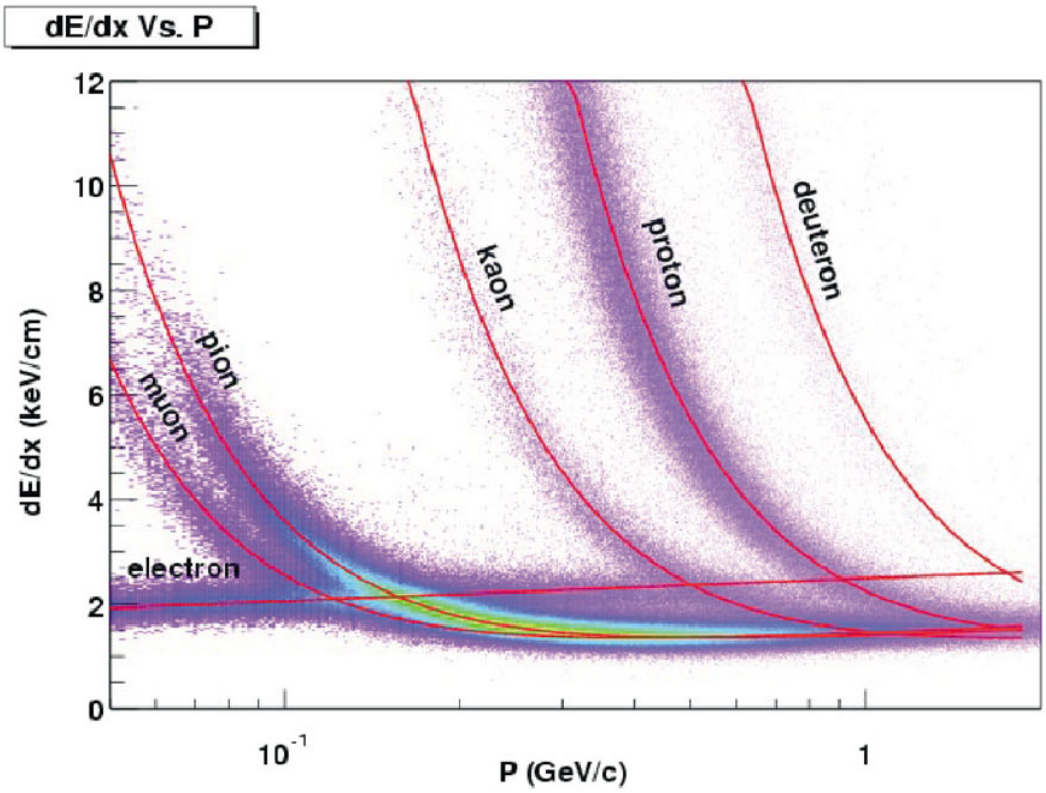

Figure 3.6: Figure from [And03] showing various bands in *dE*/*dx* versus momentum. Each band comes from a different charged hadron species. Except for electron contamination, this figure suggests particle identification is reasonable below 1 GeV/c. The bands for the most common measured particles, (π, k, p) must merge above this momentum due to overlapping velocity, as seen in Figure 3.7.

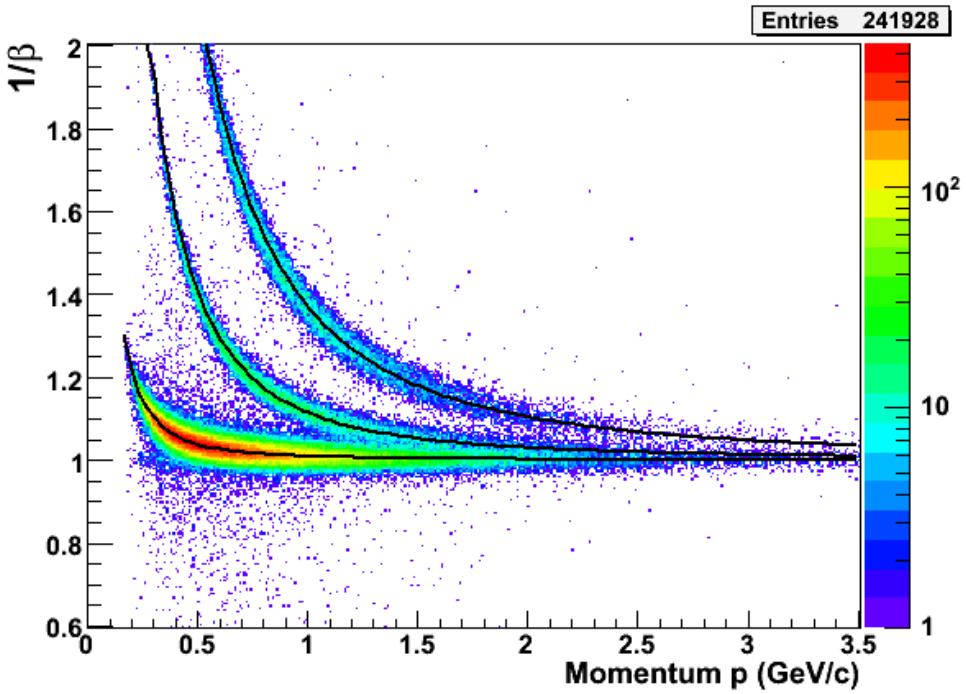

Figure 3.7: $1/\beta$ versus momentum is shown. Here it is clear that the bands begin to merge as momentum extends past 3 GeV/c. The ionization energy loss is proportional to $1/\beta^2$, so as the curves merge in $1/\beta$ the ionization energy loss becomes unable to identify particles [Un1].

Hence, our work here extends STAR's measurement of π^0 production to the high-p_T region in *d+Au* collisions. This work can also be compared to existing *Au+Au* and *p+p* collision data to strengthen the evidence for the applicability of pQCD calculations to high-p_T particle production in these collisions.

3.6 Observations in *d+Au*

d+Au collisions provide a control experiment for the *Au+Au* collision experiments at STAR. In this section we will show a couple results from STAR for these collisions, using charged hadrons. These results, due to the identification problems stated above, show some of the limitations of the measurements.

Using *d+Au* collisions for π^0 detection enhances STARs ability to detect these particles in other scenarios. This is particularly important for two reasons. The first reason is that, as an additional detection channel for high-p_T probes, π^0s have been very difficult to identify in *Au+Au* collisions due to very high combinatoric background. The second benefit of developing π^0 detection capabilities comes from STAR's heavy quark program. Charm and bottom quark production ratios are of importance, and one way to identify them is by observing high-energy electrons from B or D meson decays. Such electrons share many of the same features as photons measured at STAR.

Identified charge hadron spectra in *d+Au* collisions were measured by the STAR collaboration. Some results for protons, kaons, and pions are shown in Figure 3.8, which shows inclusive yield for momentum between 0.5 and 3 GeV/c [Ada05]. The figure is limited in p_T due to the particle identification range. It does, however, show that the charged pions differ somewhat from the heavier hadrons.

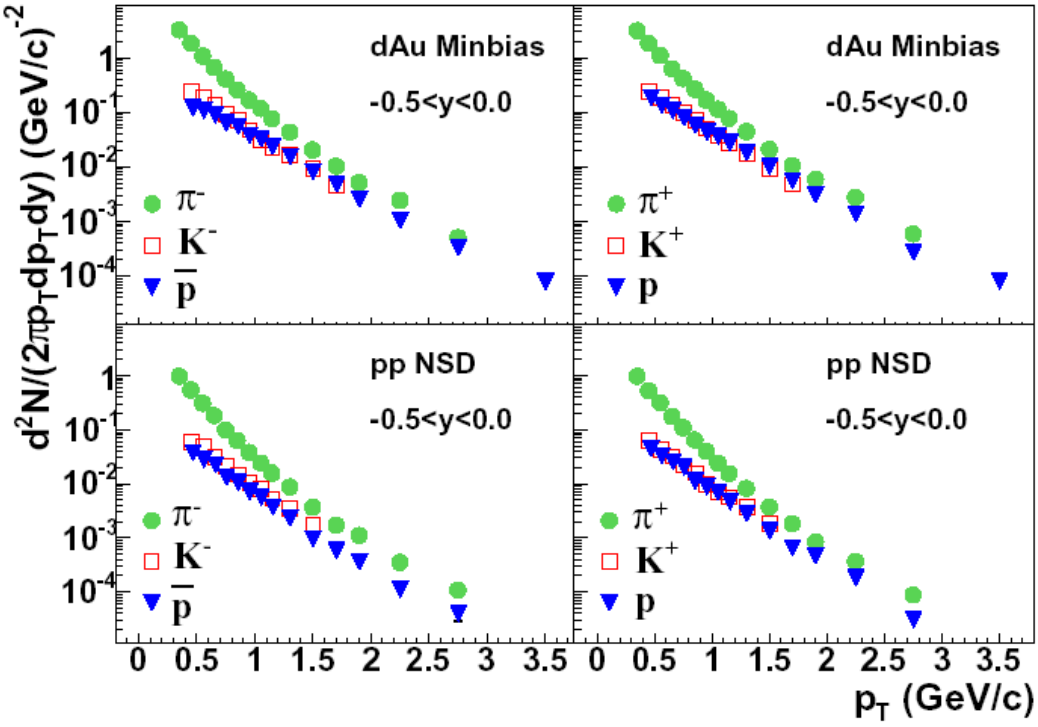

Figure 3.8: STAR results for identified hadrons in *d+Au* collisions are shown [Ada05].

STAR has also measured high-p_T hadron production in *d+Au* collisions. These measurements are of inclusive charged hadrons. The spectra of inclusive yield versus momentum are given in [Ada03] and shown in Figure 3.9. Using the data in Figure 3.9, the nuclear modification factor can be calculated. Figure 3.10 shows the nuclear modification factors R_{AA} and R_{dAu}. In the *Au+Au* data, only the central collision data is shown. For *d+Au*, the results from central collisions are shown separately from the results from minimum bias collisions, although the results are the same within systematic uncertainties.

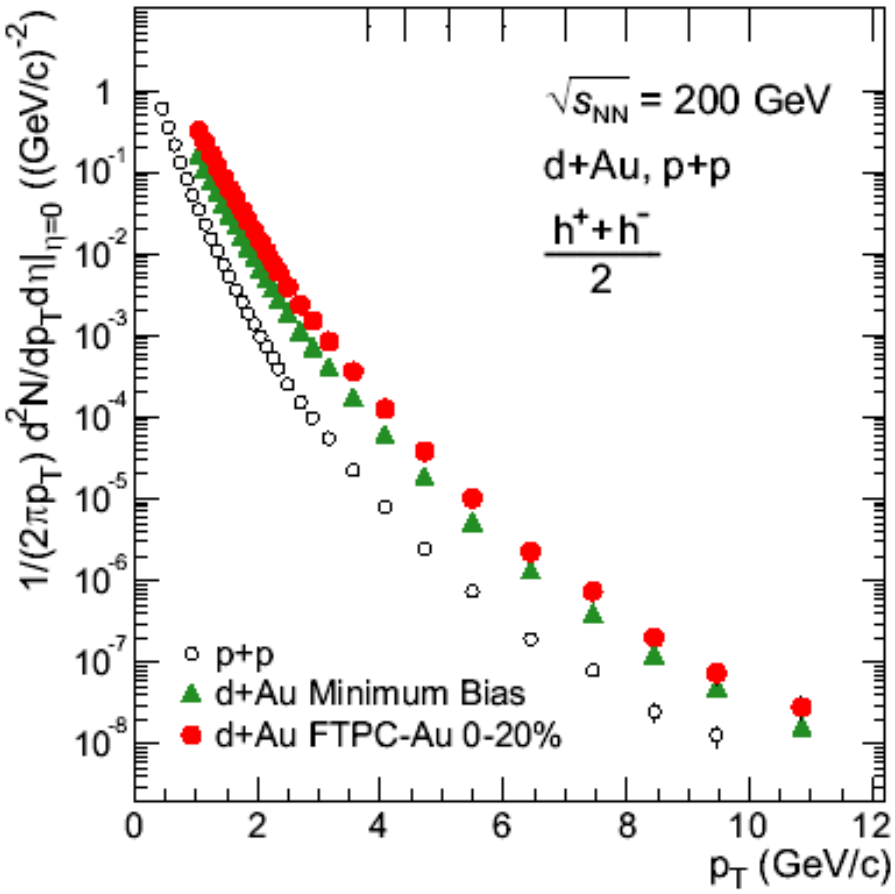

Figure 3.9: Figure from [Ada03]. The *p+p* and *d+Au* spectra for charged hadrons are shown. The *d+Au* minimum bias data covers the largest fraction of event topologies possible, while the FTPC-Au 0-20% gives the spectrum from central collisions only.

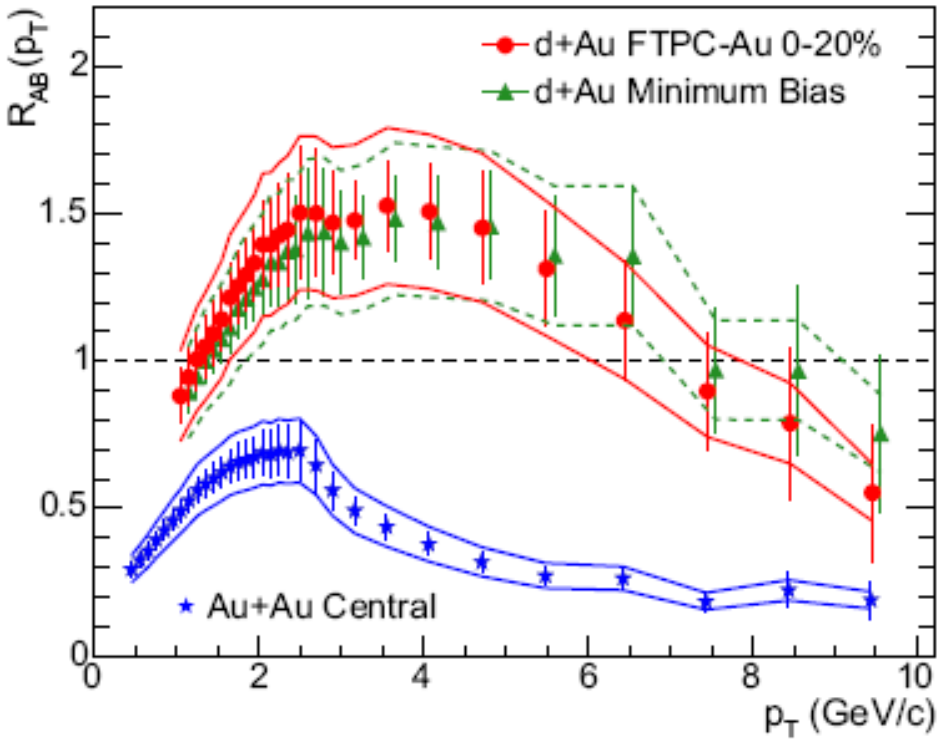

Figure 3.10: Figure from [Ada03]. The nuclear modification factors (R_{AA} and R_{dAu}) are shown for charged hadron production. The *Au+Au* results are from central collisions. Note that the *Au+Au* results are significantly suppressed and the *d+Au* results do not show that suppression. The lack of suppression is independent of the collision centrality.

In these figures two categories of *d+Au* collisions were analyzed. They are the minimum bias dataset, and the most central dataset. The minimum bias dataset selects the largest subset of events that the STAR detector can observe while maintaining a low event bias, while the central dataset is selected to be collisions with large numbers of charged hadrons produced. The central collisions reflect events where many interactions between the deuteron and Au nuclei occurred.

In *Au+Au* collisions, collision centrality must be used as a parameter for the analysis. Collisions where only the outer edges of the *Au* nuclei collide do not show the clear suppression seen in Figure 3.10. It is clear from Figure 3.10, however, that

there is little centrality dependence in *d+Au* collisions. Due to mixing of event classes, minimum bias proved to be the best event class for normalization. The result in Figure 3.10 suggests that our results for minimum bias normalization reflect similar results for the most central event class of *d+Au.*

The analysis of π^0 production at STAR in *d+Au* collisions provides a good opportunity to develop another channel for pQCD validation. It also provides an additional example of data analysis using the STAR BEMC. It extends identified-particle high-p_T measurements significantly. It adds another production channel to the repository of measurements. It is a clean channel, due to the lack of other hadrons with similar signals in the detector. The π^0 is also the lowest-mass hadron, which implies that interesting behavior may be unique to it. Although these benefits may not all be unique, they are all important to the physics goals of the STAR collaboration. The STAR detector's particular strength lies in its ability to observe large acceptance and particle species simultaneously and any analysis that brings together various parts of the detector and provides a measurement of absolute particle production is important to its ongoing development.

CHAPTER 4

STAR Detector

4.1 General Overview

The measurement of π^0s in heavy ion collisions is part of the broader goal of observing a high energy density medium possibly capable of supporting the Quark Gluon Plasma. Since such a medium cannot be observed directly, it is necessary to make many correlated measurements of the products of the medium. This work only deals with a subset of those products. However, the general collider and detector setups are relevant to this measurement and will be covered in this chapter. Details of the detector that are important to π^0 detection will be discussed.

The chapter is arranged as follows. First we will present a general overview of the Relativistic Heavy Ion Collider (RHIC), at Brookhaven National Laboratory (BNL) in Upton, NY. Then we will discuss the detector system used to observe the collisions. After that, we will be ready to discuss the particular subsystems used in the actual data collection for this work.

The ultimate goal is to measure π^0 production in the heavy ion collisions of deuterons and Au. In order to do that, the decay channel $\pi^0 \rightarrow \gamma\gamma$ is chosen, since it accounts for 98.8% of π^0 decays. The next highest channel is $\pi^0 \rightarrow e^+e^-\gamma$ at 1.2%, which has all the difficulties of the former channel and the added difficulties of

identifying high energy electrons and three-particle combinitorics. Using the first channel means that the detector system used must be good at collecting photon energy signatures, and arranging them spatially. The importance of accurate measurements of energy and position comes directly from the invariant mass expression.

$$m_{inv}^2 = 2E_1E_2\left(1-\cos\theta_{opening}\right) \tag{4.1}$$

Where E_1 and E_2 are the photon energies, and $\theta_{opening}$ is the opening angle determined by the spatial positioning of the two photons.

To test pQCD it is important for the π^0s to have fairly large transverse momentum, this ensures that the total momentum transfer is also large, which is necessary for pQCD to have predictive power. As will be discussed, STAR works well in this picture since it collects good signals using π^0s created in the central region ($|\eta|<1$).

4.2 RHIC Facility

Data was taken using collisions supplied by RHIC located at BNL. This facility covers 5300 acres, and includes several complexes. An aerial view of the facility can be seen in Figure 4.1. The facility was designed to provide nucleus-nucleus collisions at $\sqrt{s_{nn}}$ = 200 GeV/c, which is a large increase in the collision energy of heavy ion systems. Characteristics of collisions provided by RHIC and other heavy ion facilities are given in Table 4.1.

Figure 4.1: This is an ariel view of the RHIC facility in Upton, NY, facing north. Note the RHIC ring is in the background. The facilities directly producing or accelerating the colliding beams are in the top half of the picture, with the first such facility in the chain being the Tandem van de Graaff building just above the middle.

Table 4.1: RHIC compared to existing and future heavy ion facilities. Previous facilities were fixed-target and operated at high beam-energy but relatively low collision energy ($\sqrt{S_{NN}}$). A_{max} is the maximum species mass number, E_p^{max} is the maximum (equivalent) fixed-target beam energy per nucleon, $\sqrt{S_{NN}}$ is the maximum center of mass energy, and $\Delta y/2$ is the rapidity gap from the beam to mid-rapidity (LHC information updated relative to reference) [LR02]

	AGS	AGS	SPS	SPS	SPS	RHIC	RHIC	LHC
Start Year	1986	1992	1986	1994	1999	2000	2001	2008
A_{max}	^{28}Si	^{197}Au	^{32}S	^{208}Pb	^{208}Pb	^{197}Au	^{197}Au	^{208}Pb
E_P^{max} [GeV]	14.6	11	200	158	40	0.91e4	2.1e4	1.9e7
$\sqrt{S_{NN}}$ [GeV]	5.4	4.7	19.2	17.2	8.75	130	200	6000
$\sqrt{S_{AA}}$ [GeV]	151	934	614	3.6e3	1.83e3	2.6e4	4e4	1.2e6
$\Delta y/2$	1.72	1.58	2.96	2.91	2.22	4.94	5.37	8.77

The 2003 *d+Au* collisions marked the first time a heavy ion collider was used to collide different species. Many of the design goals for this run were met. General operating conditions of RHIC during the run period can be found in [Sat03]. Target luminosity and per-beam intensities met most goals and the machine delivered beams reliably throughout the run.

The key structure for RHIC is a large ring housing two sets of circular beam pipes. The ring contains the colliding beams of heavy ions or protons. Superconducting magnets along the beam lines handle beam containment. The magnets are maintained by a cryogenic system that is responsible for a large portion of the energy budget for operating RHIC. RHIC's dynamic range for acceleration is from about 10 GeV/nucleon up to 250 GeV/charge. This higher number accounts for the energy limits for Au and protons being about 100 GeV/nucleon and 250 GeV/nucleon, respectively. The 10 GeV/nucleon minimum means that collision species must be provided to RHIC by a lower energy source. In fact, collision beams are created by a series of acceleration stages.

In the next few paragraphs the acceleration of ions for collision is discussed. The focus is on the individual machines that are linked together to increase the beam

energy through different energy regimes. A full discussion of operating the two beams, including difficulties due to switching the accelerator facilities from deuterons to Au can be found in [Ahr03]. For the current discussion, however, these sources provide much of the information about the beam acceleration that follows. A schematic version of Figure 4.1 showing the facilities involved in accelerating the beams is shown in Figure 4.2.

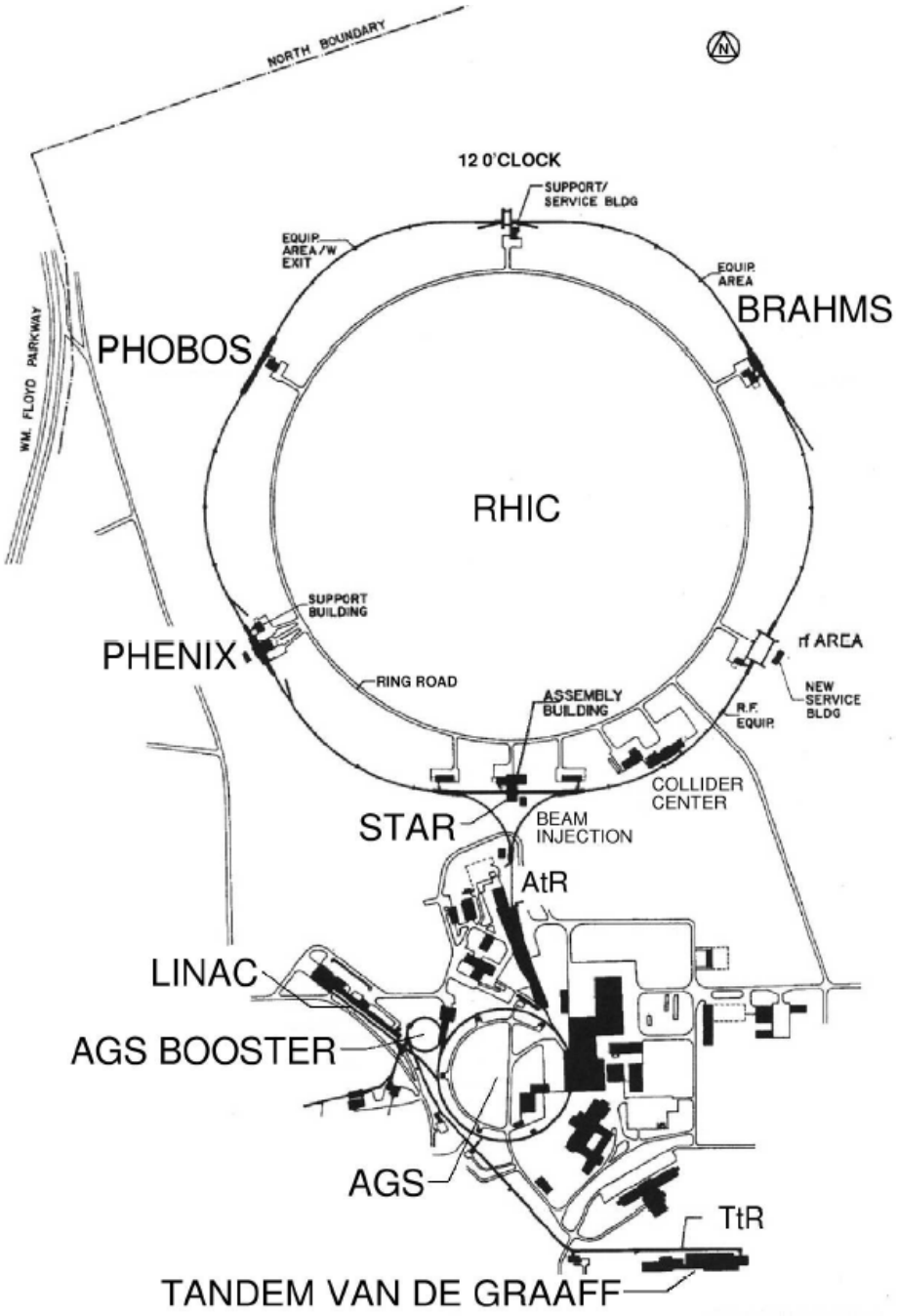

Figure 4.2 : A schematic drawing of the RHIC facility including the auxiliary facilities that feed into the primary RHIC ring. Note that the RHIC also provided collisions to the PHENIX, BRAHMS, and PHOBOS collaborations during 2003.

Heavy ions such as our Au nuclei, and the deuterons, are produced at RHIC in the Tandem Van de Graaff facility. It uses linear potential difference and a stripping foil to accelerate heavy ions in two stages. First, in a negative charge state, the ions are accelerated to a cathode at +14 MV (+8.6 MV for deuterons). Upon crossing the cathode, they are then stripped to some positive charge state and accelerated back to ground potential. The Tandem facility at BNL has two Tandem Van de Graaff accelerators. For *d+Au* collisions both were operated differently. One was configured for Au, the other for deuterons.

Both ion species were produced in the –1 charge state. They were provided by PSX-120 Cesium sputter ion sources. Thus they are initially accelerated to a kinetic energy T_{ion} = 14 MeV (8.6 MeV for deuterons), in addition to a small additional energy due to the source itself. The electron stripping at the cathode cannot be well controlled, but by charge and momentum selection upon leaving the Tandem, only those ions in the desired charge state are advanced in the TtB line to the Booster. For the Au ions, the cathode stripper in the Tandem results in a charge state of +12 in the second half of the Tandem[1]. For the deuterons, the charge state is +1 in the second half of the Tandem. Upon exiting the Tandem another stripping foil is applied to the Au beam, and the momentum and charge selection going into the TtB line require the exiting Au to be in the +32 charge state. Figure 4.3 shows a cartoon of Au ion acceleration in the Tandem, starting from the ion source and exiting to the TtB.

[1]The resulting charge state is not well defined, however, through bending and collimating, only ions at +12 in the second half of the Tandem survive all the way to the booster.

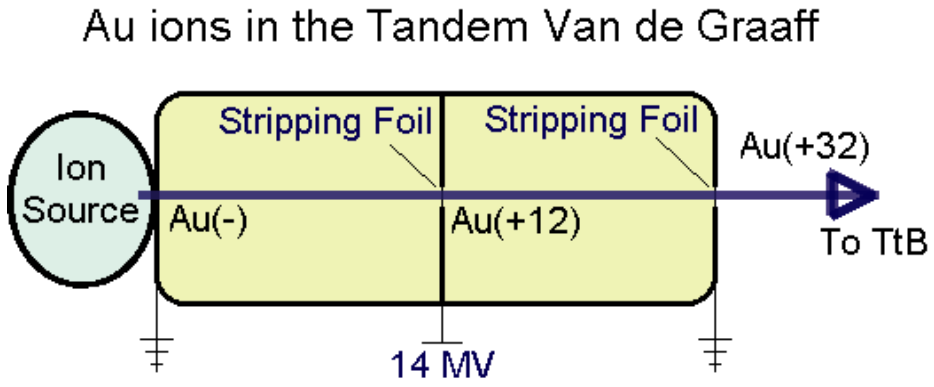

Figure 4.3: A schematic cartoon of Au ions created in the Tandem Van de Graaff. The source feeds Au^{-1} ions into the Tandem chamber. The chamber is grounded on both ends, and charged to +14MV in the center. The negative ions are accelerated toward the central plate. The Au ions go through a stripping foil in the center of the chamber. The ions are now Au^{+12} and are repelled from the central plate towards the exit. As an ion exists the Tandem chamber it crosses a second stripping foil to bring it to Au^{+32}.

The deuterons and Au ions differ considerably in how they are accelerated beyond the Tandems. For instance, the magnetic rigidities of the species are different in every containment line from the Tandems all the way to storage in RHIC. Thus, the machines used are the same, but the configurations are different. To keep this discussion coherent, we will first discuss the post-Tandem Au acceleration, then the deuteron. Also, the picture could be even more confusing. The configuration was worked on during commissioning, and a few configurations of the deuteron acceleration were tried. We will keep the discussion limited to only one acceleration configuration. The configuration discussed here is that used to produce the beams that provided our collisions. The other configurations, which were primarily used for commissioning the deuteron beam, are further discussed in [Ahr03, Sat05].

The Au ions are transferred from the Tandem to the booster through the TtR line. In the booster the Au ions are accelerated increasing their energy to 95 MeV/nucleon. From there the ions are transported to the Alternating Gradient Synchrotron (AGS)

via the BtA transfer line. The ions are stripped to a charge state of +77 before entering the AGS (only K-shell electrons remain)[Sto05, Gar01].

The booster bunches are transferred into matching RF buckets in the AGS (harmonic number h=16). After the fourth transfer the beam is accelerated, merged from 16 to 8 bunches, accelerated to full energy (10.8 GeV/nucleon), and further merged to 4 bunches. The target intensity per bunch was $1x10^9$ but only about 70% of this goal was reached usually.

Bunches are then put into the AGS to RHIC transfer line (AtR). At the beginning of this line a final stripping foil removes the last 2 electrons, and the Au ions are then in the fully stripped (+79) charge state. The ions are then injected into RHIC acceleration RF buckets operating at 28.02 MHz (harmonic number 360 – the RF system contains 360 cavities in the beam-line). Once in RHIC, the ions are then accelerated to their final energy. The acceleration occurs at the same time for both the deuterons and Au, so acceleration in RHIC will be covered after a brief description of the acceleration of the deuteron beam.

Deuteron acceleration for RHIC followed a couple different schemes. One final scheme was used for production of deuterons for collisions. That scheme is briefly presented here. Details, and discussion of alternative acceleration methods can be found in [Ahr03]. Additional details about differences in the operation of the various accelerators under the different beams can also be found in [Gar01b].

Deuterons exit the Tandem Van de Graff at 8.7 MeV/nucleon. They are transferred to the booster by the TtB transfer line. They are injected into the booster on harmonic number h = 2. During acceleration here the deuterons reach a revolution frequency that matches the proton acceleration system operating on h = 1 (RHIC is

also designed to accelerate protons). So, before full energy is reached in the booster, bunches are merged 2 to 1, leaving the system at h = 1.

At full booster energy, the bunches are transferred to the AGS. Upon entry, two booster bunches makes one AGS bunch. Four such bunches are handled in the AGS at a time, in an h = 8 structure. The AGS accelerates the deuterons to the RHIC injection energy.

In order for RHIC to constantly provide collisions in the intersection regions of the experiments, the beam velocities (and therefore, frequencies) must be related by an integer multiple. With relativistic beams it is impossible to have one beam with, e.g., twice the velocity of the other. The resulting energy differences would eliminate RHIC's design goal of producing zero laboratory momentum collisions. Also, the containment systems for the rings would not be able to support such asymmetric beams.

Thus each RHIC deuteron bunch contains the results of two booster fills. For our beams, the deuteron bunches in RHIC contained about $1x10^{11}$ deuterons. Continuing with the operation of the beams in the Tandems, transfer lines, Booster, and AGS, the deuterons were injected into RHIC at the same velocity ($\gamma = 10.52$) as the Au ions. Once both beams are ready in RHIC, they are accelerated to 100 GeV/nucleon (for Au - deuterons are 100.7 GeV due to binding energy differences).

Since the beams are traversing RHIC with identical frequencies, their magnetic rigidities are different. In fact, Au is about 24% more rigid than the deuterons. The main place where this was a problem was in the intersection regions. Here the particles not only share the same magnets, but also share the same path. In particular, the beams are bent in opposite directions by 1 mrad in the intersection regions, with

the deuteron being bent more due to the larger charge to mass ratio. This slight angle also changed the trajectory of spectator particles coming out of the collisions. Such spectators are elements for identifying events and are used by the Zero Degree Calorimeters (ZDC, discussed later) for triggering. This geometric quirk required moving the ZDCs by 10mm.

Ion species are contained in separate beam pipes in RHIC. The two beam pipes keep the beams traveling in opposite directions. The beams are also segmented in space within the beam pipes. Each bunch of beam particles is held in an RF bucket. RHIC is capable of running with as many as 110 beam buckets, and collisions were provided with 110, although the goal for the run was only 55. The RF bucket system allows the collisions to be targeted for the middle of the intersection regions around the ring. The beams are steered to be overlapping in space only in these intesection regions (IRs) around the RHIC ring. The beams are also cogged so that the bunches overlap in the middle of the IRs. More details about the characteristics of RHIC can be found in Table 4.2.

Table 4.2: Physical parameters and performance specifications for the Relativistic Heavy Ion Collider (RHIC). Adapted from [Sto05]

Physical Parameters			
RHIC circumference (m)		3833.845	
No. Intersection Regions		6	
No. Bunches/ring (including gaps)		120	
Bunch Spacing (nsec)		106	
Collision Angle		0	
Free Space at Crossing Point (m)		±9	
Performance Spcifications	**Au**	***p***	***d***
No. Particles/Bunch	$1x10^{9}$	$1x10^{11}$	$8x10^{10}$
Top Energy (GeV/nucleon)	100.0	250.0	100.7
Luminosity, average(cm^{-2} sec^{-1})	$\sim 2x10^{26}$	$\sim 1x10^{31}$	$\sim 2x10^{28}$ *

* RHIC has not provided *d*+*d* collisions. Reported luminosity is *d*+*Au*.

During the data taking for this research, the RHIC facility was host to experiments in four interaction regions. The experiments are the following. The Broad RAnge [*sic*] Hadron Magnetic Spectrometers, BRAHMS experiment, was located at 2 o'clock. The PHOBOS experiment, which is named after a moon of Mars, was located at 10 o'clock. The Pioneering High-Energy Nuclear Interaction eXperiment [*sic*], PHENIX, was located at 8 o'clock. Finally the Solenoidal Tracker at RHIC, STAR experiment, was located at 6 o'clock. [Sto05, Han03].

The research presented in this dissertation is based on collisions occurring at the STAR detector, using the deuteron and Au beams at 200 GeV. Next we consider the detector and how it is used to collect information on produced π^0s.

4.3 STAR Detector

The STAR detector is a set of several detector subsystems collecting data that synergistically produces a picture of the heavy ion collions. They form a constellation of detectors that covers a large acceptance at mid-rapidity. The STAR detector is shown in Figure 4.4. STAR is a constellation of detectors at whose heart is a solenoidal magnet. The constellation detectors are made up of two major types. The mid-rapidity detectors are either cylindrical, or part of a cylinder, and centered around the middle of the intersection region. Away from mid-rapidity, very little transverse information is to be gathered; so plate-like detectors are placed around the beam-line to collect high rapidity particle signatures. One detector performs a hybrid of both jobs, and therefore fails this generalization. It is the Forward Time Projection Chamber (FTPC).

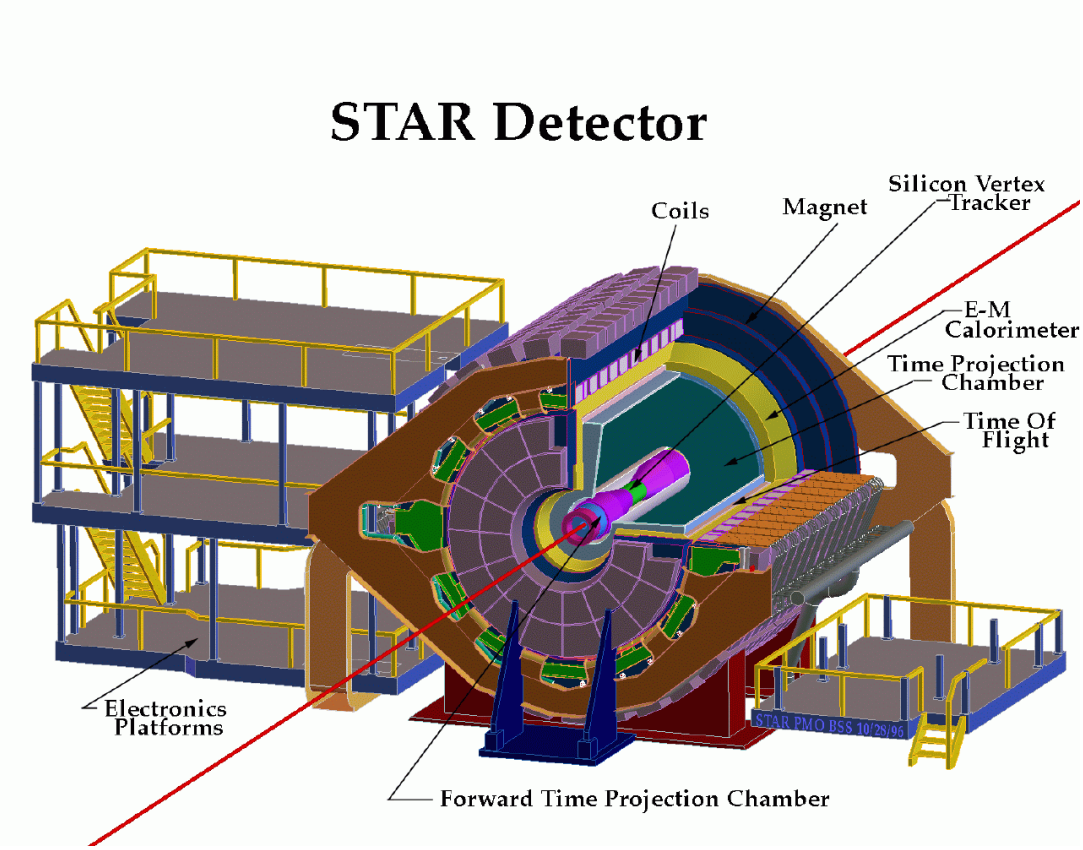

Figure 4.4: The STAR detector is shown in perspective. Note the detector is more than two stories tall, and is a squat cylindrical shape. Several detector subsystems are cylinders around the interaction region at the center of the detector. The STAR detector provides large acceptance at mid-rapidity.

The beams come in from either end of the detector. They are setup to collide in the middle, although the beam particles drift somewhat within their RF containment buckets. When a collision occurs it must produce a signature, or trigger, that the detector recognizes in order for data to be recorded. Once such a signature is detected, the STAR detector records the collision.

The primary means of triggering events during *d+Au* collisions came from the Zero Degree Calorimeters (ZDCs), which are not shown. The ZDCs, one for each end of the detector, provide a timing signature when neutral particles are created

during collisions. For the *d+Au* data, only the ZDC in the Au direction could be used. This is because the other ZDC will not see anything unless there is an interaction that leaves the deuteron's neutron essentially untouched. The bias involved in such a trigger is too problematic to use, even though it would improve the selection of events near the center of the detector.

Another important part of the detector, which is not explicitly identified, is the solenoid itself. The solenoid is a coil of conducting aluminum at radius ~2.7m from the beam pipe. This solenoid produces a large amount of magnetic flux that is mostly contained by the external iron structure of the detector. This external iron structure is designed as a return yoke for the magnetic field lines. The solenoid provides a quite constant 0.5T field inside the primary cylinder of the detector [Berg03]. Outside the primary cylinder, two large iron end caps are part of the larger return yoke system. The return yoke pulls the external magnetic fields back in toward the detector to minimize the spatial extent of the large-scale magnetic effects. Without the return yoke, many of the electronic components that operate STAR would have required special enclosures.

Once a collision occurs and triggers the ZDC, the event information is collected by the various detector subsystems that constitute the STAR detector. We will present each detector subsystem quickly, starting with the innermost, based on the 2003 arrangement.

The first detector surrounding the *d+Au* events, which was outside the beam pipe, was the Silicon Vertex Tracker (SVT), which provides high spatial resolution of tracks. Immediately outside the SVT was the STAR Time Projection Chamber (TPC). The TPC is the primary detector in STAR because it provides charged particle tracking through a large volume, thereby allowing momentum determination,

and a good measurement of dE/dx. The TPC completely covers $|\eta| < 1$, and provides reduced detection acceptance up to $|\eta| = 1.8$. The wounded Au nuclei, in collisions with deuterons, provide signatures of interest at larger η. For this reason there is an additional Forward TPC (FTPC), which increases the η acceptance by detecting energy deposition for $2.5 < |\eta| < 4$. Surrounding the TPC is the Central Trigger Barrel (CTB) that provides fast multiplicity detection. Outside of the CTB is the Barrel ElectroMagnetic Calorimeter (BEMC), which provides information about energy deposition into a lead-scintillator system. The BEMC covers $|\eta| < 1$. The BEMC also includes shower detectors that improve its spatial resolution. These detectors are called the Barrel Shower Maximum Detectors (BSMD, or SMD). The SMDs are gas-filled wire chambers that are built as part of the BEMC. There are two SMD planes, one for η, and one for ϕ.

All the detectors discussed above were online during the 2003 *d+Au* run, but only a few of them are important to this work. Hence we will discuss in more depth three of these detector subsystems in the next section. The detectors discussed are the ZDC, the TPC, and the BEMC – including the SMDs.

4.4 Subsystem Detail

The detectors necessary for this work are now discussed in greater detail. In particular we must cover how the detectors are triggered to take data, and exactly what type of data they record. We will also discuss how the recorded data is used to reconstruct event information based on the stored data. Only three of the detectors listed above are of interest here.

The ZDC subsystem is the primary means used to trigger events for nucleus-nucleus collisions. The event particles then traverse the STAR TPC where charged particles leave behind ionization trails. Finally, the mid-rapidity particles strike the BEMC where the total energy of photons is observed, among other signals in the BEMC. The BEMC also provides information based on the largest energy deposition occurring during an event. This information can be used to select special events.

4.4.1 Zero Degree Calorimeter

For the dAu collisions, large chunks of the Au nucleus remain together leaving the collision. These wounded nuclei break apart as they continue down the beam pipe, and evaporation neutrons are released. This release of neutral energy is a signature of an event. In order to isolate it, we look for the neutral energy beyond the beam steering magnets. The detectors are thus placed directly in line with the beam axis in the interaction region, but beyond the region where the charged beams are separated and resume their circular path around the collider. Hence these detectors are called "Zero Degree" calorimeters. At the beam energy used for these collisions at RHIC, these neutrons diverge by less than 2 milliradians from the beam axis, and about 99% of individual neutrons deposit at least 50 GeV in the ZDC, provided they produce a hadronic shower [Adl01]. The ZDC threshold was approximately 50 GeV.

Figure 4.5 shows a cross-section view of how the ZDCs are placed relative to the interaction points on the RHIC ring. In panel A the ZDCs are shown at 18m away from the interaction point, in both beam directions. Panel B shows the relative positions of the Au beam, and the dispersed neutrons and protons. (This figure is for *Au+Au*, but for *d+Au* the geometry is essentially the same.)

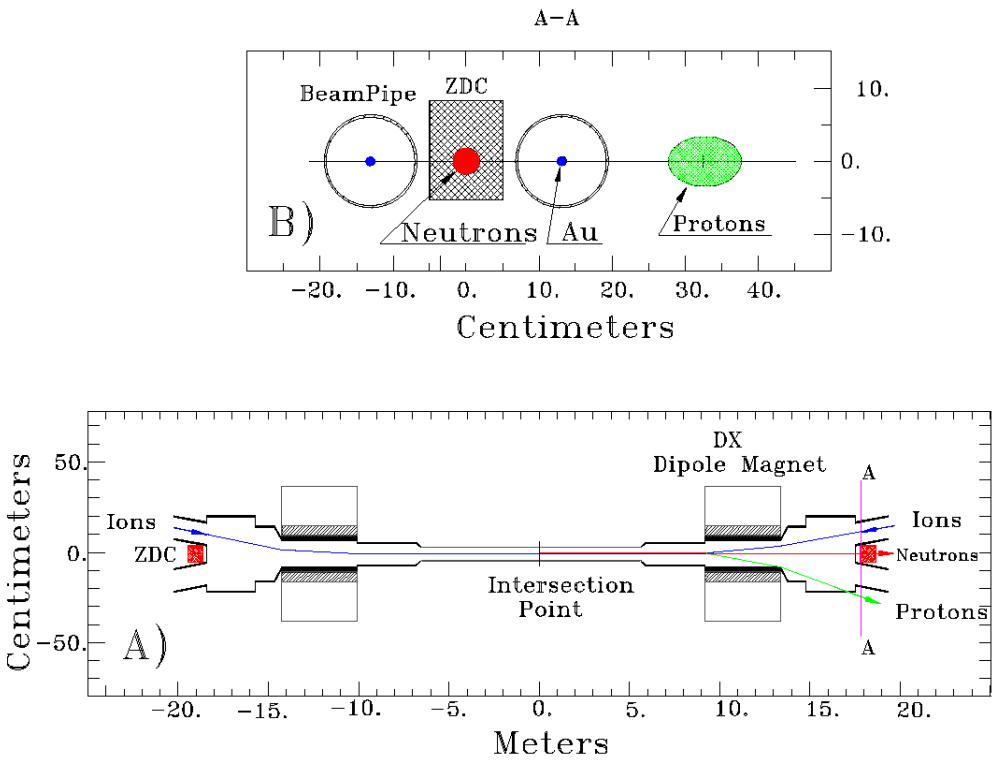

Figure 4.5: The plan view of the collision region and "beam's eye" view of the ZDC location are shown. Panel A shows the ZDCs are placed 18m from the interaction region. Panel B shows how the wounded Au nuclei's fragmenting neutrons and protons are positioned when they reach the ZDC due to the DX steering magnet.

In the collisions of interest here, there is usually no signal in the ZDC in the direction of the deuteron beam. Hence the primary signal used for triggering events with the dAu collisions was to look for ZDC energy deposition in the Au beam direction. In 2003 the Au beam was in the yellow ring which runs west to east at the STAR interaction region. Hence the collision trigger was the observation of an energy deposition in the ZDC-East.

Events triggered this way are said to satisfy the Minimum Bias trigger (indicating the least bias trigger that can be attained). This trigger was determined to sample about 95% of the *d+Au* geometric cross-section for inelastic collisions. For this

work, this sampling efficiency is taken as a systematic error. That is, the number of Minimum Bias events is said to be the number of hadronic collisions, with 5% systematic uncertainty. This is taken as an uncertainty because its application to event classes is not well known.

4.4.2 Time Projection Chamber

This detector is the heart of the STAR detector constellation. The TPC is a gas-filled cylinder situated in the solenoidal magnet at STAR and centered on the middle of the intersection region. It uses a central membrane with a potential difference of –28 kV relative to the ends of the cylinder. When charged particles from a collision traverse the TPC they curve due to the axial field of the solenoid. They also produce ionization trails in the gas. The electrons in the ionization trail are then attracted by the potential difference to either end of the cylinder. Thus they drift towards the ends of the gas chamber, traveling along the longitudinal field lines.

In order for this system to provide useful data, it is important to know the relationship between the longitudinal position of the ionization trail, and the time when the electrons will reach the end plates. The TPC was designed with resistive copper rings along its length; this ensures that the potential difference per unit z in the TPC gas is constant. The constant potential difference produces a constant electric field. This electric field provides constant acceleration on the one hand, and the gas provides velocity dependent resistance on the other. When combined, the net effect is that electrons in the TPC are swept to the ends with a constant drift velocity that is achieved almost immediately when the electrons become free. This velocity is tested at least once for every 8 hours of collisions.

The TPC cylinder is shown in Figure 4.6. It is 4.2m long with an inner diameter of 1m and an outer diameter of 4m. The inside of the TPC is filled with 10% methane and 90% argon (P10) gas [Kot03, Sor03]. With 28 kV potential, the drift velocity is about 5.5 cm/μs, so it takes about 40 μs for the complete track ionization charges to be collected at the electrodes. The TPC produces a large amount of data for each event, due to the digitization of 70 million three-dimensional pixels. This accounts for a significant fraction of the recorded data from all the detector subsystems at STAR; and is a limiting factor on the recorded event rate. The DAQ system used to record events in 2003 was only capable of recording 50 events per second without significant dead-time issues.

The magnetic field can be operated at 0.25 and 0.5 T. The selection of magnetic field imposes a minimum requirement on the p_T of the observed particle. The magnetic field and the inner radius of the TPC (0.5m) set a minimum hardware cutoff on the transverse momentum of a particle. For a particular particle x, the relationship between the transverse momentum of a particle p_{Tx} and its radius of curvature is the following:

$$p_{Tx} = \frac{q_x}{q_e} \cdot B \cdot r \cdot 300\, MeV/c \qquad (4.2)$$

Where B is the magnetic field, in Tesla, and r is the radius of curvature, in meters. It should be noted that this is a hardware cutoff for the minimum momentum to reach the gas inside the TPC. For B = 0.5T, the minimum transverse momentum (for a singly charged particle) is 75 MeV/c.

These limits, applied to real particles, are not quite so simple. Once in the TPC, particles must produce enough hits to be identifiable as tracks. So the particles must

be in the TPC long enough to present a chain of hits that can be used to find the track. In order for a particle track to be identified, it must have a minimum of 5 hits in the TPC. To illustrate this better let us consider how particles are observed in the TPC.

Particles are observed via the process of recording their ionization trails in discrete spatial bins. Each discrete spatial bin and its associated energy deposition are called a hit. For a real particle traveling through the TPC, its ionization trail will be a helix of hits. During analysis of TPC data, however, the real particles are not known. The tracks must be reconstructed by analyzing the TPC data all at once. The entire set of hits is thus put through an algorithm to reconstruct tracks.

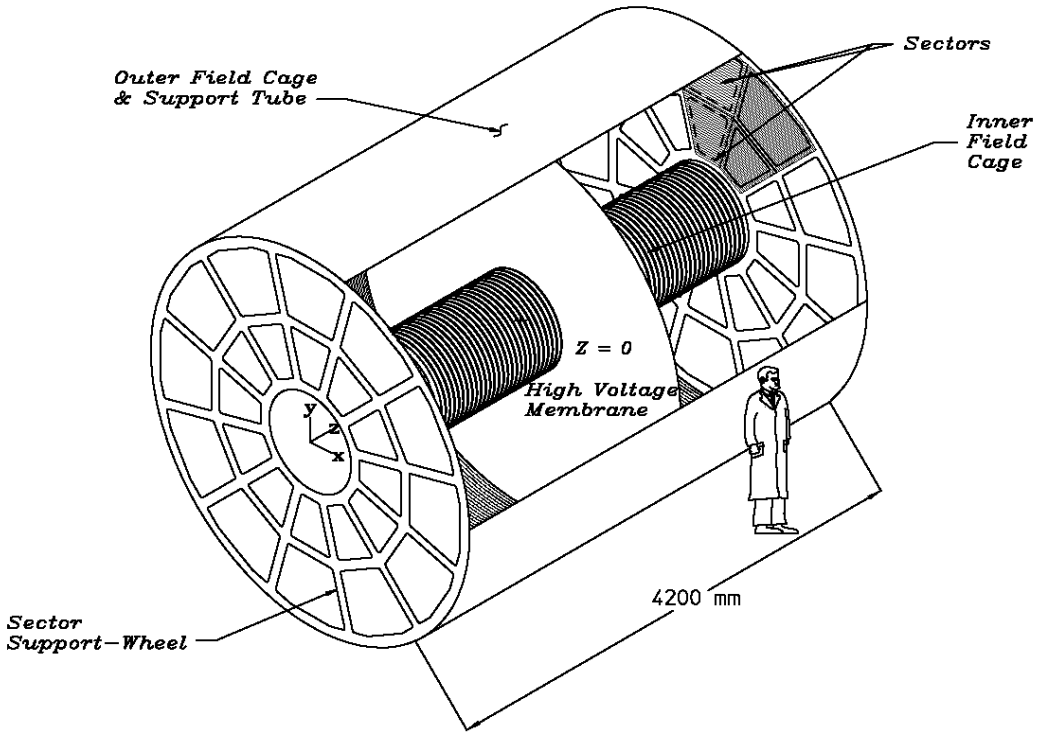

Figure 4.6: The TPC cylinder is shown. The TPC is filled with P10 (Ar 90%, CH_4 10%), which provides a medium for charged particles to ionize. It has a high-voltage central membrane and copper rings along the *z* axis. These provide a constant electric field forcing electrons to the outer ends. Electrons quickly reach a drift velocity and traverse to the ends of the TPC where electronics detect them and use timing to construct a snapshot of the inside of the detector following a collision.

The resulting tracks are then used to determine the event topology. Event topology information covers many different aspects of an event. For our analysis, the most important topological construct determined with the TPC data is the event vertex. Beyond that, however, the TPC can also be used to identify charged jets where the number of tracks in a small angular region is large. Also, STAR records enough of the central particle tracks to measure bulk properties of events to establish information about collective expansion of the colliding material and possibly measure equations of state. The tracks can also be used, by projection onto the BEMC, to

determine when charged particles contribute to the energy measured in a BEMC tower.

The vertex is determined by identifying a common source for a large number of particles. No particle decay will contribute more than a few tracks away from the vertex, and most of those would be inconsistent with the beam path, so the likelihood of a false vertex is negligible, provided the event has a modest number of primary tracks. For deuterons colliding with gold at $\sqrt{s_{nn}}$ = 200 GeV, more than 80% of the events contain more than 10 tracks, and are unlikely to reconstruct a vertex off of a secondary decay. The other 20% of the time, the event has such low multiplicity that there is likely no signal of interest. For most of those events the vertex finding algorithm fails to reconstruct a valid primary vertex. Those events are almost always excluded by analysis cuts.

4.4.3 Barrel Electormagnetic Calorimeter

The final detector subsystem used in this work is the BEMC. The BEMC is an energy gathering system designed to identify and record energy signatures primarily from photons and electrons. Since our analysis relies on measuring the $\pi^0 \to \gamma\gamma$ channel, this detector is the primary device for the measurement. Electromagnetic calorimeters contain a lot of material and cause large-scale conversions, so such detectors are outside of all the tracking detectors at STAR. In our case, the BEMC is located outside of the TPC, and covers the spatial region at radii larger than the TPC.

The information from the BEMC will often be the only data we have about decay photons. However, photons are not the only particles depositing energy in the BEMC. Other particles depositing energy cause two sources of errors. First, they

may contribute directly to background because they provide a "photon" signal that is not a π^0 photon. Second, other particles may add energy to a real photon signal. If there is a signal in the TPC, we could determine more information such as figure out what the particle was and whether or not its contribution to the energy in the BEMC could be removed. However, that sort of analysis would be unnecessarily cumbersome for the potential benefit and would lead to systematic uncertainties larger than the statistical benefit. Instead, a signal in the TPC is interpreted in this work as a sign of contamination, and we discard the associated BEMC information. Similar particles that do not leave tracks in the TPC, such as neutrons, cannot be removed this way.

The BEMC provides data about π^0 decay that is used with only minimal additional information about the event, namely the vertex, to construct the π^0s. Thus the BEMC must provide reasonable energy resolution, good absolute calibration, and accurate spatial positioning in order to determine the opening angles of decay particles.

4.4.3.1 Structure

The BEMC consists of 120 individual modules. Modules cover the pseudorapidity region from η = -1 to 0, or η = 0 to +1, and 1/60th of the full 2π azimuthal coverage of the barrel. Figure 4.7 shows a schematic of the top and side views of a module, along with the relative distance to the intersection region of the detector. This figure shows the projective design whereby the geometric structure for each tower in the module points back to the center of the interaction region. The figure also shows the substructure of the modules, where the modules are divided into 20 towers in η and 2 towers in ϕ. The top view of the module shows some of the

segmentation, while the side view also shows the layers inside a module. We will now discuss this segmentation, and thus the structure reflected in the data.

The BEMC is really three detectors built into one[2]. The primary energy measurement is made by observing light produced in scintillator material sandwiched between Pb conversion plates. Scintillator and Pb layers are alternated to producefa stacks of material providing many radiation lengths of material, and gathering light efficiently. The layers are segmented spatially in η and ϕ. Stacks of Pb and scintillator at the same ηxϕ position are called towers. Towers are arranged into modules, with each module containing 40 such towers. In a module the towers are organized at 20x2 in ηxϕ, and thus each tower covers approximately 0.05x0.05 in ηxϕ. The modules also contain two planes of shower maximum detectors. These are gas-filled wire chambers with readout pads arranged to provide η or ϕ information about a shower passing through the detector. For the η plane of the detector, there are 150 strips cutting across a module each at constant ϕ. For the ϕ plane of the detector, each set of 2x2 towers has 15 SMD-ϕ strips under it. Since there are 10 such 2x2 sets of towers, this correlates to 150 SMD-ϕ strips per module.

[2] It is actually four detectors, but at the time of the data taking only three were instrumented.

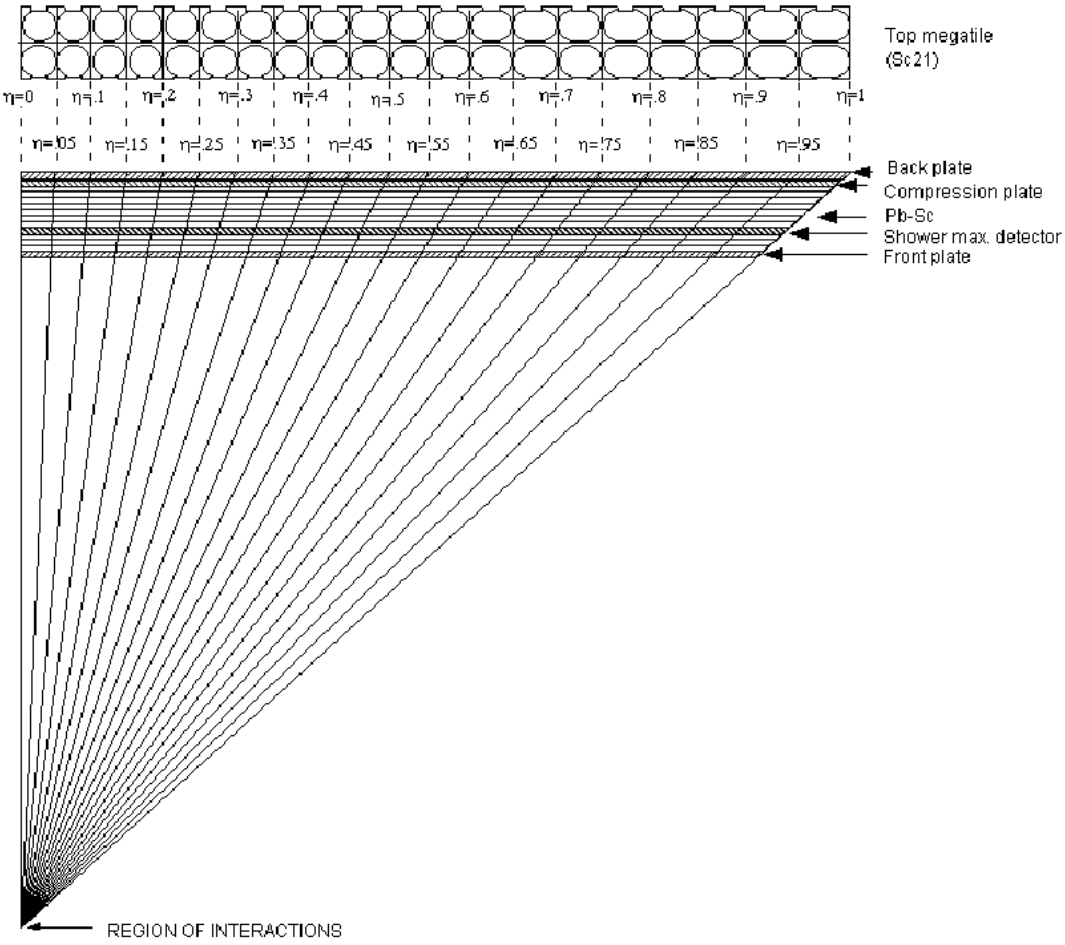

Figure 4.7: Figure from [Bed03]. A single module is shown in side and top views. Note the projective design of the towers where each sweeps out a constant 0.05 η relative to the interaction region.

More detail of the layers in a BEMC module can be seen in the cross-sectional view shown in Figure 4.8. In this figure it can be seen that there are 21 sets of stacked lead and scintillator material. Also, the position of the SMDs can be seen between the 5th and 6th layers of the lead and scintillator stack. Each layer of lead and scintillator is approximately 1 radiation length X_0 deep, and the entire detector is $20X_0$ (at η=0). Each radiation length X_0 is the mean distance over which a high-

energy electron is reduced to 1/e of its original energy due to bremsstrahlung. It is also the 7/9ths of the mean free path for high-energy photon pair production [WN02].

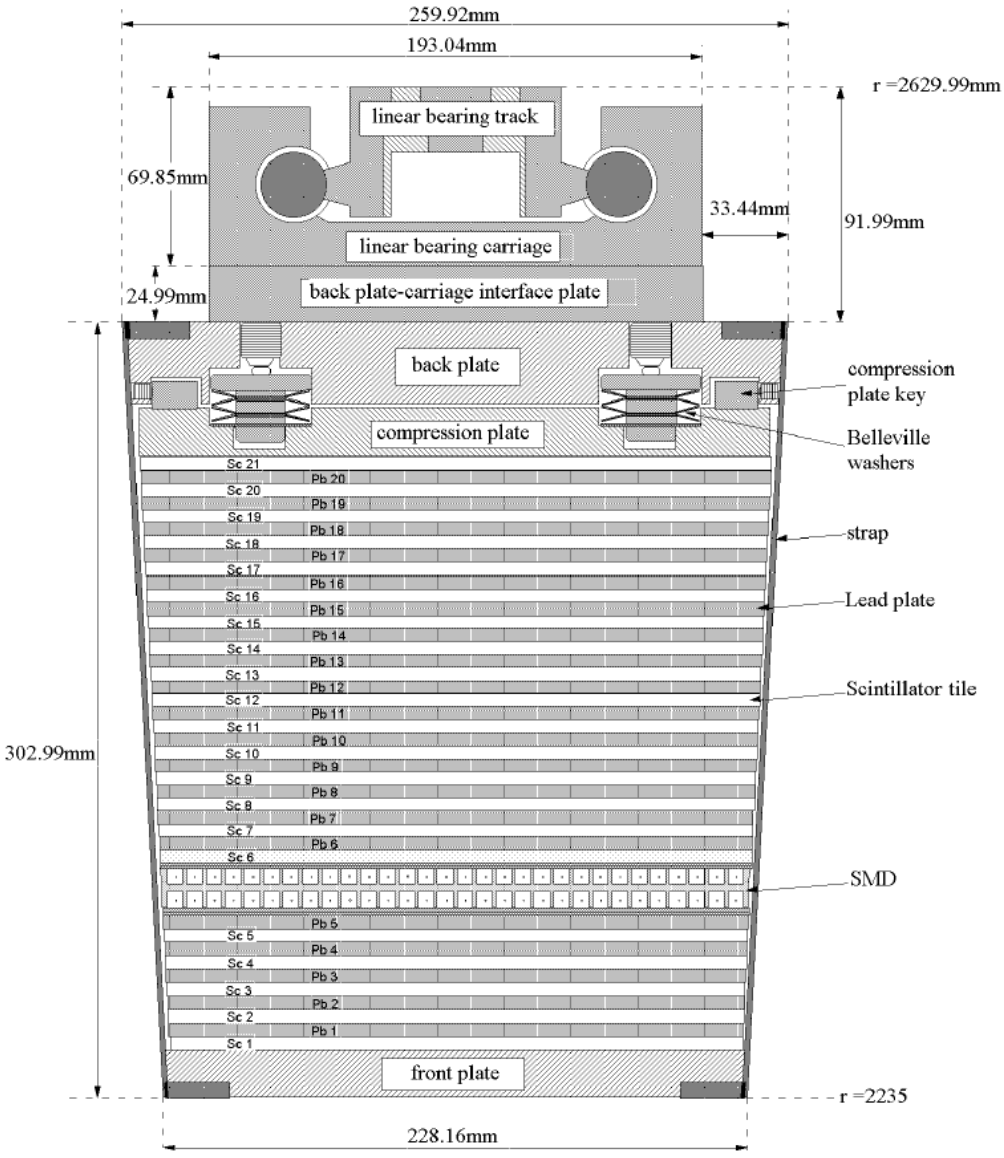

Figure 4.8: Figure from [Bed03]. This is an end-on cross-section of a BEMC module. The side to side width encases two towers. The 21 layers of Pb and scintillator can be observed, and between the 5th and 6th layers, the SMD planes are seen. Note that the SMD-η is the plane nearest the "front plate". The "front plate" is located about 224 cm from the center of the beam pipe.

4.4.3.2 Signal Creation

The light generated in the scintillator layers must be combined to form an energy signal for a given tower. To do this, the layers must be segmented so that light from a shower stays in its given tower. Also, light from all layers corresponding to the same tower must be combined to form the full energy signature for a tower. The former issue is handled by cutting an isolation groove in the layers at the boundary of each tower. The latter is handled by embedding optical fibers in each layer of each tower. A diagram showing how an optical fiber is routed, for one layer, can be seen in Figure 4.9 [Bed03]. Each of the 21 layers of each tower has one such optical fiber. The 20 fibers coming from one tower are all routed to the same PMT for energy measurements.

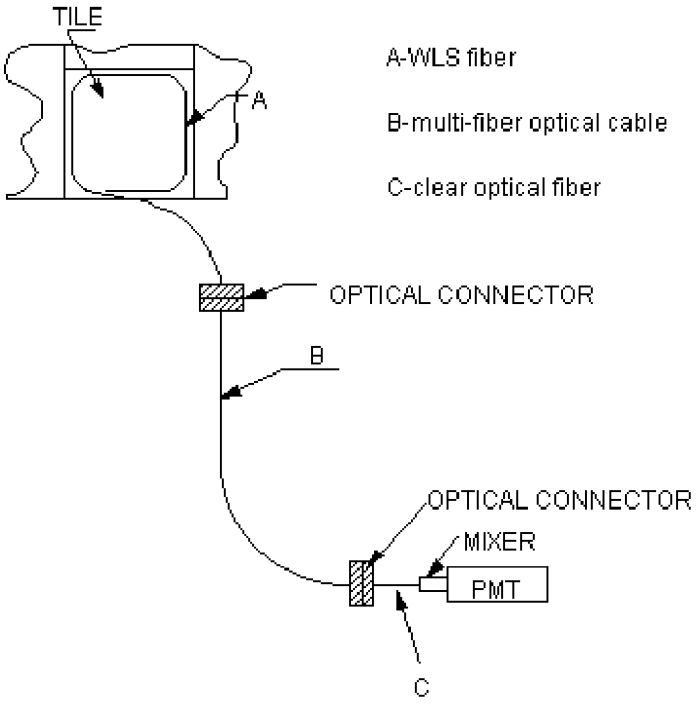

Figure 4.9: Routing of an optical fiber from a BEMC tower scintillator tile to its tower PMT. A wavelength shifting fiber (WLS) is embedded in each layer of scintillator for each tower in the BEMC. A significant amount of light generated in the scintillator material enters the WLS fiber. The fiber material reemits the light so that some of it may be trapped within the fiber due to reflection. Such light is piped out of the BEMC modules to a PMT outside of the STAR return yoke. Signals from all layers in a given tower are then mixed upon input to the tower's PMT. This way PMT response does not depend on the originating layer of the tower. The final PMT signal, after pedestal subtraction, is proportional to the energy deposited in the BEMC tower.

Light from the tower layers is collected by wavelength shifting fibers (WLS). These fibers pipe the light, changing fiber material twice, into mixers at the front of tower to photo-multiplier tubes (PMTs). Each tower has its own PMT. The 21 fibers from a given tower are all observed by one PMT. The mixer on the front of a PMT serves to remove correlation between a given tower layer and its position on a given

PMT. Therefore, signals from all layers of a given tower produce approximately identical PMT response. After calibration this system generally shows an energy resolution of about $16\%/\sqrt{E}$.

In contrast, the SMD uses image currents to determine the energy of the electromagnetic showers. The SMD only observes the shower for a small portion of its development, and the exact position where the shower starts is unknown. This and other uncertainties in SMD energy measurement make this measurement much less accurate than that for the BEMC towers. For the SMD planes, the resulting energy resolution is about $14\% + 86\%/\sqrt{E}$.

A position is associated with each energy signature. The towers and the SMDs determine the position. The position is based on the readout channel the signal comes through. For the towers, the segmentation is 0.05 x 0.05 in η x ϕ, while the SMD-η strips are roughly 0.007 x 0.10 in η x ϕ (with the η width varying somewhat), and the SMD-ϕ strips are roughly 0.10 x 0.007 in η x ϕ. The towers are significantly larger than an electromagnetic shower, so their resolution is roughly 0.025 x 0.025. The SMD-η plane has η-resolution around $0.0011 + 0.0026/\sqrt{E}$, determined by test-beam measurements. The SMD-ϕ plane has ϕ-resolution around $0.0017 + 0.0031/\sqrt{E}$ [Bed03]. Actual test beam measurements are not expected to produce the module-to-module variation (which is not expected to be large), so these numbers are estimates, and expected to be a little too low for the real data, but not by more than a few percent.

The BEMC is thus a highly segmented detector that requires a large amount of support hardware and software in order to operate. Each PMT requires its own high-voltage supply and readout electronics. The SMDs require 60 anode wires

maintained at high voltage, per module. The resulting segmentation is as follows, for the full detector acceptance of 2 units in η by 2π in ϕ. There are 4800 towers, 18000 SMD-η strips, and 18000 SMD-ϕ strips. For the 2003 *d+Au* collisions, half of the BEMC was operating. This results in 2400 towers, and 9000 SMD strips per plane.

4.4.3.3 Recorded Data

When the STAR detector registers an event, all 20,400 channels are sampled (west half of the BEMC only: 2400 towers, 9000 SMD-η strips, 9000 SMD-ϕ strips). Once the event trigger line is set, the various ADCs involved in the readout electronics record an energy signal for each channel. In the stored data, the index of the data and the detector number can be used to provide spatial information. Calibration information specific to the given channel can then used to reconstruct the actual energy signal observed by the channel. The BEMC planes all use a standard calibration scheme where a channel's status is tracked, as well as its pedestal and gain values. The STAR software system is designed to handle a 5^{th} order polynomial calibration curve for each channel, but the towers and SMDs have not been calibrated beyond the 1^{st} order gains. Determination of calibration constants beyond 1^{st} order is not expected to improve analysis significantly given the current state of systematic uncertainty in BEMC analyses.

For a given channel, then, the energy is given by the standard equation:

$$E_{ch} = (ADC_{ch} - Ped_{ch}) * G_{ch} \qquad (4.3)$$

The values for the pedestals (Ped) and gains (G) were found during post-analysis of events. Other than large electromagnetic shower energy depositions – the target data – there are two other classes of observed signatures. Those are nothing, and

minimum ionizing particles (MIPs). When nothing is observed, the pedestal is recorded. When MIPs are observed, a characteristic signature is recorded. The MIP signature should provide a peak at around 25 MeV due to the BEMC's full thickness, and the standard ionization energy deposition around 2 MeV cm^2/g in the scintillator material [Bed03, WN02, LR02]. The tower gains were further calibrated by matching electron momenta found in the TPC to energy deposition in the towers. Figure 4.10 shows the relationship between energy measured in the towers and the momentum measured in the TPC. The correlation agrees with a linear gain. This figure is part of the electron calibration carried out by Alexandre Suaide. Using this figure and additional simulation results, the final gains were set for the BEMC.

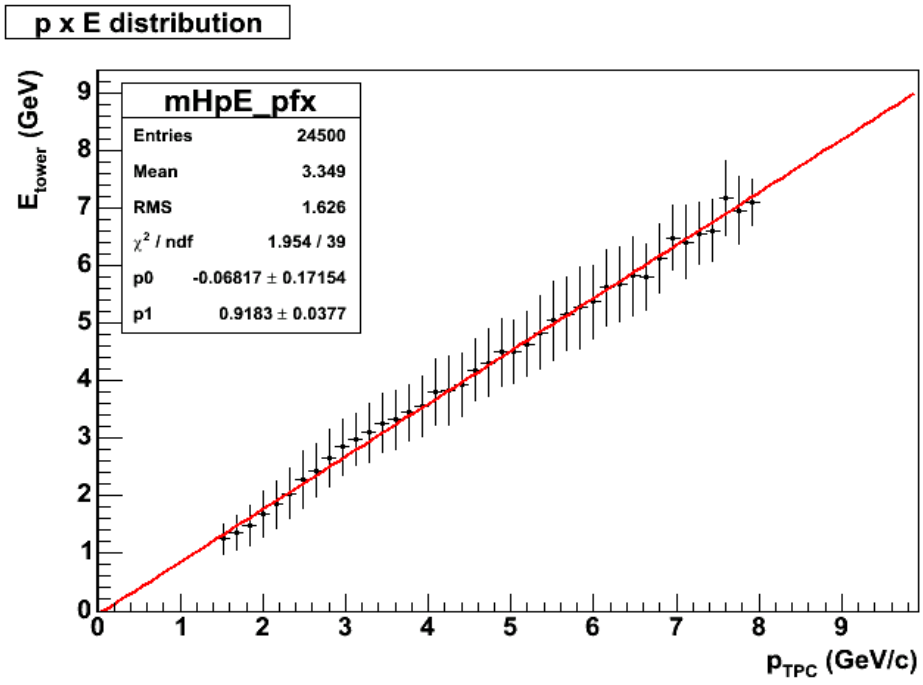

Figure 4.10: The relationship, for electrons, between the momentum measured in the TPC and the energy deposited in the BEMC. Note that the resulting calibration agrees well with a linear gain.

When real particles enter the BEMC their individual interactions lead to energy signatures. The specific types of interactions and granular structure of the BEMC are reflected in the data stored. In order to use the data, both the detector structure and the particle's interaction must be used to invert the detection process. For example, if a photon enters a BEMC module, it will shower in the lead and scintillator material. The resulting shower will be recorded as light signatures in possibly several towers. Similarly, the shower will be observed by the SMD layers, which will lead to recorded SMD energy signatures. When the event is over, all we have are the position and energy information for all the channels observing the photon. It is necessary, in order to use the data, to reconstruct the parameters of the photon from the recorded data. Given the data, though, after a small set of veto cuts, analyses must assume the data was the result of a photon.

We will now discuss how the data is used to infer real particles impinging on the BEMC. In general most particles that deposit energy above the minimum ionizing peak (MIP) level do so in such a way that all their energy (within $21X_0$ of material) is deposited electromagnetically. Thus the energy measured in the towers will be the total energy for the particle, and the particle will have showered electromagnetically A small amount of the energy (less than 2%) may punch through the detector for very high photon energies (30 GeV), but this is taken as a systematic error in the energy calibration [WN02] . For most cases, the BEMC is used to observe electrons or photons, and the reconstruction scheme for these two is the same[3]. This reconstruction method is the standard algorithm used in the STAR analysis software library.

[3] Differences are typically handled by tuning the reconstruction algorithm based on "cluster parameters", which are discussed shortly.

4.4.3.4 Signal Reconstruction

- Hits

The lowest level description of physics data for the BEMC is the "hit". A hit is simply the combination of a physical position and measured energy. All reconstruction algorithms start with this information. For the BEMC there are three sets of hits, one for each plane of the detector. That is, one set of hits is from the towers while the other two come from the SMD-η and SMD-ϕ planes.

For the reconstruction algorithm used on this data, the hits for each plane are considered separately during the next stage of the analysis.

- Clusters

Clusters of hits are then formed. The method of clustering is unique for each plane of the BEMC. However, some aspects of the clustering are shared by all planes, so we will cover them first before discussing the differences. First, all the hits are grouped by module. Then the hits for a given plane are organized in order of decreasing energy. The largest energy hit is then considered as a seed for a cluster. In the event that it exceeds a minimum seed energy, the algorithm starts a proto-cluster which may or may not meet the requirements for propagation farther in the analysis. The proto-clusters are grown by going down the list of remaining hits and appending neighbors to the cluster hits. It is important to point out that the hits may be neighbors of added hits, rather than the seed. Also, the list is only queried in order of decreasing energy. An example of the algorithm, applied to SMD-ϕ clusters is shown in Figure 4.11. This figure shows six SMD energy measurements spread out in ϕ, together with a reconstructed cluster, as indicated.

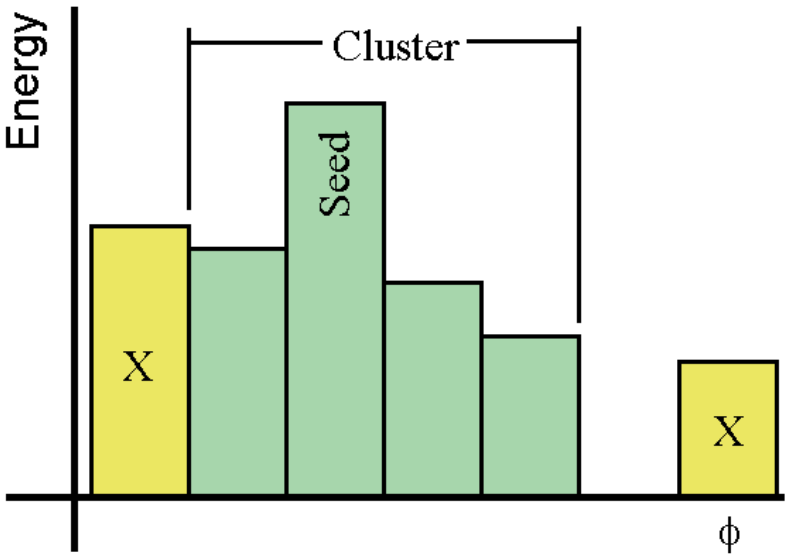

Figure 4.11: Example cluster of SMD-ϕ hits is shown. Neighbors must have monotonically decreasing energy from the seed. The strips marked with "X"'s will not be part of the cluster because they have lower energy strips between them and the seed.

Thus clusters may grow in any direction consistent with hits in the given plane, as long as the energy is monotonically decreasing. Once a cluster is constructed, the hits in that cluster are taken off the hit list. The remaining hits then go through the same algorithm again. The process is repeated until all the hits remaining fall below the limit for starting a new cluster.

We will now discuss the differences in the clustering in the three planes of the BEMC. These differences are due to the so-called cluster settings, and the restrictions on the geometrical shape of the clusters. The settings are given in Table 4.3. If the threshold for the cluster is below that of the seed, all seeds will create clusters with at least one hit, unless they are included in another cluster with a higher energy seed. To state this another way, the cluster threshold setting is essentially

unused since it is below the seed setting. Those settings are only included here for completeness. No seeded cluster will fail to exceed the cluster threshold.

Table 4.3: The Cluster Settings for the BEMC in this Work

BEMC Plane	Cluster Seed (GeV)	Minimum Energy for Add (GeV)*	Cluster Threshold (GeV)**	Maximum Hits per Cluster
Tower	0.350	0.00050	0.050	4
SMD-η	0.100	0.00025	0.025	5
SMD-ϕ	0.100	0.00025	0.025	5

* These settings are very low. Using settings like this essentially causes the clustering algorithm to include all non-negative data from neighboring channels.
** When the Cluster Threshold is below the Cluster Seed all seeded clusters will be used for analysis.

The "maximum hits per cluster" parameter determines the remaining differences between the planes. For the tower plane, the clusters must be no more than 6 hits, and those 6 hits must not be larger than three towers in η and two towers in ϕ. We did not use such large clusters, however, because photon showers are contained (99% of the energy) within 3.5 Molière radii (R_M = 1.57 for the BEMC towers). Hence all deposited energy would be contained in a single tower, except for photons that hit edges, so tower clusters are limited to 4 hits. The SMD-η plane requires all hits to be adjacent strips in increasing or decreasing η. The SMD-ϕ plane is the same as the η plane except that the strips must be adjacent in ϕ, while all being centered at the same η. The η-plane basically imposes a similar geometric requirement intrinsically, due to clustering in the same module. The ϕ-plane, however, can have adjacent strips that are not at the same η, but the algorithm does not cluster them.

- Points

Once the hits in all the planes are clustered, the final step of the data construction for the BEMC can be done. This final step is to associate related energy information in each plane to construct energy deposition events. This process is called "point making", and in an ideal setup, each point would represent a BEMC impact position

and total energy of a real photon or electron (or hadron which showered electromagnetically). A schematic of this entire process is shown in Figure 4.12.

For any particular energy deposition event, each plane of the BEMC observes independently. The response of each plane is the result of a stochastic process. As a result, real energy deposition events may or may not produce clusters in the BEMC planes. Deposition events can be classified by type, where type refers to exactly which planes of the BEMC provided data. Hence the point-making algorithms must take into account what type of point is being reconstructed.

It is important to clarify what types of points there are, and specify what types are acceptable for π^0 reconstruction. Since energy resolution is severely limited in the SMD planes, all acceptable points must have tower data. Point-making begins by selecting tower clusters, and then attempting to associate SMD information to them. Given a tower cluster, there are four possible continuations of the point making. These four come from whether or not there are SMD-η or SMD-ϕ clusters in the same place as the tower cluster. The four types are thus: (A) the point has tower energy but no SMD information, (B) the point has tower and SMD-η information only, (C) the point has tower and SMD-ϕ information only, and finally, (D) the point has tower information and both SMD-η and SMD-ϕ information.

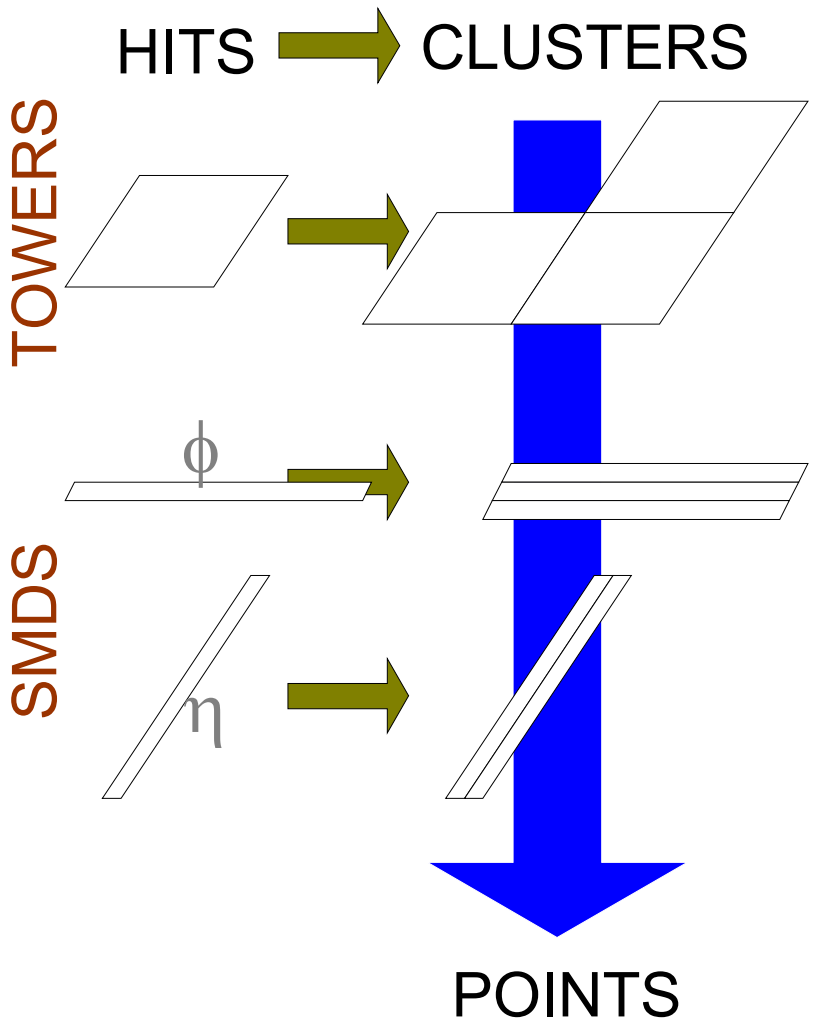

Figure 4.12: This is a schematic cartoon showing the relationship between the individual hits, clusters, and points. A sample cluster for each plane is shown. The points are the result of analyzing the clusters from all three planes simultaneously. Information from one plane is not used to perform the clustering in another.

Points that have only BEMC tower data, type (A), have very poor spatial resolution. This is because the tower size is large (~0.05ηx0.05ϕ). This alone is a good enough reason to exclude such points. There is another reason. For this analysis, the primary goal is the measurement of photons. Photons have only a 0.3% chance of not showering before the SMD plane. As a result, if the points do not have

SMD information it is most likely due to a problem with the SMD, which should be discarded. The statistical impact of losing the 0.3% of π^0 decay photons that do not shower in time, and have poor resolution, is insignificant.

When present, the SMDs provide better spatial resolution in their design coordinate. Of the three possibilities for contribution due to SMD clusters, the case where there are clusters in both planes of the SMD, type (D), is the most confusing, and will be discussed last. Presently, the two simpler cases, (B) and (C) are discussed. In these two cases, the tower cluster position is supplemented by the position of the SMD information in the design parameter of the SMD. For example, if an SMD-η cluster is present, the point is constructed with the SMD-η cluster used for the η position, and the tower cluster used for the ϕ position. If multiple SMD clusters were found in the same space as the tower clusters, then multiple points are made, and the energies are assigned based on the SMD energy ratios. For example, if two SMD-η clusters were found with their ηxϕ centers inside the area of a tower cluster then two points would be constructed. If those two SMD clusters had energies of 1 and 2 GeV, then the points would be assigned 1/3rd and 2/3rds of the tower cluster energy.

The remaining point type (D), where SMD information is available for both η and ϕ planes, is more complicated. It is also, however, the only type used in the analysis. This point type guarantees that the spatial resolution of points is better than 1 strip by 1 strip, or 0.007x0.007 in ηxϕ. Test beam results show the effective resolution is closer to 0.0035x0.0035 (see above).

For type (D), the details involved in using the cluster information to produce the points are very similar to the case where only one SMD plane is available. However,

the total number of points constructed is the smaller of the number clusters in each plane. So if there is only 1 η cluster, then only 1 point will be constructed regardless of how many ϕ clusters are available. The question remaining, then, is how are the SMD clusters selected since only 1 cluster in each plane can be reasonably applied to a particular tower cluster.

To answer this question, consider the following scenario. Two photons strike a region of the detector where all the energy is collected in one tower cluster. Photon 1 leaves $E_{\eta 1}$ and $E_{\phi 1}$ in the SMD η and ϕ planes respectively. Photon 2 leaves $E_{\eta 2}$ and $E_{\phi 2}$. The clustering algorithm does not know which two should be paired, so it finds the vector k that minimizes the following expression.

$$S = \sum_i \left| E_{\eta i} - E_{\phi k(i)} \right| \tag{4.4}$$

Requiring SMD information in both planes reduces the efficiency of the detector. The resulting efficiency is shown in Figure 4.13, which shows efficiencies for each of the SMD planes, and the combined efficiency for both planes. This measurement was carried out on all points with tower energy above 700 MeV and SMD energy above 400 MeV. This efficiency applies to general points, and is not accurate enough to draw conclusions about overall efficiency effects to specific π^0 detection efficiency.

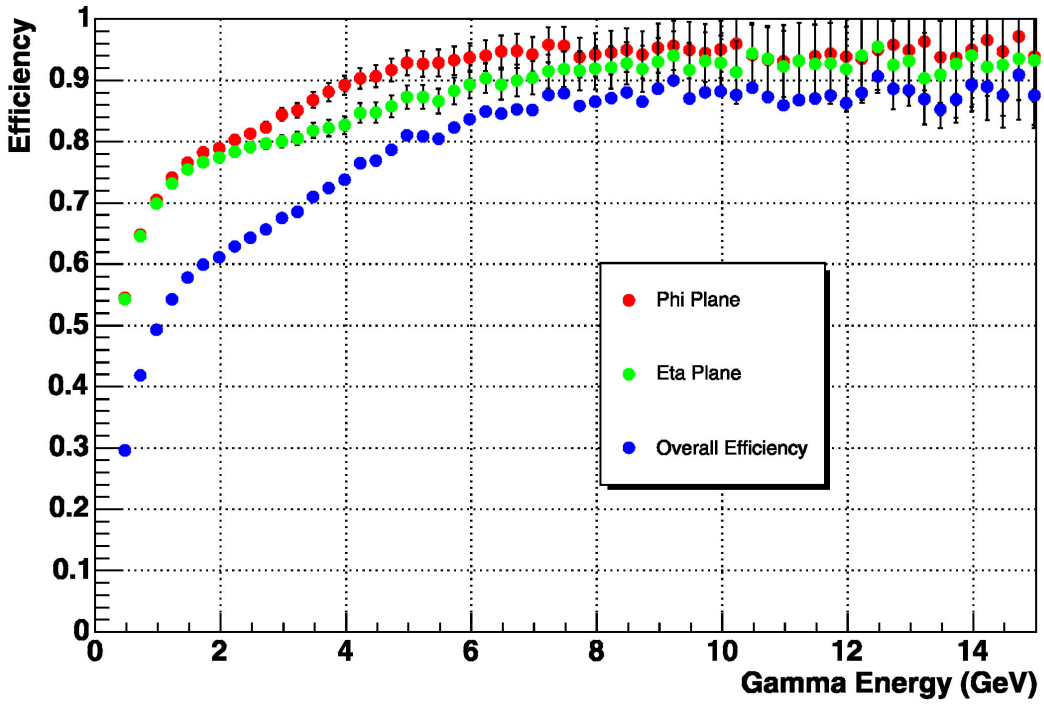

Figure 4.13: The general efficiency of the SMD planes are shown. SMD hits were found by association with a tower cluster above 700 MeV. Efficiency for the $\eta(\phi)$-plane was determined by dividing the number of points with both η and ϕ SMD information by the number of points with $\phi(\eta)$ information. Requiring energy in both SMD planes is required for spatial resolution at high p_T, and results in about 35% reduction in statistics due to efficiency.

- Point Damage

The details of the point-making algorithm produce artifacts in the data that cannot be avoided. These will be covered in depth in the data analysis chapter. For now, though, it is illuminating to discuss ways that the SMDs can systematically damage the tower clusters during point making.

The point making is affected by the SMDs only when they assign position, or provide energy ratios. The energy ratios are reasonably straightforward so we will not worry about those here. The positions, however, allow for data corruption. Because of the energy resolution of the SMDs, it is quite possible that a single SMD

cluster will be split into two such clusters. This can happen when a cluster should have three or more strips, but one of the middle strips reads out with a very low energy. Since the probability of such an effect is high (the energy resolution is $\sim 14\% + 86\% / \sqrt{E}(GeV)$, so there is about a 15% chance a strip that should read-out at 1 GeV will instead be very low), it could reasonably happen in both planes simultaneously. This would result in two points being constructed where there should be only one. This, however, should be an effect that can be simulated easily.

Another source of cluster splitting, which is not so simple to simulate as the energy resolution is when single SMD strips are off, or otherwise not measuring energies correctly. In those cases, more splitting may occur than can be simulated. This is because the simulation will depend on getting accurate information about which strips causing the splitting. The best way to deal with this problem is to identify which sections of the detector are causing the splitting, and remove them from the analysis.

4.5 Detector Review

For 2003 the RHIC facility provided *d*+*Au* collisions at $\sqrt{s_{nn}}$ = 200 GeV. During this run, the STAR detector was well situated to provide commissioning data for several of its detector subsystems. It also had a suitable constellation of detectors operational for the detection of π^0s at mid-rapidity. Using this configuration, the data for the topic of this dissertation was taken.

In this chapter we discussed the location, construction, and data structure of the detector subsystems used in this work. The primary detectors are all subsystems of the STAR detector at RHIC. They are the Zero Degree Calorimeter in the Au

direction (ZDC-East, ZDC-E), the STAR Time Projection Chamber (TPC), and the Barrel Electromagnetic Calorimeter (BEMC).

The ZDC is used in conjunction with the RHIC timing to provide a trigger so that event information can be collected from the detector subsystems. The resulting Minimum Bias trigger samples 95% of the *d+Au* hadronic cross section with 5% systematic uncertainty. The TPC and BEMC are used to identify and measure photon energies. The TPC is also used to identify the source of the tracks in an event and thereby determine the position of the actual collision. The BEMC is also used in conjunction with the Minimum Bias trigger to provide a High Tower trigger based on a large energy deposition in the BEMC during a ZDC based trigger.

With the configuration and data structure discussed here, we are ready to discuss the actual data used during this work. The systematic structure imposed on the data is discussed in the next chapter, 5, and the data and its analysis are discussed in chapter 6.

CHAPTER 5

Data Overview

5.1 Introduction

Collisions are provided by the RHIC facility at each of the intersection regions. It is up to each of the individual detectors, such as STAR, to determine when collisions occur and elect whether or not to save the data[1]. It is essential to present information about what types of collisions occurred, how they are classified by STAR, and the criteria the collisions must satisfy in order to be a recorded event in the STAR data archive.

In this chapter we will discuss the general data recorded by STAR. For example, it is important to have a rough idea of how many collisions have been sampled, and with what parts of the detector. That is, it is important to know the portion of events that match to the required operating configuration for the detector. We will cover the data used for this analysis, as well as providing some details about other collision species used at different times. With the broader information at hand, we will look more closely at the particular details of how collisions are selected and stored. When stored the recorded information is referred to as an event. The actual data recorded,

[1] A standard design ZDC system is used to sample the collision rates at PHENIX and STAR. Similar but not identical measurements were made at Phobos and BRAHMS to aid the collider operators in providing comparable event rates to all experiments.

however, is heavily dependent on the STAR detector's global configuration, which determines the types of events that will be favored. It also depends on the collision rate, because common event types will be more aggressively discarded.

The final piece of information that we will discuss here has to do with the actual cross section for collisions. We will briefly discuss STAR's overall cross-section measurement for *d+Au* collisions. This chapter will conclude with a short discussion of remaining normalization constants necessary for comparing results to theoretical predictions and other experiments. Such a discussion is appropriate here because normalization of the results from STAR depends on the biases for the recorded events.

5.2 Luminosities

RHIC has provided collisions to the STAR detector for several years now. The data taken for this work was taken during the 3rd physics run at STAR. The first two runs were in 2000, and 2001/2002, when Au on Au collisions were provided. Some of the observations in 2001/2002 suggested the need to run a control experiment, so RHIC provided *d+Au* and *p+p* collisions during 2003. Since 2003 the collider has continued to provide collisions including an additional control experiment colliding copper nuclei together. 2003 is the first year where RHIC supplied *d+Au* collisions. RHIC also provided *d+Au* collisions in 2008. Data taking for the recent run has just ended, and the data is being analyzed. For the work here, only the 2003 data were used.

In 2003 RHIC provided 20 nb^{-1} of *d+Au* to STAR. The physics program provided by RHIC is summarized in Table 5.1. Not all of this luminosity was usable though.

The STAR BEMC was installed in stages, beginning in the 2001-2002 run, and continuing through the 2006 run. For each stage of the installation, different goals were set for the detector, and a portion of the beam-time early in each run was used to stabilize the detector. The west half of the BEMC was installed for 2003. Stabilization after the year-to-year changes reduced the useable luminosity for BEMC data to 15 nb^{-1}. The actual sampled luminosity is lower due to overall beam use efficiency and to unstable BEMC operation during some periods.

Table 5.1: Summary of Beams provided by RHIC (energies are $\sqrt{s_{nn}}$)

Year	Species 1	Species 2	Species 3	Species 4
2000	*Au+Au* 56 GeV	*Au+Au* 130		
2001/2002	*Au+Au* 200	*Au+Au* 20*	*p+p* 200	
2003	*d+Au* 200	*p+p* 200		
2004	*Au+Au* 200	*Au+Au* 62	*p+p* 200	
2005	*Cu+Cu* 200	*Cu+Cu* 62	*Cu+Cu* 22	*p+p* 200
	p+p 405			
2006	*p+p* 200	*p+p* 62		
2007	*Au+Au* 200			
2008	*d+Au* 200	*p+p 200*		

*The *Au+Au* 20 GeV beam delivery lasted less than 1 day.

The actual delivered luminosity to STAR can be used to establish rough normalization between different experiments. However, better results come from establishing the geometrical cross section for collisions, then normalizing observations to that cross section. In this way, the absolute cross section for the production of a particular particle can be reported. In addition, the sampled

luminosity can be calculated after the fact by inverting the luminosity relationship. The following equations express these points directly.

$$\begin{aligned} N_{MB} &= \sigma_{MB} \cdot L \\ \frac{dN_p}{d\Omega} &= \frac{d\sigma_p}{d\Omega} \cdot L \\ \frac{dN_p}{d\Omega} &= \frac{d\sigma_p}{d\Omega} \cdot \frac{N_{MB}}{\sigma_{MB}} \end{aligned} \quad , \tag{5.1}$$

N and σ are used to denote number of counts and cross section, respectively. The "MB" subscript refers to the "Minimum Bias" event class. Here L can be used for luminosity in the first equation, and for effective luminosity in the second. That is, σ_{MB} is determined separately. Then, during collection of N_p (the number of particles ~ π^0s), N_{MB}-effective is collected. This count of N_{MB} can then be used to determine the effective luminosity involved in the observation of N_p.

For the 2003 *d+Au* collisions, the BEMC was operational beginning on the 41st day of the run. Collisions were carried out for another 41 days, so that day 82 marked the last day of *d+Au* collisions. The 41st day of the run was February 10, 2003 while the 82nd was March 23, 2003. The period before day 41 provided useful physics data to other analyses that do not depend on the BEMC and its SMDs.

5.3 Event Triggering at STAR

The collisions provided by RHIC must be identified in the STAR detector before events can be recorded. The detectors involved in the triggering were discussed in Chapter 4. The hardware used includes the ZDC, timing of the bunch crossings, and BEMC energy deposition signals. However, the way these are all combined with the data acquisition system (DAQ) is important for classification of data. The data

classification and constants associated with the classification will carry through the rest of the analysis. It is necessary to describe the classification system and collect information about it for use in analysis normalization.

The classification of events is made on the signals used to trigger them. The events themselves may provide high-energy signatures in the BEMC. They may only provide a ZDC energy deposition. Further, the data must be classified by the configuration of the detector at the time of collision. For example, sometimes the STAR detector is configured to provide a special trigger on high-energy BEMC events, and sometimes does not provide the special trigger.

STAR is built around several layers of triggering. At the lowest level, L0, various detectors are given essentially direct feeds to a trigger control unit (TCU), which looks up the appropriate action given the trigger bits from the detectors, and the states of the detectors. If an event is selected for storage, the TCU forwards information to the trigger clock distribution (TCD) boards. The TCD then fans-out trigger signals to all the detectors [Bie03]. The resulting trigger signal is used to tag the data from all of the detectors in STAR and thereby record energy signatures in coincidence with the trigger signal. The L0 trigger selection is a rather basic set of Boolean rules that can be interpreted quickly. The L0 trigger is just a fast lookup system, and can only make simple decisions about the type of event it is looking at. There are two other levels of hardware triggering, L1 and L2. Both L1 and L2 provide measurement of event topology that enables selection of some specific types of data. For example, L1 allows coarse-grain detection of beam-gas background. The slowest triggers, however, are based on software analysis of events. Direct analysis of TPC information is this type of trigger. Such slow triggers are called L3 triggers [Adl03b].

For this work, the event rate necessary to observe high-p_T π^0s is rather high. Multiple triggers are required because event rates far exceed the STAR DAQ's ability to record them to long-term storage (the DAQ could record about 50/s during 2003). Hence it is important to be able to select special events that display some particular attributes. However, it is equally important to have a well-controlled method of selecting them. The overall configuration of the data acquisition and triggering system is known as the "global setup". A global setup includes instructions for the different levels of the trigger system. Each global setup holds a definition for the triggers that are to be included during data taking. If the global setup does not include a particular trigger, no events with that trigger will be identified. An example of this is the global setup "dAuMinBias" where no high tower events were identified.

For *d+Au* collisions, the STAR detector ran with several configurations. The trigger types and raw numbers of events can be seen in Table 5.2. For the analysis presented in this dissertation, data from only three of the global setups were used. They are "dAuMinBias", "dAuCombined", and "UPCCombined". The first global setup was used to provide mostly MinBias data, and is used to develop the standard event cross-section information. The other two setups were used to provide specialized data when the BEMC observed a large energy deposition in a subset of its towers[2]. In the dAuCombined and UPCCombined setups, two "high tower" triggers indicative of large energy deposition in the BEMC were used. It should be noted that a large portion of the dAuMinBias events were not suitable for analysis here because the BEMC operation was not stable enough until day 41 (out of 82).

[2] The triggers were based on 4x4 tower patches with total ADC sums above a threshold based on the particular trigger.

Table 5.2: Global Setups during 2003 *d+Au* Run

Global Setup	# of Events Recorded
DAuMinBias	**16,574,481**
DAuCombined	**14,115,350**
UPCCombined	**3,743,270**
dAuFPD	1,187,475
dAuTOF	2,659,720
HTonly	336,687
zeroBias	459,519
pedAsPhys	301,872
pedEMC	5,599
laser	222,370
testMinBiasBBC	411,207
testFPD	98,130
jettest	133,065
testEEC	102,703
testJPsi	4,616,464
testEMC	552,735
testMinBiasHighTower	433,883
testUPC	279,083
testBBC	1,999,443
testZDC	349,678
minbiasTest	41,708

- Most totals include runs that were later found to be unacceptable. The final totals for the production triggers we used (bold) are at least 50% of what is shown.
- Some trigger types record events at a very fast rate compared to others.

The global setups include a description of the trigger mix to be recorded. For this analysis the three triggers of interest are MinBias, High Tower 1, and High Tower 2. Table 5.3 provides the total number of events recorded for each of these triggers, based on the three standard global setups.

Table 5.3: Raw event counts sorted by trigger summed over the three global setups used: dAuMinBias, dAuCombined, and UPCCombined

Trigger	Total Events	Events after Day 40
MinBias	25,730,209	16,573,803
High Tower 1	1,222,872	1,222,872
High Tower 2	839,363	839,363

5.4 Prescale Factors

In order for these global setups to be of any real value, they must enhance the chances of recording special events. Hence, the global setups also include the ability to ignore the majority of the common events. A fraction of the common events must be recorded, however, as they provide normalization of the event rates. These events also compare the detector behavior across different operating environments to ensure quality.

For this data, the Minimum Bias trigger would often provide event rates far in excess of the DAQ's ability to record. Such a mismatch would result in the detector being unable to observe events most of the time. To reduce this dead time, the Minimum Bias trigger was "prescaled" to allow the BEMC to observe exotic events a larger fraction of the time.

The BEMC provided the trigger system with exotic triggers based on large energy depositions. Two such BEMC triggers were configured. They are the High Tower 1 (HT1) and High Tower 2 (HT2) triggers. Each trigger involves an energy threshold for towers in the BEMC.

These alternate triggers could also be prescaled, and give a count target that, once hit, allows the storage of an event. Much of the time the MinBias trigger was prescaled by about 3000, so that 3000 MinBias triggers were required before one was

recorded. Similarly, sometimes the lower threshold high tower trigger (HT1) was prescaled to allow the other (HT2) to trigger more often.

A lookup table handles the prescale factors on the hardware triggers. Implementation of that table has a quirk. Each possible intersection of trigger requirements must be prescaled separately. This means that in MinBias events that were recorded under a global setup that had the HT1 trigger, there would be two types of MinBias triggers, each prescaled separately. The two types of triggers would be (A) MinBias without HT1, and (B) MinBias with HT1. If MinBias was prescaled by 3000, then MinBias events satisfying the HT1 requirement would only be recorded on the 3,000th event where both conditions where satisfied. An example of this situation is given for the MinBias, HT1, and HT2 triggers in Table 5.4.

Table 5.4: Example of the prescaling of multiple event trigger classes during the observation of 3 million MinBias triggers.

Trigger "bits"	Total Events	Recorded Trigger	Trigger Prescale	Recorded Events
MinBias Only	3,000,000	MB	3,000	1,000
MinBias &	20,000	MB	3,000	6
HT1		HT1	10	2,000
MinBias &	0	MB	0	0
HT2[1]		HT2	0	0
MinBias &	2,000	MB	3,000	0[*]
HT1 & HT2		HT1	10	200
		HT2	1	2,000

[1] – All HT2 events are also HT1 events, so MinBias & HT2 cannot occur unless HT1 also triggers.
[*] - No minimum bias events satisfying HT2 will be recorded because the prescale factor system requires 3,000 to be observed before one is recorded.

This leads to statistical trouble if large prescales occur often in rare event classes and the runs are too short[3]. The example in Table 5.4 above shows that a run where 2,000 HT2 events are recorded will not contain a single MinBias event that satisfies

[3] The full data taking for a year is referred to as a run. Individual data-taking periods of usually less than an hour where the detector operates continuously, are also called runs.

HT2. For a single-run this is a statistical concern, but causes no practical trouble. However, if hundreds of such runs occur, the MinBias data sample will be missing a significant portion of its high-energy spectrum of various particles since those particles may trigger HT2 and be prescaled out of the dataset. For this analysis, only runs with a large number of all event classes were used. Thus, this statistical issue should not affect this work.

5.5 Cross Sections

In the last chapter the efficiency of the MinBias trigger to select the *d+Au* hadronic cross section (σ_{dAu}) was briefly discussed. The purpose at that time was merely to discuss the triggering system. It is, however, important to present the measured cross section, as determined by STAR.

Further, it is necessary to determine the best estimate of how to compare *d+Au* collisions to other collision systems. Comparing the number of binary collisions of the constituent nucleons is the usual course of action here. That is, the number of produced particles, and therefore the cross section, is expected to scale with the number of nucleon-nucleon collisions. Some interactions, however, are expected to scale with the number of participant nucleons rather than the number of independent collisions. The first type is indicative of "binary" scaling and the second indicates "participant" scaling. For the observations here, binary scaling is expected to hold.

Both the number of binary collisions and the cross section are qualities of the events themselves. That is, the MinBias events have an associated cross section and an average number of binary collisions. While for HT1, the cross section is lower but

the average number of binary collisions is higher. These measurements must then be tagged with the event type to which they apply.

Since these measurements are intrinsic to the data, they are not appropriately a theoretical consideration. However, these measurements are experimental results external to this work. For these reasons, the measurements are best presented and discussed here. They will be used for comparison of analysis results in chapter 8. Since we will be normalizing the measurements to the MinBias results, we only quote MinBias results here. Based on Monte Carlo Glauber calculations [Adl02, Cho03], $\langle N_{bin} \rangle$ = 7.5+/-0.4, and the geometrical hadronic cross-section, $\sigma_{\text{dAu-hadronic}}$ = 2.21+/-0.09b. These calculations incoporate the Hulthén wave function of the deuteron [KLN04, HS57].

5.6 Scaling of HT1 and HT2

The high tower triggers pose an interesting example of how alternate triggers are scaled for comparison. As stated above, we do not give the $\langle N_{bin} \rangle$ and cross-section for high tower events. Instead, the results gathered from these trigger datasets are normalized through their underlying MinBias events.

When data is collected for a high tower event, it occurs in a sea of MinBias events. These events provide a straight-forward source for normalization which we use. Extending the example in Table 5.4, for that run, the 2,200 HT1 events were recorded during the same run where 1,006 MB events were recorded. Since HT1 had a prescale of 2, anything measured in the HT1 dataset is only ½ of what actually occurred. At the same time, 1,006 x 3,000 = 3,018,000 MB were observed (2,000

were lost due to rounding). So normalization of HT1 is found by using the prescales and recorded MB event counts to determine the appropriate MB normalization.

5.7 Summary

This chapter has described the general structure of the datasets. This includes details about which data was taken at what time during the run. The interplay of taking several datasets simultaneously was discussed. The various datasets must all be folded together to produce useful results, so any inherent problems must be taken into account.

The ability to combine the results from the multiple datasets in a useful way depends greatly on normalizing the overall data structure. Normalization is necessary both internally and externally. The internal normalization is handled by restricting the normalization to the MinBias event class only, and tracking the prescale factors assigned to each trigger type during the course of the full run. External normalization is necessary to compare the results here with other experiments, and provide absolute measurements of particle production. The normalization factors were presented here in terms of the cross section and $<N_{bin}>$ determination.

An overall sense of the operation of the detector for the *d+Au* run can be seen in this chapter. The beams were provided over a span of 82 days. During that time more than 40 million events were recorded at a rate of about 50/second. However, the total observed events were much higher due to trigger mixing and prescaling. The electronics observed on the order of 10 nb^{-1} with a cross section of ~ 2b. Thus the total number of observed events to sift through was on the order of $2x10^{10}$.

The analysis now has enough information on the selection of events and normalization across different event types. From the last chapter, enough groundwork is laid to discuss the data from the individual detectors. Hence, we will now present the analysis of the data for collection and counting of π^0 signatures.

CHAPTER 6

Data Analysis

6.1 Data Analysis Background

This is the first section of the analysis chapter. In this section, the background details for the analysis are presented. This section gives an overview of what is to be measured, details on the resulting signals, and covers analysis issues that must be understood.

The groundwork for the analysis is laid in the following order. First we will present the particular measurement goals. Then we will discuss the attributes that are present in the data. Following that, we will specifically cover each cut that is used in the analysis. Finally, we will discuss the other issues that impact the data analysis.

Many of the issues presented are strengthened by actual observations in the data. When possible we will show these effects directly.

6.1.1 Analysis Goal

This dissertation aims to provide the cross-section for inclusive π^0 production in *d+Au* collisions at $\sqrt{s_{nn}}$ = 200 GeV. Paramount to such a measurement is the ability to actually observe, and thereby count, the π^0s produced in those collisions. We have

presented the detector configuration in the chapter on experiment setup. What we will do in this section is develop the analysis system for the real data. Using this system we will produce measurements of the actual number of detected π^0s in the collisions. This is the first step in developing the actual cross sections, which also require knowledge of the event cross-section itself, and the absolute efficiency of the detector system. Both of those additional topics will be discussed following the presentation of this part of the data analysis.

For this analysis the $\pi^0 \to \gamma\gamma$ channel is the only process taken into account. This channel covers 99% of the produced π^0s. We are interested in observing these particles when they have high p_T, in order that the result is useful for comparison with fragmentation functions at large energy transfer. Thus we are primarily interested in the decay photons of large p_T π^0s (where large is taken to be above a few GeV/c). The BEMC provides the set of candidate γ's. Relativistic kinematics provides the machinery for reconstructing candidate π^0 pairs. Combinatorics plays the ringleader of the analysis. The resulting signal quality suffers from effects due to the BEMC, high momentum, and combinatorics. Cuts are used to improve the signal quality. Specifically, the photon signal is carefully sculpted by imposing requirements on the photon candidates, and the events are scoured to remove those of low quality.

In the sections that follow we will introduce the important attributes of the data analysis. These will allow us to quickly cover the impact of various observations. Then we will discuss how the data is improved by imposing cuts that attempt to remove, in a unbiased way, data that disproportionately confuses the desired signals. That is, we will introduce and discuss the set of cuts on the data attributes deemed to be beneficial to this work. At that point it makes sense to do some background

testing of the quality of the data selected by our cuts. Such testing is suggested in an effort to present material that is immediately useful, now, to verify the behavior of the data, and will also be useful, later, in verifying the behavior of simulation data used to examine the efficiency of the system. Following this we will be in position to collect the actual π^0 yields for the datasets of interest.

6.1.2 Data Attributes

During the data analysis, several attributes of the data became prominent, but were really beyond the scope of discussion at that time. These items are loosely categorized as conceptual areas that directly impact the viewpoint necessary to understand analyzed data. It is important to discuss these before we move on, because the framework of understanding will greatly aid the discussion of making absolute measurements presented in the next section. That is, the attributes discussed here must be understood, and verified to be present when calculating the efficiencies for each of the measured yields.

The identified attributes that we will cover are as broad as possible and cover specific details of the analysis that are unique concepts. It is true that much of the information here can be seen as basic to the sort of analysis we are doing. However, the specific way that these topics apply to this analysis is of particular interest here, because we will discuss precisely how they impact our target particles, detector, and the dataset itself. Since it makes little sense to simply present these issues in a stand-alone format, each topic will be introduced first at the peril of boring the reader with well-known effects, and its application in this analysis will then be discussed.

The goal of this section is to cover several topics that are addressed in different places, and often without directly calling out the particular details of the topics that are delicate in this analysis. With the material presented here, it is our hope that references made later will be easier to follow without an excessive amount of explanation.

6.1.2.1 Energy Asymmetry Effects

One of the cuts in the yield analysis is to require the energy asymmetry of the candidate photon pair to be less than 0.5. This requires that the less energetic of the two photons have no less that 1/3rd the energy of the larger one, or: $E_1 < 0.75\ E_0$, $E_2 > 0.25\ E_0$, where E_0 is the energy of the π^0.

Energy asymmetry is one of several ways of effectively imposing a decay topology cut. Because of the relationship between invariant mass and the energy of decay photons (see Appendix C), this cut is also an opening angle cut. The question can be asked, why not just use an opening angle cut then? And further, if the energy asymmetry cut is superior, what is the resulting work environment that should be understood when working with an energy asymmetry cut?

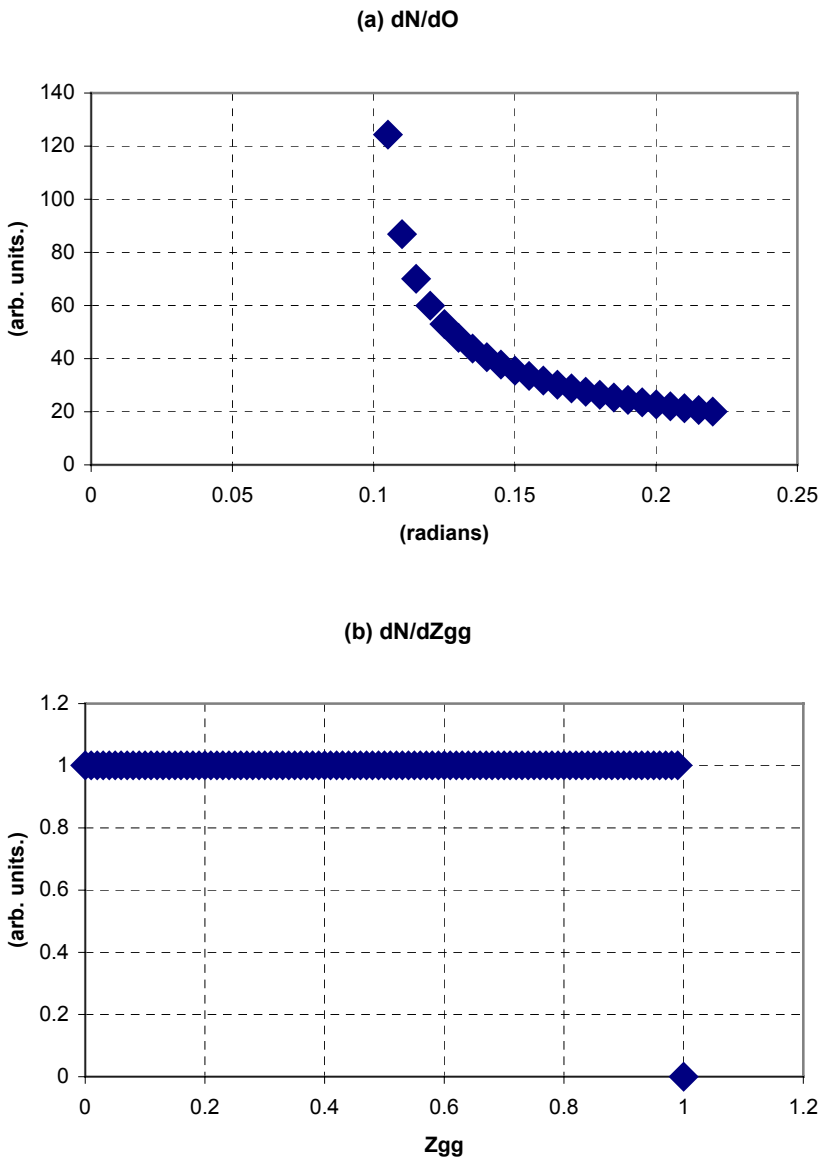

Figure 6.1.1: The probability distribution for decays as a function of (a) opening angle, and (b) energy asymmetry. The plots are chosen for an arbitrary particle with $\gamma = 20$. Note that the function in (a) is singular at the minimum angle of 0.1000 radians. The density as a function of energy asymmetry is constant up to the maximum asymmetry, β. See Appendix D for more information.

The energy asymmetry paradigm is preferable to the opening angle paradigm for two primary reasons. The first is found in observing the distribution of decay photon

systems. Figure 6.1.1 shows distributions of decay densities as a function of (a) opening angle and (b) energy asymmetry. The resulting parameters of interest in (a) are that the distribution is singular at the smallest opening angle, where $\cos\theta = 2\beta^2 - 1$, or $\theta \approx 2/\gamma$, and the distribution drops off to 0 at $\theta = 180$ degrees. For (b) the resulting parameters of interest are that the distribution is flat, at $1/\beta$, for all energy asymmetries between 0 and the maximum asymmetry that happens to also be β. In this case the energy asymmetry viewpoint is much cleaner to deal with in terms of relating the effective fiducial cut resulting from a particular parameter cut choice. Since β can be taken to be nearly 1 for all π^0s in this work, the effective phase space cut leaves exactly the cut parameter itself. That is, if we chose the cut $\varepsilon_{asym}<0.5$, then the cut leaves 0.5 of the phase space.

The second reason that the energy asymmetry cut is preferable is because of background. The majority of the background contribution, especially in the π^0 mass peak, is due to low energy photons being mixed with high energy photons. The resulting pairs can produce an invariant mass that we cannot remove, and the pairs themselves often cannot be cut due to opening angle. The energy asymmetry cut, however, guarantees that only similar energy photons (where $E_2 > 1/3\ E_1$) are used to construct the signal. It is also true that the energy asymmetry is rapidly falling off in terms of reconstructability at high energy asymmetry. That is, we simply cannot observe the low energy photon, so we might as well cut these candidate pairs.

The nature of this attribute of photon pairs is important to this analysis. Different aspects will be discussed later in this dissertation. All of the relevant aspects of the effect have been presented and justified here, so that those later sections will not be require lengthy discussion. In particular, we covered several points. The energy

asymmetry cut is superior to an opening angle cut. It results in a well defined fiducial volume based on a chosen cut. It removes background well.

6.1.2.2 Alternate Triggers

When *d+Au* collisions occur the detector must be made aware of them. This was discussed in more detail in chapter 4, but we will highlight some of that again quickly. The trigger with the least possible bias, developed for this collision system, was primarily the use of the ZDC-East detecting a neutral energy signature. Since the Au nuclei travel from west to east at STAR, this detector samples the evaporation neutrons from wounded Au nuclei in the outgoing Au beam. Essentially this would trigger events if the Au nucleus lost a low-energy (in its rest frame) neutral particle. This is a likely event in all *d+Au* collisions because the system's total momentum is heavily leaning in the direction of the Au nuclei, and there is always an excess of nucleons coming from the Au side in the collision. When an event is detected in this arrangement, it is said to satisfy the "minimum bias" trigger. The event itself is said to be a "minimum bias event".

Due to the number of stored particles in each beam of the collider, minimum bias events occurred at rates in excess of 10,000 events/sec. The data storage system can only store 50-100 events/sec, so the vast majority of the events that occur have to be discarded. But these events are likely to have things we wish to see, such as the rare large momentum transfer fragmentations that produce high-p_T π^0s. Hence it is beneficial to be able to pick out exotic events and store them separately. For this reason the STAR detector has a triggering system that allows various attributes of individual events to be determined rapidly, and the decision to record a given event

can be made on those attributes. Thus, when an event's attributes satisfy the requirements for an exotic trigger it can be recorded.

For the 2003 *d+Au* data collection, two such exotic triggers were used that provided enhanced π^0 detection at high p_T. They were called the "high tower 1" (HT1) and "high tower 2" (HT2) triggers. They are differentiated from the minimum bias (MB) trigger because they directly target events with a large signature in the BEMC potentially due to photons. The high-tower triggered events must satisfy the MB requirement and provide a 4x4 barrel tower region with a total ADC signature above a specified level. The trigger levels were roughly 2.5 and 4.0 GeV for the HT1 and HT2 triggers, respectively.

In order to analyze these alternate datasets, there are some clarifications to make. First, an event may be either MB or HT1, or both. This same line of discussion applies to HT2 also, without loss of generality. Even though HT1 events must satisfy MB, they are not necessarily "recorded" as MB. If they were, the MB dataset would be biased towards the HT1 events. However, all production rates are based on the number of MB events needed per each production event. Even in the HT1 or HT2 trigger datasets, it is necessary to know how many corresponding MB events occurred. This is handled by recording the prescale for the MB events, and counting the number of MB events. The prescale is a number, chosen before the run, that reflects how many MB events must be seen in order for one to be recorded.

The exotic triggers are, of course, insensitive to events with low-p_T π^0s. However, they should be quite efficient at collecting events with π^0s whose decay photons exceed the trigger threshold. In between, however, the triggers must transition from "off" to "on". This is called the "turn on region". Above the turn on region the high

tower triggers should agree with each other and with the minimum bias spectrum, provided the detector configuration has not changed between the datasets. Thus, the raw yield per minimum bias event for the triggers can be expected to fall on the same line, once the turn on region is passed.

Using data from these triggers requires some additional analysis beyond the minimum bias analysis. The differences can be isolated to cuts placed on the data before analysis. The details of the additional cuts are taken up later in this chapter in the section about analysis cuts.

6.1.2.3 Energy Thresholds

When detecting energy signatures the lowest detectable value must be understood. It is also important to know how precisely that lowest value, or threshold, can be observed. In this part we will briefly cover the various places that threshold effects are important to using the BEMC as a detector.

The BEMC was operated with 22,500 independent channels during the 2003 run. The working channels were almost all configured in such a way that a "zero" would be observable, thus all energy above 0 would be detected. Certainly, however, data near zero is almost all noise, and of limited use. The high tower triggers also employed energy thresholds for triggering events. The details of the data quality and how it is handled near these thresholds has wide reaching implications in the analysis.

The nature of energy distributions in these collisions is that they fall quite rapidly with increasing energy, especially at low energies. It is reasonable to have 10 times fewer data for energy changes of about 1 GeV. Because of the large amount of noise that would be stored, a threshold is used to remove the low energy data that is

essentially noise-dominated, and provides too low a signal to do anything useful anyways. However, even with such a threshold required for stored data, there is still a tendency for low thresholds to result in data dominated by noise. So it will often be necessary to establish an additional threshold, in software, to improve detector uniformity.

For the high tower triggers, this is a somewhat more insidious problem, because the trigger threshold is established in the hardware. That is, the trigger selection must occur based on the total ADC readout of a 4x4 tower region. This cannot be corrected for gain. Hence two neighboring towers could effectively trigger on different energies, such as 2.2 and 2.7 GeV, during the actual data collection. Such a hardware configuration difference would result in twice as many events triggered on the lower trigger. For this reason, analysis software must impose an additional trigger requirement based on gain-corrected energy.

Energy threshold related effects affect all parts of the analysis. Where necessary, we will point out when the detector uniformity is at risk from these effects. We will also provide explanation of methods to remove non-uniformity issues.

6.1.2.4 Point Construction Impact

The data that is used for the photon reconstruction comes from the BEMC's tower, SMD-η, and SMD-ϕ planes. The data from those planes is made up of energy signatures for individual channels, and the position information of those channels. The layout of the planes, and the method for producing the energy signatures, or "points", was discussed in the detector description in chapter 4. The individual pieces are combined in code in a process called "point construction". The algorithm used to

construct the points generally does well to describe individual energy deposition events. However, there are limitations to any algorithm used, and in this case they directly sculpt the resulting data and impose limitations on the reconstructed π^0 signature. We will discuss those effects here, as generally as possible.

The point reconstruction also directly depends on the configuration of the detector. Points cannot reliably be constructed where there are missing channels in the detector, or where the SMD has broken anode wires. The resulting dead channels provide zero energy, or just noise, during a real energy deposition. The algorithm used in our analysis cannot construct points across these dead regions, but will often identify the regions on opposite sides of the dead regions as independent points.

Besides dead regions, the geometric configuration of the detector contributes to limitations of the point reconstruction. The spatial resolution is the key limiting feature. Other features that impact the analysis, though, include the module edges, and the fact that the SMD-η plane strips do not have constant η width. Presently we will concentrate on the resolution and discuss the other effects momentarily. When two energy depositions occur close to each other (within 0.05η x 0.05ϕ) the SMD must be used to distinguish between them. In order to reduce background, however, we require that all points include clusters in both the SMD-η and SMD-ϕ planes. This means that the two energy deposition events must be far enough apart in both planes to make distinct signatures.

The manifestations of these effects in the reconstructed data are referred to as "cluster splitting" and "cluster merging". We will quickly cover the signatures of these in the data.

Cluster splitting destroys signals, but usually in such a way that candidate π^0s are lost in an unbiased way. In general it is caused by loss of energy information in the SMD, but it can also occur when energy is spread between two modules. When the splitting is limited to the SMD the impact is minimal unless it results in split points, which is unlikely unless both planes of the SMD have problems at the same time. Except for the module edge effect, cluster splitting is a result of localized problems in the detector, and thus reduce the average signal across the whole energy spectrum of points. When the energy deposition is due to photons, the shower signature is always contained in about 3 SMD strips (but the radius does grow with energy), so it is extremely unlikely that an appreciable increase in split clusters, in both planes simultaneously, would show much of an energy dependence.

Cluster merging is entirely a geometric effect that can be minimized during point reconstruction. It can be further minimized during analysis. During point reconstruction, thresholds are used to exclude low energy signatures. There are several such settings for each plane. Decreasing these thresholds allows two things. The first is that clusters may become large, but they will not merge due to the construction algorithm requiring decreasing energy signatures in subsequent contributing signals[1].

The second effect of lowered thresholds is that we may pickup additional, low-energy clusters in the SMD planes. These low-energy clusters may split tower clusters into multiple points. Additional points generated this way may be part of the

[1] Clusters may grow due to the inclusion of nearby hits that were below threshold. Tower plane clusters may grow by adding on any adjacent tower in the module. In the SMD-η direction, clusters may only grow by adding a low energy hit adjacent to the current cluster at either higher or lower ϕ. In the SMD-ϕ plane, sets of ϕ strips at the same η may grow, within the given module, by the inclusion of an adjacent strip at either smaller or larger η.

original energy signal that would have not have been split if higher thresholds were used. Hence, using the additional cluster information can reduce the number of incorrectly merged points.

During analysis we can further minimize the effect of merged clusters by not imposing such strict requirements on SMD signatures. That is, by selecting points that only require a hit in one SMD plane, we will allow points that were made by splitting a tower cluster based on the information in one SMD plane. This allows more cluster splitting than the more strict two SMD plane requirement. However, we will thereby pickup the resolution of a single SMD plane, which means that in one direction the resolution is about half a tower (0.025 - η or ϕ, compared to 0.003 for both SMD planes).

The minimum separation of clusters in SMD planes is roughly 0.014 radians. When two planes are required, both planes must meet this separation requirement. The resulting angular resolution is $0.014 \times \sqrt{2} \approx 0.02$ radians. This has a direct impact on the detection of all π^0s. The decay photons cannot be separated if they are closer than the resolution for the given point selection criteria. We use the two plane requirement, so the opening angle θ must be larger than 0.02 radians. If we apply this to the invariant mass reconstruction, we obtain the limit $m^2 = E_1 E_2 \theta^2 > E'^2 \cdot 4 \times 10^{-4}$. We can apply this to the π^0 mass to get the energy limit, in the middle of the barrel, for the smallest opening angle. For these conditions, we find $E' < 6.75$ GeV/c^2, for zero energy asymmetry. This corresponds to a maximum p_T of 13.4 GeV/c. This is a rough number, because at higher η's, the γ-resolution is worse due to larger overall momenta for a given p_T. However, we expect that the BEMC's detection efficiency begins to drop off for p_T around 13 GeV/c.

These point creation issues are expected to be handled properly in simulations. Observation of the effects in the simulation is necessary in order to determine if the simulation is accurate. The cluster splitting is handled by removing the portions of the detector where the problem occurs. This is an overall reduction in efficiency. The cluster merging is the result of the limited resolution of the point-making algorithm. There are two observable effects.

The first effect is that the acceptance of π^0s with opening angles smaller than 2 towers is reduced because the decay photons cannot be very close in ϕ or η. (If the separation is less than 2 towers the SMD is required to separate signals). This begins to affect the signal for π^0s with p_T above 2.5 GeV/c[2].

The second effect is that at high-p_T the separation may become too small for even the SMD to resolve. The SMD requires two strips of separation in each plane (the angular separation for two SMD strips is at least 0.014 radians, for both planes the total is 0.02 or larger). The impact of this effect is that the efficiency starts to be reduced above p_T = 13.5 GeV/c because the resolution begins to impact the fiducial volume of the energy asymmetry cut (that is, small energy asymmetries cannot be observed). The second effect completely covers the energy asymmetry cut of 0.5 at p_Ts above 15.5 GeV/c (footnote this applies to η = 0; at higher η the cuts come in earlier; refer to the relativistic kinematics appendix). An ancillary effect of the cluster merging problem is that once in this p_T range the opening angles, if observed (not merged), will be too large and contribute to constructed masses that are too high

[2] The limitation is strictly angular. $p_T \approx 2m/\theta$, at mid rapidity. Here, the angle is 0.1, and the mass is 0.135 GeV, so p_T is roughly 2.7. 2.5 is more conservative, since a separation of 2 towers is often across two modules.

6.1.2.5 p_T Smearing

The energy detection of the BEMC is assigned based on the tower plane energy measurement. The resulting energy resolution of the points is thus $16\%/\sqrt{E}$. This carries over directly to the measurement of the p_T of the detected π^0s. The effect of applying this resolution to well-defined particle p_Ts is called p_T smearing.

The analysis of π^0 yields is not based on counting individual π^0s. Instead, the parameters of π^0 candidates are histogrammed, and the histogram is analyzed. The sample of π^0 candidates is divided into p_T bins for histogramming. The sizes of the bins are chosen to minimize the error in the counting statistics. Because of the p_T smearing, particles may be reconstructed into the wrong bin. In general any bin's π^0s may be smeared into any other bin, however the effect is usually limited to only one or two bins of displacement.

When particles are reconstructed into a higher p_T bin the effect is called "feed up". The opposite case is called "feed down'. Because of the nature of the detector resolution, the probabilities for any particular particle contributing to either of these effects are roughly the same. Thus the only impact due to this effect is going to be due to natural distributions.

The production spectrum, as a function of p_T, is steeply falling. The falling spectrum means that "feed up" is much more of a problem than "feed down". This asymmetry requires us to worry about p_T smearing.

6.1.3 Analysis Cuts

This analysis utilizes several cuts in order to reduce background presence in the data, and to improve the signal quality. In this section we will discuss each of these cuts explicitly. It is often possible to tune a cut for a particular analysis. Tuning is typically handled by minimizing the relative error that results from the cut. The resulting error is just the combination of the signal to background contribution and the counting contribution. The former contribution increases as cuts are opened, while the latter decreases. The minimum of the system is the goal. However, for this analysis we wish to target one set of cuts to multiple analyses, namely multiple p_T ranges in the data, so we tend to choose reasonable cuts rather than tuned cuts.

6.1.3.1 Run Selection

Data recording at STAR for the 2003 *d+Au* run was segmented into "runs". The difference between the two being time scale. The latter type of runs involved recording ~100k events over ~1 hour.

The status of the entire STAR detector over the course of one of these runs is usually well defined. If no problems are encountered during such a run, the run is marked for later use. Also, the time period between runs is when the configuration of individual detector subsystems is changed. Such changes sometimes result in that portion of the data being compromised in a way that cannot be determined during the data-taking. However, such problem data can be removed later by simply discarding the affected runs.

For this analysis, we used the standard restricted dataset suggested by the STAR QA analysis, and then we made further cuts to ensure the quality necessary for this analysis. The standard QA analysis is a simple verification that each run showed no obvious problems during data collection, and was not found to have any major signs of problems during post-analysis. However, this QA only provides a starting point.

The first cut made beyond this run list is the data availability. This cut is not analysis-based. It is a simple reduction to the overall data. The computer farm used to analyze the stored data will sometimes drop data files, and sometimes fail to execute some analysis jobs (where a job is carried out on roughly 5000 events). This results in the occasional loss of all data from a particular run. Also it results in a statistical reduction in the data available from a given run.

Three other sets of restrictions are applied to the list of runs used for analysis. The first is the removal of events where the BEMC data is suspect. These runs typically had a low average energy per BEMC point, but another class of runs where the BEMC was not fully operational falls under this category. The BEMC data was good starting on day 41. The second is the removal of additional runs where the TPC is suspect. Such runs had a low number of tracks per recorded event. The last intentional cut is the removal of all runs that did not have at least 25,000 MinBias events. This cut was chosen to ensure that run-based QA had enough events to provide reasonable statistics, and to ensure that assumptions made in the data normalization did not introduce large systematic uncertainty.

The resulting reduction of available runs due to each type of selection cut is shown in Table 6.1.1. The net effect is to reduce the total number of usable runs to 183. The remaining number of events is provided, in detail, in Section 6.2.4 – Normalizing the Yields. The full run list can be found in Appendix J.

Table 6.1.1: Run Selection Cuts. The reduction of the usable number of runs due to problems with data access and quality assurance tests is shown.

Selection Cut	Runs	
	Cut	Remaining
STAR "Good" Runs		453
"Day 41 Cut"[1]	127	326
Data Availability	4	322
Bad BEMC Data	7	315
Bad TPC Data	3	312
25,000 MinBias Events	129	183

[1] one run from day 40 is included.

6.1.3.2 Acceptance Restriction

The BEMC coverage of η x ϕ = (0,1) x (-π,π) includes some regions where towers or SMD strips were not operating properly, and either missing or corrupt in the recorded data. The operating configuration, and hence which channels were missing or corrupt, changed in time during the whole 2003 data taking. These channels reduce the detector's acceptance.

The impact of reducing the detector's acceptance is to remove some data. The amount of data depends on how aggressively the data is segmented. It is possible to determine the detector's acceptance on a run-by-run basis. For example, Figure 6.1.2 shows the expected detector acceptance for run 4049021, with the top three panels showing the tower, SMD-ϕ, and SMD-η tables. The last figure is a combination of all three detector planes. This method includes significant small sample statistical problems, and introduces systematic uncertainty. The opposite method, however, where once acceptance is selected for the entire data-taking period, eliminates the statistical problem above, but reduces the data sample.

Due to large systematic uncertainty in other parts of this analysis, it was determined that the global approach to the detector acceptance is the most effective, provided regions that are questionable for only part of the data-taking are included in the analysis. That is, sections of the detector having problems less than 20% of the time are included in the analysis. This amounts to less than 10% of used acceptance. Thus less than 2% of the time-integrated acceptance is in question.

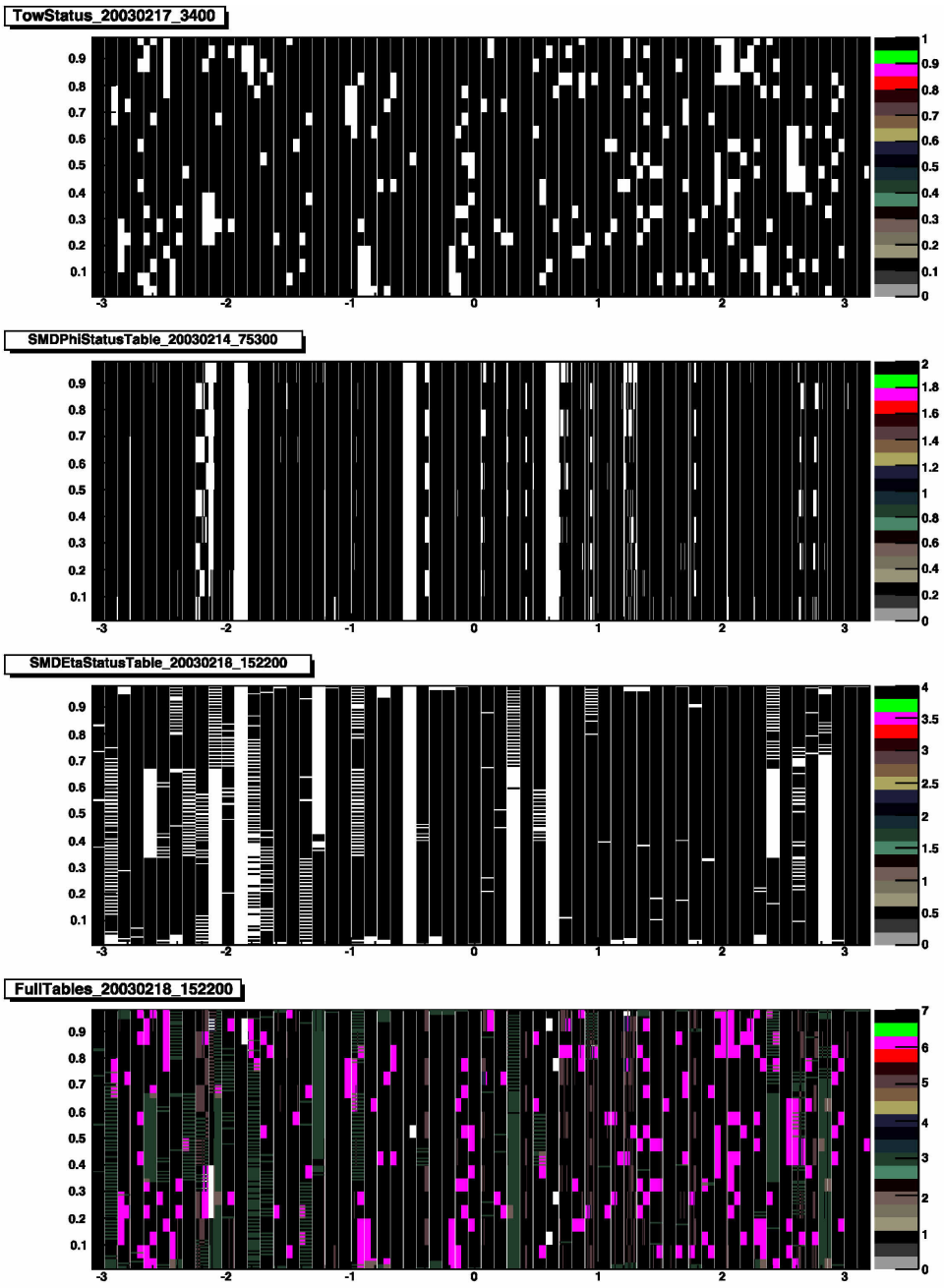

Figure 6.1.2: The status tables are shown for run 4049021. The upper three, in order, show the tower, SMD-ϕ, and SMD-η tables. The bottom is a sum of the upper tables, where a region must be completely black to indicate the status is good. This is the basis for intentional acceptance reduction based on excluding modules (the white vertical gaps in the middle two panels correspond to full modules).

In order to determine the allowable acceptance region, the 183 analysis runs were queried. For those runs, the points in a given module were normalized to the number of events in the run, and the expected acceptance of the module. The latter allowed inclusion of modules where, for example, 50% of the module was reliably inactive. The resulting normalized point distribution can be seen in 2-D histogram format in Figure 6.1.3, which shows the density of points segmented in ϕ as a function of analysis run. Fifteen modules were excluded from the overall analysis. They can be seen by the gaps in Figure 6.1.3. The removed modules are also listed in Appendix I.

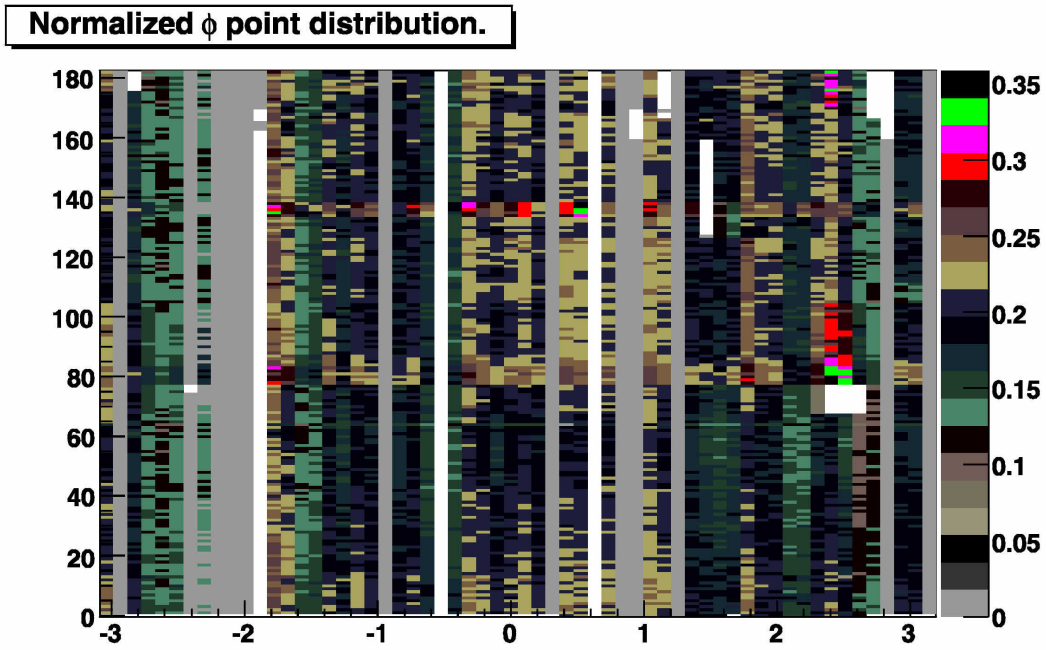

Figure 6.1.3: The normalized ϕ-distribution of points over the 183 analysis runs. Note that there are fifteen ϕ regions where there is no data. Regions that were masked before analysis appear as solid gray rather than white. The normalization scale on the right is arbitrary.

6.1.3.3 Vertex Definition

Events are recorded when the system observes a valid trigger. A valid trigger, however, does not necessarily indicate an event that we wish to analyze. In fact the system may trigger on background, however, even real events are sometimes unwanted. The least useful real event is one that triggers the system, but does not provide enough data to determine where the vertex of the event was.

We cut events where such a vertex definition could not be made. The observable signal in the data, for this effect, is that the vertex is assigned to 0. The vertex-selection cut, therefore, simply rejects events that have the *z*-component of the vertex at 0. Events with reconstructed vertices may also have a *z*-component of 0. The machine representation of 0 in such an event corresponds to a ΔZ of 1×10^{-7}, which should reject only a statistically insignificant couple of events with good vertex over all of our data.

The cut at 0 has been tested on our data and the effect can be seen in Figure 6.1.4. The figure shows that a spike is removed, but the underlying distribution is very reasonable after the cut. No sharp dip indicating removal of good events is seen. For the primary dataset, the rough effect of this cut is the removal of 4.17×10^{6} out of 23.94×10^{6} events, or 17.4%. The positioning of this cut in the analysis sequence greatly impacts the percentage, and it should only be taken as a rough estimate.

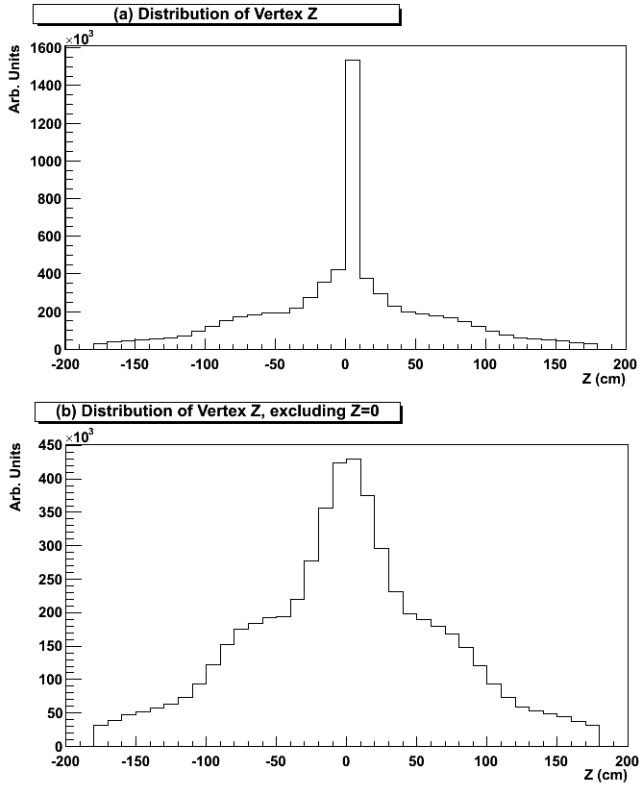

Figure 6.1.4: This figure shows the result of imposing a cut removing events where Z is exactly 0. Events with failed vertex reconstruction are assigned 0, however good events may also have $Z = 0$. Panel (a) shows the dataset before the cut, and (b) shows it afterward. The lack of a dip in the panel (b) indicates that very little real data is lost.

The real data is only allowed to have a reconstructed vertex between –180cm and +180cm. For our analysis, we further limit the vertex to $|Z| < 60\,\text{cm}$, in order to improve signals dependent upon geometric effects. Furthermore, this is the cut used in simulation analysis, and thus eliminates some systematic uncertainty.

Vertex definition is based on having enough tracks in the TPC in order to find a common crossing point near the center of the beam pipe. Events where the number of tracks is too low to provide a vertex are the primary events removed by requiring the

vertex to be defined.[3] Thus this cut effectively biases us towards events that have good TPC signals. This is discussed later when we present the trigger efficiency and show that most lost events do not have a π^0 that we wish to measure, so the effective yield is pushed down only slightly.

6.1.3.4 SMD Requirement

The BEMC tower plane, like any electronic detector, is subject to noise. It also has a very coarse granularity for this analysis. In fact, given the size of the BEMC towers, the maximum p_T that a π^0 can have and still have its decay photons always resolved, is about 3 GeV (resolving γ's with towers requires separation of 0.10 in η or ϕ, or that the pair cross module boundaries, the latter case causes reduced acceptance). In order to reduce noise effects, and improve the resolution of the system, we required both SMD planes to have energy signatures.

The impact of this cut on the detected π^0s was discussed above under the data attributes. By limiting the analysis to points with both SMDs triggered, we reduce our number of counts, but we gain purity of the identified particles. This is helpful because for some bins in the analysis, the background contribution to the invariant mass histograms peaks under the π^0 mass, while in some others, the "turn on" of the histogram occurs at the π^0 mass. Both of these problems are alleviated by reducing the background contribution, provided it is reduced more than the signal loss due to the SMD cut.

[3] Other events, such as the mentioned events outside the range, are also cut, but are a very small portion

6.1.3.5 TPC Track Veto

Many particles other than π^0s contribute energy signals to the BEMC. The additional signals may contribute additional points to the analysis, or they may be added to energy signatures of real π^0s. This effectively increases background and impares energy resolution.

Many of these particles are charged hadrons, which leave characteristic ionization tracks in the TPC gas. The ionization electrons then drift to the ends of the TPC due to the high electric field. The charge distribution resulting from the ionization of particle tracks is digitized over the volume of the TPC [And03]. The resulting volume-charge pixels are matched to a helix structure. This process is the basis for track generation in the STAR software system. This charged-particle track reconstruction is well handled in the STAR software system, and a list of found tracks is available for each event.

Projecting the charged hadron tracks on to the BEMC provides a way to correlate BEMC points with these tracks. By removing points that have an associated hadron track, we can thus improve both the combinatoric background, and the energy resolution at the same time.

It is important to note the negative impacts of this cut. Almost all have to do with high p_T π^0s. First since high-p_T π^0s are fragmented off of high-p_T partons, the additional parton fragmentation is likely to produce a jet of particles that hits the BEMC near the π^0s photons. Second, most TPC tracks that project to the BEMC do not deposit much energy but instead produce a MIP signature of about 250 MeV. For high-energy points (~4 GeV), the energy resolution is already worse than this.

6.1.3.6 BEMC Multiplicity

The BEMC generally has very low multiplicity in *d+Au* collisions. Using the high tower triggers, of course, the multiplicity increases. However, the multiplicity is still fairly limited, and the distribution suggests a reasonable cutoff at 70 points. The distribution can be seen in Figure 6.1.5.

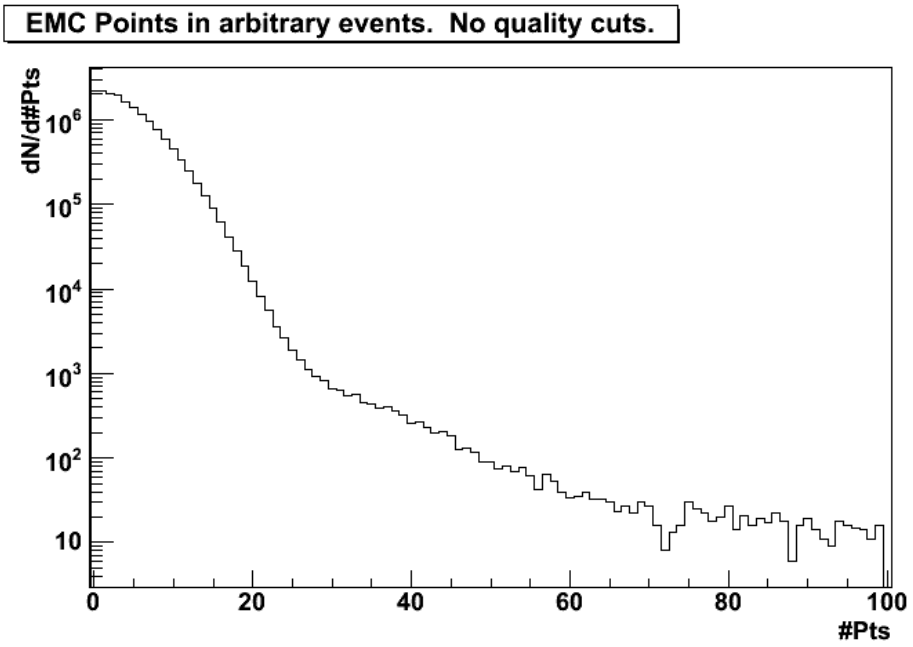

Figure 6.1.5: The distribution of the number of events with a given number of EMC points. This includes all triggers, so high tower events are present, however, the transition of the slope around 30 points is not due to trigger selection. That and the apparent saturation above 70 suggest that 70 is a reasonable cutoff.

We can cut events above this, however it is reasonable to ask why we would want to cut out events with high multiplicity. The two reasons that apply here are the following. High multiplicity events have a high probability of being due to a detector malfunction. Those events could be individually tested in order to determine if there was a malfunction. The second reason for the cut, a more general reason than the

first, saves us from actually looking for these malfunctions. The reason is that we count π^0 statistically. This means that unique events providing very high-p_T π^0s could not be used anyways, due to the resulting statistical error. Any signal we will use here must be a coherent sum of a large number of π^0s, and recovering single events to identify a particle are not helpful in this regard.

6.1.3.7 Energy Asymmetry

The energy asymmetry was discussed in the data attributes section above. It is clear from that discussion that we must make a cut on this parameter. In order to choose a reasonable cut range for this, we observe the actual energy asymmetry in the real data. Figure 6.1.6, panel (a) shows the invariant mass distribution for the minimum bias data with π^0 p_T given by $2.0 < p_T <= 2.5$GeV, while panel (b) shows the energy asymmetry of the entries with mass between 100 and 200 MeV. The drop-off at high asymmetry is observed, but the effect is minimal at 0.5. In order to avoid the steep drop-off, and improve the signal to noise ratio, this analysis sets the energy asymmetry cutoff at 0.5.

The effect of this energy asymmetry cut can be seen in Figure 6.1.7. Figure 6.1.7 is a duplicate of the mass distribution in panel (a) of Figure 6.1.6 with the energy asymmetry cut applied. Comparison of the resulting distribution with that in Figure 6.1.6(a) shows the major effects the energy asymmetry cut causes. First, the low-mass background is reduced by about 70%. Also, the overall background signal is reduced by about 40%. At the same time, the signal is reduced by less than 10%.

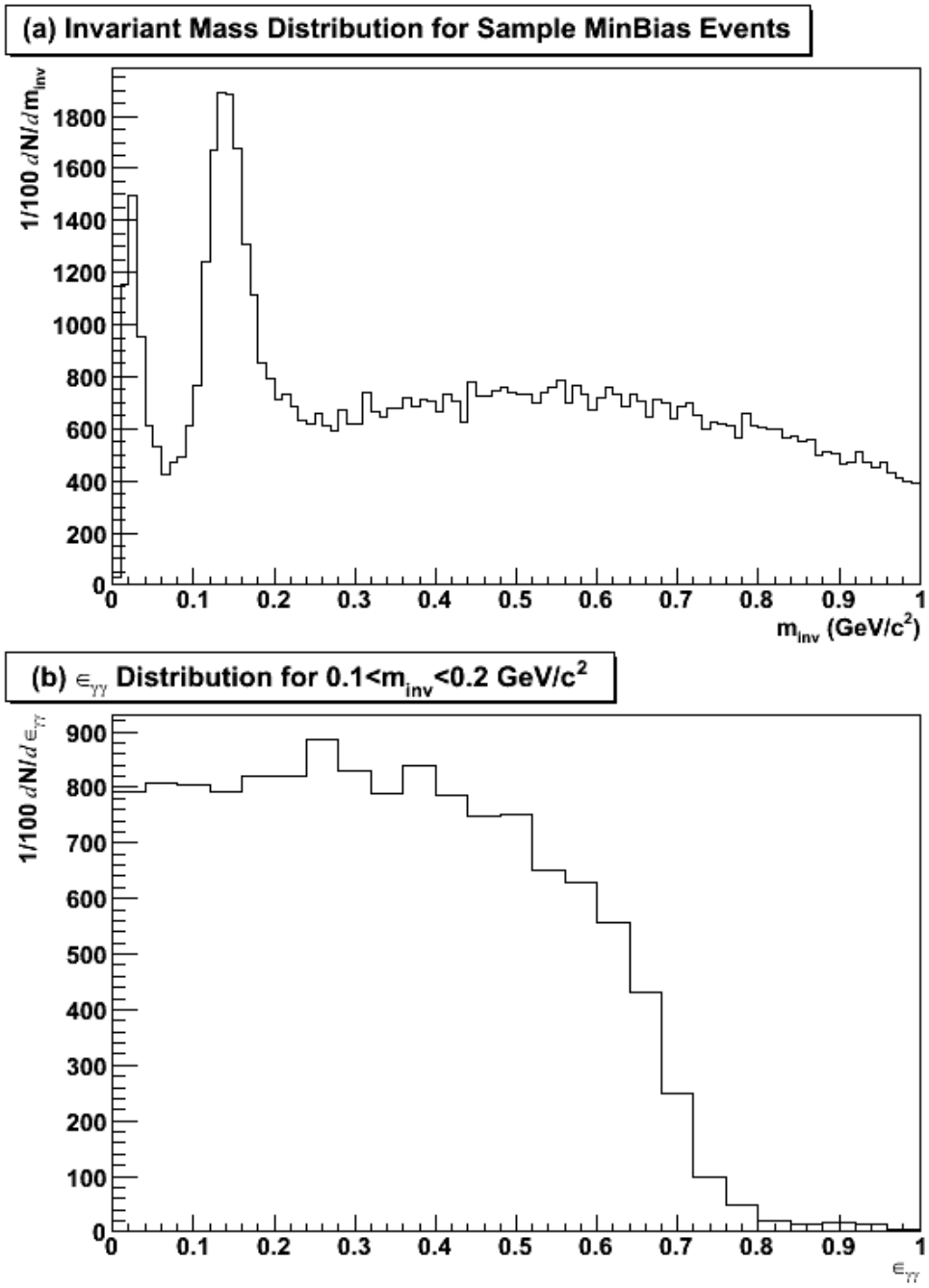

Figure 6.1.6: The invariant mass distribution of π^0 candidate pairs with $2.0 < p_T < 2.5$ GeV/c. The energy asymmetry of the π^0s in the real data approximates a flat distribution for asymmetries below 0.5. Panel (a) shows the invariant mass distribution for the examined π^0 pairs. Panel (b) shows the energy asymmetries for the pairs, from (a) with $0.1 < m_{inv} < 0.2$ GeV/c^2.

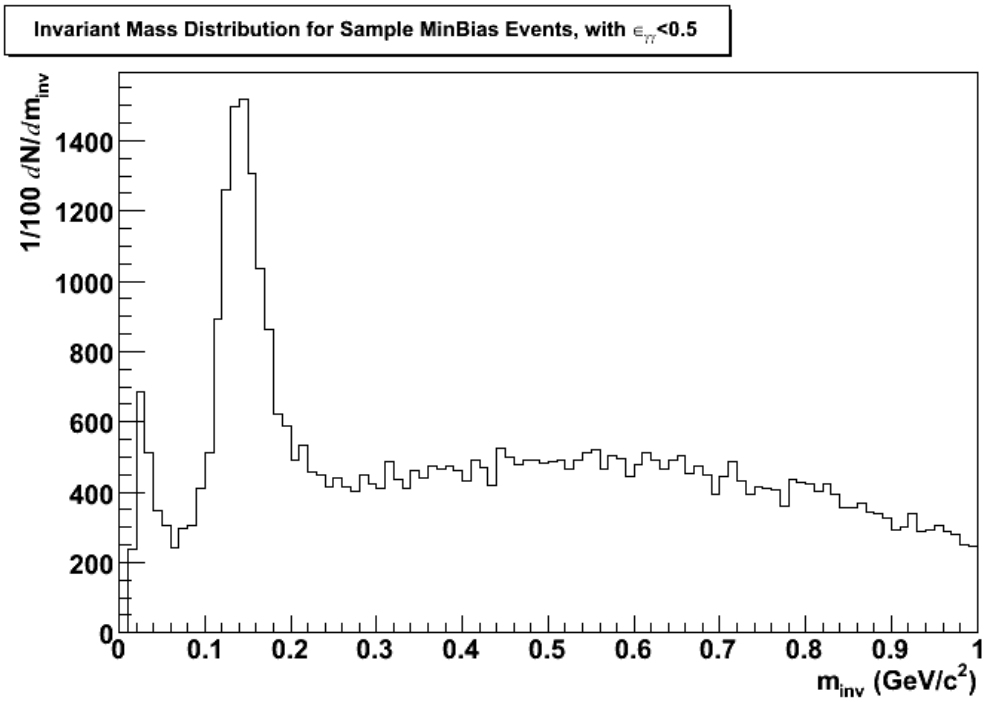

Figure 6.1.7: Effect of adding the energy asymmetry cut to panel (a) of 6-6. The low-mass region is decreased somewhat. Also, the background is reduced by about 40% while the signal is reduced only about 10%.

6.1.3.8 Trigger Cuts

A pair of high tower triggers enhances STARs ability to record rare events. For this analysis, high-p_T π^0 yield was enhanced by using these triggers. This enhancement occurs because high-p_T π^0s, upon decay in the $\gamma\gamma$-channel, release a photon with $E_T \sim p_T/2$. This photon may then impinge upon the BEMC tower plane, providing a high tower trigger. However, the use of such data requires careful consideration of the data quality issues involved. Here we will briefly discuss the motivation and resulting cuts used to verify the quality of the high tower trigger data.

The high tower triggers are based on STAR's BEMC. The tower plane of the BEMC provides special information regarding the highest ADC value observed in the tower array for each event. The reported value can be tested for its magnitude and in this way the high tower trigger conditions are tested for each minimum bias event. Thus, the events recorded as high tower 1 or high tower 2 are simply minimum bias events with an additional BEMC tower above a threshold.

There are a few problems with this system. The first is that events recorded as high tower 1 or 2 may not actually have a large energy deposition. That is, an event may simply be a spurious high ADC reading that is not actually correlated to a high-energy deposition. Second, the towers do not always contain all the energy from single photons, since they may hit on the border of two or more towers. This effect results in reduced trigger efficiency in the turn-on region of the trigger because the triggering event will have to hit near the center of the trigger tower. Third, the high tower trigger is ignorant of the actual triggering particle or particles. That is, a high-p_T π^0 may not be correlated with the trigger tower of an event if it is triggered by another particle such as a solo γ. Fourth, there is no guarantee that the high tower triggers actually reflect a particular E_T. All towers have some variation in their gains. As a result a wide variety of E_T's may produce fairly large ADCs.

For the reasons given, it is necessary to retrigger high tower events. In particular, it is necessary to determine whether or not a candidate π^0 was capable of triggering the event. That is to say, the given π^0 must be capable of triggering, but need not produce the actual highest ADC tower. A deviation from the hardware system was used. The deviation comes from retriggering based on point E_T rather than tower ADC. The hardware trigger tries to approximate turning on all towers for triggerring

at a single energy, but since the system includes analog to digital conversion (ADC) measurements from 2400 channels and a wide spread in signal gains, E_T retriggerring introduces significant risk for deviation from the real hardware mechanism. The differences between the results using the hardware-based trigger, and those obtained by applying the software E_T trigger, provides a means of estimating the threshold and trigger systematic errors. This point will be discussed and justified shortly.

The absolute trigger ADC thresholds for the high tower 1 and high tower 2 datasets were ADC > 8 (turning on at 9) and ADC > 13 (turning on at 14), respectively. These trigger ADCs are the result of a bit-level algorithm that essentially divides the real ADC by 32 to produce the trigger ADC (tADC). Since the average gain on the towers is around 0.35 GeV/tADC, this corresponds to average thresholds of 3.15 GeV for high tower 1, and 4.55 GeV for high tower 2. There is also, unfortunately, a large spread in the gains, and a sizable tail towards high gains. These introduce systematic uncertainty in the actual trigger turn on that is very difficult to analyze without also knowing the degree of accuracy in the gains. The distribution of tower gains can be seen in Figure 6.1.8.

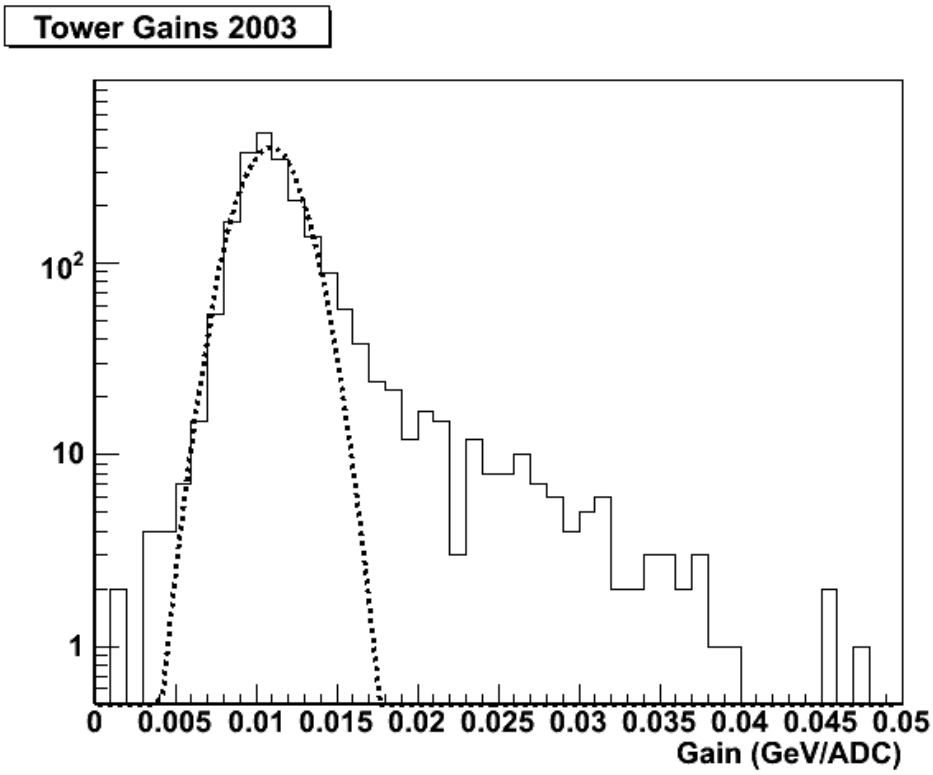

Figure 6.1.8: The distribution of tower gains for 2174 towers with good gain during the 2003 *d+Au* collisions at STAR. The distribution is fit with a normal distribution whose mean is 1.090×10^{-2} GeV/ADC, and width is 1.836×10^{-3} GeV/ADC. This distribution, together with oscillations and inaccuracies in the actual gains is a source of systematic uncertain in the threshold behavior of the high tower triggers.

Due to the nature of summing data over the entire data-taking period, the gains are expected to oscillate. Also, the distribution of gains is not a normal distribution. The alternate retrigggering option of duplicating the hardware response would enable the channels with higher gains (and therefore lower ADC signals) to provide more data. Because of the expected oscillation of the gains, and the gain curve's (Figure 6.1.8) deviation from a normal distribution, the conservative approach of retriggering on E_T was chosen. Retriggering on E_T removes the some hardware turn-on effects, but due to some of the channels having very large gains their hardware setting is still

beyond the software trigger, and they will continue to exhibit "turn on" behavior in the produced results.

Software triggering on E_T, combined with a comparison of E_T in conjunction with the hardware trigger, will both be analyzed in the simulation section as a means to determine systematic uncertainty. Figure 6.1.9 shows the raw yield for three different means of selecting high tower events. It shows that the systematic uncertainty in the yield is less than the statistical uncertainty for p_T-bins at 1 GeV or more above threshold. The trigger values were chosen in the range where more than half of the barrel could cause triggers. This reduces dependence on a small number of trigger towers, but reduces the detection of π^0s at threshold. This method also suggests the need to run simulations at higher E_T thresholds where more of the barrel should be capable of triggering. In the turn-on region where the largest problems lie, it is useful to have a measurement of uncertainty such as this. Other problems that may have been missed are likely in such a critical part of the data.

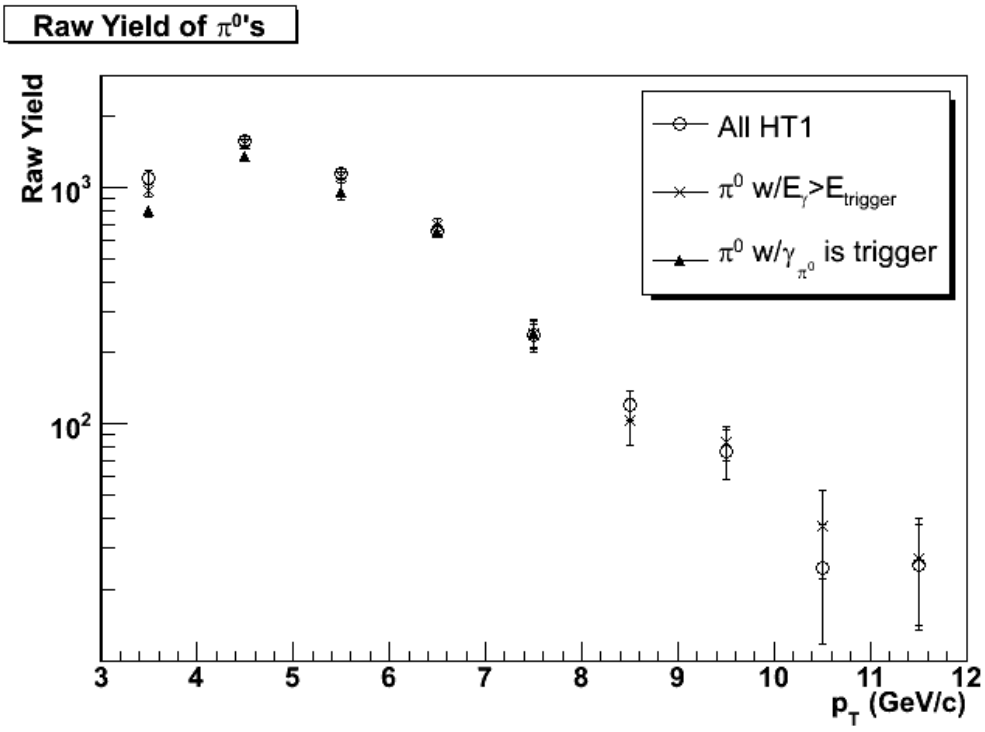

Figure 6.1.9: The raw yield for three methods of selecting π^0s from high tower data. The top points include all π^0s from high tower 1 events, while the "x"'s and triangles require the π^0 to generate a γ that either satisfies the E_T trigger, or corresponds to the trigger tower, respectively. This shows that for a tower threshold of 3.2 GeV, once the π^0 p_T is above 4.0 GeV, the uncertainty in the count is about 10% and improves at higher p_Ts.

6.1.4 Other Data Problems

Several other problems were found in the data at various stages of the analysis. For the final analysis, the problems were either removed or ignored, thus they are not discussed directly. However, we present these issues here to showcase effects that have been observed.

The data production system associated with the BEMC is setup to automatically remove most of these problems. The vast majority possible problems with the BEMC signals actually come from improperly calibrated channels. However, there are also

some module-based, crate-based, and readout electronics-based issues that were observed.

6.1.4.1 Hot Towers

Early analysis showed that a large amount of background occurred due to a handful of towers that had improper calibration. By eliminating these towers in the analysis, the combinatoric background is improved. This also improves analysis of the high tower data because these hot towers often lead to an increased rate of triggers from the bad towers.

Figure 6.1.10 shows the number of points associated with each tower for run 4066012, based on the early data analysis. There are about a dozen hot towers that provide spikes on the histogram. Later on, these towers were identified, and marked as "bad" in the software status tables. Thus, later analyses did not use these towers.

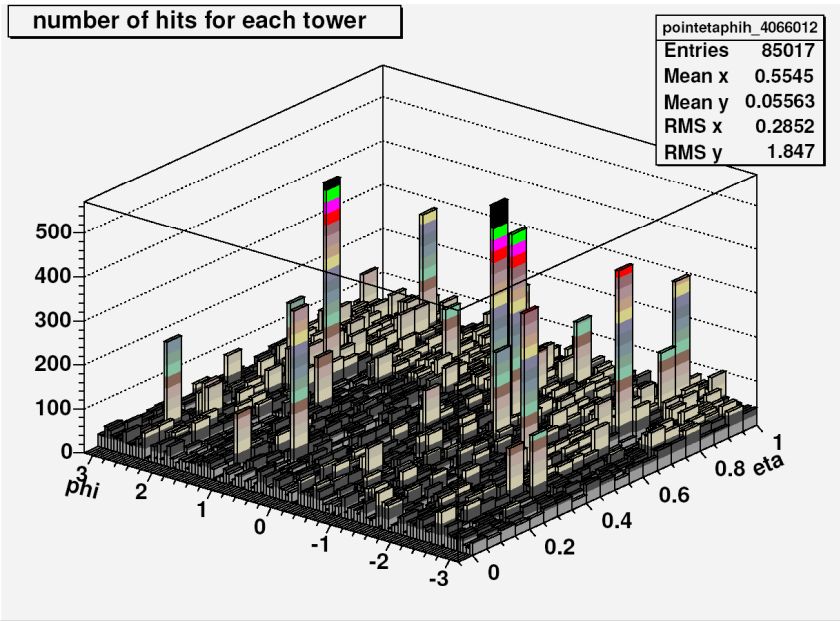

Figure 6.1.10: The number of times each tower contributes to the BEMC points is shown for run 4066012. There are about a dozen towers that provided a much larger number of points than average. These hot towers were later removed from the analysis using status tables.

6.1.4.2 Event Corruption

Several effects were tracked down to corruption of BEMC crates. These were called “ghost events”, “n*256”, and sometimes “ghost pedestals”. Various analyses were done to try to understand these effects, and possibly recover the data, however, they are best handled as lost data for our analysis.

In later versions of the production software, any data that was impacted by these effects were simply set to zero. The resulting dataset, then, has holes where these corrupt events occurred. For the analysis system used here, this is not a major issue, because we normalize to the portion of the detector that does not have statistically significant problems with missing data. Hence the event corruption is safely ignored as long as the analysis system is averaged over a large amount of data such that the

corruption is minimal, or if the corruption is large, the corrupt regions are removed. Both of these are the case in this work, so the effects can be safely ignored.

6.1.4.3 Configuration Tables

Analysis of BEMC data relies heavily on having accurate configuration information. Each plane of the BEMC has essentially three configuration tables (footnote: A fourth table, called "gain" is uniformly set to 1, and although it is referenced in the analysis software, it is essentially unused because of this.) These tables can change on an event-by-event basis. In practice, however, the tables are determined once per run, once per fill, or once per year. The tables are checked on each event, upon entry into the BEMC recalibration software.

The three tables are for "status", "pedestal", and "calibration". They are meant to reflect the current state of each channel of the detector. Hence there are 2400 tower entries for each table, and 9000 SMD entries, for each plane, for each table. The tables are based on many individual analyses, some of which were discussed in the BEMC detector presentation.

We must verify the applicability of the detector to our analysis, rather than try to show that all the other analyses satisfactorily setup the detector for applicability. That is, in order to use the BEMC data, we must determine the impact of accepting these configuration tables as-is. To do this, we will consider the impact of bad configuration data in each of these tables, and discuss how it affects the analysis.

The BEMC tower status table essentially sets the acceptance for the detector. Of course, a dead channel will not fire even if the status table claims it is ok, so the status table can have two types of problems. The problems are that the table may mask a

good channel, or a bad channel may be enabled. The first case simply reduces our acceptance, which should be easily simulated because the status is applied to the simulation too. The second case causes problems in our analysis, because we must estimate this effect or remove the data during the final stages of analysis.

The BEMC tower calibration table is used in conjunction with the pedestal table to determine the energy deposited in a tower. If these are wrong, they will most likely result in reduced energy resolution. The net effect is that the π^0 signal will have a mass that is too wide, or at the wrong energy. Both effects, however, will not destroy the π^0 signal itself, they merely distort the signal. The total number of counts will be unaffected except to introduce systematic uncertainty due to additional background contamination. So, these tables do not pose a major risk for cross-section analysis, though they may skew related measurements of the π^0 mass position.

The SMD status tables are analogous to the tower status tables, when the analysis requires SMD signals. The resulting acceptance effects, and cleanup of the signal, should be picked up the same way as the tower status. This is a further reason that effects must be observed and analyzed with all detector planes taken into account. Hence, they must be done with nearly final data.

The SMD pedestal and calibration tables have basically not been determined with a high degree of granularity. That is, reasonable values for these have been assigned, but only in application to the entire 2003 *d+Au* run. Thus time variations in the detector response are not reflected in the pedestal and calibration tables. This is not a major problem, however, because any channels that are really far off are disabled, and the differences that remain simply widen the SMD resolution a little. It is already $14\% + 86\%/\sqrt{E}$ [Bed03]. Also, the detected energy in the SMD is only used for

positioning, unless a tower cluster is going to be split into 2 or more points. When tower clusters are to be split, the energy is assigned based on the ratio of the SMD energies. In our case problems in the tables are smoothed out a little, since we require signals in both SMD planes for all points. Thus, the energy splitting is based on the average of the two planes. The net effect of having only general results for the configuration tables only widens the reconstructed mass peaks and may move it higher or lower.

The method for determining our sensitivity to these tables the following. For the calibration and pedestal tables, we simply accept the resulting resolution and mass shifts. For the status tables, we determine an average behavior of the detector, and match any simulation work to that.

6.2 Raw Yield Analysis

6.2.1 Introduction

In this section we will develop the raw yields for d+Au π^0 production at $\sqrt{s_{nn}}$ = 200 GeV, over all azimuth, and with $0 < \eta < 1$. The background sections will allow us to jump right over some of the sticking points of the analysis, and cut right to the results.

It is important, however, to discuss the methods used for extracting the yield. So those will be covered first. Then we will present the bin-by-bin results of the yield counting. Each counting method has a set of associated parameters that must be collected. In each case we will collect the appropriate parameter results. After that, the results will be collected into a set of yield curves and tables that will be used later to determine the actual cross-section measurements.

The final two parts of this section deal with systematic errors and normalization. Each cut imposed has the potential to increase the systematic error significantly. After extracting the yields, we will be in a good position to observe how the cuts affect those yields directly, so this is the best opportunity to analyze those sources. The normalization analysis is carried out, primarily, on the π^0 yield. For example, given the complexity of the analysis system, verification of individual energy signals from the detector is simply too far removed from the yield to provide a simple way to validate yield measurements. The goal of the normalization analysis is to provide a basis for matching results from various analyses. In particular, it will be important in matching the simulated data to determine the absolute yield.

The current section, thus, is exclusively dedicated to measuring π^0 signals in the real data. The quality of the photon signatures used in the π^0 analysis cannot be based on event-level analysis due to the risk of biasing the data. Similarly, other measurements of the quality of the BEMC or TPC signals, beyond that discussed in Section 6.1, risk adding additional bias. This bias risk occurs because the signals themselves cannot easily be improved by looking at parameters of lower order than the actual π^0 yield, since these yields are very close to the detector behavior and are the dominant physical process contributing to the data observed. Instead, the normalization part of this section presents an argument for why the data can be considered under control. That means that the quality of the signal will be accepted as-is, and we will work to match it in the simulation analysis in section 3 of this chapter.

6.2.2 Methods

The π^0s coming from these events are counted using energy deposition in the BEMC. Thus they are detected by observing signals made by their decay photons. There are many other such energy deposition sources, not the least of which is radiative fragmentation that produces its own photons in the BEMC. Each energy deposition event in the BEMC forms a point, so we must determine, for each point, if it is part of the signal we are interested in. Each point is considered a candidate photon, and cuts are used to remove candidate photons that are not the decay daughters of π^0 decay.

It is necessary to reconstruct the π^0 from the candidate photons. Observing individual π^0s is possible, but any counting results are really only statistical. That is,

we cannot say, for certain, that two points definitely came from a π^0. Since this analysis is concerned with measuring π^0s directly, we don't try to individually identify them. Rather, we look directly at statistical distributions of the π^0 candidates.

Each set of two points in the BEMC is a candidate. Its points can be used to reconstruct the properties of a particle that electromagnetically decayed due to internal anti-particle annihilation. The candidate's points, in this case, are treated as photons. Thus the candidate mass can be calculated as discussed in Appendix C:

$$m_C^2 = 2E_1E_2(1-\cos\alpha), \tag{6.2.1}$$

We collect large sets of such candidates, and combine them into analysis bins. In this analysis, the bins are based on p_T. The analysis bins are presented in Table 6.2.1. Other parameters than p_T are restricted in analysis, but not binned, they form the phase space of interest and are represented by cuts on the analyzed data. The phase space for the candidate particles is: $e_{asym} < 0.5$, $0 < \eta < 1$, $E_{i\,min} > 0.35$.

Table 6.2.1: Analysis p_T bins used.

Bin #	p_T Range	Bin #	p_T Range	Bin #	p_T Range
0	0.0-0.5	8	4.0-4.5	16	10.0-11.0
1	0.5-1.0	9	4.5-5.0	17	11.0-12.0
2	1.0-1.5	10	5.0-5.5	18	12.0-13.0
3	1.5-2.0	11	5.5-6.0	19	13.0-14.0
4	2.0-2.5	12	6.0-7.0	20	14.0-15.0
5	2.5-3.0	13	7.0-8.0	21	15.0-16.0
6	3.0-3.5	14	8.0-9.0	22	16.0-17.0
7	3.5-4.0	15	9.0-10.0	23	17.0-18.0

Once all the candidate pairs are collected for a given bin, we histogram their masses to produce a spectrum such as that in Figure 6.2.1 for photon pairs with 1.5 <= p_T < 2.0 GeV/c. At this point it is clear that there is a statistical peak in the data,

which correlates to a real particle signal. However, it is also clear that some of the entries in the histogram do not come from π^0s.

6.2.2.1 Primary Counting Method

When the situation is as clean as it is in Figure 6.2.1, we can safely analyze the data by fitting the histogram with a function made up of a Gaussian distribution plus a polynomial background. The fitting is carried out using the root™ software system maintained by the Cern software group. The exact fit function we used in Figure 6.2.1 is

$$F(m) = \frac{N_{\pi^0}}{d_{bins} w_{\pi^0} \sqrt{2\pi}} \exp\left(-\frac{\left(m - m_{\pi^0}\right)^2}{2w_{\pi^0}^2} \right) + \sum_{i=0}^{3} c_i m^i \,, \qquad (6.2.2)$$

where d_{bins} is the density of bins in the histogram, N_{π^0}, w_{π^0}, and m_{π^0} are the parameters for the π^0 counting (number, width, and mass, respectively), and the last term is a 3rd order polynomial background function. This sort of fit can have its systematic error contribution approximated by analyzing its dependence on the background function. In this case, the background function can easily be modified under the peak by extending or reducing the range of the fit. For this particular channel, as a result of modifying the parameters of the fit, we observed the number of π^0s range from 3.83×10^4 to 4.16×10^4. Thus, the number of counts for this histogram would be 4.00×10^4 with about 1% statistical error, and 5% systematic uncertainty.

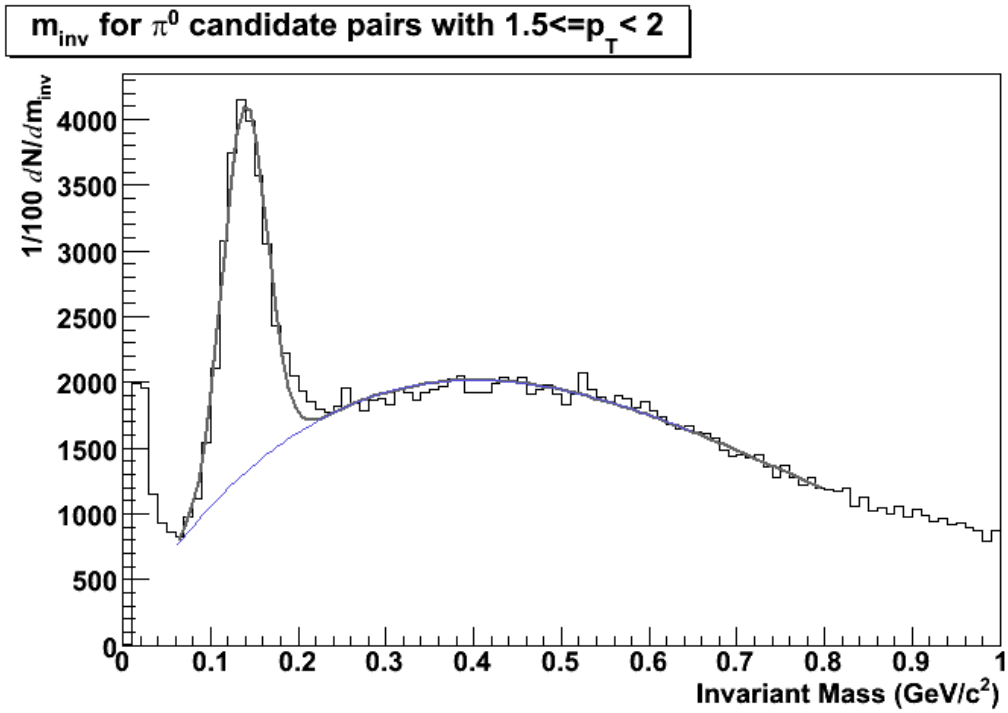

Figure 6.2.1: This is a sample invariant mass histogram. This figure shows a standard Gaussian plus polynomial background fit to the data. By varying the range of the fit, figures like this were used to determine the systematic uncertainty in the procedure. This channel has roughly 5% systematic uncertainty.[1]

Many channels simply do not look like Figure 6.2.1. There are various qualities that these other channels show, some of which are trigger dependent, while others have to do with making measurements at the limit of the statistics. One other class of problem channels is that where the acceptance eliminates the low mass region of the histogram, essentially "turning on" in the π^0 mass peak. Figure 6.2.2 shows example spectra for p_T and trigger restrictions with the π^0 mass peak is obscured.. In panel (A) the invariant mass of photon pairs is shown for MinBias events when the pair satisfies $6 < p_T <= 7$ GeV/c. Panel (B) is High Tower 1 data with $8 < p_T < 9$ GeV/c. The π^0 yield in each of these cases must be measured using some method, and the choice of

[1] The data shown is from the primary minimum bias dataset used during analysis.

method contributes to the systematic error. Actually, in the more extreme cases, e.g. where the statistics are limited and the low mass region is cutout, simply choosing to count the signal in a bin may contribute a very large systematic uncertainty.

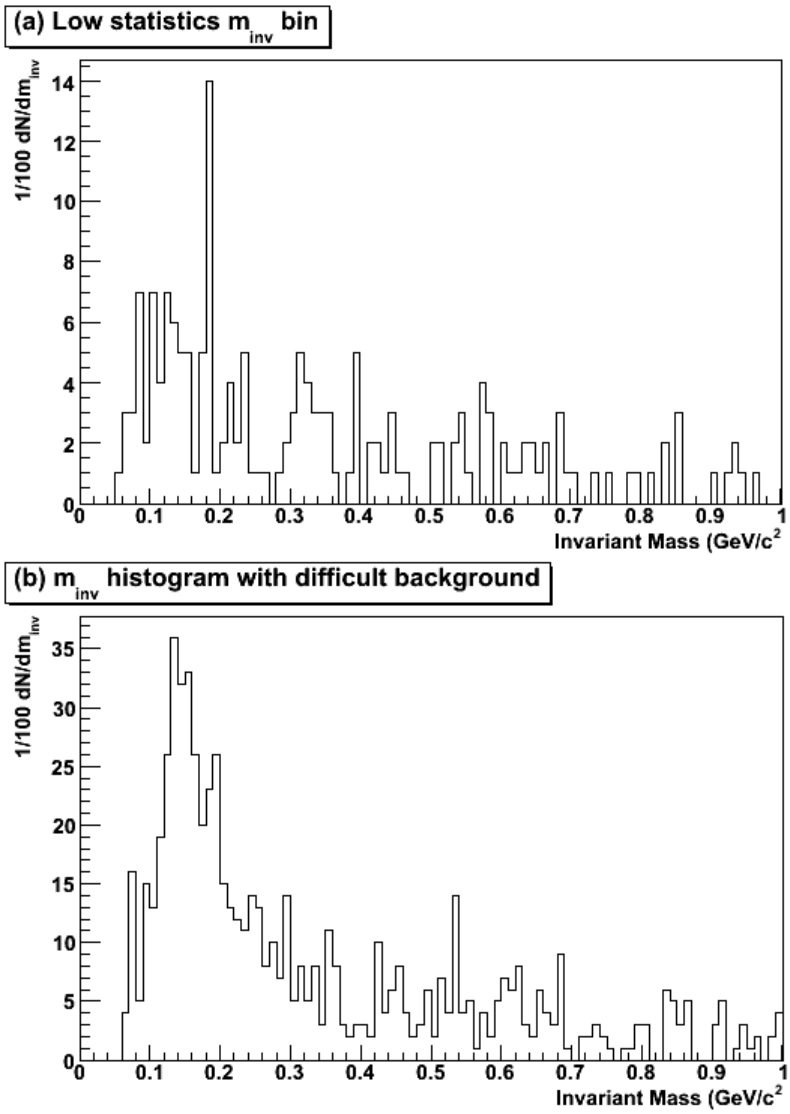

Figure 6.2.2: This figure shows examples of invariant mass histograms where determining the π^0 count can lead to large systematic error. Panel (a) shows a bin where the statistics are very low (this is the invariant mass histogram of photon pairs from MinBias events with 6.0 < p_T <= 7.0 GeV/c). Panel (b) shows a bin where the background is peaked under the π^0 mass peak (for this figure, 8 < p_T <= 9 and the trigger is High Tower 1).

Alternate counting methods will now be covered briefly. First we will present some variations of the user-based method described above. After that it will be necessary to also discuss one automated method.

6.2.2.2 Alternate Primary Counting Methods

In the case of extremely large low-mass signal, it is sometimes necessary to include a low-mass exponential into the fit function. That is, we add $B_2(m) = A\exp(Bm)$ to the fit function. In some cases the fit algorithm has a hard time locking on the right part of signal because of quality. In those cases we limit some of the parameters of the fit in order to force the system to put the mass peak on the π^0 mass. The final special fitting routine we use, which requires special circumstances or extremely noisy signals that are expected to all be π^0s, is to simply fit a stand-alone Gaussian. In the case of the stand-alone Gaussian, we often get a normalization term that must be deconvolved to recover the number of counts ($N_{\pi 0}$ in equation x above). All of these primary counting methods are essentially the same as the primary method presented above, except that limitations are placed on fit parameters, or modifications are made to the expected background shape.

- Bin-Summing Method

Another method was employed to determine the degree to which the previous yield measurements might misinterpret poorly shaped invariant mass histograms. For example, sometimes the primary counting method does not seem to adequately handle channels where the mass peak has a few bins that "spike". Figure 6.2.3 shows an invariant mass spectrum where the fit appears to undershoot such a spike.

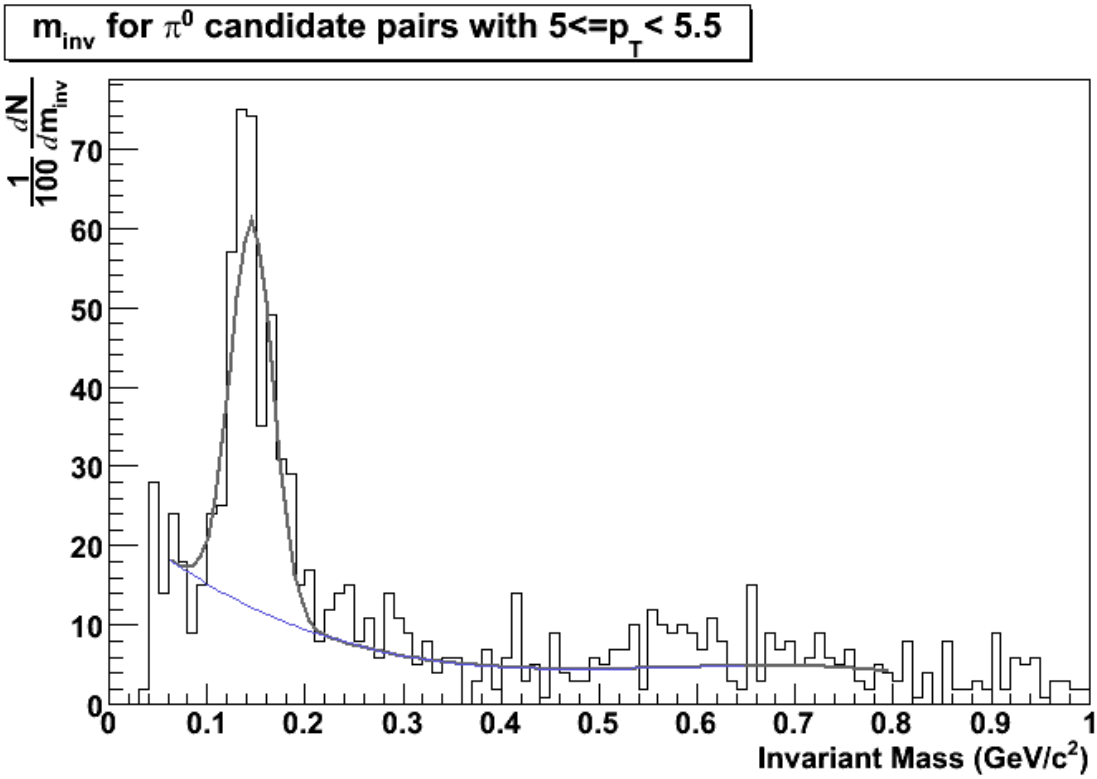

Figure 6.2.3: The standard fitting algorithm is used to extract counts using the Gaussian plus polynomial method. The method appears to undershoot the main spike of the distribution. This behavior suggested the need to test the data against an alternate fitting method.

Due to these invariant mass histograms an alternate fitting method was tested. For the alternate method the central idea is to remove the background then count the remaining bin totals. First, the primary counting method is used to establish a fit for the background. Then, instead of fitting the remainder with a Gaussian, we simply sum the remaining bins in the mass-range around the π^0 mass peak. To keep this method well defined, the range was chosen to be 0.08 GeV/c^2 to 0.22 GeV/c^2. This selection takes into account three different sources to the selection of range, which all vary as a function of p_T (a complication that is avoided by selecting only one mass range). The three sources are the following. First, the p_T-bin size is too large to make

fine-grain measurements, since the individual parameters can change from one end of each p_T bin to the other. Second, the width of π^0 peaks range from 0.020 GeV/c^2 up to 0.035 GeV/c^2. Finally, the chosen range, which does not center on the mass of the π^0, is chosen to deal with the fact that the mass and width increase, as a function of p_T. The mass changes from 0.134 GeV/c^2 to 0.160 GeV/c^2. The width changes from 20 MeV/c^2 to 35 MeV/c^2 (the width varies bin-to-bin, as well as steadily increasing as a function of p_T).

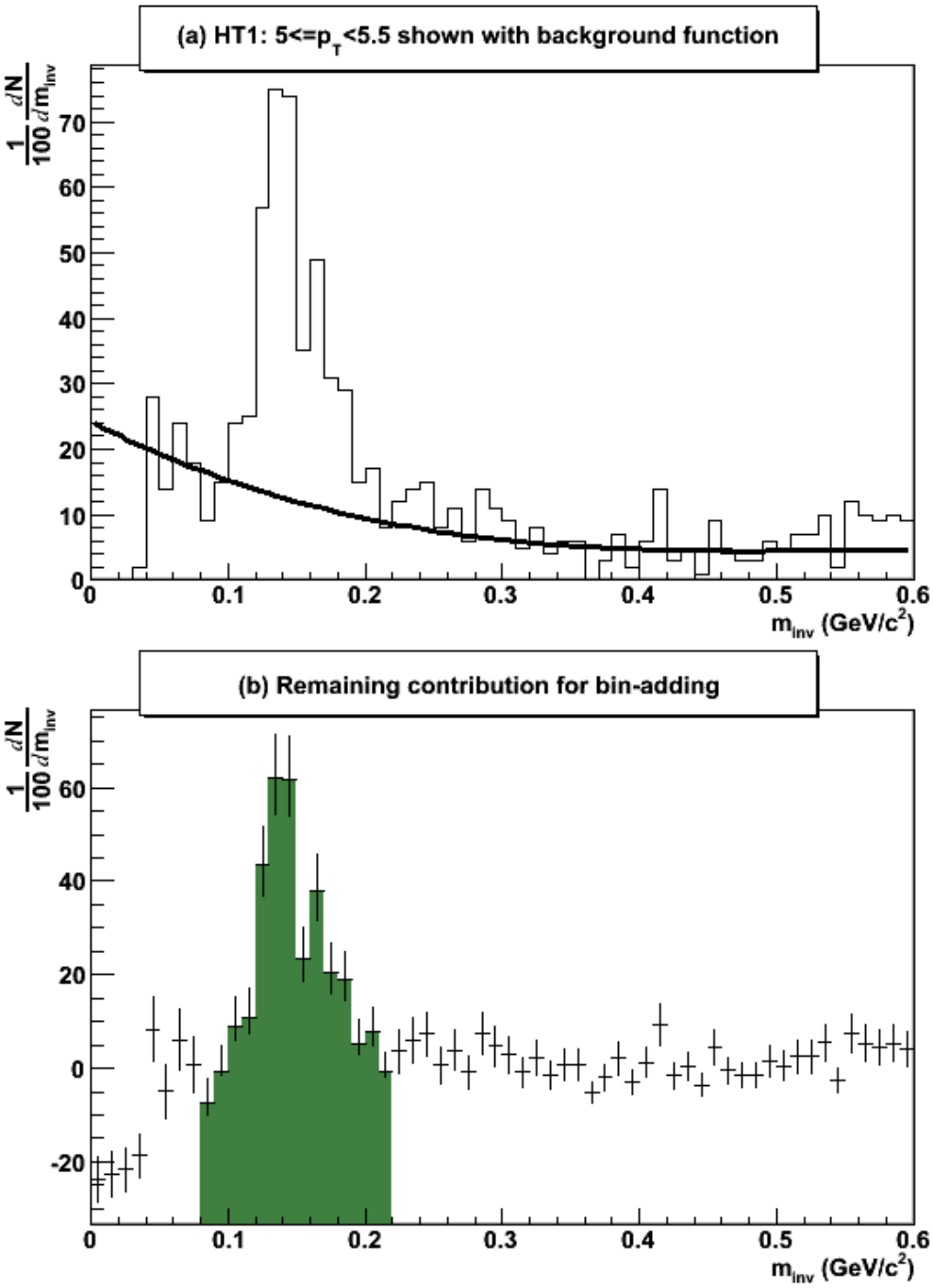

Figure 6.2.4: The bin-counting method is shown in this figure. Panel (a) shows the histogram in question and the best-fit 3rd order polynomial estimation for the background. Panel (b) shows what remains of the original histogram after the background has been removed. The shaded region is summed up to get a measurement of the π^0-production in this analysis bin.

Figure 6.2.4 shows an example of this bin-counting method. The first panel shows the mass histogram itself and the best-fit background function. The process at this step is to remove the background contribution and sum up the remaining measurements in the bins from 0.08 to 0.22. In this case, the sum of the bins is 2.92×10^2, whereas the Gaussian plus polynomial fit, from Figure 6.2.3, gives 2.67×10^2. The method used to examine the systematic uncertainty, however, gives an uncertainty in the former method of 2.6×10^1. The difference between the two methods is 2.5×10^1. Similar results were found for almost all analysis bins. In only a small number of cases was it necessary to expand the systematic uncertainty to account for larger counting results from this fitting method.

- Automated Method

The final counting method discussed was used for automated analyses. For automated analyses it is important to employ a method that does not have "decisions" involved, nor to use one that requires fits that may fail. The analyses of interest are those where we need to make many repetitive measurements, e.g. later we will measure a "standard" yield in subsets of the data that are only a fraction of 1% of the whole dataset. From those measurements the distribution of the resulting yields is used to verify the quality of the fits, and no single fit should be used without care taken to establish systematic error due to the use of this method.

The automated method starts with creating a 12-bin histogram of invariant masses between 85 and 205 MeV/c^2. The first two bins, and the last two bins are used to estimate a linear background under the remaining 8 bins. Since the width of the π^0 signal we measure is about 20 MeV/c^2 this misses about 5% of the signal, which

cannot be reliably counted and is always within the statistical error or this method.[2] Figure 6.2.5 shows an example mass spectrum analyzed with the automated method, and a comparison to the first method discussed, where a Gaussian plus polynomial function is fit to the data. Panel (a) shows the standard invariant mass histogram and fit using the first method above, for the p_T region between 1.5 and 3.0 GeV/c of the data from run 4049021, using the standard cuts. The various regions of the counting method are shown along with the actual histogram in panel (b).

For this data, the standard Gaussian plus polynomial fit worked well. The result was about 550±60 π^0s detected. The statistical error in this fit is 12% and is calculated by the fitting software, it is also consistent with the total number of counts in the peak region being about 1000, which is the approximate signal plus background total (it is, however, a little high for simple counting statistics). Also, for this region, and the quality of the fit, an overall 10% systematic uncertainty applies to this measurement.

[2] Typically this method is used on small data samples. The signal in these measurements is about 200 counts, and the statistical error in the method is about 20 counts.

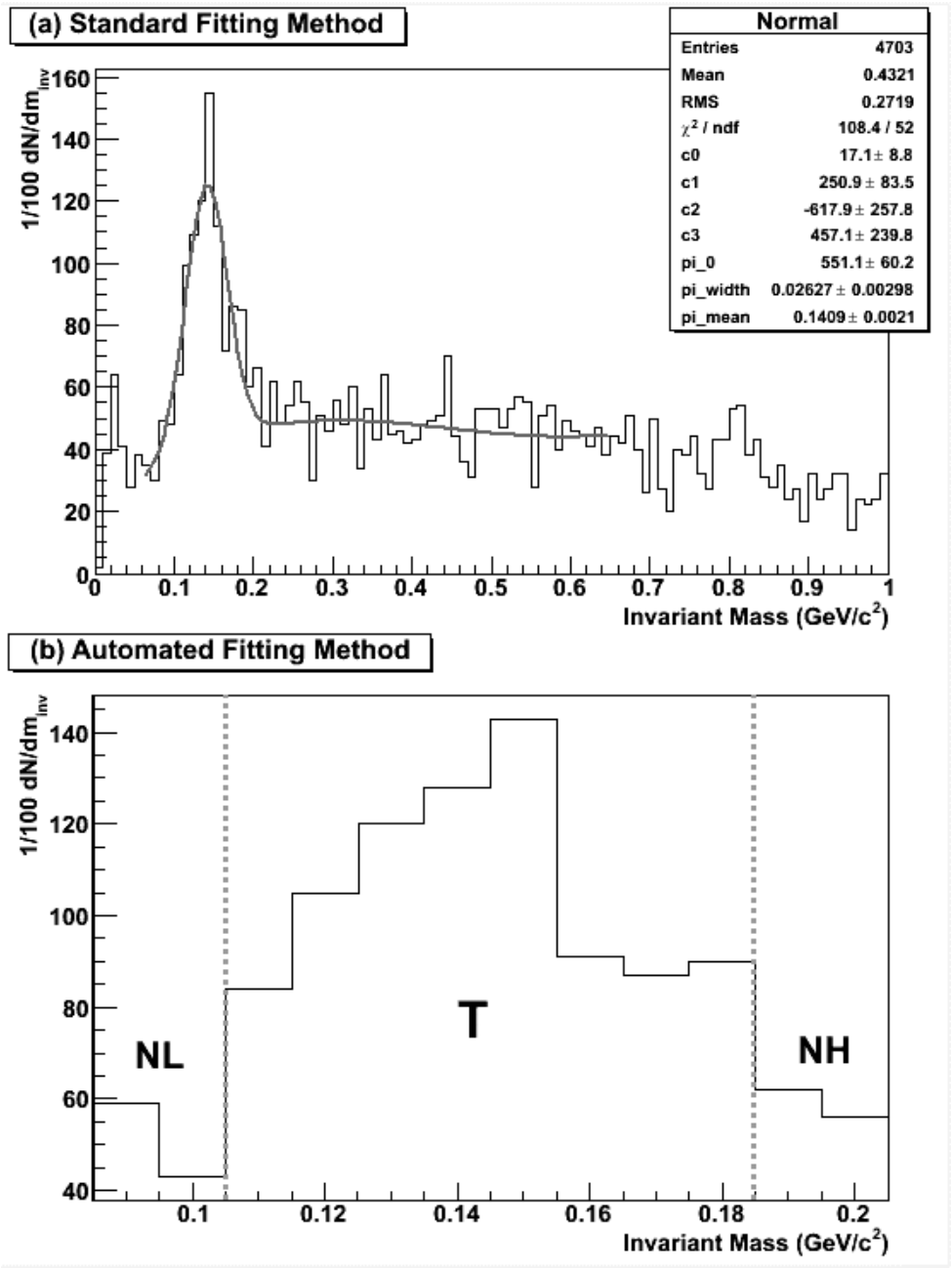

Figure 6.2.5: An automated method was used to quickly identify the overall quality of the dataset. Panel (a) shows the invariant mass histogram for photon pairs from run 4049021 using the normal cuts, in the p_T range 1.5 to 3.0 GeV/c. Panel (b) shows the automated interpretation. The methods disagree systematically, and suggest an overall 10-15% systematic uncertainty in using the automated method. See the text for more information. (Chuck has requested that fit panels be removed from all figures where they can be removed… this will be done for the final version, or ealier.)

The signal is found using the equation $S = T - 2(N_L + N_H)$, where S is the number of counts in the signal, T is the number of counts between 105 and 185 MeV/c^2, N_L is the number of counts between 85 and 105 MeV/c^2, and N_H is the number of counts between 185 and 205 MeV/c^2. The error in the signal counts, δS, is taken to be the basic counting statistics involved in the whole system, or $\delta S = \sqrt{T + N_L + N_H}$. For the histogram in panel (b) we obtain the following measurements. $N_L = 102$, $T = 848$, $N_H = 118$, $S = 408$, and $\delta S = 33$. Thus the methods disagree somewhat, the first method giving 550 ± 60 compared to 408 ± 33 for the second method. The bin-summing method is generally expected to agree, within 5-6 standard deviations with the actual measurement, and relative measurements will diminish the impact of systematic uncertainty and provide a useful way of comparing data between runs. The automated method is, thus, used primarily for diagnostic purposes, and carries systematic error on the order of 25%, in the p_T bin shown here. The p_T bin used in analysis here, 1.5 GeV/c to 3.0 GeV/c, is the only p_T bin where this method is used during the analysis.

6.2.3 Yield Counting

In this section we present the collection of detected π^0 parameters for the various trigger datasets. We will present the representative invariant mass histogram of each channel, and discuss when alternate yield methods need to be used. The results are collected into minimum bias, high tower 1, and high tower 2 datasets.

The representative invariant mass histogram is determined as follows. For any given invariant mass histogram, up to nine fits were made using the primary counting

method. The primary counting method depends on the selection of the mass range for the fit. To determine the systematic effect of this dependence, the nine fits are made. Once the nine sets of results are gathered, a representative is selected whose detected π^0 count falls in the middle of the range for all the fits. At that point, the spread of the results in the remaining eight fits gives the systematic uncertainty in the fitting method. A further extension of the systematic uncertainty was collected based on whether or not the bin-summing method agreed with the primary counting method. If it did not, the systematic uncertainty for the histogram of interest was expanded to agree with the bin-summing method.

6.2.3.1 Minimum Bias

Figure 6.2.6 contains 12 panels showing the minimum bias results for the p_T bins between 1.0 and 8.0 GeV/c. The last two bins, 6.0-7.0 and 7.0-8.0, suffer from limited statistics, but there it is still reasonable to measure the yield in these bins. The panels are arranged in increasing p_T bin from left to right, then down to the next row. Each panel shows number of counts versus photon-photon invariant mass.

All bins in Figure 6.2.6 were fit with the Gaussian plus polynomial fit function. The parameters of each fit can be seen in its respective panel. The resulting yields are collected later with the results from the high tower 1 and high tower 2 yields presented in the following sections.

As discussed in the preceding section, each panel of the figure is the representative fit for the given figure. The actual limits of the fit were allowed to vary, and the fit that gives the most central number of counts is used in this figure. This was done because the fit shape varies greatly across the analysis bins, and a

conservative approach to estimation of systematic uncertainty is prudent. The results bear out that the systematic uncertainty from this source is very similar to the statistical uncertainty in the fit. Reducing this uncertainty is therefore of limited value to this work.

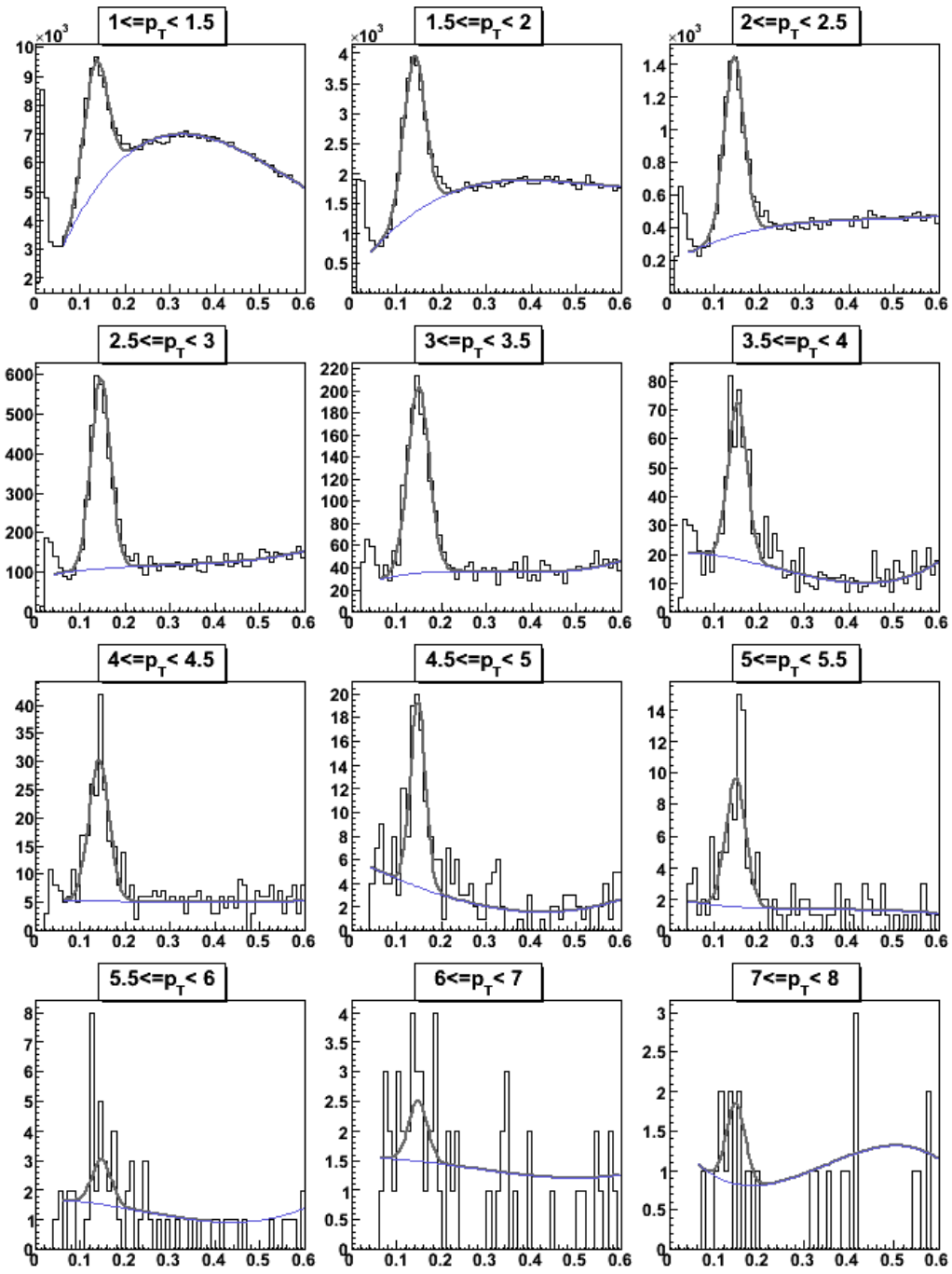

Figure 6.2.6: The invariant mass histograms are fitted for minimum bias data in analysis bins 2 through 13. Only the last bin required modification to the standard fitting algorithm, in order to force the mass peak to be in the right range. The *x*-axis is the invariant mass of photon-photon pairs. Each panel shows the number of counts for each given invariant mass channel.

6.2.3.2 High Tower 1

The yield counting for the High tower 1 dataset is shown in Figure 6.2.7. This figure shows invariant mass spectrum fit results for 10 analysis bins ranging 4.0 <= p_T < 10.0 GeV/c. For these analysis bins, some of the difficulties discussed above were encountered. The bins with p_Ts centering on 7.5 and 8.5 both required limiting either the width of the signal, the mass of the π^0, or both. This is primarily due to the algorithm locking onto the signal turn-on as the π^0-mass peak.

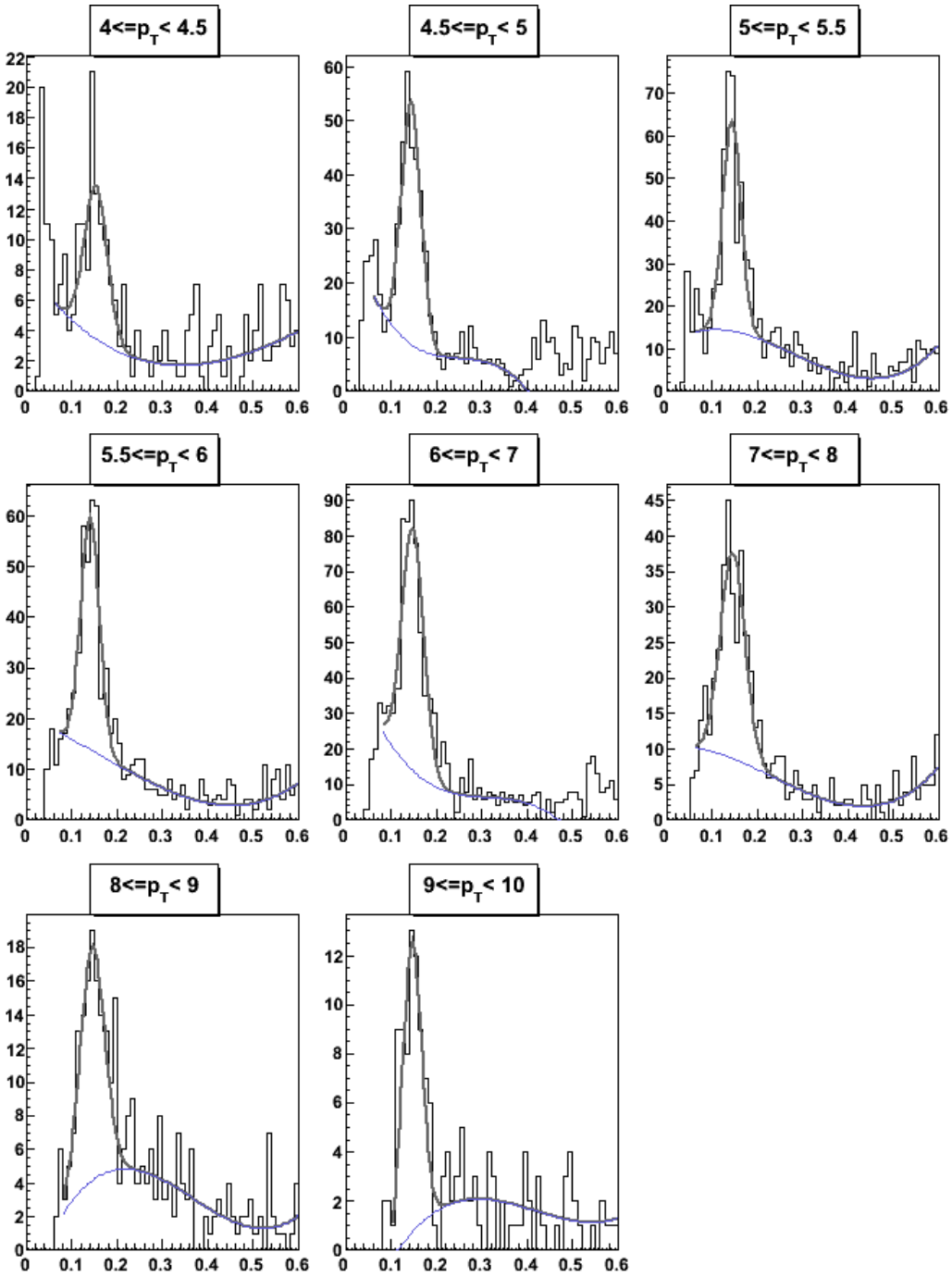

Figure 6.2.7: This figure shows the invariant mass histograms and associated fits for the high tower 1 dataset, for p_Ts between 4 and 10 GeV/c. The 7 to 8, and 8 to 9 GeV/c p_T figures required modified fit functions to isolate the π^0 peak correctly. In both cases the mass and width were pinned to 148 MeV and 27 MeV, respectively.

In order to be counted in these histograms, each photon-photon pair must contain one photon that satisfies the software trigger requirement of 3.2 GeV. This is not the same as the real hardware requirement and leads to large systematic uncertainty in the lowest bins. For this analysis, that systematic uncertainty does not limit the final results.

6.2.3.3 High Tower 2

The invariant mass histograms for the high tower 2 dataset are presented in Figure 6.2.8. Eight analysis bins are presented with 6.0 <= p_T < 13.0 GeV/c. Due to the threshold getting under the mass peak in all bins from 9 GeV/c on, the mass and width parameters had to be closely monitored in all these bins. The limits imposed on these fits are given in Table 6.2.2.

Table 6.2.2: Artificial limitations on fit parameters for high tower 2.

p_T - range	Mass Restriction (MeV/c^2)	Width Restriction (MeV/c^2)
9 to 10 GeV/c	-	27
10 to 11	148	21
11 to 12	148	-
12 to 13	-	21

For high tower 2, the software trigger employed required one of the two photons in each candidate pair to exceed 5.2 GeV. This requirement does not match the hardware trigger exactly, and contributes to large systematic uncertainty in the first two bins. However, this uncertainty is handled by comparison to the other triggers.

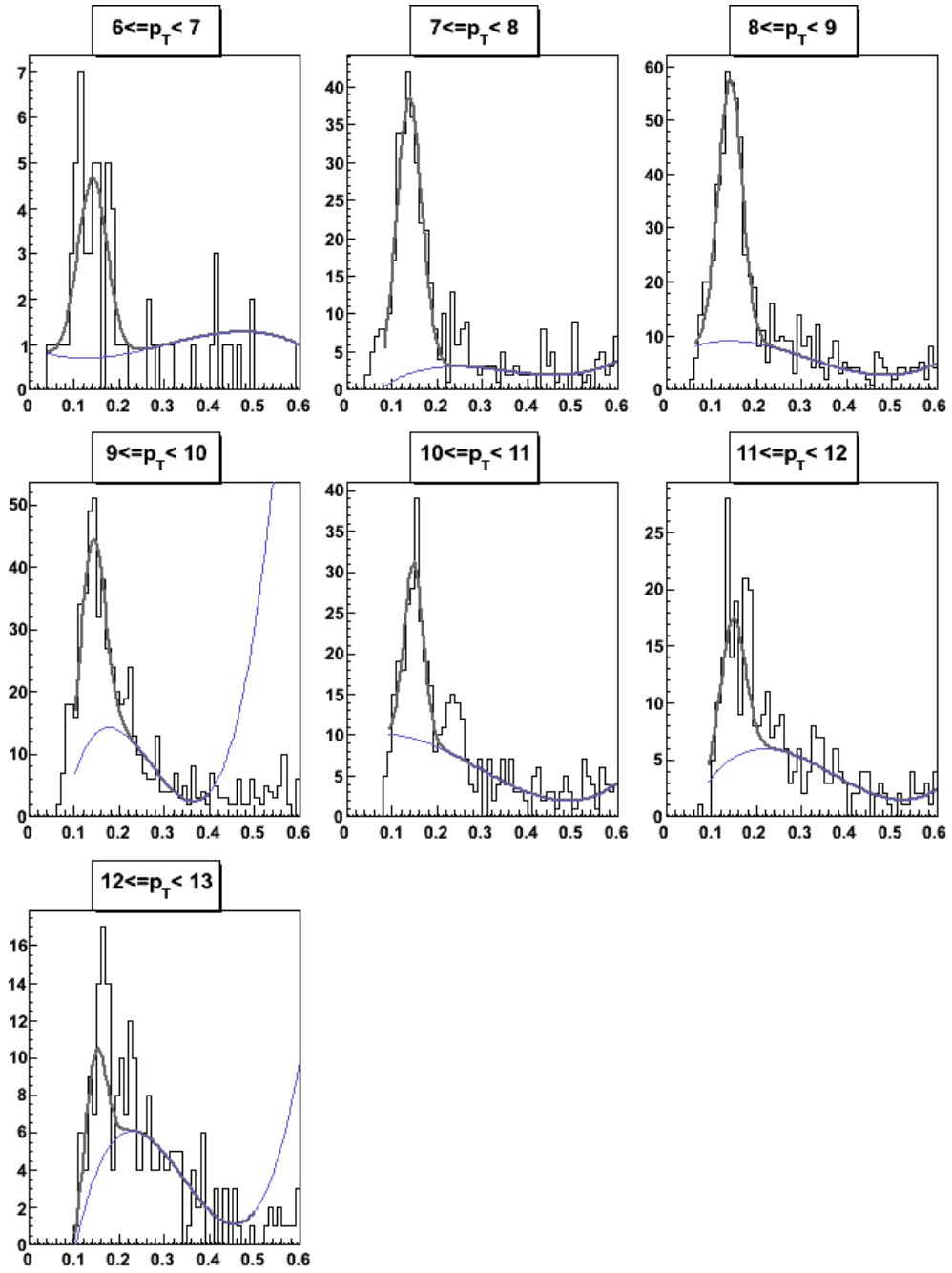

Figure 6.2.8: The invariant mass histograms for the high tower 2 dataset are shown. The p_T coverage of these is 4 to 13 GeV/c. The final 4 panels of this figure required restrictions to the fitting function. For the 9 to 10 panel, the width was restricted to 27 MeV/c^2. For the 10 to 11 panel, the width was restricted to 21 MeV/c^2 and mass to 148 MeV/c^2. For the 11 to 12 panel the mass was restricted to 148 MeV/c^2. The final panel had its width restricted to 21 MeV/c^2.

6.2.4 Normalizing the Yields

The yields presented are the raw number of counts observed for each signal bin. In order to use these, we must normalize them to the number of events that occurred. We ultimately want to normalize to the total cross-section for hadronic interactions $\sigma_{\text{dAu-hadronic}}$, so that the inclusive cross-section for π^0 production can be calculated. Hence we need to normalize to the number of hadronic collisions that occurred during the data taking. Once that is known, we can multiply the rate per hadronic collision by $\sigma_{\text{dAu-hadronic}}$ to determine the π^0 production cross section.

We do not have a count of all hadronic collisions. We do have counts of the number of minimum bias collisions that occurred during the data taking. This number of collisions has been determined to capture about 93% of the dAu-hadronic cross-section for our detector [Ada03].

For the minimum bias data, there are only two slight complications. The first complication is the question of how much of the π^0 signal was not triggered. That is, of the untriggered 7%, how many of those would have produced a π^0. This is expected to be a rapidly falling function of the π^0 p_T because of the increasing requirement of a hard-scattered parton in order to produce the observed p_T. At worst, the missing π^0s are uncorrelated with trigger turn on, which means that 7% of all π^0s are lost. At best, there is a p_T above which all events with π^0 p_T above that level will be triggered. Thus, ignoring the effect completely is no worse than a 7% systematic uncertainty. Because of the further systematic uncertainty that we pick up in the embedding analysis, which will be presented later, at low p_T it is not useful to try to quantify the impact of the minimum bias trigger at low p_T. This, combined with the

expectation that the contribution is minimal when the energy transfer is large compared to the mass of the particle, suggests that we are missing less than 1% of the total production for p_Ts above 1 GeV/c. The second complication with the minimum bias dataset is that we deliberately do not record every observed minimum bias event. The number of events, of a particular trigger, observed in order for one event to be recorded is a number referred to as the "prescale factor". This becomes an issue because the per-event yield is determined by taking the total number of detected π^0s in a given analysis bin and dividing it by the number of minimum bias events. Such a prescription is only accurate if the production rate per minimum bias event is constant. This assumption is not true, however, because the detector configuration changes in time.

Prescale factors fall into a more general discussion of unrecorded data that includes the dead-time of the detector. For our analysis, however, we can ignore the dead-time because we normalize to the number of recorded minimum bias events. It is then possible to multiply by the cross-section for minimum bias to obtain the cross-section of interest. For STAR, the actual cross-section for minimum bias events in 200 GeV *d+Au* collisions is consistent with the result from Monte Carlo Glauber calculations of 2.21±0.09 barns [Ara06]. Since we normalize to the number of recorded minimum bias events, the prescale factors can be ignored for minimum bias because, by definition, they will cancel provided the production rate stays constant. This is seen in the observed π^0 rate per minimum bias event found for the i^{th} p_T bin using equation (6.2.3).

$$
\begin{aligned}
& d^2N(p_{Ti})/dp_T d\eta \\
&= \frac{1}{\Delta p_{Ti}} \frac{1}{\Delta \eta} Y_{MBi-recorded} \cdot PSF_{MB} / N_{MB-recorded} \cdot PSF_{MB} \qquad (6.2.3) \\
&= \frac{1}{\Delta p_{Ti}} \frac{1}{\Delta \eta} Y_{MBi-recorded} / N_{MB-recorded}
\end{aligned}
$$

Here the left-hand side is the differential yield (not Lorentz invariant). The other factors are the p_T-bin size, Δp_{Ti}, the recorded yield and minimum bias event counts, $Y_{MBi\text{-}recorded}$ and $N_{MB\text{-}recorded}$, and the prescale factor for minimum bias, PSF_{MB}. Note, however, that this formula assumes a constant production rate for $Y_{MBi\text{-}recorded}$ per minimum bias event, which is an oversimplification and will be dealt with shortly.

For the alternate triggers, the normalization is a larger problem. The number of events depends on the acceptance of the BEMC. The triggering of the events depends upon the particles themselves. Regions with poorly calibrated towers trigger more or less often than others. For the presentation here, however, we will limit the discussion to the prescale factors. Other effects on the normalization will be handled in the simulation work later.

For the measurement, we must know how many π^0s were generated per minimum bias event. For this reason the alternate triggers must be recorded together with sample minimum bias events. Typically only 1% or less of the minimum bias is recorded. We record a much larger fraction of the alternate triggers but not necessarily the same fraction all the time. For each trigger type, a fixed number of events are observed between each two events that are recorded. This number is called the prescale factor for that trigger. So there are separate prescale factors for high tower 1 and high tower 2, both of which are much closer to 1 than the minimum bias prescale factors. The resulting yield calculation does not cancel these prescales.

The calculation is further complicated by the fact that, since the factors do not cancel, if they are not constant, they must be carefully handled. Let us first consider the situation when they are constant in order to then extrapolate to the other case. In this case, the resulting yield is similar to equation (6.2.3) and is shown in equation (6.2.4).

$$d^2N(p_{Ti})/dp_T d\eta = \frac{1}{\Delta p_{Ti}}\frac{1}{\Delta\eta} Y_{HTi-recorded} \cdot PSF_{HT} / N_{MB-recorded} \cdot PSF_{MB} \tag{6.2.4}$$

These numbers only stay constant over small time intervals, which translate to about 100,000 events. Thus modifying this equation for millions of events is necessary. The small dataset yields Y_i cannot be measured in more than one or two of our analysis bins, and we cannot normalize to the number of HT events observed because the trigger is not well controlled. This normalization, thus, is easiest to accomplish by normalizing to the number of minimum bias events, which is under control.

If we can take the per-event yield in a high tower trigger to be constant[3], then we can determine what the yield is by examining how the recorded yield is constructed. The derivation in equations (6.2.5), below, shows this.

[3] It is not constant because the detector changes. This effect is a handled in normalization of the simulation results where it is treated as a systematic uncertainty.

$$
\begin{aligned}
Y_{HTi}^{meas} &= \sum_{r\in Runs} Y_{HTi}^{r-meas} \\
&= \sum_{r\in Runs} y_{HTi} \frac{N_{MB-total}^{r}}{PSF_{HT}^{r}} \\
&= \sum_{r\in Runs} y_{HTi} \frac{N_{MB-recorded}^{r} \cdot PSF_{MB}^{r}}{PSF_{HT}^{r}} \\
&= y_{HTi} \sum_{r\in Runs} \frac{N_{MB-recorded}^{r} \cdot PSF_{MB}^{r}}{PSF_{HT}^{r}}
\end{aligned}
\tag{6.2.5}
$$

From these, it is clear that we can determine y_{HTi} (the yield per event in bin i, for HT data) directly, by observing that the sum on the right is proportional to the "expected number of recorded HT events". This is true because the ratio of high tower events to minimum bias events should be constant, for well-controlled triggers, and the number recorded is scaled by the PSF_{HT}. Specifically, we have (6.2.6).

$$
\begin{aligned}
N_{MB-recorded}^{r} \cdot PSF_{MB}^{r} &= N_{MB-total}^{r} \\
&= N_{MB-total}^{r} \frac{N_{HT-total}^{r}}{N_{HT-total}^{r}} \\
&= R_{HT}^{MB} N_{HT-total}^{r}
\end{aligned}
\tag{6.2.6}
$$

Unfortunately, this does not make the equation above simpler, because the "correct" number of high tower events could not be measured. Instead, we simply solve equation (6.2.5) for y_{HTi}.

Thus, for this data, we need the number of analyzed minimum bias events for every run, and we need the ratio of the prescale factors. Using our standard dataset, after imposing the run selection requirement of 25,000 minimum bias events with $|Z| < 180$ cm, we obtained these counts and the resulting normalization factors for our raw yields obtained in the last section. The counts are shown in Table 6.2.3.

Table 6.2.3: Event counts for two event classes. Events were selected from 183 runs. Those runs were selected because they have more than 25,000 MinBias events with |VertexZ|<180cm.

Dataset	Counts	Description
Minimum Bias	7.463×10^6	Sum of all MinBias with $\|Z\|<60$
High Tower 1	4.466×10^5	High Tower 1 events in the Min Bias above
High Tower 2	2.691×10^5	High Tower 2 events in the Min Bias above
HT1, with prescales	2.512×10^8	Sum in equations (HTderv) for HT1
HT2, with prescales	2.083×10^9	Sum in equations (HTderv) for HT2
Alt-Minimum Bias	1.305×10^7	Same as above, with $\|Z\|<180$
Alt-High Tower 1	7.847×10^5	Same as above, with $\|Z\|<180$
Alt-High Tower 2	4.685×10^5	Same as above, with $\|Z\|<180$
Alt-HT1, with prescales	4.306×10^8	Sum in equations (HTderv) for Alt-HT1
Alt-HT2, with prescales	3.503×10^9	Sum in equations (HTderv) for Alt-HT2

6.2.5 Additional Systematic Uncertainty

Each cut used in the analysis was one of two types. They were either digital or analog. The digital cuts are the ones that look for the existence of something in the data. The triggers themselves are digital cuts, as are the following; the point-quality cut requiring all three planes of the BEMC fire in order to use a point; the charged particle veto; and the exclusion of runs based on number of events. The remaining cuts, however, are analog cuts. They use restrictions based on continuous variables.

Each cut based on a continuous variable is expected to contribute some amount of systematic uncertainty. Each cut, however, is expected to only contribute minimally to this uncertainty, unless, for some reason, there is a dramatic change in the detected distribution with a small change in the parameter of interest. The main parameters that must be checked are the following two. The Z vertex restriction on analyzed events should be varied slightly to see if the per-event yield changes much. Similarly, the cut based on energy asymmetry of accepted pairs should be varied slightly (and corrected for phase space in the decay).

Analysis of data with the energy asymmetry limited to 0.6 instead of 0.5 provided the results found in Table 6.2.4 for each primary analysis bin (some higher p_T bins were excluded due to poor statistics, and the poor systematic uncertainty already seen in those bins). This table also includes the results for the Z vertex study discussed next. For the energy asymmetry analysis, most bins where additional uncertainty was found produced uncertainties similar to that already in the analysis. This is not the case for the low p_T-bins for the high tower trigger data. This is because only highly asymmetric decays produce photons above threshold, thus, near the energy threshold this cut adds significant systematic uncertainty.

Since both of these uncertainty analyses used the same primary dataset and counting methods, used for the regular analysis, the resulting measurements are correlated to the earlier measurements. Thus, if the observed difference in any bin is below the known uncertainty in the method, the observed uncertainty is not included in the tabular results. Also, since the dataset is the same for both analyses, the statistical uncertainty is not considered in determining the systematic uncertainty. Both of these choices are conservative methods to handle complicated correlations whose analysis would only provide marginal reduction in the uncertainty.

Similar analysis was carried out on the full dataset, but with a limitation on the event Z vertex of 70. This is a conservative direction because the quality of the signals goes down as Z increases. Also, in the increasing Z direction the additional event contribution is rapidly changing with Z, thereby magnifying any systematic effects. For normalization purposes the number of events must be given for each event class in this analysis at $|Z| < 70$ cm. They are 8.352×10^6 for min bias, 2.798×10^8 for high tower 1, and 2.316×10^9 for high tower 2. The candidate photon pairs were collected for these events, and the extracted yields and resulting additional

uncertainties were collected. Table 6.2.4 presents these additional systematic uncertainties for each analysis bin..

Table 6.2.4: Additional systematic uncertainties due to analysis cuts are shown. This table includes BEMC turn-on effects, *Z*-vertex effects, and energy asymmetry effects. Systematic uncertainty for the latter two effects are measured only when the observed effect is larger than the known uncertainty in the measurement method.

Dataset	Yield Y	Yield Sys. %	Y_{70} $\|Z\|<70$	Ratio Y_{70}/Y	Extra Sys. %	$Y_{0.6}$ $\varepsilon<0.6$	Ratio $Y_{0.6}/Y$	Extra Sys. %
MBHisto2	3.18e4	16.4*	3.52e4	1.0109	-	3.69e4	1.0341	-
MBHisto3	1.66e4	7.8**	1.84e4	1.0095	-	1.99e4	1.0010	-
MBHisto4	6.44e3	10.2	7.12e3	1.0121	-	8.00e3	0.9660	-
MBHisto5	2.68e3	5.2	2.95e3	1.0166	-	3.42e3	0.9404	2.9
MBHisto6	1.03e3	4.9	1.13e3	1.0200	-	1.38e3	0.8957	9.2
MBHisto7	2.96e2	11.5	3.44e2	0.9629	-	4.29e2	0.8280	12.8
MBHisto8	1.43e2	14.0	1.58e2	1.0128	-	1.98e2	0.8667	-
MBHisto9	6.78e1	19.2	7.33e1	1.0350	-	9.47e1	0.8591	-
MBHisto10	4.45e1	26.7	4.78e1	1.0417	-	5.62e1	0.9502	-
MBHisto11	8.06e0	47.1	9.22e0	0.9782	-	1.73e1	0.5591	-
MBHisto12	7.23e0	44.3	8.99e0	0.8999	-	7.68e0	1.1297	-
HT1Histo8	6.58e1	18.2	8.46e1	0.8959	-	3.20e2	0.2467	75.1
HT1Histo9	2.40e2	20.0	2.54e2	1.0526	-	4.31e2	0.6682	26.5
HT1Histo10	2.67e2	9.7	2.88e2	1.0328	-	3.59e2	0.8925	4.6
HT1Histo11	2.44e2	17.2	2.80e2	0.9708	-	3.68e2	0.7957	11.0
HT1Histo12	4.17e2	9.8	4.95e2	0.9385	-	4.20e2	1.1914	16.4
HT1Histo13	2.04e2	10.3	2.19e2	1.0377	-	2.44e2	1.0033	-
HT1Histo14	9.44e1	10.4	1.00e2	1.0516	-	9.37e1	1.2090	18.1
HT1Histo15	5.77e1	14.6	6.23e1	1.0317	-	6.26e1	1.1061	-
HT2Histo12	3.06e1	14.7	2.52e1	1.3503	31.8	1.12e2	0.3279	65.6
HT2Histo13	2.35e2	12.3	2.14e2	1.2211	18.4	4.87e2	0.5791	40.3
HT2Histo14	3.27e2	22.9	3.72e2	0.9775	-	4.46e2	0.8798	-
HT2Histo15	2.18e2	14.2	2.29e2	1.0586	-	2.91e2	0.8990	-
HT2Histo16	1.12e2	28.6	1.45e2	0.8589	-	1.32e2	1.0182	-
HT2Histo17	6.71e1	47.7	5.06e1	1.4746	-	7.35e1	1.0955	-
HT2Histo18	3.76e1	39.9	3.67e1	1.1393	-	6.38e1	0.7072	-

* - Additional systematic of 25% comes from BEMC turn-on.
** - Additional systematic of 10% comes from BEMC turn-on.

One other source of systematic uncertainty in this analysis comes from the threshold behavior of the detector channels. Both the tower and SMD energy cutoffs are set fairly low in this work (0.350 and 0.100 GeV, respectively). This low cutoff

means that essentially all signal change due to moving the thresholds adds or removes data in a region dominated by noise. Also, changing this cut will greatly affect the efficiency of the detector relative to the other cuts, thus analyzing the systematic uncertainty here will require matching the analysis parameters while determining the change in efficiency.. The turn-on behavior of the efficiency, which changes rapidly with p_T, dominates this measurement and is conservatively placed at 25% for the 1.0 to 1.5 GeV minimum bias bin, and 10% for the 1.5 to 2.0 GeV minimum bias bin.

For the yield extraction, all the methods have now been discussed. The yield of π^0s was collected for each analysis bin. During that collection, the details of the detector acceptance and the cuts used in the analysis were documented so they could be matched while measuring the detector efficiency. Further, for all channels we have presented quantitative values for all uncertainties in the analysis.

6.2.6 Yield Results

The yield results for the three triggers have been normalized, and will now be presented. The bin-wise values can be found in Appendix G. These yields were discussed above in more detail. In broad strokes, the yields were extracted from the minimum bias, high tower 1, and high tower 2 datasets, using only good portions of the detector and reliable data-taking periods. The data was also restricted by cuts on charged particles, event position within the detector, and decay phase space. Note also, these yields are normalized to the number of minimum bias events scaled up by 7% for the inefficiency of the minimum bias trigger at identifying the whole $\sigma_{dAu\text{-}hadronic}$. The missing portion of the trigger does not contain a relevant portion of the π^0

yield, this contribution is taken to be zero. The systematic uncertainty due to this effect is small compared to other systematic uncertainties in the yield extraction.

The Lorentz invariant yield results are shown in Figure 6.2.9 for all three triggers, presented as a function of π^0 p_T.[4] The minimum bias, high tower 1, and high tower 2 data are shown as the circles, 'X's, and triangles, respectively. The error bars shown are statistical, dominated by yield counting.[5] The band represents the systematic uncertainty due to the yield counting method, sensitivity to the analysis cuts, and presence of π^0s in the untriggered portion of $\sigma_{\text{dAu-hadronic}}$. The systematic uncertainty due to the analysis cuts was determined by varying the cuts. The sensitivity of the yield was taken to represent the uncertainty. Beyond those checks, remaining uncertainties in the analysis regime are handled by matching of the detector behavior in the embedding analysis in the next section of the dissertation.

[4] The p_T assigned to each point is the p_T at which the production spectrum is equal to its average value over the given bin [LW95].

[5] That is to say, the statistical error is the combination of the yield counting and event counting, but the event counting statistical error is less than 0.1%, which can be neglected compared to the yield counting that is always more than 1%.

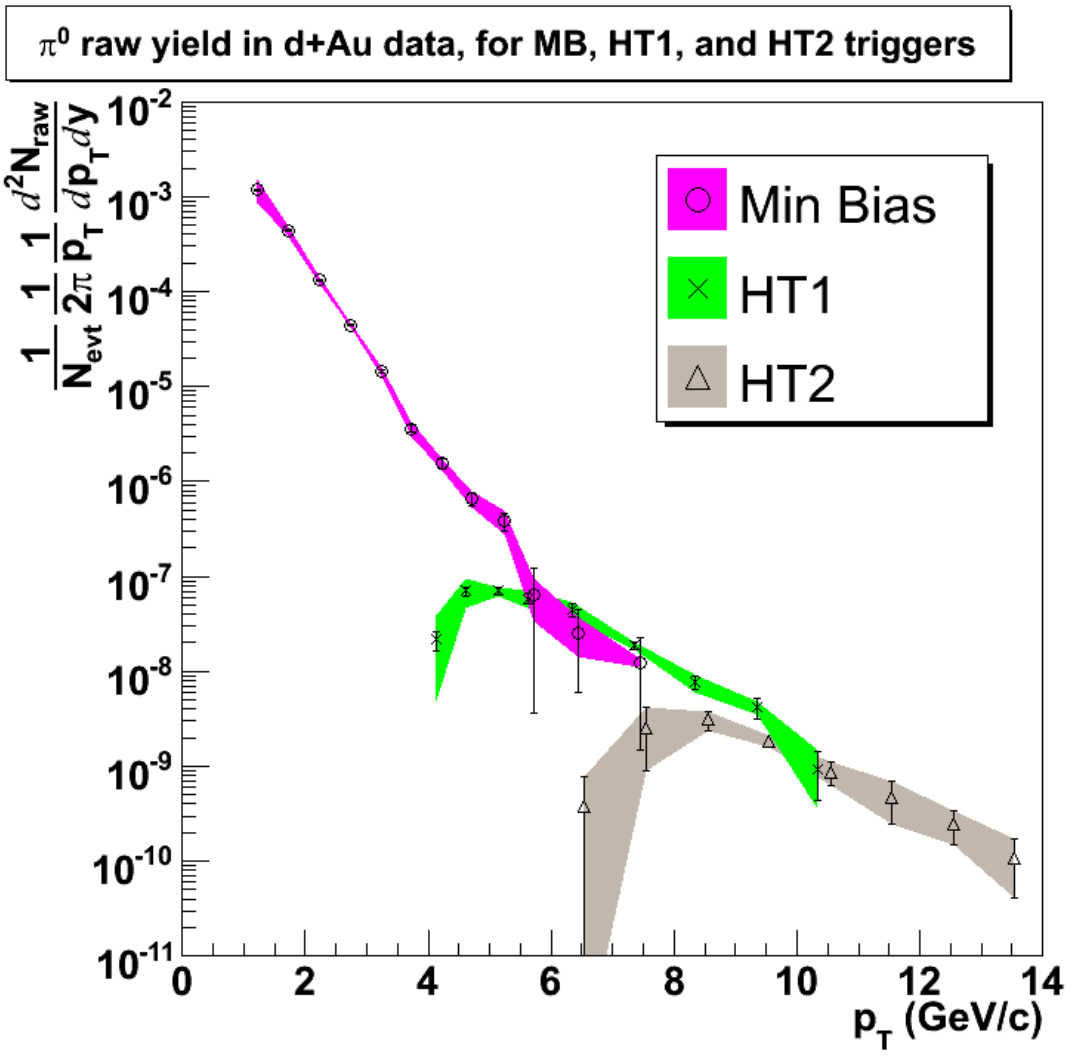

Figure 6.2.9: The normalized Lorentz invariant yields are shown for the three data sets. The largest legitimate bin is 12 to 13 GeV/c, however, it still has large uncertainty. The three datasets are represented from left to right in the diagram. Note that the overlap region is reasonable, since the detector acceptance changes somewhat from one dataset to the next and the triggers are just turning on for the next trigger as the previous one becomes statistically limited. (HT1 and HT2 points are shifted -100 MeV/c and +100 MeV/c, respectively.)

6.2.7 Standardizing the Data

The yield analysis includes variation in the data that cannot be directly verified using simulation. The sources of the variation must be carefully studied for normalization in the simulation. Specifically, we must know to what degree the actual yield of π^0s remained consistent across the varying detector behavior. To do this, we must discuss the attributes that cannot be directly verified, and therefore have only approximated models in the simulation. This discussion will cover alternate analyses of the data in a way that requires recounting events rapidly. Hence, the analysis here uses the automated version of the yield counting discussed earlier in this chapter. Namely, we histogram the invariant masses between 85 and 205 MeV/c^2, using 12 bins, then use four bins, two on each end, to estimate a linear background.

The degree to which results apply across the entire dataset, or the time-dependence of the data, was checked with this method. This is necessary because the changes in the detector configuration may have resulted in dramatic changes in the rate for recording π^0s. So it is important to establish the degree to which this data is internally consistent, so that results apply to the entire dataset. For example, when simulating the detector response, since the detector is changing, the validity of the simulation comes into question. Thus we will show here that the behavior of the detector was actually quite consistent over the data-taking period, which will establish the validity of the simulation work later in this chapter.

The method used to analyze this is to determine the particle yield in a "standard bin". The standard bin was chosen to allow the most segmentation of the data without eliminating data unnecessarily. This is best illustrated by discussing the actual parameters used. We used all π^0s in minimum bias data, with the data

segmented by run. The cuts used were the same as the yield analysis above except that we only restricted Z to 180cm from the center of the barrel. This leaves open the p_T selection, which we chose to be between 1.5 and 3.0 GeV/c. We segment the data by the data "runs" which were determined by the personnel operating the experiment during the data taking, under guidelines set by the STAR community. Because of this segmentation, and the set of cuts for data selection, we must have a minimum number of events per run in order to obtain a reasonable number of counts and thereby keep the errors in the process minimized. For our analysis, we required that runs have at least 25000 minimum bias events that pass the $|Z|<180$ cm cut. The number of events was used to normalize the π^0 counts in the "standard bin" to create a "standard yield" for a given run.

The "standard yield" for each run passing the 25000 event cut was collected. The resulting set of values was histogrammed, and the results can are presented in Figure 6.2.10. The shape of the figure, and the associated X^2 of 3.5 / 11, suggests its interpretation as sampling from a reasonable statistical distribution with some self-organizing behavior, as expected from the STAR BEMC. Hence the figure was fitted with a Gaussian to establish the population mean and standard deviation. It should be noted that the observed standard deviation of about 25% is much larger than the statistical error in any particular count, so it reflects at least one other source of variation. There is not, however, a large deviation from the Gaussian shape, such as low-end or high-end satellites which would indicate large portions of the data-taking where extensive sections of the detector changed status from good to bad or vice-versa. Nor are there tails or apparent asymmetry.

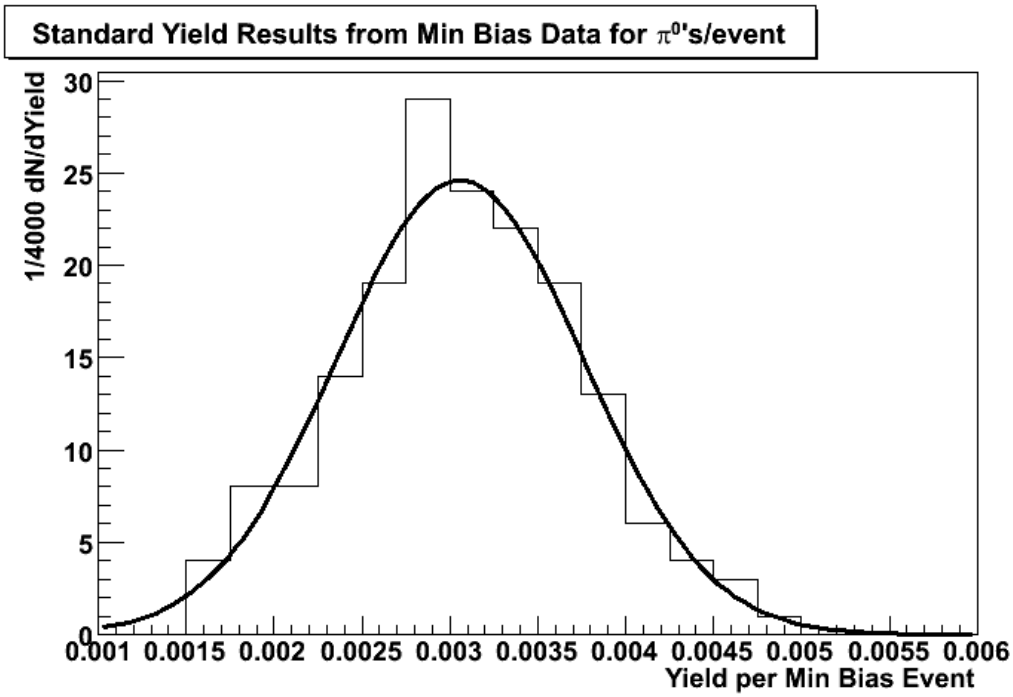

Figure 6.2.10: The π^0 yield per minimum bias event was collected for most of our analysis runs, and histogrammed. The resulting distribution is well-shaped, and indicates that the data is under reasonable control. The X^2/n.d.f. for this fit is a bit low at 3.5/11 which is consistent with the shape being partially due a complex self-organizing system, like the STAR BEMC and its support staff.

As additional evidence that the data is under control its time dependence was tested. The method used above required collecting yield information from runs with reasonable statistics. Figure 6.2.11 shows the per-event yield from the automated method plotted as a function of increasing run number. This presentation would display a rough indication of time-dependence. The result shows grouped time-dependence, but no consistent trend. There is also no evidence that the performance of the detector changed greatly at any point in time.

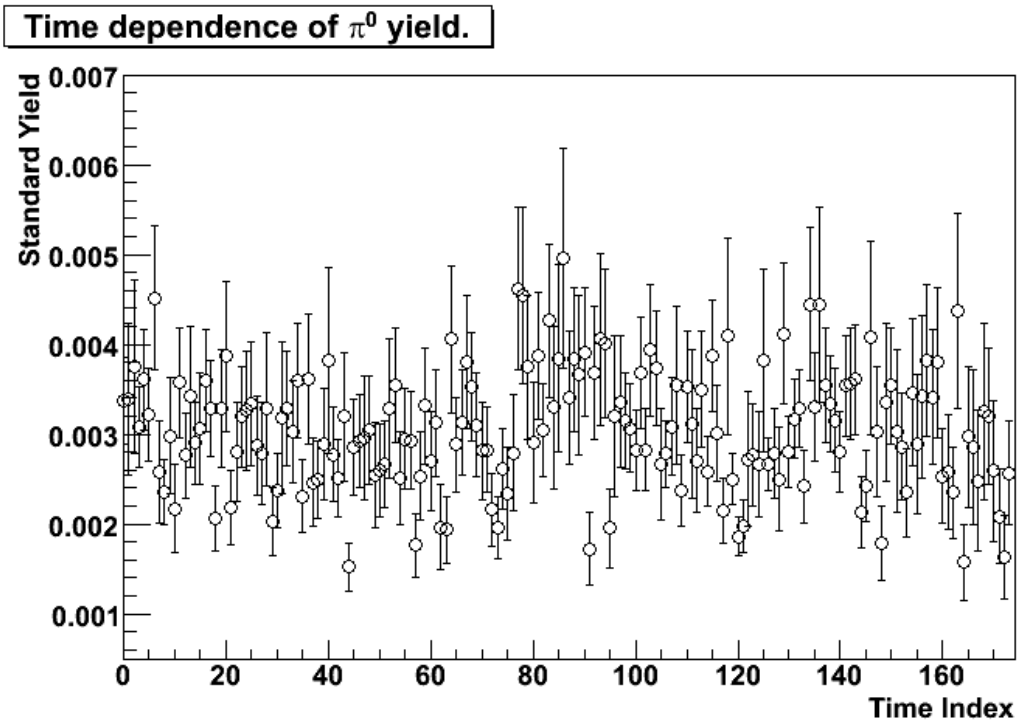

Figure 6.2.11: Time dependence of the "standard" π^0 yield per event. Notice that there is no clear dependence. This analysis uses the automated fitting method, so it has 15% systematic error, in addition to the statistical errors shown.

This analysis shows that the general behavior of the data is consistent. The evidence suggests that although variation in the data-taking qualities of the detector did change, the average behavior of the system is consistent and roughly on the scale of the statistical uncertainty in the data. This applies primarily to the most well-determined analysis bins, since some bins have statistical uncertainty that is much larger than the variation hinted at here.

6.2.8 Conclusion

The raw yields for π^0s have been collected. For each analysis bin, one or more trigger types generally provide per-event yield information with around 15%

statistical and 15% systematic uncertainty (expanding to 50-80% near the end of the p_T range). In order to use these to determine the inclusive cross-section for π^0 production, the efficiency of the system must be known. That is the subject for the next section of this chapter.

6.3 Embedding Analysis

6.3.1 Introduction

This dissertation deals primarily with the measurement of absolute cross-section for particle production. The means of measuring the cross section, however, are based on measuring detected yields. Detected yields are observed because there was some underlying population of particles that went through a set of physical processes, became electronic signals, and ultimately were observed in the data through a process of reconstruction. It is essential, for absolute measurements, that the entire signal production and reconstruction process be known and analyzed for contributions to signal loss. The convolution of all the sub processes involved in recording real events, and thus real particles, and turning them into analyzed data or identified particles can be modeled. The modeling results are then used to convert the observed yields to the total yields.

Model-based simulation of the real events is not generally done for systems more complex than proton-proton scattering, because the physics processes at work contain many assumptions and become highly dependent on which model is used in the energy regime of interest [WG91, WG94]. Furthermore, it is the goal of high-energy nucleus-nucleus collision experiments to determine which models match reality. Using a model to select the simulated events may unnecessarily beg the question. Once the model dependencies are determined, nucleus-nucleus collision simulation software, such as HIJING could be used [Sav98]. A more practical and simpler simulation approach is used here. Particles of interest are simulated with simple

production distributions, and their physical processes are then evolved using Monte Carlo methods in GEANT, and STAR detector simulation software [GEA]. This includes all processes, starting with the particle's decay, all the way to generation of signals in the various parts of the detector. Simulations further mimic the real data collection system in that the resulting data is prepared in exactly the same format as the real data. Additional information is carried along with the resulting simulated data to be able to exactly determine what signals came from which simulated particle track.

For many simulation analyses there is benefit in actually injecting the simulated signals into preexisting data. This process is known as "embedding". The resulting dataset is known as "embedding data", or "embedded data". The value of embedded data depends heavily on the ability to simulate combinatorial effects with background data. That is, if the simulated particles, when combined with random signals from real events, produce observable effects, then embedding is important. In order to observe all such signals, it is important for the relative abundance of simulated particles to match the real production rate. Further, if the rate is matched, correlations between the simulated particles and the real event would have to match real particle behavior. The looser requirement of matching the production rate simply cannot be done for most of our analysis bins, and the question of matching real particle behavior is mute. For use in this research, then, embedding analysis serves as a quality test. If large combinatorial effects are seen, we are prompted to do further analysis.

Correlation with background real events proved an insignificant impact to the simulated particles. This can be seen in the produced invariant mass spectra where almost no background signal due to close correlations is seen. These spectra are

discussed later in this secion. Thus the embedding events were simply used as plain simulations of candidate particles and detector response.

Simulations are only as good as the models used to construct them. Hence, simulation-based results are only applicable in a regime that is at the intersection of all models involved. It is, therefore, important to know the limits of applicability of all portions of our simulations.

The simulations in this analysis are mostly based on well-understood processes. In broad strokes, the general divisions of the simulations are the following. First, the desired particles are "created" at the event vertex with some sort of distribution. Because of the physics of high-energy collisions, and symmetry arguments, this is usually simulated well, except for the fact that the transverse momentum distribution cannot be handled at this point in the simulation since it would cover many orders of magnitude; this will be covered again shortly. The simulated particle is then combined with a "detector model" (a file describing the bulk materials used in the construction of the detector) and fed into the GEANT software tool that tracks the particle through the detector and handles any physics processes, such as decay or scattering, extremely well. GEANT does not become a modeling limitation unless the energies involved are below the MeV scale, above the TeV scale, or involve low branching ratios (10^{-5}) or long decay chains. Once GEANT has determined a picture for the particle in the detector the energy deposition in sensitive regions must be converted into software signals. It is this final part of the simulation where time-dependence and detector quality must be simulated, processes that usually have only limited data.

The primary problem with the simulation is creation of signals for the BEMC layers. There are two reasons this is a problem. The first is related to the actual

signal generation. The second is matching the actual operational configuration of the detector.

The signal generation is based on some assumptions that are not exactly true. The conversion of energy deposition into recorded ADC values is based on two expectations. First is the assumption that all the channels of the BEMC operate the same as the sample module used in the test-beam experiment. This is a generally reasonable assumption since the bulk materials are essentially the same, but the exact details of each module vary somewhat. The second expectation is that the various configuration constants, the gains and pedestals, can be used to accurately generate a function that can turn ADC value into energy and vice-versa.

Matching the operational configuration of the detector is a much trickier problem. In order to do this, the configuration must be known well, and the configuration must be simulated properly. Additionally, though, the configuration varies in time, and that variation must be accounted for in any simulation analysis. The embedding data was generated from only a small subset of the real data, reflecting only a small time window in the entire data collection.

Efficiency results are highly dependent on the accuracy of these simulations. For this reason, it is important to verify the quality of the simulations as well as possible. In a later section of this portion of the dissertation there is an overview of the simulation data with an emphasis on how well the simulations reflect the detector operation during real data acquisition. Differences will lead directly into systematic errors, and therefore will be categorized and measured so that they can be easily accounted for in the final efficiency results. All dependencies will show some small systematic effects. Many, however, will simply be reflecting a bias related to another parameter that has large systematic uncertainty. Thus it is important to establish a

base systematic uncertainty that can be used to suppress effects that that are clearly insignificant in comparison.

Once the simulated data is ready, and used to produce embedding, it is analyzed to produce the efficiency results. The analysis is a mirror of the yield analysis used on the real data. Mirroring the earlier process is done to reproduce idiosyncrasies and thereby reduce systematic errors related to analysis methods. For the measurements presented here, this calculation is a little bit tricky.

There are three reasons why this part is tricky. The first is that the transverse momentum distribution is not yet simulated and must be done during the analysis. This point was discussed briefly above as a limitation of the simulation of the desired particles. The second reason, although with less impact, is that the event distributions in the simulation and real data are slightly different. The final tricky part of this analysis is that the detected particles are not necessarily detected with the parameters that they were simulated with. Thus, a particle may be identified outside of the bin it was simulated in. For this reason it can be difficult to assign the statistical errors associated with the numerator and denominator in the simple efficiency calculation: ε = #Detected/#Simulated. Similarly, the actual correlation of the numerator and denominator can be rather complicated because the statistical process is not a straight binomial distribution.

The embedding analysis that follows covers the items outlined above. First we will briefly discuss the exotic triggers, and how they must be handled in embedding. It is important to highlight exactly what the embedding data consists of, so this will be covered next. The simulated data is embedded into real data, which produces some benefits that we will discuss. Then we will compare the quality of the

simulation to the real data. At this point we are prepared to analyze the embedding data to extract the simulated π^0 counts. This section will finish up by highlighting the total resulting systematic uncertainty for each yield bin, and finally presenting the overall efficiency for each yield bin.

6.3.2 High Tower Triggers

Data was taken using three trigger configurations. These configurations are important to the simulation analysis because the simulation of a high transverse momentum π^0 will cause an embedding event to satisfy the alternate trigger requirements. This occurs in real data also. In such a case the π^0 is said to "trigger" the event. For this reason efficiency results will be needed for each trigger configuration separately. With the differences from trigger to trigger representing the contribution of the simulated particle to the actual trigger efficiency.

The reason the trigger efficiency must be studied is that there is a portion of the π^0 transverse momentum spectrum where the trigger "turns on". In that region the ability of the π^0 to produce the trigger affects its detection efficiency. For example, only highly asymmetric decays of a 3.5 GeV particle will exceed a 3.2 GeV trigger requirement. However, these triggered events will not yield detected π^0s because the particle causing the trigger will have $\varepsilon = 0.83$, while our analysis has a cut on $\varepsilon < 0.50$. The situation is actually not quite this simple, because the real high tower triggers are based on ADC values, not actual energy deposition.

For real events, it is not necessarily the case that the π^0 be the source of the largest energy deposition in the BEMC. Hence, measuring the turn-on effect of threshold photons produced by decaying π^0s has some risk of introducing a systematic error.

However, there are several reasons why this is not a major problem. The first is that, provided a large-p_T π^0 is fragmented from one of the jets in an event, the probability that another large-p_T particle is fragmented is small. If two such particles are produced they are probably not from a single parton's fragmentation, but instead from two correlated jets. Such a production process has very low probability. These low probability scenarios are further suppressed in the analysis because of the steeply falling production spectrum for high-p_T particles. For example, the number of events where another particle provides the high-p_T trigger, and a 3.5GeV π^0 are produced, is dependent on the ratio of the production of that trigger particle to the actual π^0 production at 3.5 GeV. It is expected that unless the triggering particle is also nearly 3.5 GeV it will represent a very small class of events compared to all events with a 3.5 GeV π^0.

We must, however, determine the error associated with this sort of mixed turn-on. To reduce this source of error, we required that π^0s in the real data be able to satisfy the software trigger on their own. Thus of all produced π^0s, all that satisfy the software and hardware triggers will be counted in the real data, and some extra π^0s that only satisfy the software trigger will also be counted. Due to problems with the application of the hardware trigger to the recorded data, some additional π^0s get through which only satisfy the software trigger. Under the right conditions (namely that real π^0s may require additional particles to trigger events in a given p_T-range), the latter set of π^0s may dominate the detected particles. The combined hardware and software method will thus underestimate the appropriate simulation results near threshold. The alternate software-only method, which includes the particles that may have gotten into the real data, will overestimate. These two methods provide

bounding conditions for the turn-on behavior, and will be used to calculate the range of π^0 detection efficiency at threshold. This uncertainty was found to be quite large in the lowest p_T bins for the high tower triggers. However, more precise results from overlapping trigger datasets provide tighter bounds on the production.

In section 6.1 we compared several methods of retriggering high tower 1, see Figure 6.1.9. It showed that most high tower triggered events with a π^0 were indeed triggered by their π^0s. The largest discrepancies came in the trigger turn-on region where the π^0 yield is suppressed relative to other triggering particles. For example, near the turn-on region only π^0s that decay very asymmetrically will cause triggers while other sources, such as decay photons or MIPs that shower in the BEMC, cause a larger portion of the high tower triggers. This uncertainty is small compared with the trigger threshold uncertainty presented later in this section.

Aside from the discussion of how events are triggered, there is one additional way in which efficiencies measured in the high tower datasets can vary from the minimum bias. The difference is due to the fact that much of the high tower data was taken during a time when the minimum bias trigger was prescaled by a large amount. The majority of this occurred during a time-window late in the data taking. Therefore, the high tower data, to a large extent, reflects a time frame in which the detector configuration could vary greatly compared to the majority of minimum bias. Due to the very restrictive acceptance cuts, this is not expected to be a large effect compared to the statistical and systematic uncertainties in the high tower data. These problems, based on the acceptance discussion in chapter 4, can account for no more than 10% of the detector for no more than 20% of the time, or essentially 20% of the efficiency

(0.9*0.9) for 20% of the time. This means about a 4% effect, which can, again, be safely ignored.

As discussed above, it is necessary to analyze the embedded data separately for each of the triggers. This is due to three reasons. First, because the high tower triggers form separate datasets that are different from the minimum bias, and therefore each should be carefully considered separately from the others. Second, the high tower triggers each have a turn-on region in which the π^0 yield in the real data first increases, and then decreases. If this turn-on region can be properly simulated then the overlap of the different triggers can be extended. Finally, the detector configuration may have changed, although this requires no additional analysis. Because of these reasons, each of the triggers will be analyzed separately to determine the appropriate efficiencies for their respective datasets.

6.3.3 Embedding Data Overview

Several sets of embedding data were produced and made available on the RHIC Computing Facility (RCF). The two primary ones were used for this analysis. The first data set was embedded into 2 minimum bias runs, with a total of 750,000 events. The second set included 1,500,000 events and was embedded into 6 runs. The former data set included simulated π^0s with p_T range up to 15 GeV/c, while the latter included p_T's up to 25 GeV/c. The details of these datasets are summarized in Table 6.3.1.

Table 6.3.1: Data souce information for embedding analysis.

	Dataset #1:	**Dataset #2**
Events:	1,000,000 (1.21×10^5 used)	1,500,000 (1.34×10^6 used)
π^0 per event:	1	1
ϕ-range:	2π	2π
η-range:	-0.3 to 1.2	-0.3 to 1.2
p_T-range:	0 to 15 GeV/c	0 to 25 GeV/c
Runs used:	4036043	4034028
	4049021	4035018
		4036043
		4044004
		4049021
		4059014
Identification:	ID#1085593583	ID#1130984157

It should be noted that for the minimum bias analysis, all runs with run IDs before and including 4040024 were excluded due to having low average energy per event. This problem does not mean that the embedding data is bad, only that the data has to be handled so that the problem does not affect any measurements. Also, 4044004 included a mixture of MinBias and High-Tower triggered data. As a result, about 3% of the embedding was embedded into High-Tower events.

Both of these problems are handled by correlating any observed measurements to the simulated signals that were embedded. That is, the background data was suppressed by only analyzing data that was produced by simulation, or modified by the simulation. This method loses some potential benefits due to the interaction of simulated and background signals. For π^0 analysis, such benefit is limited. The simplification of the embedding analysis due to only using correlated signals is more useful than the possible benefits of correlation with background, as discussed next.

6.3.4 Benefits of Embedding

There are several possible ways of using embedding to give information about interaction with the background events. The most obvious is to observe the way that the simulated particle's signals interact with the background events to form modified or additional signals in the analysis. For example, background photons may be combined with simulated photons to provide counts in the $\gamma\gamma$ invariant mass spectrum. Also, however, the background events can corrupt the simulated signals due to close proximity of real and simulated particles. The impact of such corruption can be studied by analyzing the embedding data. Another major use of the embedding is to verify that the detector quality in the simulation matches the real data. Finally, as a corollary to the last usage, the observed simulation results can be normalized to the embedding data it is in, and can then be applied with a correction factor to other data taken with different detector configurations.

For high multiplicity collisions where there is no preferred collision direction, the mixing of simulation and real signals is expected to provide a good measure of combinatoric backgrounds. This is particularly the case where the particles of interest are not due to fragmentation of a high-energy jet. Unfortunately the most likely collision systems to fit this description are heavy nuclei that collide centrally, such as *Au+Au* or *Cu+Cu*. Even in those cases the applicability of mixing simulation with background must be carefully analyzed. In *d+Au* collisions, events will almost always have a preferred direction with which real π^0s would be correlated, providing combinatoric behavior that cannot be exactly simulated without introducing model dependencies. As we will see, however, the deviation between uncorrelated and

correlated behavior is within the uncertainties of the analysis, and therefore any model dependencies can be ignored.

Aside from analyzing these background interactions, most analyses of embedding data are really only analyses of simulated data. From here on, both types of analyses will be referred to together, and where necessary the distinction between simulation and embedding will be made. The distinction is not of great importance outside the specific cases discussed here, and will be used interchangeably outside this section of the dissertation.

We compared the invariant mass signal generated with simulation points only, to that with both simulation and background. Because of the fact that the simulations were made with one π^0 per event, the simulation signal is expected to swamp any direct background signals (those due to background π^0s) above the region where the real number of π's per event is below 0.04 (since the embedding is made in uniform p_T, where $0 < p_T < 25$ GeV/c). However, the resulting combinatoric background due to simulated π^0s with background event data should still be reasonable. Real data contains about 0.04 π^0s per event at p_Ts below 3 GeV/c once the efficiency is accounted for. The quick swamping of the background, and also the low impact of combinatorial background are presented in Figure 6.3.1 which shows (a) the invariant mass spectrum for simulation plus background, (b) the invariant mass for simulation only (using a one-tower MC isolation cut), and (c) the ratio of the detected π^0s. Similar ratios are determined for various p_Ts, where the proportion of simulated π^0s should approach 1 at high p_T, which is observed.

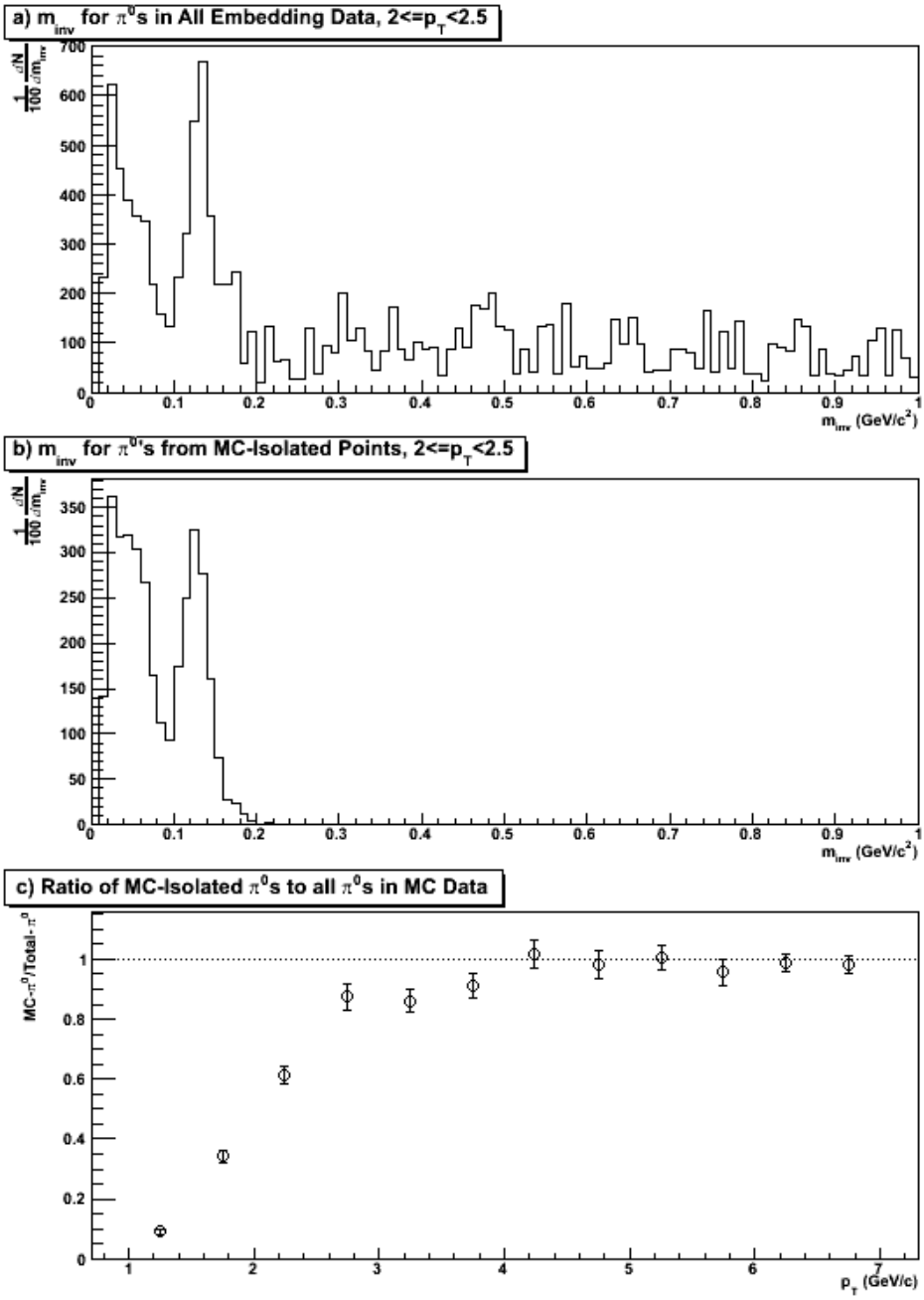

Figure 6.3.1: The effectiveness of the Monte Carlo isolation cut is analyzed. Panel (a) shows an invariant mass histogram for the MC data and its background. Panel (b) shows the effect of imposing the isolation cut. Panel (c) shows that the ratio of MC-Only π^0s to MC-Plus-Background π^0s asymptotically approaches 1, indicating the isolation cut does not remove a significant portion of the simulated π^0s.

Comparison of signal degradation due to background mixing with real particle signals is the second stated use for embedding data. That is, sometimes a second particle will overlap with a π^0 photon and skew its signal. Before trying to deconvolve this issue it is important to understand the goals of such an analysis. This sort of contamination can only serve to modify the energy and position of real data points. In the case where the contaminating particle can be identified by means outside of the BEMC, we already cut the data, and the effect is discussed shortly. In the other case, the Monte Carlo analysis would be straightforward, as we would know the before and after energy depositions in the BEMC. However, in the real data, we do not have a useful way to pick candidate BEMC points that were created by multiple particle hits. We do know, from combinatoric analysis of charged particles, discussed below, that no more than 15% of all π^0s will have a photon with additional neutral energy. The clustering algorithm will remove most of this contamination. The remaining contamination will most likely increase the detected energy if the clustering algorithm cannot remove it. Here two effects improve the situation. The first is that it is very rare to have additional neutral energies above a few GeV in an event, so π^0s above 4 GeV are not likely to have significant contamination. Second, when the energy is skewed, the reconstructed mass is also skewed. Our invariant mass analysis earlier in this chapter shows that below 4 GeV the invariant mass is inflated by about 5%. Taking this relatively small error in conjunction with the fact that the π^0 mass increases with p_T, it is safe to assume that inflated mass is not due to contamination from additional neutral energy. Thus, given the scale uncertainty in the energy measurements already present, analysis of combinatoric interactions with neutral background energy is not necessary.

Combinatoric interplay between π^0s and background data do play an important role. Above we argued that they do not significantly degrade the photon signals. They do, however, lead to vetoed photons. That is, the charged-particle veto cut must be verified to meet the same degree of impact in the simulation and the real data. The degree to which it does match, and the amount of data that is cut, gives an estimate for correcting the yields due to the cut, and an estimate for the expected neutral particle contamination, respectively.

There is no obvious reason to assume that embedding into Minimum Bias data will provide the same combinatoric relationships seen in various π^0 p_T bins. A detailed analysis across collision models, matching the energy profiles so that the correlation of background in simulated events matched the background in real events could be used. Such a method would create our entire spectrum of π^0s, but it would introduce model dependencies. Alternately, a general analysis will pick up an overall uncertainty in-lieu of model dependencies. We will take the later approach and show that the overall uncertainty is negligible compared to the uncertainties in the yield and efficiency analyses (the efficiencies are discussed later, but the overall effect is that all p_T bins carry systematic uncertainty greater than 10%).

The impact of background combinatorics in the Monte Carlo data was analyzed by studying the charged-particle veto cut. The ratios of π^0s found with and without this cut were taken for the Monte Carlo data, and the real data. Figure 6.3.2 shows the ratio of detected π^0s before and after the TPC veto cut, for real data and Monte Carlo data. The statistical error in the Monte Carlo results is approximated by the scatter of the points above 2 GeV/c. It can be seen that the real data dependence on this cut is consistent with that seen in simulation.

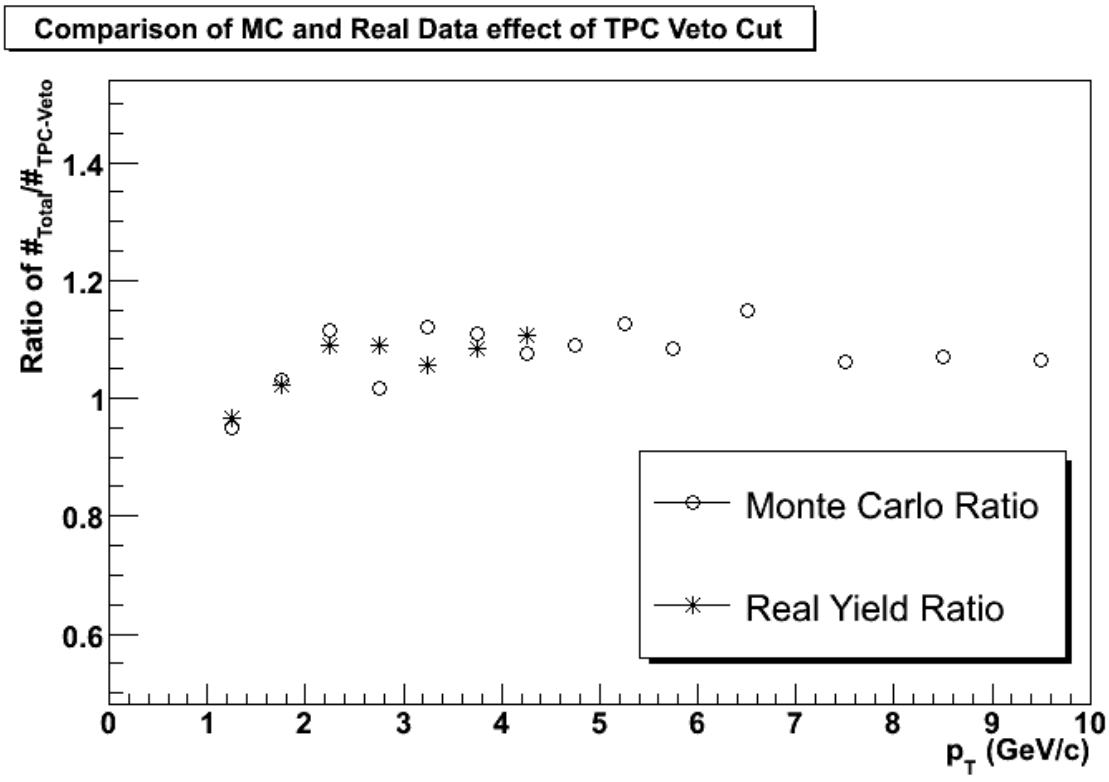

Figure 6.3.2: The effect of the charged-particle veto cut is shown for the embedding and the real data. The real data is only shown for minimum bias events where the statistical error bars allow meaningful interpretation. The Monte Carlo results have statistical errors on the order of the fluctuation in the ratio above 2 GeV/c. This figure shows that the correlation in the embedding does a good job of approximating the correlation in the real data. The systematic uncertainty in the match is taken to be less than 2%.

The analysis of the charged particle veto cut showed that 8% of π^0s could be expected to be randomly correlated with a charged particle, for both the embedding, and the real data. Any discrepancy between the two data sets would be an argument for correlated background. Although there is likely correlated background in real data, this study shows that correlated background cannot contribute more than 2% of the signal. Such an effect can be ignored compared to the other systematic effects.

Neutral energy correlations are expected to be of approximately the same order as the charged particle correlations. Thus, the effects of correlated background

interfering with the signal are suppressed to less than 2% of the total yield, and of that 2%, only a small fraction will be damaged due to the unmeasured impact of additional neutral energy of sufficient magnitude. The remaining 8% of the neutral energy correlation is accurately handled by the detector simulation.

To clarify the discussion, BEMC points are expected to be contaminated with close depositions of additional correlated and uncorrelated neutral energy. The approximate rates, based on charged particle correlations with the π^0 signal, are 1% and 4% for individual photons, respectively (individual photons are affected roughly half as much as π^0s). The uncorrelated 4% is expected to be handled correctly by the detector simulation, but will not skew energies more than the existing scale uncertainty of 5%. However, the 1% correlated points cannot be studied with the flat-p_T dataset used. If a realistic p_T spectrum was used, this 1% still could not be studied due to the limited statistics of the background data and dependence on models used to produce the correlation. Even still, of this 1% suspected of contamination due to additional neutral energy, most will be isolated by the SMD and have the energy split amongst multiple points. This sort of energy splitting is already responsible for fixing the 4% of π^0s with uncorrelated neutral energy contamination, and is simulated.

6.3.5 Embedding Quality

The most direct use of the embedding data is to determine the accuracy of the detector response in the simulation. The degree to which this can benefit us depends greatly on the set of variables that can be compared. For embedding comparison we consider the types of distributions that can be formed in the simulation and in the real data.

Simulated π^0s provide us with reconstructed BEMC points, and reconstructed π^0s, so the set of comparable parameters comes from these. From the points, we can examine the η and ϕ distribution of points. From the π^0s, we can compare the energy asymmetry of the decay photons, the η and ϕ of the reconstructed pair, and the quality parameters of the invariant mass histogram – the width and position of the mass peak.

Comparing the simulated photons with those from the real data in the embedding runs is now discussed. For dataset #1, the η and ϕ distributions of the simulated and real BEMC points can be seen in Figure 6.3.3. In (c) and (f) the ratio of simulated points to real points is shown. Both of these should be constant within statistics. One can see that there are a lot of places in the ϕ-distribution where the ratio is certainly not constant. However, the underlying ratio does appear to be fairly constant. This is not quite the case with the η-distribution, where there are no major differences, but the background has a shape at higher η that is not duplicated in the simulation very well.

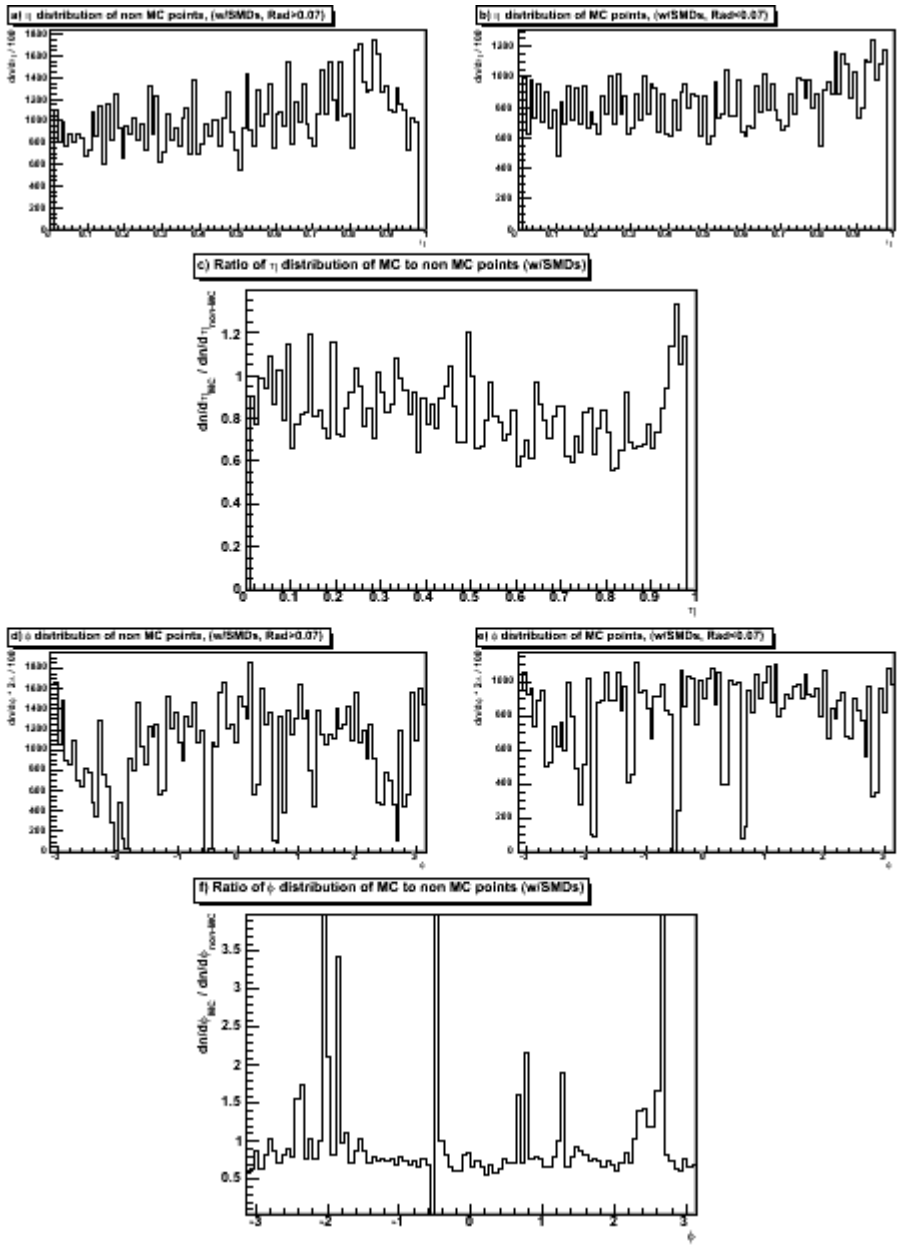

Figure 6.3.3: The embedding data and their respective background runs are compared for η and ϕ dependencies. Panels (a)-(c) are for η while (d)-(f) are for ϕ. Each set of three panels shows: (a) the real data; (b) the embedding data; and (c) the ratio of the embedding to the real data. This pattern repeats in (d), (e), (f), for ϕ. The η-plots show that there is a discrepancy at large η, which is not a major concern. However, the differences in ϕ are more troublesome. The ϕ problems are mostly handled by masking part of the detector. The remaining problems are indicative of systematic uncertainty in the acceptance, which is below 4% once time-dependencies are factored in.

Because of the early state of the BEMC (before day 40), the background data in the embedding is of even less direct use, since much of it was embedded into these earlier runs. However, the data simulated and then embedded into these runs is not bad, only the background signals from the real data in these runs are of limited use. This is true because the simulation is based on the configuration tables of the BEMC. Those tables do not necessarily reflect the actual state of the BEMC, particularly in the early runs. To highlight this point, we analyzed the data in Figure 6.3.3 by separating the data into the two runs in dataset #1. The results are Figure 6.3.4 and Figure 6.3.5, for runs 4036043 and 4049021, respectively. As one can see, there is a large discrepancy in the large ϕ portion of run 4049021 (seen in the lowest plot). This was supposed to be the "good" run. From this it is clear that the embedding data must be compared to the runs where the real π^0 signals are measured, and not to the background run into which the embedding was done.

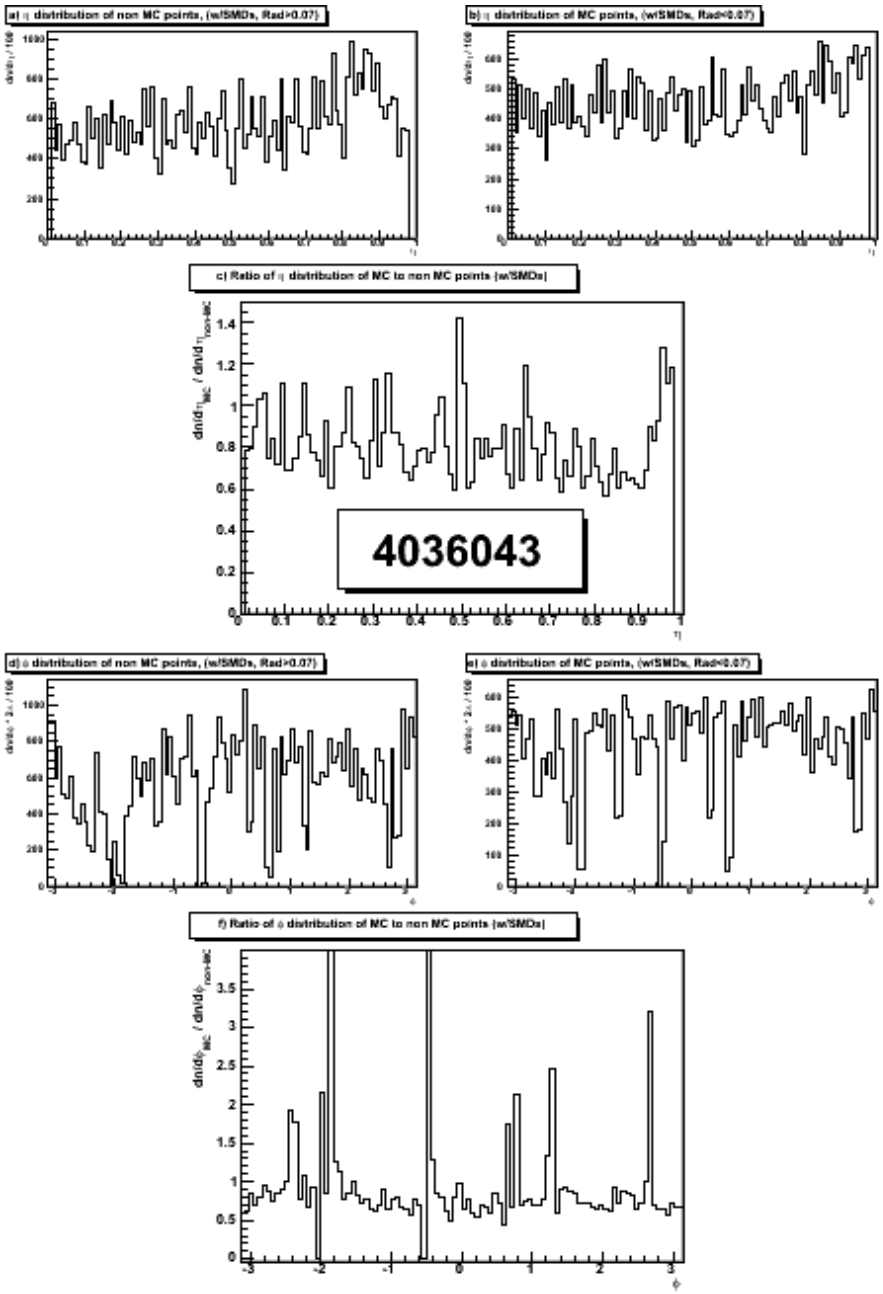

Figure 6.3.4: Same as Figure 6.3.3, but only for embedding data from run 4036043 (similar plots are shown in Figure 6.3.5 for run 4049021). This, and the next figure, show that η and ϕ discrepancies in the embedding do not correlate with the background data from their respective runs. This is of only minor impact because the background data correlations do not provide realistic correlations with the simulation data. Also, this matching is unimportant because the matching of the detector response shown here must be matched to the analysis runs rather than the simulation runs.

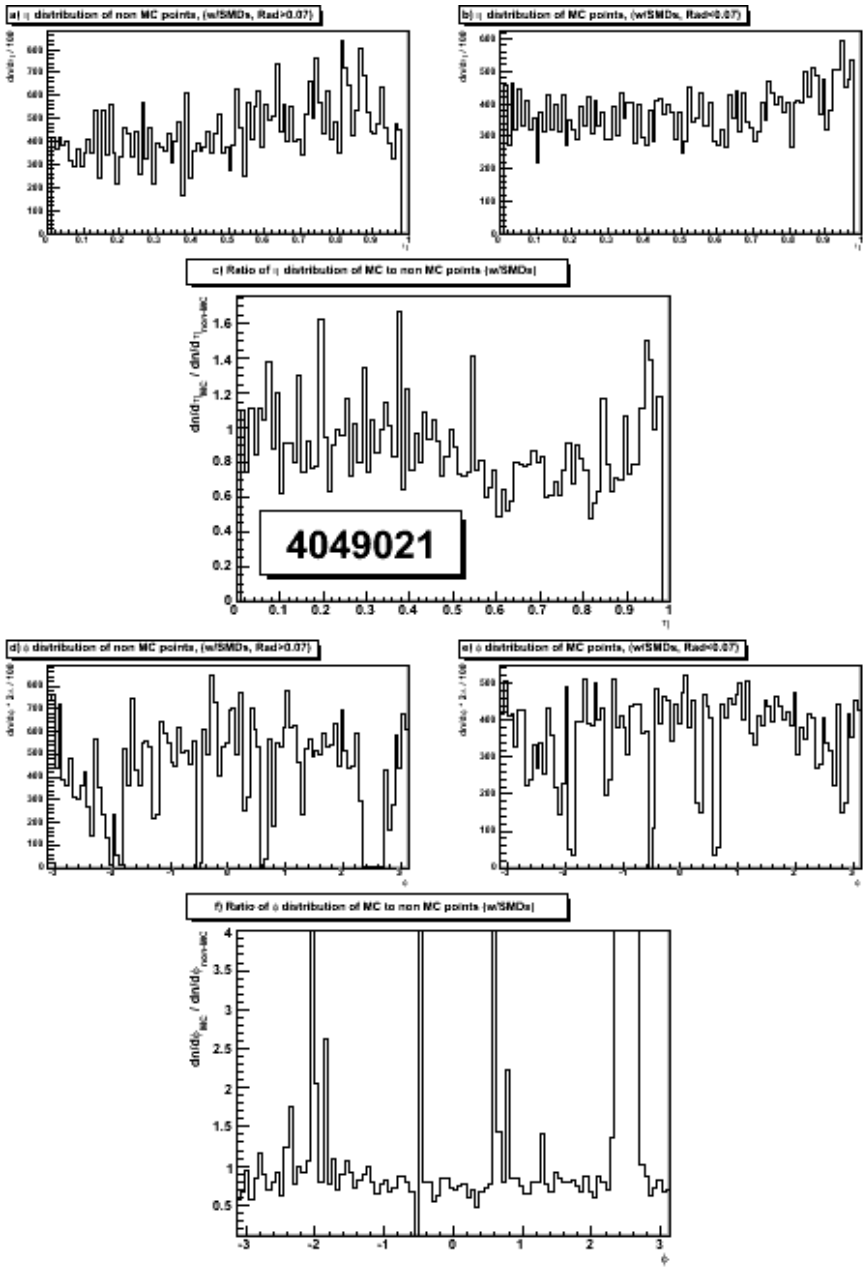

Figure 6.3.5: Same as Figure 6.3-3, except this figure is limited to embedding data from run 4049021. Run 4049021 is accepted on our good run list. The overall behavior mimics what is seen in Figure 6.3-4 for run 4036043, indicating some general disagreement with background. However, it is clear that there is a section of ϕ where the background data is simply missing. This gives a general example of about 4% of the data, over time, that disagrees with the data acceptance used in the analysis. The smaller spikes showing up in both runs are indicative of problems spanning the entire data-taking period. Those sections of the detector were usually masked from the analysis.

The photon candidate pairs allow us to compare the distributions of embedding and real pair parameters. Figure 6.3.6 shows the η-distribution of real and embedding pairs, while Figure 6.3.7 shows the ϕ-distribution. The real data was taken using pairs whose invariant mass is between 80 and 220 MeV/c^2, with $3.0 < p_T < 3.5$. These cuts improve the signal to noise in the real data, but do not remove it completely. Except for the large spike in the real data at ϕ~-3, the distributions are reasonable, once the size of the background is taken into account.

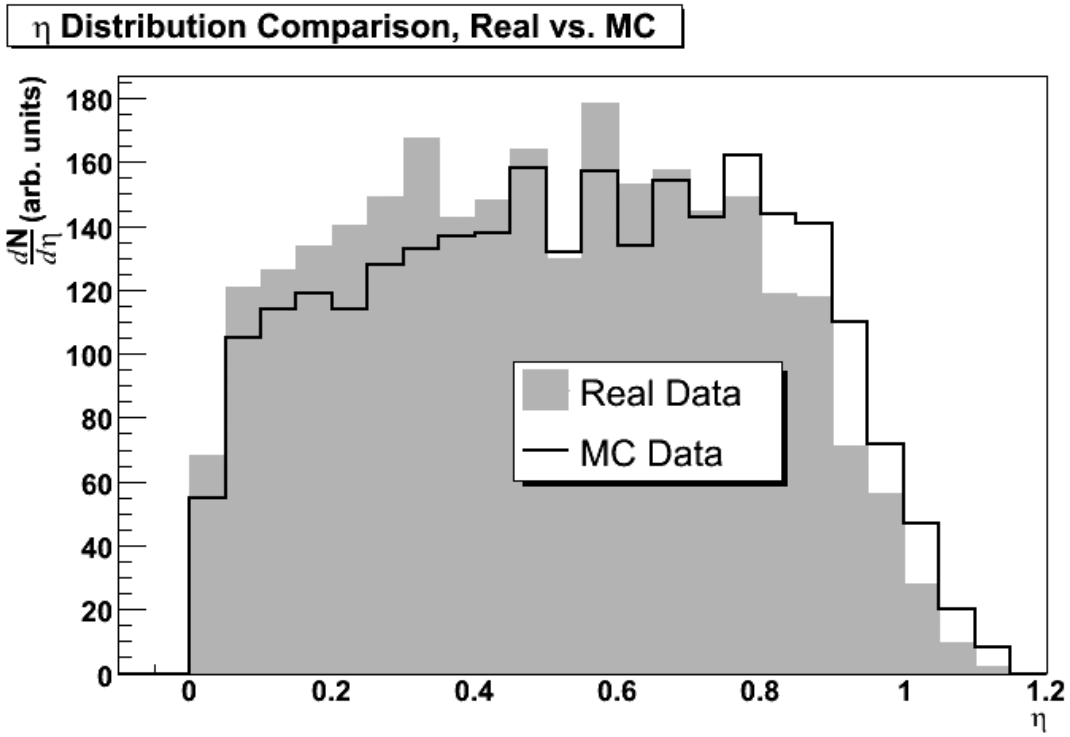

Figure 6.3.6: The η-distributions of the real and embedding pairs is shown. The real data is slightly skewed towards lower η's, but there are no gross differences between the distributions. These histograms are scaled to have the same number of counts.

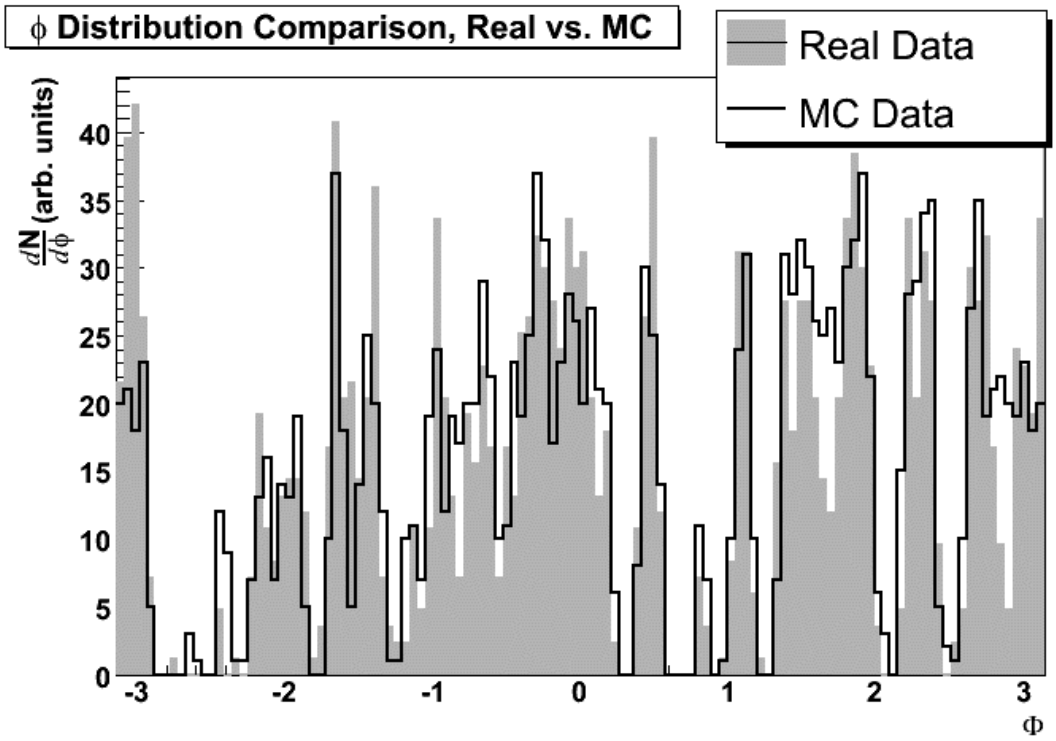

Figure 6.3.7: The ϕ-distributions of real and embedding pairs are shown. There is generally good agreement, but some of the behavior is different. In particular, there is a spike in the real data around ϕ~-3. Also, there are dips in the real data that do not show in the embedding. These effects are due to changes in the acceptance with time, and mostly cancel in collection of yields. However, a 4% systematic uncertainty due to the acceptance is included in the overall real to embedding data matching. These histograms are scaled to have the same number of counts.

The energy asymmetry of the embedded π^0s should be tested against those that we find in the real data. In the analysis section we discussed the energy asymmetry dependence of the real particles. The salient points were that the natural distribution includes a flat distribution of the e_{asym} distribution of π^0s in nature, and a convolution with decreasing detection efficiency at high e_{asym} which leads to a fall off as the asymmetry goes to 1. Figure 6.3.8 shows the distributions of energy asymmetry for the real data and embedding data.

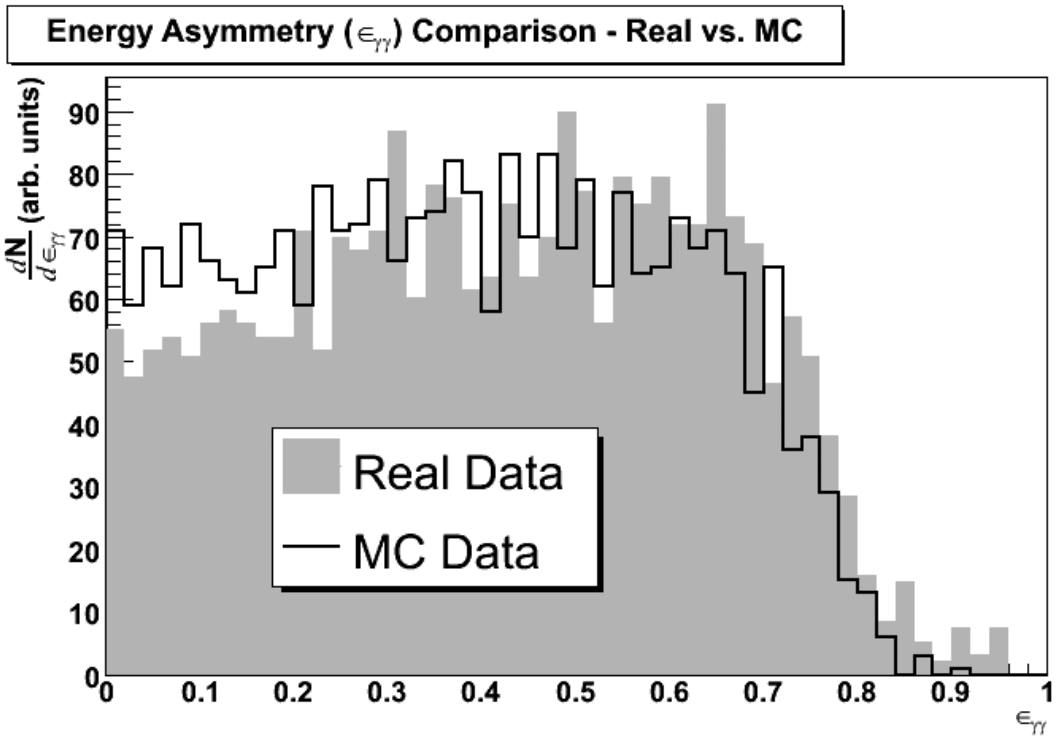

Figure 6.3.8: The energy asymmetry of real and embedding pairs are compared. The pairs are required to have minv between 80 and 220 MeV, and p_T between 3 and 3.5 GeV. The histograms are scaled to have the same number of counts. The real data has background pairs that are biased towards high energy asymmetry thus leading to a rise before reaching the cutoff around 0.8. The total background is about 25% of the total real signal.

The remaining items that can be tested are the dependencies of the Guassian fit parameters with p_T. That is, when the invariant mass spectra are fit, the mass position and width are determined for the π^0-peak. These parameters differ between the embedding and real data. Figure 6.3.9 shows comparison plots of these reconstructed masses and widths. The observed differences seem to suggest an energy-scale problem as well as a general mismatch in the energy uncertainty. The energy scale is set by processes that are well controlled, thus we are forced to consider other sources. In actuality, both of the problems can be explained by one general claim. The detector model is more precise than the actual detector. The general precision of the

model affects the width of the mass peak in the simulation, and it also affects the minimum opening angle in η and ϕ, as well as the overall minimum opening angle where both η and ϕ angles are at their respective minimums. In the simulation, the average spatial resolution due to increased precision compared to the real system is improved, so the minimum opening angle is smaller, which allows the construction of a smaller mass since $m \sim p\theta$. This dependency is what pushes the mass up in the simulations above 6 GeV/c. In the real data, the dependency affects data at lower momentum, turning on at about 2 GeV/c.

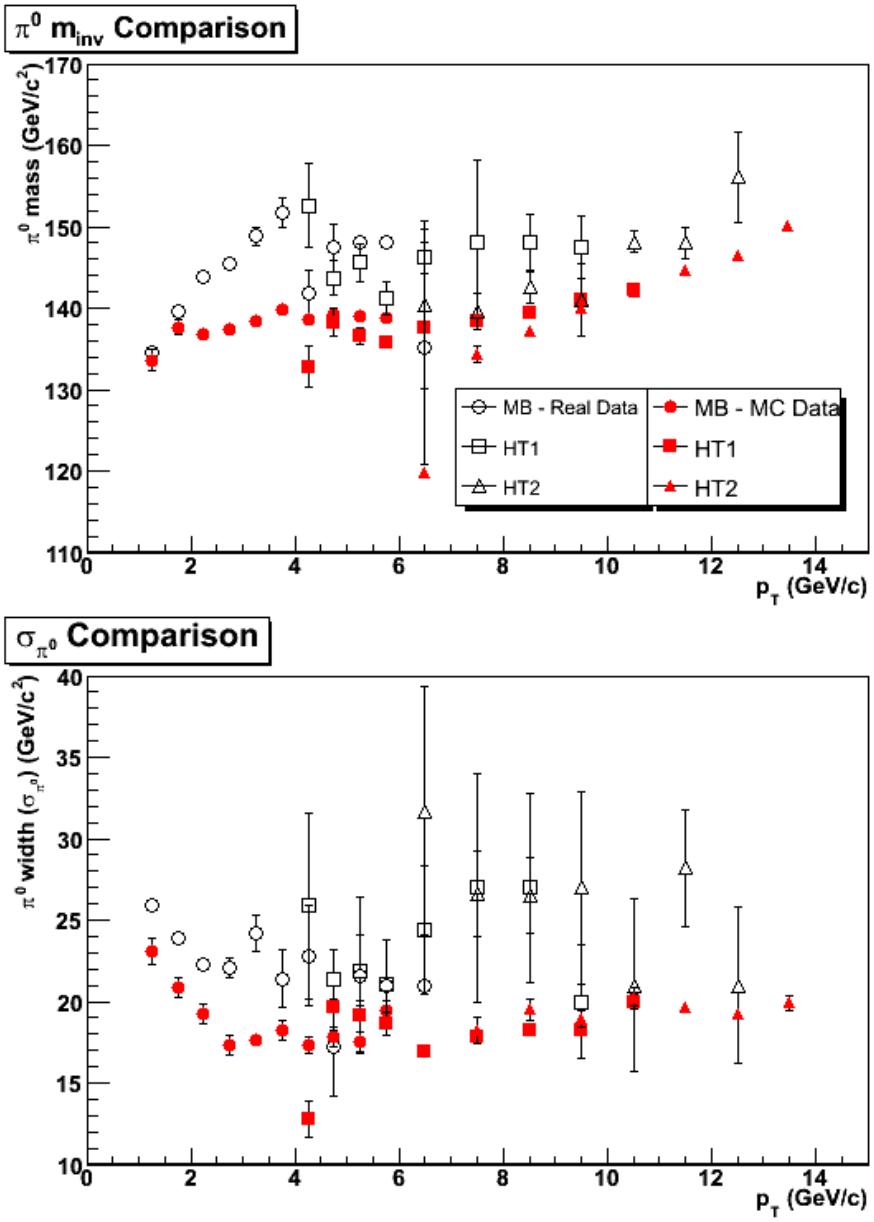

Figure 6.3.9: The dependences of the mass position and width, as a function of p_T, are presented for the real and embedding datasets. The upper panel shows the position of the invariant mass while the lower panel shows the width of the distribution. After the initial turn-on of a trigger, the general trend is for the mass to increase. Agreement in some bins is evidence that the overall energy scale is correct. The divergence of the real constructed mass is most likely due to addition of background energy that is combinatorically accurate, but not energy-scale accurate in the embedding. The width plot shows that the energy spread is too ideal in the simulation, however, the overall agreement is very good.

6.3.6 Handling of Embedding Issues

This portion of the section is a recap of the issues we have to contend with, and how they will be handled during actual analysis. These issues were all presented above, but how they are handled was not necessarily discussed. We will briefly present each issue topic and how it is handled.

The first issue to discuss is the handling of the exotic triggers. That is, the method used to handle the high-tower triggers. The real high tower triggers either were or were not caused by the π^0s that we are studying. In the embedding analysis, the only high tower triggers we can get are those that are caused by the π^0s themselves (via decay photons). Hence the easiest way to deal with this is to require that in the real data we only analyze high tower events that were triggered by the candidate π^0. This will not provide the inclusive yield, so it cannot be used. Instead, in the real data, all π^0s that generate a photon above a threshold (3.2 GeV for HT1, 5.2 GeV for HT2) will be included in the analysis. Since gains are not identical, this threshold does not provide a flat trigger requirement across the entire detector. For this reason, the actual trigger requirement (ADC >= 288 or 416 for HT1 or HT2) and the energy threshold requirement will both be used on the embedding data to determine the maximum uncertainty due to the method.

The datasets themselves are the source of the second problem that must be handled. In particular, the p_T-distribution of the simulated π^0s does not match the real production distribution. The simulation was created with a flat p_T spectrum, which cannot properly simulate the "feed up" or "feed down" of π^0s that were created in different p_T bins than where they were observed. In particular, the production

distribution is steeply falling, so that there are far more candidate π^0s that may be feed up to higher p_T bins than there are high-p_T π^0s that feed down to lower p_T even though the latter case is more probable per π^0. In order to handle this we need to simulate the production distribution during the analysis. This is a "chicken and egg" problem because we need to know the production distribution in order to do the simulation correctly so that we can determine the correct production distribution. Luckily, the only thing we really need to know is the shape of the distribution, not the overall normalization. The shape for π^0 production in *d*+*Au* is similar to that in *p*+*p*. In fact, differences in the two are of theoretical importance (see chapter 2). Thus, we can safely assume the shape is similar to that of the *p*+*p* distribution. The overall normalization divides out so it is set arbitrarily.

We can then analyze the simulated data by weighting the invariant mass histogram entries by the *p*+*p* yield at the p_T of the simulated π^0. Then, when we have gone through the entire analysis and generated the *d*+*Au* production distribution, we can use it, if it is very different from the original simulation distribution, to generate a new embedding analysis. The difference, when compared to the first embedding result would then be the systematic error we will assign to this issue.

The weighting function used was $w(p_T) = p_T / (1.95 + p_T)^{11.341}$ which is a standard power-law type weighting function for $d^2N/dp_T d\eta$.

Similar to the p_T-distribution is the *z*-distribution. For the embedding, only a small number of runs were used, and these runs primarily collected minimum bias data. They are, however, also are used to simulate the high-tower triggers as well as minimum bias. As a function of time, the distribution of the *z*-vertex for events changed. Also, for the high-tower triggers, events whose vertex position effectively

increases the energy signals in the BEMC are more likely, thereby skewing the recorded event vertex distribution for high-tower events. The differences between embedding and real distributions, although small, were taken into account. Figure 6.3.10 shows the overall scaling factor applied to each event, as a function of its vertex-*z* and trigger. It should be noted that the difference in the resulting efficiencies were below 4%, and therefore within the systematic uncertainty of the measurements.

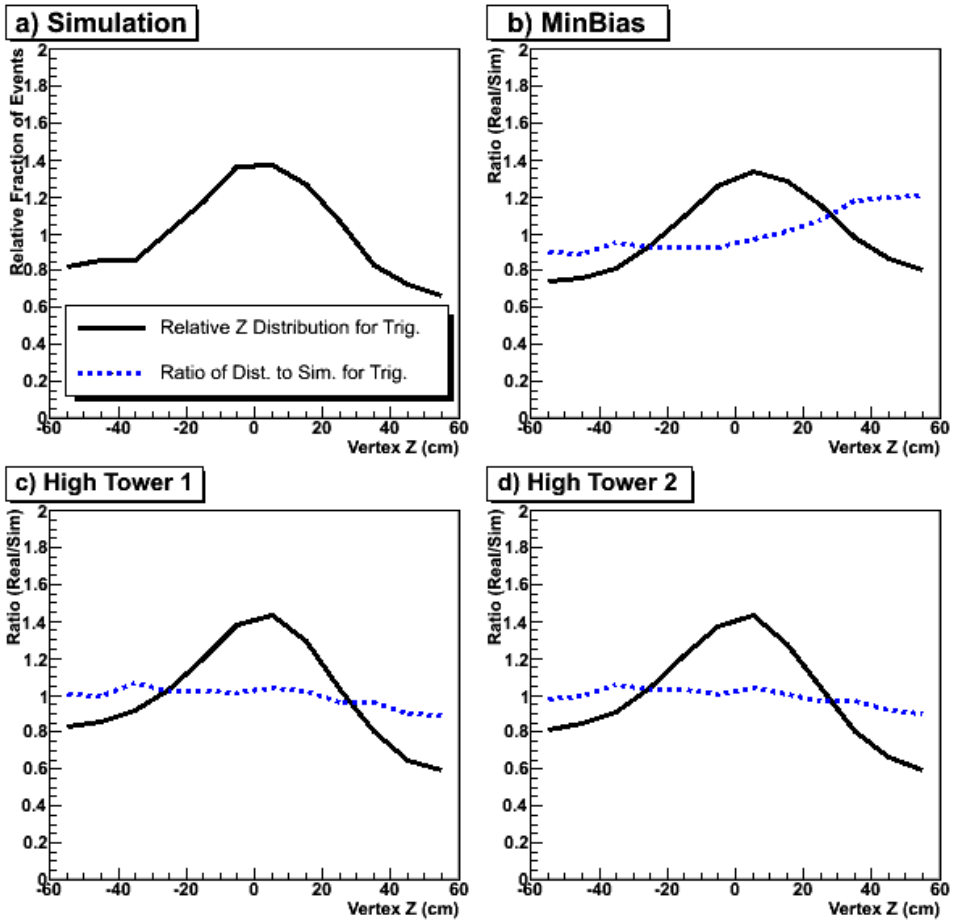

Figure 6.3.10: The distribution of the vertex-*z* for the various trigger sets is shown. The black lines show the real vertex distribution, scaled so that a value of 1 would be consistent with a flat distribution. The dashed blue lines are the ratio of real to embedding, and are the values used to scale the embedding data based on the vertex Z of the embedding event. Panel (a) shows distribution for embedding data. Panels (b), (c), and (d), show the distribution and correction factors for minimum bias, high-tower 1, and high-tower 2, respectively.

Simulated signals interacting with background were verified to be of approximately the same combinatoric significance in the real data and the embedding. Beyond combinatorics, they are of minimal use due to unrealistic energy and spatial distribution. We ruled out the use of looking for π^0 signals created by combinatoric effects between the simulated decay photons and the background events. The only bins where this might make a difference were p_Ts below 3 GeV/c, as suggested in Figure 6.3.1. The results above 3 GeV/c suggest that no significant contamination of the π^0 peak is coming from random combinatorics, and the background structure below 3 GeV/c is cleaner than that above, so we conclude combinatoric effects do not produce π^0 signals.

The remaining issues with the embedding data involve matching the simulated distributions with the real data. The η and ϕ distributions of BEMC points were shown to be in reasonably good agreement between the real and simulated data, especially when pairs were considered. The differences are due to a compromise between several different issues.

The primary source of disagreement between the real data and the simulation is that the detector acceptance changes over time. Some sections of the detector were very unreliable, and were removed from the analysis. Others, however, were perhaps 80% reliable, and removing them from the data would significantly reduce the total available data. Analysis of the detector configuration over time showed that 7 of the good 45 modules of the detector were providing no data for between 10% and 20% of the runs. Also, some modules became relatively hot, showing excess counts per event, for about 5% of the time. The problems with the detector that were not random with time, and were not in random portions of the detector, were generally cut. In

some instances, however, the threshold for such exclusion allowed marginal data to pass through.

The various resulting detector configurations could not reliably be analyzed separately since many of the p_T-bins in the analysis have limited statistics and cannot be tallied in smaller time bins. The overall result, then, is that 20% of the acceptance is questionable about 20% of the time. This general result includes the 5% of the data that has a large portion of the detector near, but below, the threshold for exclusion. This is a systematic uncertainty that adds 2% to the measured cross section, with a 2% above and below systematic uncertainty band.

One other disagreement between the embedding and real data is in the turn-on behavior of the various triggers. It is intrinsic to the nature of trigger turn-on that sizable uncertainty is present if the event rate varies considerably as a function of the turn-on energy, which is the case here. The course of estimating and containing these effects are two-fold. First, the real data is analyzed in two ways, one accepting all events where a π^0 is reconstructed with a photon above threshold, the other way requires that the π^0 be the actual triggering particle. The former gives the best estimate of the production distribution while the latter gives the most conservative case for how low the production can be. The second stage of handling the turn-on is to verify, based on the results, that at least one dataset provides constraints on the production with uncertainty consistent with the overall measurement. Since, as will be seen, the second stage is met, there is minimal benefit to be gained by increasing the accuracy of the simulated turn-on effects.

The final point that can be addressed regarding the embedding data is the extent to which the energy asymmetry, mass, and width of the reconstructed π^0s match

between real and simulated particles. These questions directly lead to uncertainty in the final result. The energy asymmetry is handled by observing that it is indeed flat within the chosen cut of $e_{asym} < 0.5$, once allowance is made for noise under the mass peak. The reconstructed mass and width are only approximately matched, and will incur a systematic error. The primary factor in this error is the mass, since the width error is not expected to impact the counting of π^0s. For the mass, however, some bins do have reasonable reconstructed mass, which strengthens the argument that the increased mass has to do with energy-dependent effects in the background. The energy scale of the BEMC is set by the electron calibration (see chapter 4), and is not in question above a percent or so. The additional energy contributed by combinatorics is only expected to affect 10% of the π^0s and then only by a few percent, leading to an overall energy difference of 1-2%. The other possible cause of the shifting mass peak is the opening angle dependence. The difference between measured width and simulated width suggests that the simulation takes the detector to be too ideal. If this is the case, it is likely that the minimum angular separation is smaller in the simulation than in the real data. The mass dependence on p_T is expected to be linear with this opening angle cutoff (since, in the small angle approximation, $m^2 = E_1 E_2 \theta^2$.

The differences between the real and embedding data distributions, from most sources, are not expected to contribute more than 2% to the systematic uncertainty. There are a handful of such sources, so for any given bin these minor effects may contribute as much as 5% total systematic uncertainty. The major source of uncertainty in the embedding analysis is the trigger turn-on region. This effect will

be tallied for each bin, and will be seen to dominate all bins where the existing systematic uncertainty is below 10%.

6.3.7 Embedding Analysis

The previous section laid the groundwork for the analysis of the embedding data. The first part of the analysis here is to provide basic measurements of the embedding data, and where necessary, compare those to real distributions from the yield analysis. We will then provide a detailed examination of the expected p_T distribution and provide the relevant weighting function that we will use. Following that part, the two major measurements in the embedding data will be made for the various triggers, these will use slightly different methods of triggering to prove an estimate of the systematic uncertainty in the trigger turn-on. Finally the last section of the embedding analysis will present the resulting efficiencies, with a complete description of their region of applicability.

6.3.7.1 Basic Measurements

The particle yields observed in the embedding are normalized to the number of particles simulated. For this work, the primary embedding efficiencies were calculated using dataset #2 described in 6.3.3 above. There it was stated that 1.34×10^6 simulated π^0s were analyzed with p_T flat between 0 and 25 GeV/c, and covering $-0.3 < \eta < 1.2$. The simulated π^0s were generated uniformly across all azimuthal angles. We begin by identifying exactly how many simulated π^0s are in each bin. These totals can be found in Table 6.3.2.

Table 6.3.2: Tally of the simulated π^0s in the analysis p_T-bins.

p_T Bin range (GeV/c)	Simulated π^0s; N	$\delta N/N$
1.0-1.5	17727	0.75
1.5-2.0	17879	0.75
2.0-2.5	17782	0.75
2.5-3.0	17685	0.75
3.0-3.5	17869	0.75
3.5-4.0	17699	0.75
4.0-4.5	17735	0.75
4.5-5.0	17801	0.75
5.0-5.5	17743	0.75
5.5-6.0	17719	0.75
6.0-7.0	35723	0.53
7.0-8.0	35777	0.53
8.0-9.0	35331	0.53
10.0-11.0	35627	0.53
11.0-12.0	35339	0.53
12.0-13.0	35737	0.53
13.0-14.0	35675	0.53
14.0-15.0	35780	0.53
15.0-16.0	35543	0.53
16.0-17.0	35720	0.53
17.0-18.0	35887	0.53
18.0-19.0	35524	0.53
19.0-20.0	36338	0.53

6.3.7.2 *Z* Distribution

Earlier in this chapter we discussed the differences between the *z* vertex distributions in the real data sets and embedding. Specifically we showed that each trigger corresponds to a slightly different *z* vertex distribution than that shown in the embedding data. The differences are less than 20% in all bins, and less than 10% in more than 60% of the bins.

Instead of verifying that these differences are insignificant (lead to systematic uncertainties below 2%), the difference in the vertex position is handled by weighting events based on their *z* vertex. This weighting exactly corresponds to the ratios

shown in Figure 6.3.10. The results of this weighting are included in the p_T results in the following discussion.

6.3.7.3 p_T Distribution

Here we discuss the production p_T distribution, and how it is simulated during the embedding analysis. This is necessary because the π^0s were simulated for analysis with a flat p_T spectrum. The flat simulation was necessary in order to simulate a reasonable number of high-p_T π^0s, which are suppressed by many orders of magnitude relative to their low-p_T cousins.

The π^0 production distribution for *d+Au* collisions is expected to be the same as the production of charged hadrons in *d+Au*. Figure 6.3.11 shows the STAR charged-hadron spectrum presented with the fit function $w(p_T) = (1.95 + p_T)^{-11.341}$ as a function of p_T. The ratio of the data to the fit is shown in the lower panel. This form for the fit function is essentially the same as that shown in Chapter 3 (Equation 3.2). Although the fit looks reasonable, this is still a log scale. Fortunately, this curve does not need to be an exact match because the only thing that matters is the relative shape. The shape provides the feed up and feed down contributions due to incorrectly reconstructed π^0s. The absolute scale will be divided out.

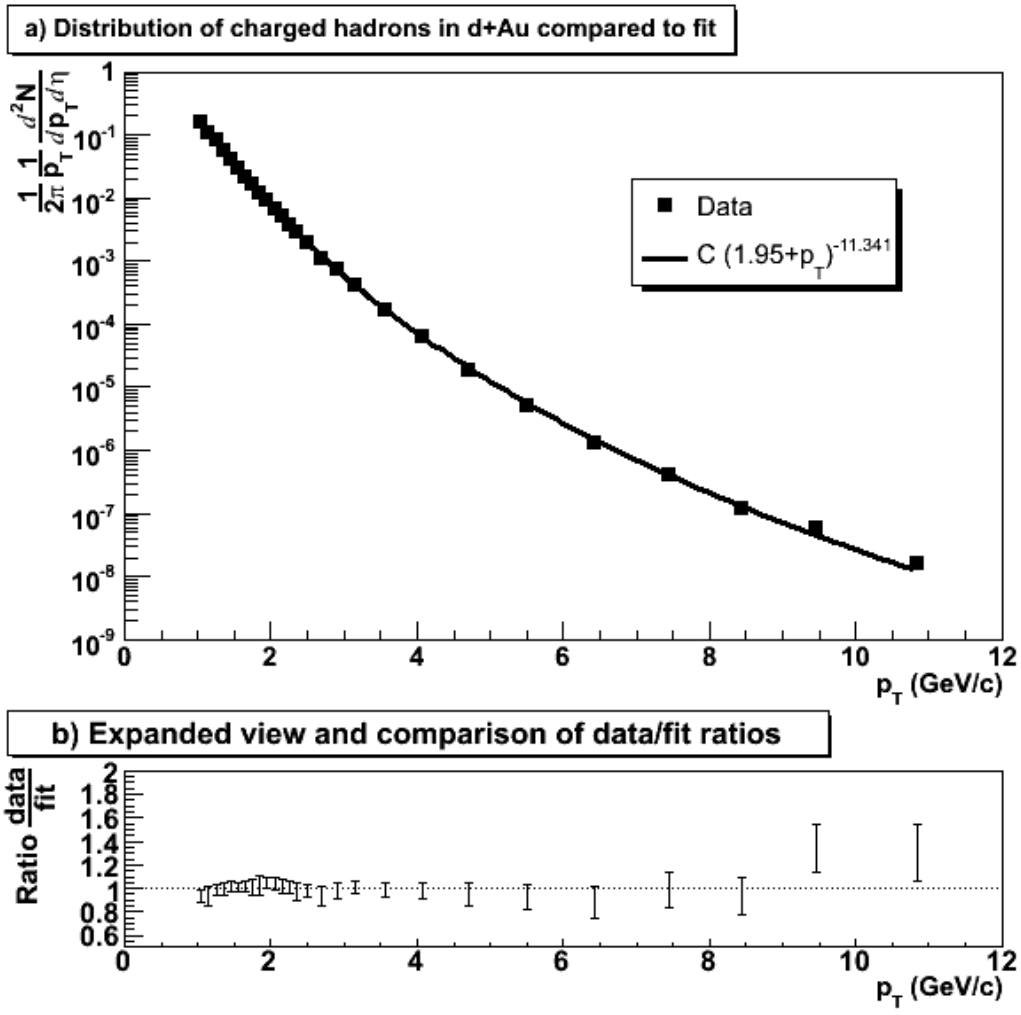

Figure 6.3.11: The expected p_T distribution is determined by fitting the form $w(p_T) = C(p_0 + p_T)^n$ to the charged hadron spectrum from *d+Au* collisions. Panel (a) shows the charged hadron spectrum for *d+Au* measured at STAR in minimum bias collisions [Ada03], together with the fit results. Note that the error bars are smaller than the data points in panel (a). Panel (b) shows the ratio of the data to the fit function from panel (a) to illustrate the agreement more clearly.

This is, nevertheless, a source of systematic uncertainty. The systematic uncertainty can be examined by observing the results of using a different function. An earlier form chosen for the p_T weighting was $w(p_T) = \exp(-2p_T)$. Using this function we obtained a second set of efficiencies, which will be compared to the

results with the better weighting. The results of both types of weighting will be discussed in the yield and efficiency results sections that follow. Except where clarity is necessary, this discussion will not show figures for the alternate weighting, because the reader should be drawn to the more accurate weighting results. The tabular results, however, will be presented for both sets.

In order to determine the efficiency, we used the straightforward method of weighting the simulated and detected particles separately. That is, the simulated particles in a given p_T bin are weighted by the z and p_T dependencies to get the bin total of simulated particles. Then their decay photons are reconstructed into the parent particles, which are also weighted by the weight of the original simulated particle, but may have different detected parameters. These are collected, and the resulting histogram is fit to obtain the detected total for a given bin. There is no restriction that the reconstructed π^0s actually come from the given bin. The formula for the simulated total of weights in a bin is $\Sigma w_{Bin} = \sum_{\pi^o \in Bin} w_{p^T}(\pi^0) w_Z(\pi^0)$. For each bin, the raw number of π^0s and the resulting Σw_T are given in Table 6.3.3, this is an extension of Table 6.3.2. The statistical error is the error in the number of π^0s normalized to the weight, $\frac{\delta \Sigma w_{Bin}}{\Sigma w_{Bin}} = \frac{\delta N}{N}$.

Table 6.3.3: Tally of the weight of simulated π^0s in the analysis p_T-bins. The separate weights are listed for each trigger type due to the *z*-weighting effects..

p_T Bin range (GeV/c)	Weight of Simulated π^0s, using power law (using exponential)		
	Min Bias	High Tower 1	High Tower 2
1.0-1.5	4.486e-2 (3.663e-2)		
1.5-2.0	1.212e-2 (1.927e-2)		
2.0-2.5	3.624e-3 (9.098e-3)		
2.5-3.0	1.218e-3 (4.085e-3)		
3.0-3.5	4.586e-4 (1.799e-3)		
3.5-4.0	1.836e-4 (7.563e-4)		
4.0-4.5	7.984e-5 (3.158e-4)	7.988e-5 (3.159e-4)	
4.5-5.0	3.702e-5 (1.304e-4)	3.702e-5 (1.304e-4)	
5.0-5.5	1.802e-5 (5.305e-5)	1.802e-5 (5.304e-5)	
5.5-6.0	9.182e-6 (2.138e-5)	9.190e-6 (2.140e-5)	
6.0-7.0	7.609e-6 (1.200e-5)	7.614e-6 (1.201e-5)	7.614e-6 (1.201e-5)
7.0-8.0	2.443e-6 (1.882e-6)	2.442e-6 (1.881e-6)	2.442e-6 (1.882e-6)
8.0-9.0	8.686e-7 (2.873e-7)	8.676e-7 (2.870e-7)	8.676e-7 (2.870e-7)
9.0-10.0	3.437e-7 (4.366e-8)	3.437e-7 (4.368e-8)	3.437e-7 (4.367e-8)
10.0-11.0		1.475e-7 (6.606e-9)	1.475e-7 (6.606e-9)
11.0-12.0		6.604e-8 (9.686e-10)	6.604e-8 (9.686e-10)
12.0-13.0		3.199e-8 (1.432e-10)	3.199e-8 (1.432e-10)
13.0-14.0		1.615e-8 (2.109e-11)	1.625e-8 (2.109e-11)
14.0-15.0		8.622e-9 (3.080e-12)	8.523e-9 (3.080e-12)
15.0-16.0			4.621e-9 (4.413e-13)
16.0-17.0			2.615e-9 (6.410e-14)
17.0-18.0			1.534e-9 (9.212e-15)
18.0-19.0			9.075e-10 (1.305e-15)
19.0-20.0			5.694e-10 (1.913e-16)

6.3.7.4 Yield Results

Two measurements are needed to determine the efficiency of the detector. The first is how many particles were simulated in the detector, which were collected in the last section. The second is the number of particles that were successfully reconstructed during analysis, that is, the number of particles that were detected by the analysis software. The p_T and z weighting used in the last section are reapplied here. Each candidate π^0 pair is reconstructed. Each pair's mass is then tallied and

weighted based on the underlying event's z vertex and simulated π^0s p_T. Here we will present the measurements for each analysis bin, including the secondary measurement for alternate weighting to estimate the systematic uncertainty.

We will use the same analysis bins used in the yield analysis for the real data. This is done because the real and simulated distributions will overlap exactly in a given bin, and the resulting efficiency will be directly applicable to that bin in the real data. That is, for these measurements, it does not matter where the yield is plotted, because it applies to the bin as a whole. Hence we will simply give either the center of the bin, or the bin limits, when presenting the embedding yields and efficiencies. When the efficiencies are applied to the real data, a given bin's point will be plotted at the position where the weighting function is equal to its average over the entire bin.

For the embedding analysis the background π^0s can cause a major problem with the analysis when low-p_T simulation bins are allowed to be analyzed in the higher p_T bins. This happens when background signals, possibly due to noise or real high-p_T π^0s, reconstruct as high-p_T π^0s but occur in an event that has a low-p_T simulated π^0 and therefore gives large weight relative to the simulated π^0s in the same bin. During yield analysis, if we include this event, the associated weight will be very large compared to the standard weighting of the particles that should be reconstructed in the given bin. Thus the invariant mass histogram will have large spikes due to these signals that are many bins removed from their appropriate location. While analyzing a given p_T bin, we include embedding data where the simulated π^0 decay photons match to included BEMC points however, because this is not guaranteed to eliminate background data, some real signals occur and get into the data. These data, however,

will also have large statistical uncertainty due to their source being only one or two candidate pairs.

The resulting datasets were combined into invariant mass histograms for each p_T bin, using the standard analysis regime. This regime will be discussed again in the next part of this section. The invariant mass histograms are shown in Figures 6.3.12(a-c) along with the Gaussian fits used to extract the parameters of the distributions. (a) shows the histograms for the minimum bias while (b) and (c) are for high tower 1 and high tower 2 respectively. These figures are separated by p_T bin, and show the standard analysis bins used in this work. Although included, p_T bins above 15 GeV are not important to this work, thus the poor fits do not impact this work but allow a starting point for future work. The minimum bias data is limited to p_Ts below about 6 GeV/c, but the yields are collected above this range for comparison to the other triggers, similarly, the high tower 1 data is collected above 11 GeV.

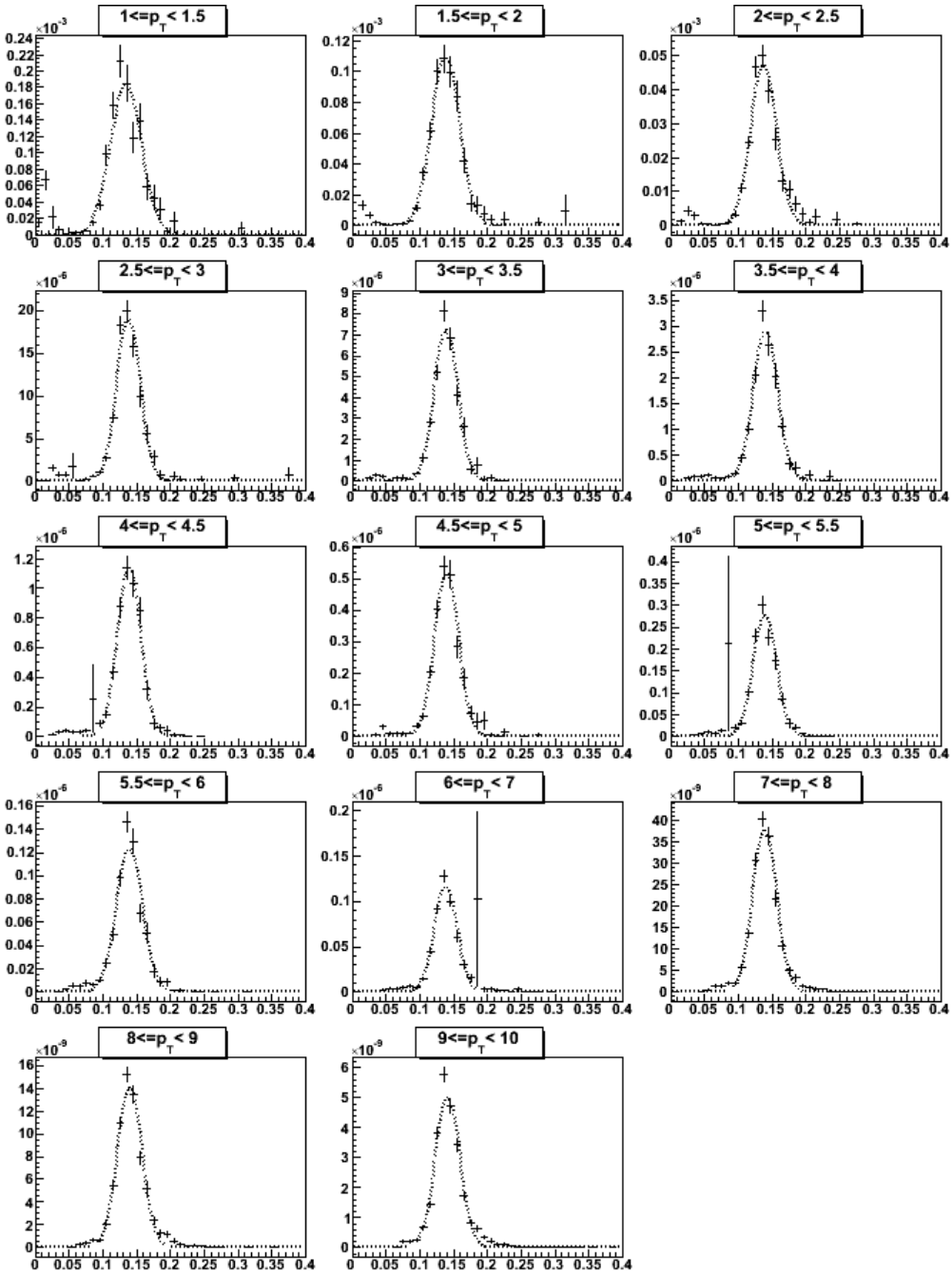

Figure 6.3.12a: The invariant mass histograms for simulated MinBias data are presented with the results of fitting a Gaussian distribution to each. Standard analysis bins from 1 GeV to 10 GeV are presented. See text and tables for detailed fit parameter results and a discussion of weighting functions used.

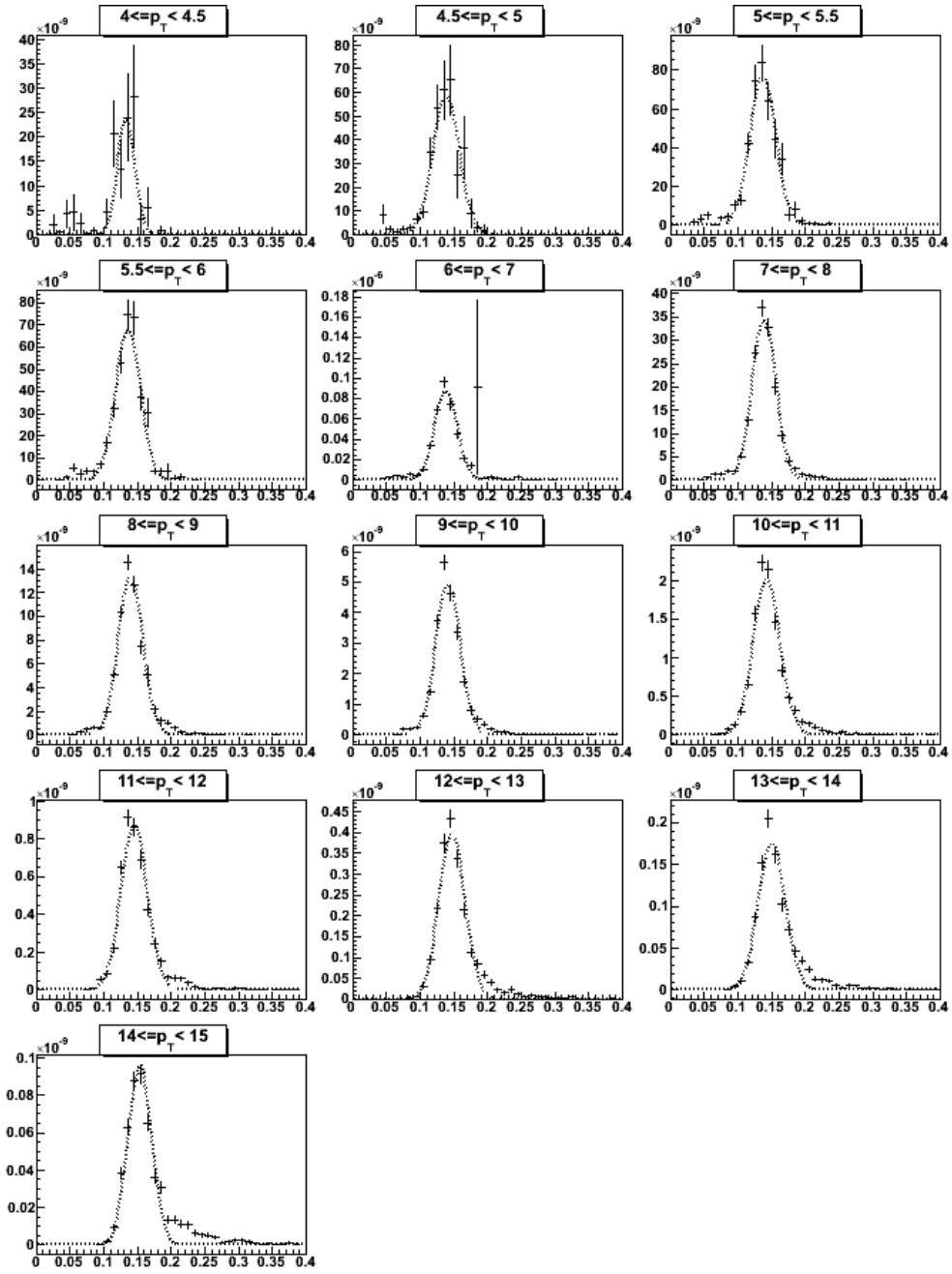

Figure 6.3.12b: The invariant mass histograms for simulated high tower 1 data are presented with the results of fitting a Gaussian distribution to each. Standard analysis bins from 4 GeV to 15 GeV are presented. See text and tables for detailed fit parameter results and discussion of weighting functions used.

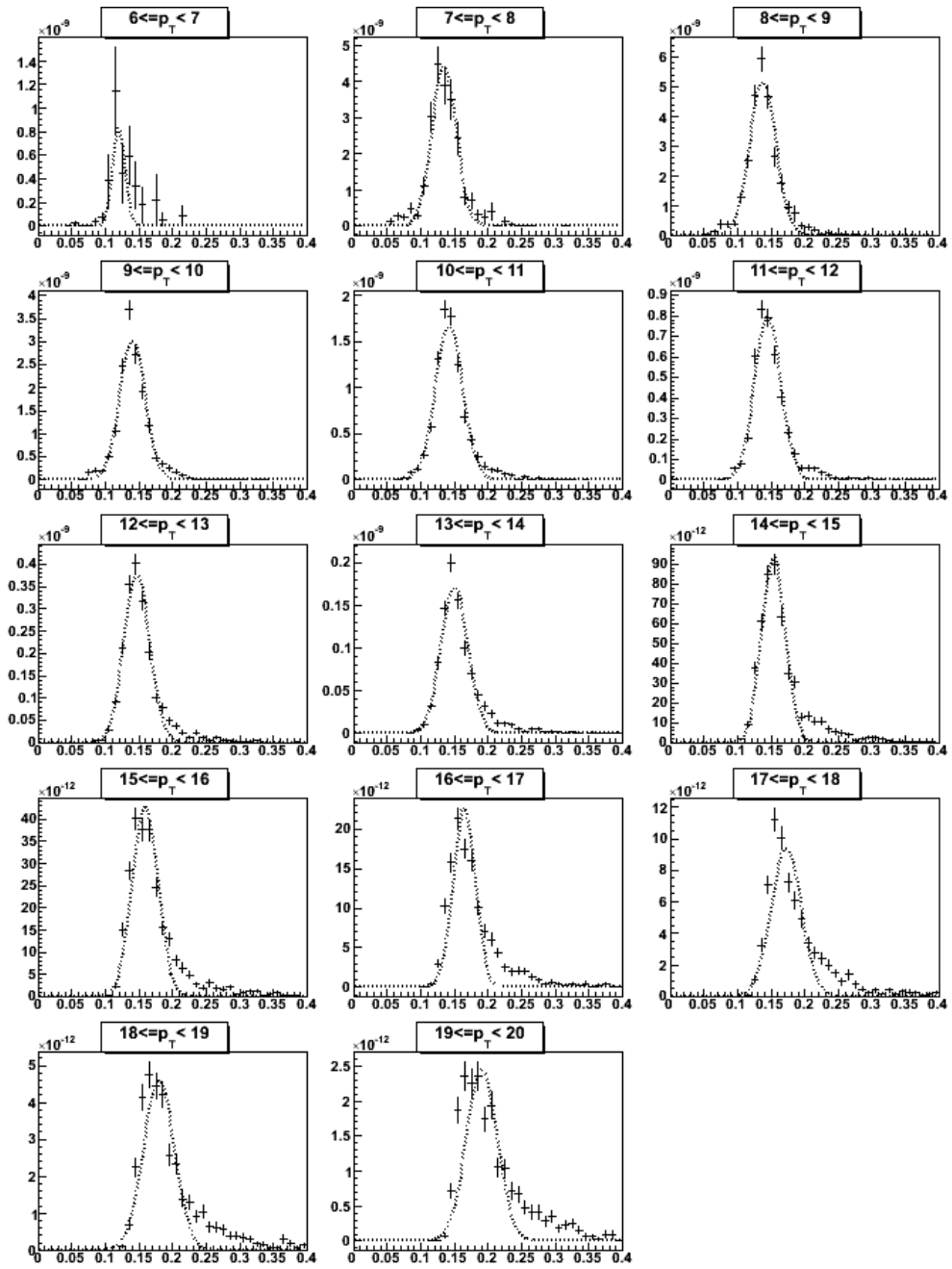

Figure 6.3.12c: The invariant mass histograms for simulated high tower 2 data are presented with the results of fitting a Gaussian distribution to each. Standard analysis bins from 6 GeV to 20 GeV are presented. See text and tables for detailed fit parameter results and discussion of weighting functions used.

Using these invariant mass histograms the pertinent values for a Gaussian fit can be extracted. Each bin was thus fit to extract the effective number of counts in the peak, the width of the distribution, and the position of the mass peak. The positions of the mass peaks are not of direct importance here, but were presented in Figure 6.3.9 for comparison to the real data.

The parameters of the fits were collected. These parameters provide a count of the reconstructed π^0s. Comparing these counts to those in Table 6.3.3, we can establish the efficiencies for the analysis bins. Also, in that table, we have information for the exponential fit. The collected results are now presented in Table 6.3.4 below for the yield and fit parameters of the power law fit and the resulting efficiencies. The efficiencies in Table 6.3.4 are the primary correction factors for this work, and only the associated systematic uncertainties remain to be determined.

Table 6.3.4: Efficiency results for the power-law weighting.

p_T Bin	Const.	δC	Width	δW	Yield	δY	Eff.	δEff
Min Bias		5.9		3.4		6.8		6.8
1.0-1.5	1.84e-4	(%)	2.31e-2	(%)	1.06e-3	(%)	0.0236	(%)
1.5-2.0	1.10e-4	4.5	2.09e-2	2.7	5.75e-4	5.3	0.0474	5.4
2.0-2.5	4.69e-5	4.1	1.92e-2	2.9	2.26e-4	5.0	0.0624	5.1
2.5-3.0	1.91e-5	4.0	1.73e-2	2.6	8.30e-5	4.8	0.0681	4.9
3.0-3.5	7.23e-6	4.0	1.76e-2	2.5	3.19e-5	4.7	0.0696	4.8
3.5-4.0	2.90e-6	4.3	1.82e-2	3.0	1.32e-5	5.3	0.0719	5.4
4.0-4.5	1.15e-6	4.4	1.73e-2	2.7	4.97e-6	5.1	0.0622	5.2
4.5-5.0	5.19e-7	4.4	1.78e-2	3.2	2.32e-6	5.5	0.0627	5.6
5.0-5.5	2.78e-7	4.4	1.75e-2	3.2	1.22e-6	5.4	0.0677	5.5
5.5-6.0	1.24e-7	4.5	1.94e-2	3.5	6.03e-7	5.7	0.0657	5.7
6.0-7.0	1.16e-7	3.1	1.69e-2	2.3	4.93e-7	3.9	0.0648	3.9
7.0-8.0	3.80e-8	3.1	1.78e-2	2.2	1.69e-7	3.8	0.0692	3.8
8.0-9.0	1.41e-8	3.0	1.82e-2	2.3	6.43e-8	3.8	0.0739	3.8
9.0-10.0	5.05e-9	3.2	1.81e-2	2.2	2.30e-8	3.9	0.0669	3.9
HT 1								
4.0-4.5	2.37e-8	22.2	1.28e-2	8.7	7.59e-8	23.9	0.0009	23.9
4.5-5.0	5.84e-8	12.9	1.96e-2	7.3	2.87e-7	14.8	0.0078	14.8
5.0-5.5	7.65e-8	8.2	1.91e-2	5.4	3.66e-7	9.8	0.0203	9.8
5.5-6.0	6.78e-8	5.8	1.86e-2	3.5	3.16e-7	6.8	0.0344	6.8
6.0-7.0	8.73e-8	3.6	1.69e-2	2.6	3.70e-7	4.4	0.0486	4.4
7.0-8.0	3.44e-8	3.2	1.78e-2	2.2	1.54e-7	3.9	0.0627	3.9
8.0-9.0	1.33e-8	3.0	1.82e-2	2.4	6.08e-8	3.8	0.0701	3.8
9.0-10.0	4.94e-9	3.2	1.82e-2	2.1	2.25e-8	3.8	0.0655	3.8
10.0-11.0	2.01e-9	3.3	2.00e-2	2.5	1.01e-8	4.2	0.0685	4.2
11.0-12.0	8.69e-10	3.1	1.95e-2	2.1	4.26e-9	3.8	0.0645	3.8
12.0-13.0	3.98e-10	3.2	1.93e-2	2.2	1.93e-9	3.9	0.0603	3.9
13.0-14.0	1.76e-10	3.3	1.99e-2	2.4	8.79e-10	4.1	0.0544	4.1
14.0-15.0	9.63e-11	2.7	1.74e-2	1.6	4.20e-10	3.5	0.0486	3.5
HT 2								
6.0-7.0	8.53e-10	-	9.39e-3	-	2.01e-9	-	0.0003	8.0%
7.0-8.0	4.40e-9	7.5	1.82e-2	4.6	2.00e-8	8.8	0.0082	8.8
8.0-9.0	5.15e-9	4.7	1.96e-2	3.7	2.52e-8	6.0	0.0290	6.0
9.0-10.0	3.02e-9	3.9	1.89e-2	2.6	1.43e-8	4.7	0.0416	4.7
10.0-11.0	1.67e-9	3.6	2.03e-2	2.8	8.50e-9	4.6	0.0576	4.6
11.0-12.0	7.96e-10	3.2	1.96e-2	2.2	3.91e-9	3.9	0.0592	3.9
12.0-13.0	3.77e-10	3.3	1.92e-2	2.3	1.82e-9	4.0	0.0566	4.0
13.0-14.0	1.71e-10	3.4	1.99e-2	2.4	8.56e-10	4.1	0.0530	4.1
14.0-15.0	9.37e-11	3.0	1.74e-2	1.7	4.08e-10	3.5	0.0479	3.5
15.0-16.0	4.32e-11	3.5	1.90e-2	2.2	2.06e-10	4.2	0.0446	4.1
16.0-17.0	2.27e-11	3.5	1.63e-2	1.9	9.25e-11	4.0	0.0354	4.0
17.0-18.0	9.37e-12	4.5	2.23e-2	3.4	5.25e-11	5.6	0.0342	5.7
18.0-19.0	4.59e-12	4.7	2.32e-2	3.6	2.67e-11	5.9	0.0294	5.9
19.0-20.0	2.46e-12	4.7	2.29e-2	3.1	1.42e-11	5.6	0.0249	5.6

Similar analysis of two datasets provide comparable results from which systematic uncertainty can be drawn. The data above was compared to the exponential weighting method, and also to an alternate trigger turn-on behavior. The latter was done to identify the p_T region in the data where trigger turn on systematics may be ignored, and to identify where uncertainty in the turn on mechanism can lead to large differences in the resulting efficiency. Table 6.3.5 shows results for both the exponential weighting method and the alternate trigger turn-on behavior, and their impact on the systematic uncertainty. This table also includes the systematic uncertainty in the counting method compared to the bin-summing method.

The overall systematic uncertainty from various methods of counting and triggering generally are within the counting errors for the yields (from section 6.2) for the respective bins. There are two primary situations where the errors are too big to be overshadowed by the counting errors in the yields. They are: the trigger turn-on region, and the very large disagreement in the exponential weighting method at high-p_T. The former is certainly overestimated, but is in an overlap region where only one set of data is needed to establish results. The later is generally unimportant in this work because the p_T-range of the real data is limited and does not reach the p_Ts where the problems become pronounced.

Table 6.3.5: Efficiency results for power law and exponential weighting, and alternate trigger turn on method. The results are then used to provide conservative systematic uncertainty for each p_T Bin.

p_T Bin	Power Law		Exponential				Systematic Uncertainty (%)			
	Eff	δEff	Yield	δY	Eff	δEff	w*	Turn On	# - π^0	Total
Min Bias										
1.0-1.5	0.0236	6.8	1.05e-3	6.8	0.0290	6.8	17.7	0	3.8	3.8
1.5-2.0	0.0474	5.4	9.50e-4	4.9	0.0439	5.0	3.9	0	0.2	0.2

p_T Bin	Power Law		Exponential				Systematic Uncertainty (%)			
	Eff	δEff	Yield	δY	Eff	δEff	w*	Turn On	# - π^0	Total
2.0-2.5	0.0624	5.1	5.68e-4	4.8	0.0624	4.9	0.1	0	2.2	2.2
2.5-3.0	0.0681	4.9	2.73e-4	4.9	0.0668	5.0	1.9	0	1.4	1.4
3.0-3.5	0.0696	4.8	1.22e-4	4.5	0.0678	4.6	2.6	0	0.3	0.3
3.5-4.0	0.0719	5.4	5.30e-5	5.3	0.0701	5.4	2.6	0	1.5	1.5
4.0-4.5	0.0622	5.2	1.93e-5	5.2	0.0611	5.3	1.8	0	1.4	1.4
4.5-5.0	0.0627	5.6	8.09e-6	5.6	0.0620	5.7	1.1	0	0.9	0.9
5.0-5.5	0.0677	5.5	3.65e-6	5.8	0.0688	5.8	1.6	0	1.6	1.6
5.5-6.0	0.0657	5.7	1.39e-6	4.7	0.0650	4.8	1.1	0	3.0	3.0
6.0-7.0	0.0648	3.9	7.98e-7	4.5	0.0665	4.5	2.6	0	4.3	4.3
7.0-8.0	0.0692	3.8	1.39e-7	5.0	0.0739	5.0	6.3	0	4.7	4.7
8.0-9.0	0.0739	3.8	2.43e-8	5.7	0.0846	5.7	12.6	0	5.0	5.0
9-10.0	0.0669	3.9	3.21e-9	5.3	0.0735	5.3	9.0	0	6.5	6.5
HT 1										
4.0-4.5	0.0009	23.9	2.72e-7	24.0	0.0009	24.0	4.5	800	14.0	800
4.5-5.0	0.0078	14.8	9.83e-7	15.0	0.0075	15.0	3.5	135.2	3.1	135.2
5.0-5.5	0.0203	9.8	1.04e-6	9.6	0.0196	9.6	3.5	95.9	5.2	96.0
5.5-6.0	0.0344	6.8	7.05e-7	7.9	0.0329	7.9	4.4	49.5	6.6	49.9
6.0-7.0	0.0486	4.4	5.85e-7	5.2	0.0487	5.2	0.2	26.9	3.8	27.2
7.0-8.0	0.0627	3.9	1.25e-7	5.0	0.0665	5.0	5.6	11.0	3.9	11.7
8.0-9.0	0.0701	3.8	2.28e-8	5.7	0.0794	5.7	11.8	5.3	5.1	7.4
9-10.0	0.0655	3.8	3.17e-9	5.2	0.0726	5.2	9.7	1.9	5.8	6.1
10-11	0.0685	4.2	5.5e-10	8.1	0.0830	8.1	17.4	1.3	6.9	7.0
11-12	0.0645	3.8	7.8e-11	5.9	0.0809	5.9	20.3	0.5	6.6	6.6
12-13	0.0603	3.9	1.2e-11	7.5	0.0810	7.5	25.6	0.0	6.2	6.2
13-14	0.0544	4.1	1.6e-12	7.7	0.0763	7.7	28.7	0.2	8.9	8.9
14-15	0.0486	3.5	2.0e-13	5.6	0.0636	5.6	23.6	0.4	12.9	12.9
HT 2										
6.0-7.0	0.0003	8.0	2.27e-9	41.1	0.0002	41.1	58.7	2900	13.4	2900
7.0-8.0	0.0082	8.8	1.27e-8	9.8	0.0067	9.8	21.5	114.7	5.5	115
8.0-9.0	0.0290	6.0	8.72e-9	8.7	0.0304	8.7	4.6	48..4	6.0	48.8
9-10.0	0.0416	4.7	1.85e-9	6.5	0.0424	6.5	1.8	31.5	7.7	32.4
10-11	0.0576	4.6	4.5e-10	9.6	0.0681	9.6	15.4	16.9	6.5	18.1
11-12	0.0592	3.9	7.2e-11	6.3	0.0741	6.3	20.1	9.0	6.4	11.0
12-13	0.0566	4.0	1.1e-11	7.5	0.0768	7.5	26.3	6.6	6.1	9.0
13-14	0.0530	4.1	1.6e-12	7.8	0.0749	7.8	29.3	2.8	8.5	8.9
14-15	0.0479	3.5	1.9e-13	5.7	0.0623	5.7	23.2	2.9	13.2	13.5
15-16	0.0446	4.1	3.1e-14	8.4	0.0705	8.4	36.7	1.4	13.6	13.7
16-17	0.0354	4.0	3.8e-15	8.2	0.0593	8.2	40.3	1.2	9.5	9.6
17-18	0.0342	13.3	4.4e-16	11.9	0.0477	11.9	28.2	0.6	13.3	13.3
18-19	0.0294	5.6	6.7e-17	10.4	0.0513	10.4	42.7	0.4	5.6	5.6
19-20	0.0249	5.6	8.0e-18	11.0	0.0418	11.0	40.4	0.0	5.6	5.6

*The alternate weighting is not used to establish the systematic uncertainty. Rather, it is a rough measure of how inaccurate the results can be if a very incorrect weighting function is used.

6.3.8 Efficiency Results

This section provides the resulting efficiencies found in the embedding analysis. The application of these efficiencies is dependent upon knowing the degree to which they may be applied, and the accuracy to which they can be applied. Roughly speaking, this means we need to provide a couple additional pieces of information, along with the efficiencies, in order to determine the errors that will be incurred during application. Of course, we must provide the resulting statistical accuracy. Also, we will highlight the requirements upon matching this analysis to analysis of real data. In order to do that, we will specify the restrictions on matching to the embedding data. Finally, we will provide an estimate of the incurred systematic error due to changes in the most sensitive parameters of the dataset.

For this analysis, we duplicated the yield analysis used on the real data. That is, the intentional cuts are the same and the analysis parameters are the same. It should be noted that event selection in embedding drove the selection of the z cut that was in the yield analysis. For the analysis parameters, we only have the point-making settings of 0.350 GeV for tower clusters and 0.1 GeV for the SMD clusters. The cuts for this analysis are presented in Table 6.3.6

Table 6.3.6: Cuts imposed in embedding analysis.

Parameter	Imposed Cuts
z	$\|Z\|<60$; Z is not 0 (the latter forces vertex reconstruction)
# BEMC Points	$N < 70$
# of BEMC Planes	Points must have tower, SMD-η, and SMD-ϕ clusters
MIP Contribution	Points must not have projected TPC global tracks
e_{asym}	Candidate pairs must have $e_{asym}<0.5$

High tower trigger data analysis also required that pairs must have at least one of their photons above the high tower trigger energy for the desired triggers. Recall that these are 3.2 GeV for high tower 1, and 5.2 for high tower 2, as hardware triggers. Simulation analysis showed that software triggering could not produce hardware trigger behavior in the turn on region without large uncertainty. For this work the alternate triggers fill in the spectrum in the turn on region. More direct simulation of the hardware triggering is possible but not feasible, because it requires verification of the detector model turn-on of each tower in the BEMC. The resulting improvement in uncertainties would remain dependent on how many events have a non-π^0 photon with energy above threshold.

In order to apply the efficiencies developed in this section, the detector configuration must match that used in this analysis. For this embedding analysis we used the detector's status tables for the collection period of the embedding runs. In addition 15 of the BEMC modules were masked due to poor data performance. These match those in the yield analysis in Section 6.2, and can be found in Appendix K. The matching of the embedding to the real configuration cannot simply be made with these tables and masked modules, instead the degree to which these masks result in well-controlled distributions of the low-level data must be verified. This was briefly discussed earlier in this section, and showed deviations on the order of 20% for about

20% of the data taking period, or an overall total impact of about 4% to the real data analysis.

Using the analysis configuration discussed above, the embedding data was analyzed to produce invariant mass histograms for each of the p_T bins. These are shown in Figure 6.3.12(a-c) in the previous part of this section.

The efficiencies are determined by dividing these yields by the number of π^0s simulated in each bin. The efficiencies are now plotted. The results are shown in Figure 6.3.13, which is a graphical representation of the first three columns of Table 6.3.5 as well as the total systematic uncertainty in the final column of that table. The figure shows the overall efficiency and the full set of systematic uncertainties. The error bars represent the statistical errors in the number of counts of the embedding yield, and the number of simulated particles. The bands show the systematic uncertainty in the efficiency at each p_T. The primary systematic uncertainty here is due to a few sources. One source is the ambiguity in the fitting algorithm including comparison of two reasonable fitting methods and slight modifications to their limiting parameters. Another source is the trigger turn on, which includes several questions related to the uniformity of the detector and presence of additional particles that were not simulated. These effects were discussed in detail earlier in this section.

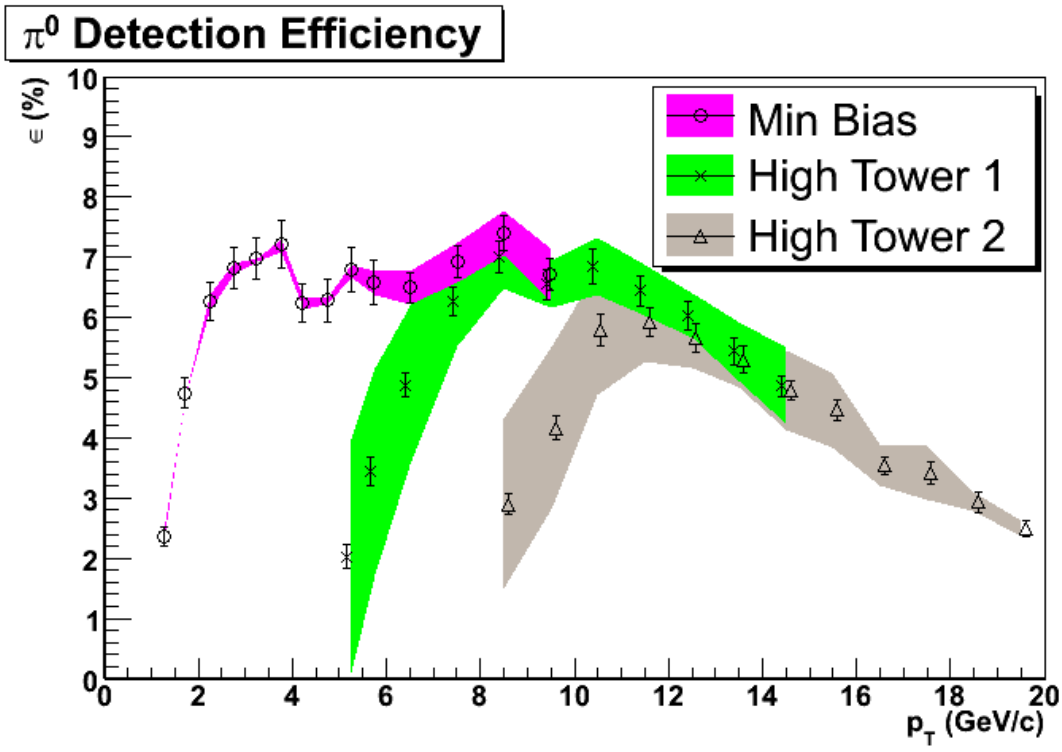

Figure 6.3.13: The efficiencies for MinBias, High Tower 1, and High Tower 2 are presented. These apply to the real data analyzed earlier in this chapter. They are for the specific set of cuts used in the analysis, and require the detector acceptance to match the cuts used in this analysis. See the text for more details about the statistical error sources and systematic uncertainty.

Above the turn-on of the high tower triggers, the differences in the efficiencies are a reflection of the average acceptance of the detector. Since this acceptance must be handled as part of this embedding analysis, it shows up here. It was discussed above that the acceptance, which directly reflects the detector configuration, must be matched in order to use these results, and the differences between the triggers are an example of why.

These efficiencies will be used in the remaining sections of the thesis to convert the raw π^0 yields into cross sections. The graphical representation in Figure 6.3.13 is helpful for the reader to quickly assimilate the information, but we also need the

information in a form that is useful for the analysis. The values for this figure, and the underlying examination of systematics, can be found in Table 6.3.5.

CHAPTER 7

Results

7.1 Introduction

The data developed in the last chapter provides the basis for calculating the absolute cross-section for π^0 production at STAR in the *d+Au* collisions. The results are determined by calculations using the measurements from those data, and by careful application of the normalization corrections. In order to simplify some of the dependencies, several sources of data and normalization will be presented here. In addition, outside sources of comparison data will be presented here.

This chapter will begin with a section highlighting the results from the last chapter. The yields, efficiencies, and the associated systematic uncertainties in the matching of analysis and embedding data will be coved. The end of this chapter covers, in detail, the selection of p_Ts relevant to plotted data points. This discussion is important to the placement of the data points, but only really effects interpretation of the results. Thus, rather than putting it before the results, the results include the effects even though they are presented first.

With this information available, it will be possible to test the results against the predictions of pQCD. Also, the degree of agreement with other experiments and

measurements of other particles in the same collisions is of interest. The results of these tests and comparisons can be found in chapter 8.

7.2 Measurements

The data developed in the last chapter provides the basis for calculating the inclusive π^0 yields and therefore cross section. There are only a few remaining details to show, which will be covered in the next section. Except for the selection of appropriate p_T for a given analysis bin, the remaining details do not impact the results within the systematic uncertainty, though they will be discussed.

One such problem, the p_T selection, will be covered shortly. For the present discussion, however, the results will simply be given at the appropriate p_T, and the method will be discussed later in this chapter.

The results are given in Table 7.1 and are shown in Figure 7.1. Figure 7.1 shows the inclusive yield, separated into the three trigger types, spanning the range from $1.25 < p_T < 13.0$ GeV/c. All systematic uncertainties included in the shaded bands. The table shows the details for each trigger and analysis bin for the yield extraction and efficiency measurement. These are a simple duplication of tabular results given for chapter VI. The statistical and systematic uncertainties in the yield analysis and the embedding analysis are added in quadrature, since there is no real correlation between the uncertainties. It should be noted that some of the uncertainties are very large, and should be considered as relative measurements. For example, the first bin of the high tower 2 data has a systematic uncertainty of 2902%. This indicates that the measurement may go a factor of about 30 times larger or 30 times smaller. This does not mean that the measurement is consistent with a negative result.

Table 7.1: Differential inclusive yield results for π^0 in *d+Au* collisions.

Trigger	Bin p_T (GeV/c)	Yield/N_{evt}	Efficiency	Total Yield/N_{evt}	Statsistical Error	Systematic Uncertainty[t]
Min Bias	1.22	1.11e-3	0.0236	4.70e-2	7.0(%)	12.2
	1.72	4.12e-4	0.0474	8.69e-3	5.6	7.8
	2.23	1.23e-4	0.0624	1.97e-3	5.5	10.5
	2.73	4.19e-5	0.0681	6.15e-4	5.7	6.8
	3.23	1.36e-5	0.0696	1.95e-5	6.8	14.1
	3.73	3.38e-6	0.0719	4.70e-5	10.6	21.5
	4.23	1.44e-6	0.0622	2.32e-5	14.3	14.1
	4.73	6.11e-7	0.0627	9.74e-6	17.2	19.2
	5.23	3.63e-7	0.0677	5.36e-6	22.1	27.0
	5.73	6.00e-8	0.0657	9.13e-7	94.5	47.2
	6.44	2.39e-8	0.0648	3.69e-7	76.2	44.5
	7.45	1.14e-8	0.0692	1.65e-8	87.5	11.7
High Tower 1	4.23	1.97e-8	0.0009	2.19e-5	33.0	807.2
	4.73	6.43e-8	0.0078	8.24e-6	18.3	140.7
	5.23	6.47e-8	0.0203	3.19e-6	13.8	96.7
	5.73	5.40e-8	0.0344	1.57e-6	14.1	55.0
	6.44	4.10e-8	0.0486	8.44e-7	15.3	37.7
	7.45	1.73e-8	0.0627	2.76e-7	10.5	15.6
	8.45	7.08e-9	0.0701	1.01e-7	16.3	22.1
	9.45	3.87e-9	0.0655	5.91e-8	24.6	15.8
	10.45	2.04e-9	0.0685	2.98e-8	53.4	61.9
High Tower 2	6.44	3.62e-10	0.0003	1.21e-6	40.0	2901.9
	7.45	2.41e-9	0.0082	2.94e-7	15.5	131.8
	8.45	2.96e-9	0.0290	1.02e-7	10.7	53.9
	9.45	1.76e-9	0.0416	4.23e-8	20.7	35.4
	10.45	8.19e-10	0.0576	1.42e-8	16.7	33.8
	11.45	4.48e-10	0.0592	7.57e-9	82.1	48.9
	12.45	2.31e-10	0.0566	4.08e-9	29.5	40.9
	13.45	1.01e-10	0.0530	1.91e-9	40.2	63.9

[t] Includes systematic uncertainty from Table 6.2.4.

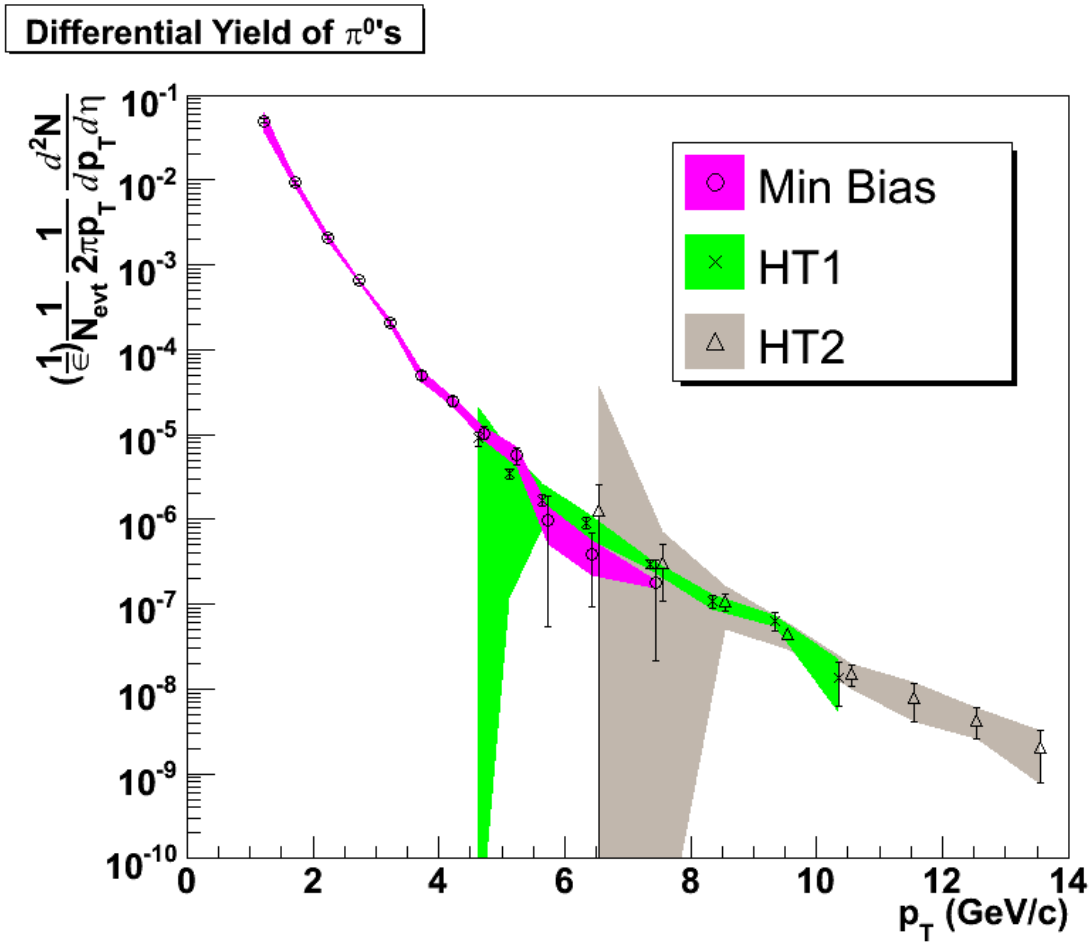

Figure 7.1: The final result for the inclusive differential yield of π^0s in *d+Au* collisions at $\sqrt{s_{nn}}$ = 200 GeV. Note that some bins (especially the low and high-p_T bins for each trigger) have large systematic uncertainty bands. This is a result of a conservative estimate of the behavior of the trigger turn-on mechanism for the barrel and can be taken as an extremely safe bounding of the behavior. The overlap in the triggers suggest at least one trigger set is reliable in each reported p_T bin.

7.3 p_T Selection

The measurement of absolute cross sections depends greatly on the ability of the analysis to account for many systematic effects. Other analyses, which aim to make relative measurements, can settle for using systematically inaccurate methods, as long

as the inaccuracies cancel. Typically these methods result in errors on the order of 5-25%. However, the same measurement is made in two datasets, both of which pick up the error. The final product of that type of analysis is the ratio of the two measurements. In that ratio, the errors cancel. The measurement here is absolute, and thus all the possible systematic uncertainties come through the entire process. The only place systematic uncertainties cancel is when their sources have the same effect in both the real and simulation analyses. It is only safe to state that they cancel if the source of uncertainty is known to be reproduced correctly in the simulation. For example, the method used to construct photon information from data in the barrel, although it contains uncertainties, is duplicated in the simulation and real data analysis, so these uncertainties are taken care of adequately in the correction procedure using simulations.

Most sources of error in the measurements here have been presented. There is, however, one source that can still cause problems. That source is the positioning of measurements on the p_T-axis. The measurements made for this analysis are bin-based, meaning that the production of the particles of interest are gathered based on whether their measured p_T falls within a bin. Thus measured yields, and therefore cross sections, apply to an entire bin. Thus we must consider the question of the p_T to assign to a measurement for a given bin. Since this sort of question occurs often in bin-based analyses the question has been addressed in [LW95].

The basic result stated in [LW95] is that when a theoretical production function is known, the measured value across a bin should be plotted at the position in the bin where the theoretical function is equal to its average value across the bin. For consideration here, though, we have a theoretical production function whose accuracy is not well known. We show, in Appendix H, that the bin-positions found from the

"guess" function can be used to plot the results, and that the resulting distribution will provide a better estimate for the guess function. Further, it follows that the "guess" function and resulting data positions must only be accurate in places where the calculated position is very different from the bin center. The additional impact of the "guess" comes in bins where the efficiency changes across the bins, which is only a concern at low p_T.

7.4 Theoretical Production Spectrum

The last section explained that the data points for each p_T analysis bin should be plotted at the position within the bin where the theoretical distribution is equal to its mean across the entire bin. In order to determine such positions for our data here, a theoretical production spectrum is needed. The data are expected to follow the empirically determined common functional form discussed earlier. Evidence of the wide-spread use of this form can be found in [Arn82, Abe88, Alb90, Adc02]:

$$E\frac{d^3\sigma}{dp^3} = \frac{1}{2\pi}\frac{1}{p_T}\frac{d^2\sigma}{dp_T d\eta} = \frac{C}{\left(A + p_T\right)^{\alpha}}, \qquad (7.1)$$

where C, A, and α are fit-parameters.

For the determination of point-placement, the overall normalization constant C need not be determined. The first-round determination of A and α was carried out using the production spectrum for STAR's charged hadrons [Ada03]. Fitting the functional form to the data gives the parameters: C = 4.37e4, A = 1.95, and α = 11.341. The charged hadron spectrum, and the best-fit values are given in Table 7.2.

Table 7.2: The yields for STAR's charged hadrons are given, as well as the results for the each p_T bin from the fit function [Ada03].

Bin p_T	$d^2N/dp_Td\eta/2\pi p_T$	Error	Fit Result
1.05	1.6e-1	1e-2	1.71e-1
1.15	1.1e-1	1e-2	1.18e-1
1.25	8.1e-2	4e-3	8.22e-2
1.35	5.8e-2	3e-3	5.80e-2
1.45	4.2e-2	2e-3	4.13e-2
1.55	3.0e-2	1e-3	2.97e-2
1.65	2.2e-2	1e-3	2.16e-2
1.75	1.6e-2	1e-3	1.58e-2
1.85	1.2e-2	1e-3	1.17e-2
1.95	9.1e-3	4e-4	8.71e-3
2.05	6.8e-3	3e-4	6.54e-3
2.15	5.0e-3	3e-4	4.94e-3
2.25	3.8e-3	2e-4	3.76e-3
2.35	2.8e-3	2e-4	2.88e-3
2.50	1.9e-3	1e-4	1.95e-3
2.70	1.1e-3	1e-4	1.18e-3
2.90	7.2e-4	5e-5	7.34e-3
3.16	4.1e-4	2e-5	4.06e-4
3.56	1.7e-4	1e-5	1.73e-4
4.07	6.2e-5	4e-6	6.32e-5
4.71	1.9e-5	2e-6	2.01e-5
5.50	5.2e-6	6e-7	5.63e-6
6.44	1.3e-6	2e-7	1.46e-6
7.45	4.0e-7	6e-8	4.03e-7
8.45	1.2e-7	2e-8	1.28e-7
9.46	5.0e-8	9e-9	4.47e-8
10.84	1.6e-8	3e-9	1.23e-8

The data developed in the last chapter were used to determine the yields presented earlier in this chapter. For those calculations, we had to guess at the results here in order to establish appropriate p_T weighting in simulation. That was somewhat necessary, as this situation is a "chicken and egg" problem. The results could not be plotted without assuming a production distribution, but the production distribution cannot be verified without the results being available.

To complete the justification of the assumed production distribution, we now compare the production distribution to the real data. This comparison is shown in Figure 7.2. The fit function used, and the final yields, agree well below 10 GeV/c. Above that value the data is always above, but consistent with the weighting function. There are two reasons that the data above 10 GeV/c can be ignored, in terms of determining a new weighting function and repeating the analysis. The first is that the weighting function directly effects the determination of efficiency. However, the efficiency is under control in these high-p_T bins and does not vary much across the span of 1 GeV, which is the scale of importance to the measurement. The second reason is that the weighting function's only other use is the assignment of p_T, but in this range the p_T response is already flat enough that the points are nearly in the middle of the bin, and therefore would only move the p_T by 0.01 to 0.02, which is negligible compared to the systematic and statistical uncertainty already evident in those bins.

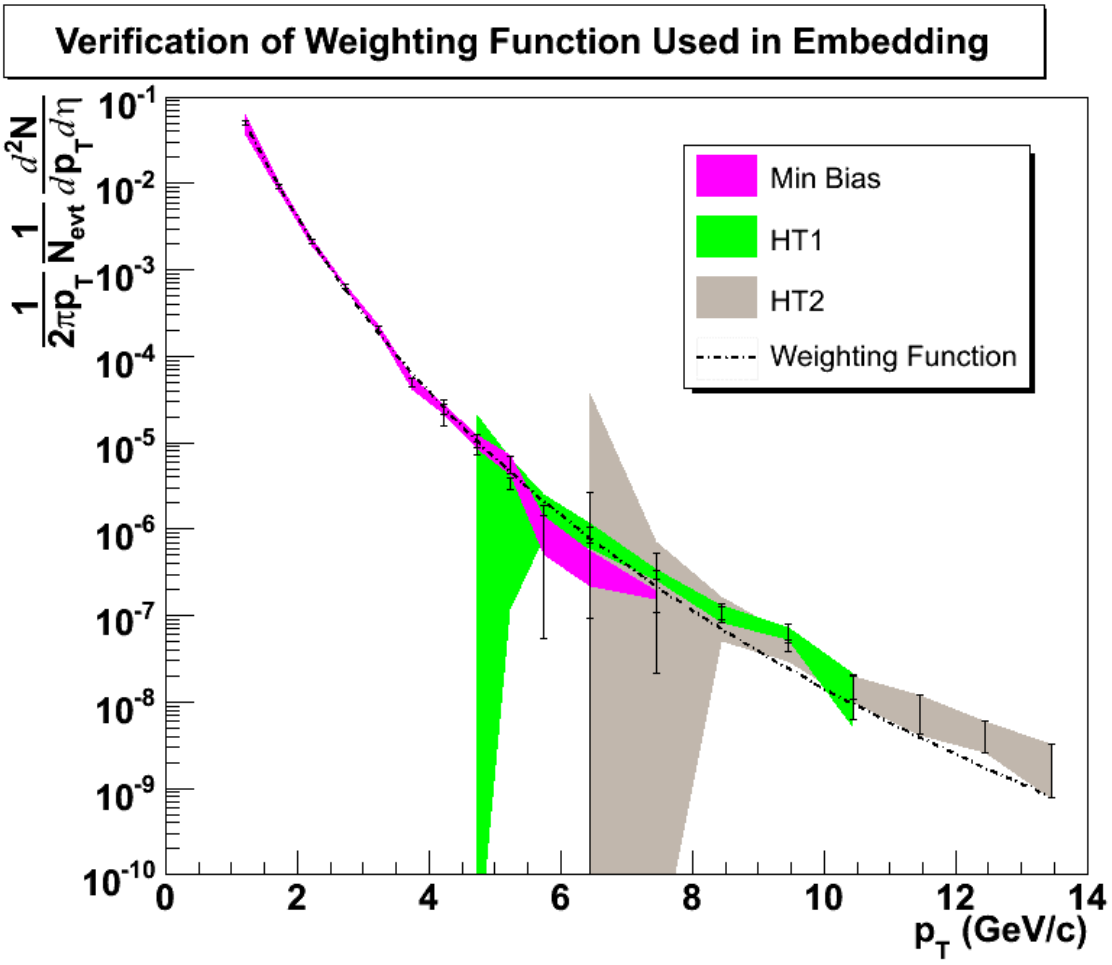

Figure 7.2: Verification of the yield parametrization used to extract the efficiency of STAR for detecting π^0s. The fit is very good up to 10 GeV/c where it remains consistent with the final measured yield. The shape is used to position the point-p_T and provide the proper ratio of simulated particles in the given bin. Above 10 GeV the data points are already almost in the centers of the bins, and the efficiencies are under control, so the results will be unaffected by repeating the process with a new fit function.

CHAPTER 8

Discussion & Conclusion

8.1 Introduction

In this chapter we will discuss how the current work fits into the analysis goals of the STAR collaboration and the particle physics community. The primary discussion here is to compare datasets and test the validity of pQCD calculations in *d+Au* collisions. These *d+Au* collision results also serve to limit the available models describing effects due to the parton structure modifications of the Au nucleus on the collisions. To that end we will present several ratio plots and draw some conclusions. This chapter will conclude with a discussion of ongoing issues related to measurement of π^0s at STAR.

The results developed in this work form a piece of the broader picture of *d+Au* collisions. There are many parallel investigations of this dataset within STAR and the larger particle physics community. The most directly comparable works are those whose goal is to determine the limitations of pQCD calculations in these collisions, specifically concerning hadron production at p_T over 3 GeV/c. This story is set in the larger framework of RHIC's *p+p* and *Au+Au* collisions. It is to these datasets that our results must be compared.

8.2 Theoretical Details

pQCD provides a framework for calculation of cross-sections for inclusive particle production in p+p collisions at high p_T. The applicability of this procedure outside of the p+p regime is of great interest since Au+Au collisions show deviation from pQCD when only simple modifications of the system are allowed [Adl03] The prescription for applying pQCD is described in Chapter 2, but we will briefly cover it here.

The cross-section for π^0 production can be determined using the factorization theorem which allows the incoming partons a and b, to be described by structure functions $f_A^a(x_a)$ and $f_B^b(x_b)$ which are the probabilities, for given Bjorken-x (x_a and x_b), that particles A and B contain partons a and b. The theorem provides a framework to determine how often collisions of these partons will produce other partons (c) which are then described by a fragmentation function $D_c^C(z_c)$, which is the probability that c produces the particle C with momentum fraction z_c. The benefit of this picture is that, provided pQCD is applicable, the structure functions and fragmentation functions are independent of the interactions used to measure them. Strong interactions, however, are also dependent upon the energy scales at which measurements are made, so the structure functions and fragmentation functions may change depending on the momentum transfer involved in the parton process [Col84].

For the experimental data discussed here, all measurements are made at the same collision energy and are thus comparable in that sense, although the structure functions may be modified by different nuclei. Furthermore, varying the momentum transfer, Q^2, used in the calculations allows for a determination of the uncertainty in

the calculation. For this work, however, the ideology behind factorization is what is being tested. This is true because *p*+*p* data using both STAR and PHENIX have shown that NLO pQCD works, however, in *Au*+*Au* it appears to not work.

pQCD calculations for *Au*+*Au* collisions involve the parton distribution function in Au nuclei, which is modified from that of the proton. The extent of the modification has not been determined experimentally. In particular, the gluon saturation model for the gluon distribution function in Au nuclei can provide a reasonable match to *Au*+*Au* data. This sort of initial-state effect must eliminated as an explanation for observed results in order to establish the QGP.

In order to test *Au*+*Au* results, the collision system is compared, using Glauber-model calculations, to an overlapping set of independent *p*+*p* collisions where this system matches the "effective" number of *p*+*p* collisions in a *Au*+*Au* collision. Figure 8.1 shows the nuclear modification factor for charged hadrons in *Au*+*Au* collisions from the STAR collaboration. These results include $\langle N_{bin} \rangle$ results from [Adl02] with minor corrections as stated in [Ada03b].

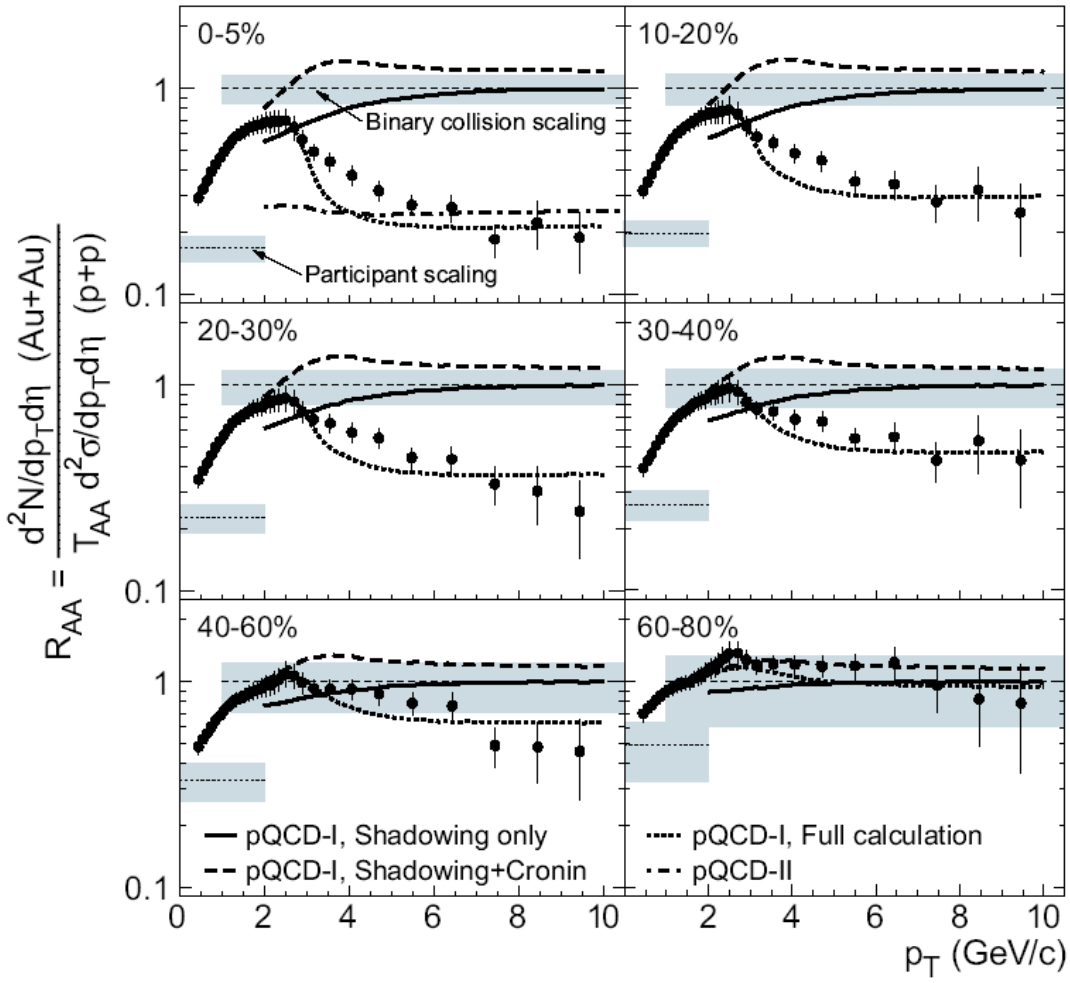

Figure 8.1: Figure taken from [Ada03b]. Comparison of hadron $(h^+ + h^-)/2$ signals in *Au+Au* 200GeV to binary-scaled *p+p* 200 GeV. Data is grouped by collision centrality. 0-5% centrality is the most central bin. pQCD calculations compare different possible explanations for the deviation from binary scaling in the central bins. *d+Au* collisions share initial-state features of the *Au+Au* collisions and help to eliminate some of these possible scenarios for the scaling violations in central *Au+Au* collisions.

Below $p_T \sim 2$ GeV/c pQCD is not expected to be a good prescription for calculation of inclusive production cross-sections. Above 2 GeV, however, the *p+p* cross sections can be calculated within pQCD. This is evident in the most peripheral bins of the R_{AA} above (lower panels), where the pQCD calculations with all the

modified scenarios for various effects is always very close to the p+p cross section (at 1). This data is relevant for $(h^+ + h^-)/2$.

The picture is also clouded by the results reported by Gallmeister, Greiner, and Xu [GGX03]. The production of hadrons from Au+Au collisions, if QGP is not formed, must be due to the arrangement of partons before the collision, or with bulk interaction after the collision. In [GGX03] it is shown that the lack of high-p_T hadrons in Au+Au collisions could be due to hadronic scattering after the collision (therefore, a final-state effect).

In order to compare the π^0 data collected here, reference data for p+p collisions is required. Relevant data for π^0 comparisons in p+p come from STAR and PHENIX. The STAR data has limited statistics and is expected to be about 20% below the scale of our measurements. The PHENIX data comes from [Adl03d] where the total p+p cross section of 42mb [Ada03b] is divided out of the result. STAR p+p data comes from [Sto05]. The relevant power-law result from PHENIX is $9.36\,\mathrm{GeV}^{-2}c^3\left(1+p_T/1.212\right)^{-9.97}$. The STAR and PHENIX p+p π^0 reference data are shown in Figure 8.2, and given in Tables 8.1 and 8.2. Figure 8.2 shows the inclusive per event yield of π^0s in p+p collisions, where the line is a power-law fit to the PHENIX results. STAR and PHENIX agree within systematic uncertainties.

Table 8.1: PHENIX p+p π^0 data.

p_T	Cross Section	Uncertainty*
1.215	3.733e-1	6.117e-3
1.719	6.052e-1	1.075e-3
2.223	1.221e-2	3.011e-4
2.726	3.308e-3	1.181e-4
3.228	9.987e-4	5.652e-5
3.730	3.385e-4	2.456e-5
4.232	1.187e-4	2.906e-6
4.733	4.726e-5	1.990e-6
5.234	2.206e-5	1.096e-6
5.735	1.113e-5	5.005e-7
6.236	4.999e-6	3.172e-7
6.737	3.003e-6	2.304e-7
7.452	1.080e-6	9.530e-8
8.457	4.853e-7	5.832e-8
9.460	1.643e-7	3.166e-8
10.861	5.227e-8	1.169e-8
13.250	1.190e-8	4.910e-9

* Uncertainty is statistical only.
- This data is relative to the p+p inelastic cross section (~42mb).

Table 8.2: STAR p+p π^0 data.

p_T	Inv. Yield (GeV^{-2})	Uncertainty (%)*
1.24	8.76e-3	10.2
2.30	2.36e-4	9.5
3.34	2.04e-5	12.1
4.36	3.32e-6	8.6
5.38	5.48e-7	7.5
6.39	9.85e-8	11.7
7.41	2.68e-8	76.7
8.42	1.25e-8	69.3
9.42	6.43e-9	79.4

* Uncertainty is statistical only.

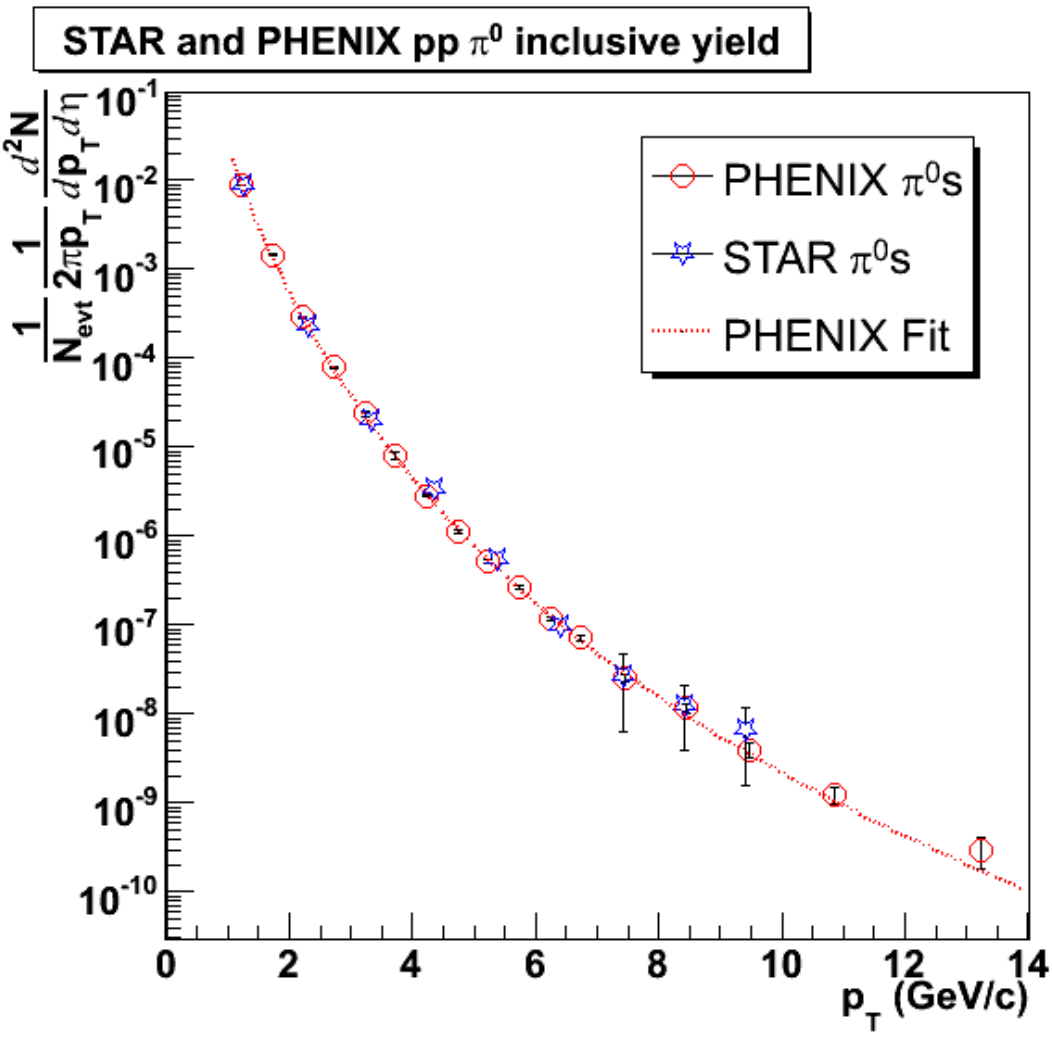

Figure 8.2: Results from the STAR and PHENIX collaborations showing the π^0 total yield. The PHENIX collaboration's power law fit is shown. The PHENIX results are those in [6] with the *p+p* inelastic cross section divided out.

The large suppression of high-p_T particle production in central *Au+Au* collisions can be explained in several ways. One experimental goal of RHIC experiments is to prove that the high energy density medium created in *Au+Au* collisions produces the quark gluon plasma (QGP), and that the QGP is the source of the high-p_T particle suppression, but this is not the only possible explanation in the absence of *d+Au*

results. One type of explanation is that the incoming nucleus has saturated gluon densities. Such an effect is an initial-state effect. In order to disentangle this type of effect RHIC provided *d*+*Au* collisions, where initial-state effects in the Au nucleus would still be present, but the high energy density of the *Au*+*Au* collision system would be absent in the transverse direction.

Although several production channels are available for analysis of high-p_T suppression in *Au*+*Au* collisions, π^0s provide a unique signal. π^0s are also of interest because they can be detected at high p_T while charged hadrons become very difficult to identify at high p_T since the characteristic energy deposition of various charged hadrons begins to overlap. Because of these considerations, we will compare the π^0 inclusive production data gathered here to similar data gathered by PHENIX. We will further compare this data with π^0 data gathered in 200 GeV *p*+*p* data. These comparisons provide further evidence of the reliability of STAR BEMC-based analyses, and they provide evidence that initial-state effects do not lead to high-p_T particle suppression such as that seen in 200 GeV central *Au*+*Au* collisions. Due to the behavior of high-p_T particle production in *d*+*Au* collisions it is clear that pQCD provides a framework for calculation of cross sections in *d*+*Au* collisions, a result that is being seen across all the detectors at RHIC for the 200 GeV energy regime.

8.3 Data Comparison

The analysis carried out for this dissertation was part of a wider effort to understand the processes involved in using data from the STAR BEMC. Since the time the data was taken for this dissertation the detector has been upgraded, and many

of the details discussed in collaboration meetings have been included into the current operating state of the detector.

Due to collaborative commissioning of the detector and its software during the data taking, and later during data reconstruction, several analyses whose goals included the measurement of π^0s in *d+Au* collisions were carried out. This situation provided similar results using many different analysis regimes. In order to establish the reliability of the results herein, it is useful to compare them directly to one other π^0 analysis result from STAR.

The results we now compare to are those presented in the Ph.D. dissertation of Alexander Stolpovsky [Sto05]. The work used the same *d+Au* data sample from 2003. The primary differences between this work and his are the following. The software system was still in flux at the time of his results. Also present in his analysis were results from *p+p* collisions which are known to have limited p_T range due to triggering issues and were thus not analyzed here. His method of counting signal also differed from what is presented here. Namely, in high p_T bins where the number of counts is small, the method employed was to sum up all invariant mass counts in the mass window around the π^0 mass, and subtract the integral of a fitted background function. This is the same general method used in the bin summing method used, in part, to determine systematic uncertainty.

The results of the discussed analysis are shown in Figure 8.3 and compared to the results presented here. This figure has two panels. The upper panel shows all analysis bins from [Sto05]. The three trigger types are present in the analysis, with Minimum Bias starting at low p_T, followed by High Tower 1 starting at 4.37 GeV, and High Tower 2 starting at 4.38 GeV. For clarity, High Tower 2 points are shifted

by 100 MeV (higher) when they overlap with High Tower 1. The upper panel also shows a power-law fit to the data, $Y = 5.241e2(1.381 + p_T)^{-9.888}$. The lower panel uses this fit to determine how the values compare to the data presented in this dissertation. As in earlier plots, the circles are Minimum Bias, 'X's are High Tower 1, and triangles are High Tower 2. Note that the general trend is for the data presented here to be about 25% higher than in the results from Stolpovsky. The discrepancy is most likely due improved understanding of detector performance and matching between simulation and real data. Runs where detector performance does not match nominal quality restrictions were removed entirely. This method leads to larger error bars in some analysis bins since the usable data sample was reduced.

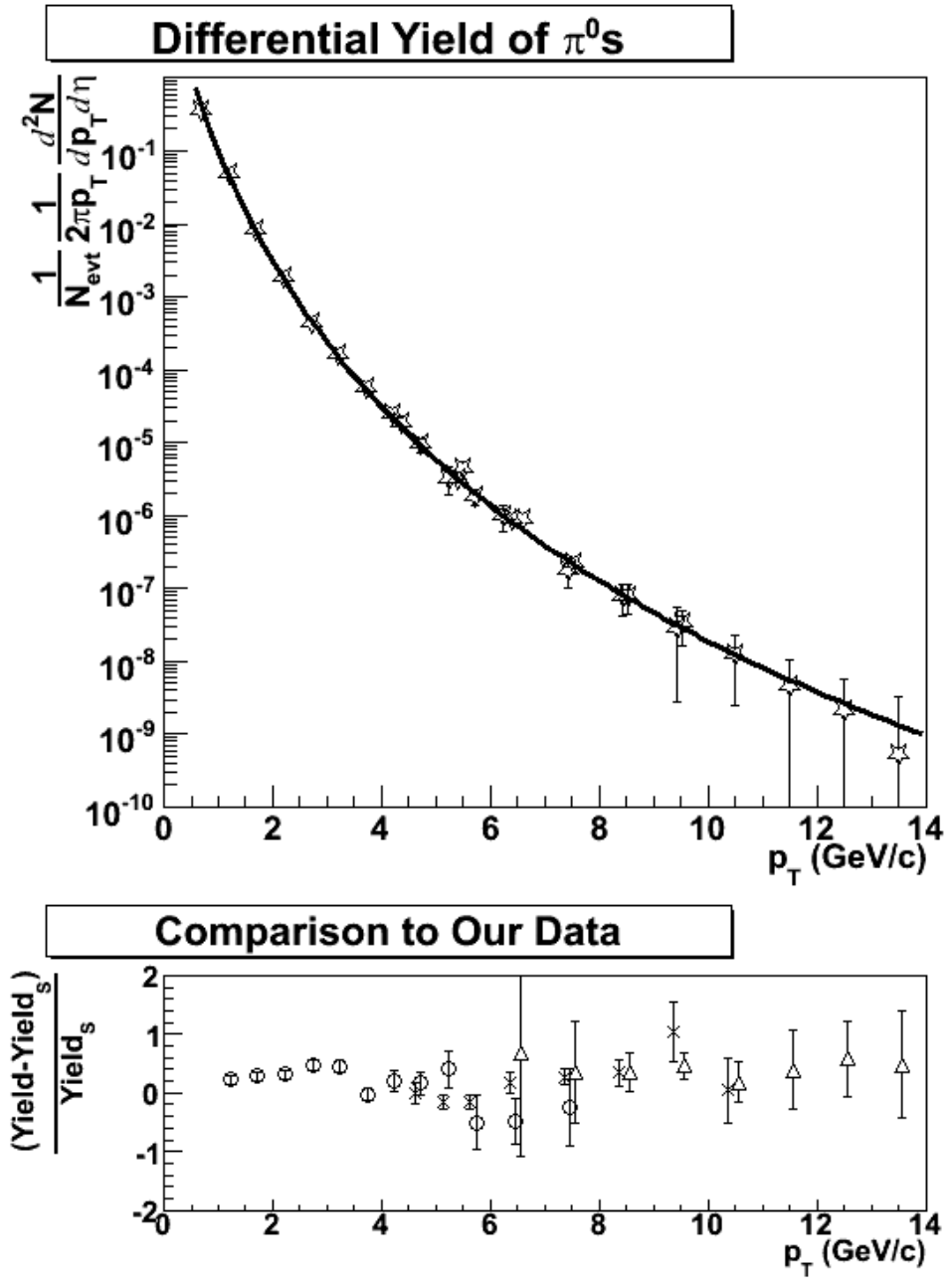

Figure 8.3: Results from alternate analysis of STAR data by Alexander Stolpovsky [Sto05] are compared. In the upper panel the results in [Sto05] are displayed together with a power-law fit to the data. In the lower panel our yield is compared to Stolpovsky's results and show an overall trend where the results developed here are consistently about 25% higher. This difference is discussed in the text.

Our data can also be directly compared to similar data collected by the PHENIX collaboration. Their detector is designed for good resolution of high-energy photons and therefore can measure π^0- and η-signals readily. The PHENIX collaboration has produced *d+Au* data that provides excellent reference spectra for our work.

PHENIX and STAR sample slightly different portions of *d+Au* interactions. The difference occurs because the exact portion of the cross section sampled by each experiment is determined by its respective trigger bias. Glauber model calculations were carried out to determine the effective number of binary collisions $\langle N_{bin} \rangle$ for each experiment, due to these trigger biases. For PHENIX, $\langle N_{bin} \rangle$ is 8.5±0.4 for the full minimum bias data set [Adl03c]. While for STAR, $\langle N_{bin} \rangle$ is 7.5±0.4, also for a similar minimum bias data set [Ada05]. Figure 8.4 shows a direct comparison of this measurement and the PHENIX *d+Au* inclusive π^0 spectrum, scaled to match the $\langle N_{bin} \rangle$ of the STAR minimum bias trigger. The lower panel shows the ratio of the two measurements.

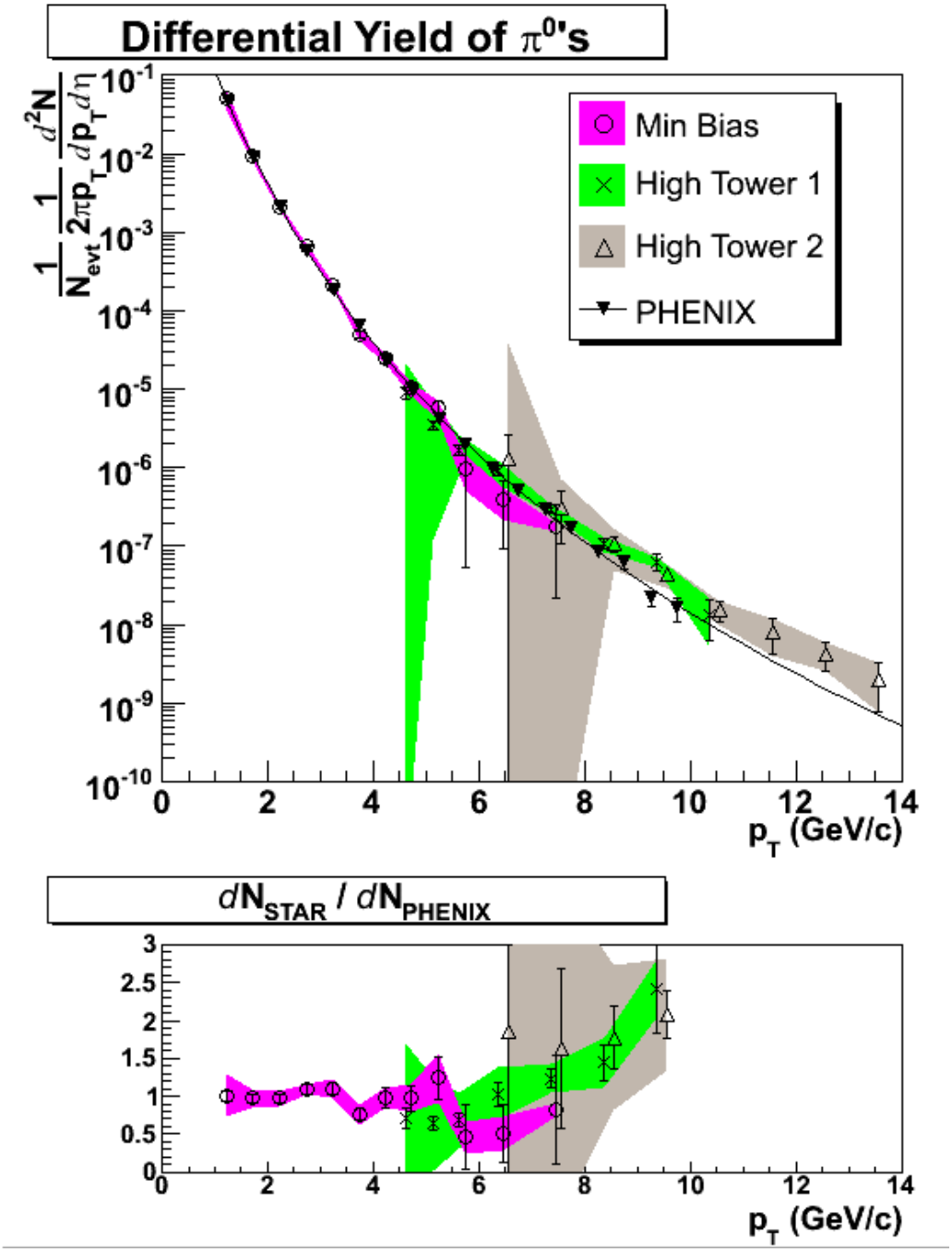

Figure 8.4: The inclusive π^0 yield in *d+Au* collisions is presented for STAR and PHENIX. The yields are shown together with a power-law fit to the PHENIX results in the upper panel. The lower panel shows the ratio of our results to those of PHENIX, which only extend out to 9.5 GeV/c. Note that there is quite good agreement in bins with both low systematic and statistical uncertainty.

The Figures 8.3 and 8.4 show that the data presented here fit well with parallel measurements from STAR and PHENIX. These comparisons show that the STAR BEMC produces reliable measurements and that those measurements are consistent with other experiments. The differences between STAR BEMC measurements with similar datasets, however, do beg additional understanding of the complexities of using this system. The primary pure physics result of interest here will now be discussed.

8.4 R_{dAu}

The primary measurement here, with impact to physics questions, is the nuclear modification factor R_{dAu}. The *Au+Au* result was shown above in Figure 8.1. The large departure from unity in central *Au+Au* collisions indicates the collision system does not behave like an incoherent set of nucleon-nucleon collisions. A duplicate measurement in *d+Au* collisions is used to determine the impact of the wave function of the Au nucleus on the system.

Using the PHENIX π^0 cross section as the *p+p* reference, R_{dAu} was calculated for the π^0 yields measured in this dissertation. The results are shown in Figure 8.5. The upper panel shows the results from all datasets. The lower panel shows the bins with the best constraints on uncertainty, the statistical uncertainty is shown in the error bars, while the uncorrelated systematic uncertainty for each point is shown in the band around the data. The 15% band around 1 includes scale uncertainty between the two experiments, as well as the uncertainty in the $\langle N_{bin} \rangle$ calculations for each experiment.

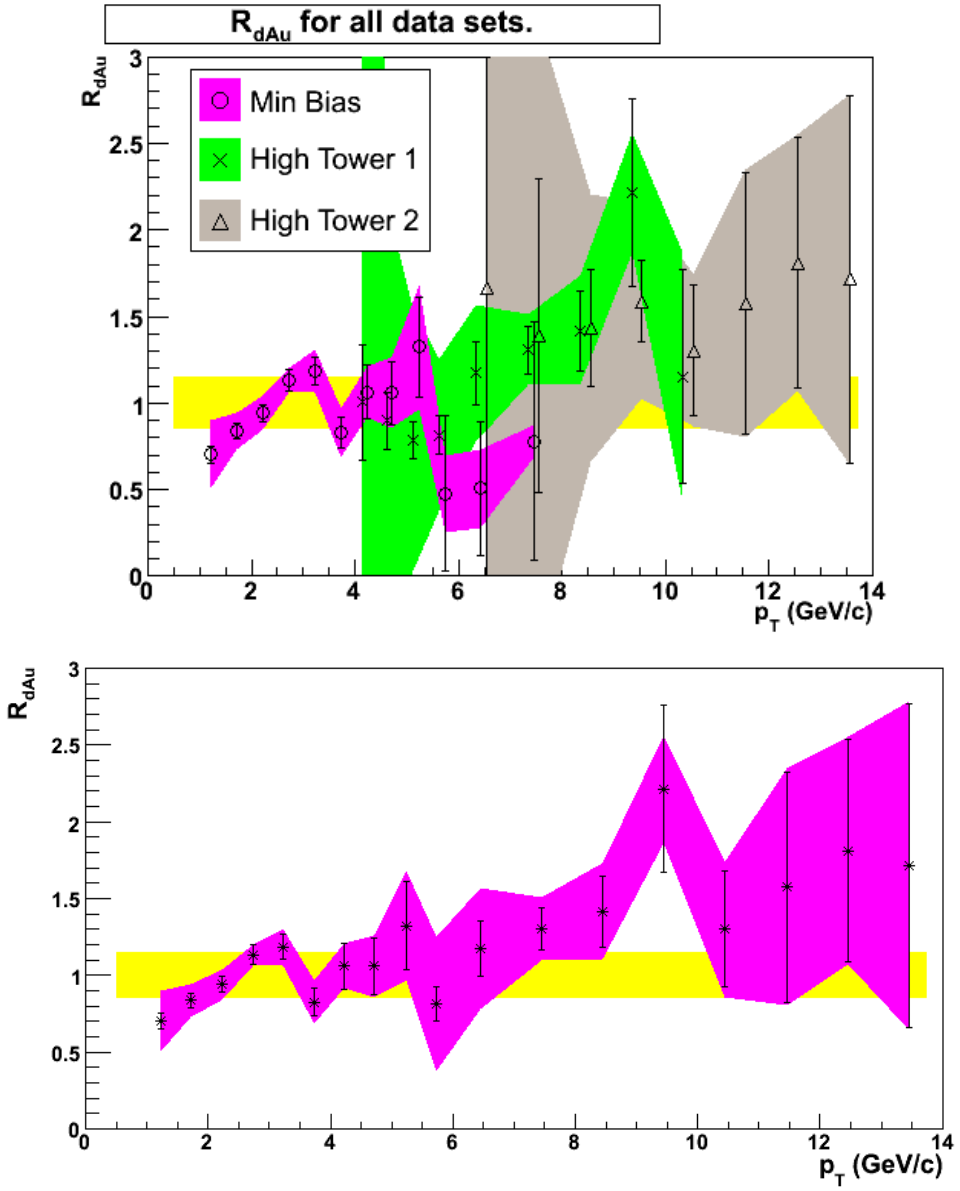

Figure 8.5: R_{dAu} for π^0s in collisions at $\sqrt{s_{nn}}$ = 200 GeV. The upper panel shows results for all datasets while the lower shows only the best point from each set. R_{dAu} was calculated from the π^0 results developed in this work, compared to the reference π^0 data for *p+p* collisions from the PHENIX collaboration. The data points show statistical error bars and systematic uncertainty band. Another band, around 1, indicates the scale uncertainty between the two data sets. An initial rise is expected due to Cronin enhancement. Beyond the initial rise the data agrees with $\langle N_{bin} \rangle$ scaling. This is in stark disagreement with *Au+Au* results.

Figures 8.6 and 8.7 provide comparison data for that shown in Figure 8.5. Figure 8.6 shows similar R_{dAu} results from the PHENIX collaboration, taking care to separate the measurements from two detector subests [Adl03c]. This figure also shows the *Au+Au* reference data. Although the results shown in Figure 8.5 have large uncertainty, the data is consistently at or above 1, while the *Au+Au* result from PHENIX, which is consistent with similar results from STAR, is much lower. The figure also shows some differences based on which portion of the PHENIX detector was used for analysis (PbGl: Pb-Glass, PbSc: Pb-Scintillator). Figure 8.7 shows a similar measurement of R_{dAu} from STAR [Sto05].

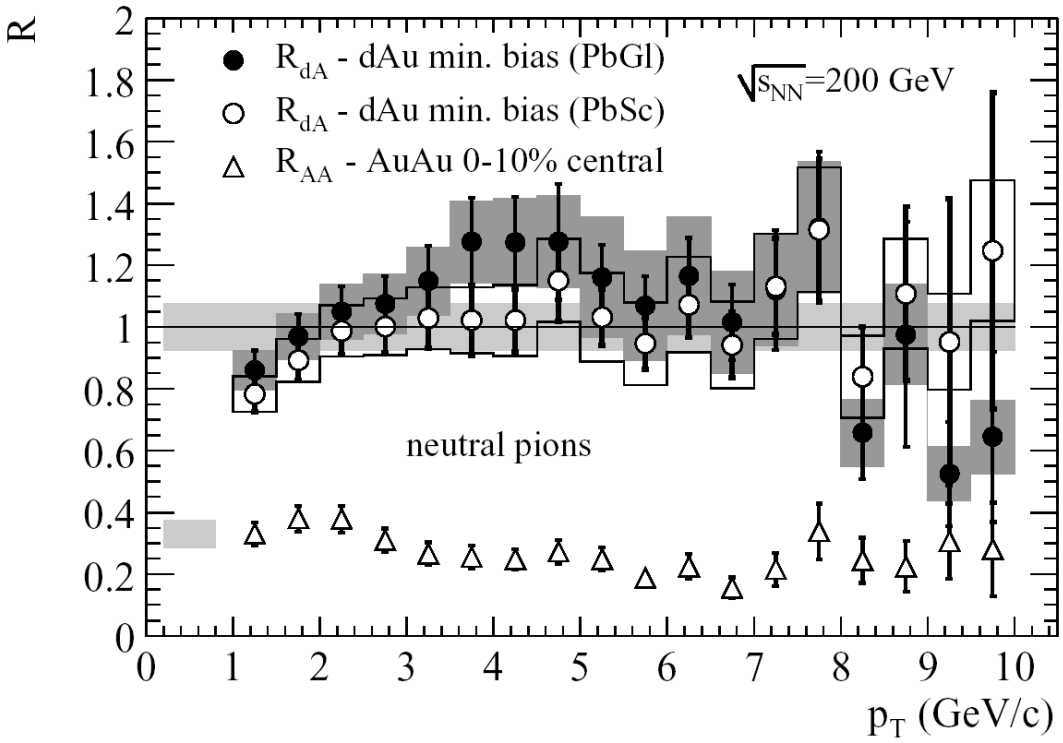

Figure 8.6: PHENIX R_{dAu} for π^0s at $\sqrt{s_{nn}}$ = 200 GeV. These results are very similar to figure 8.5. Also shown is R_{AA} for π^0s which is significantly lower than R_{dAu} here, as well as for our results above.

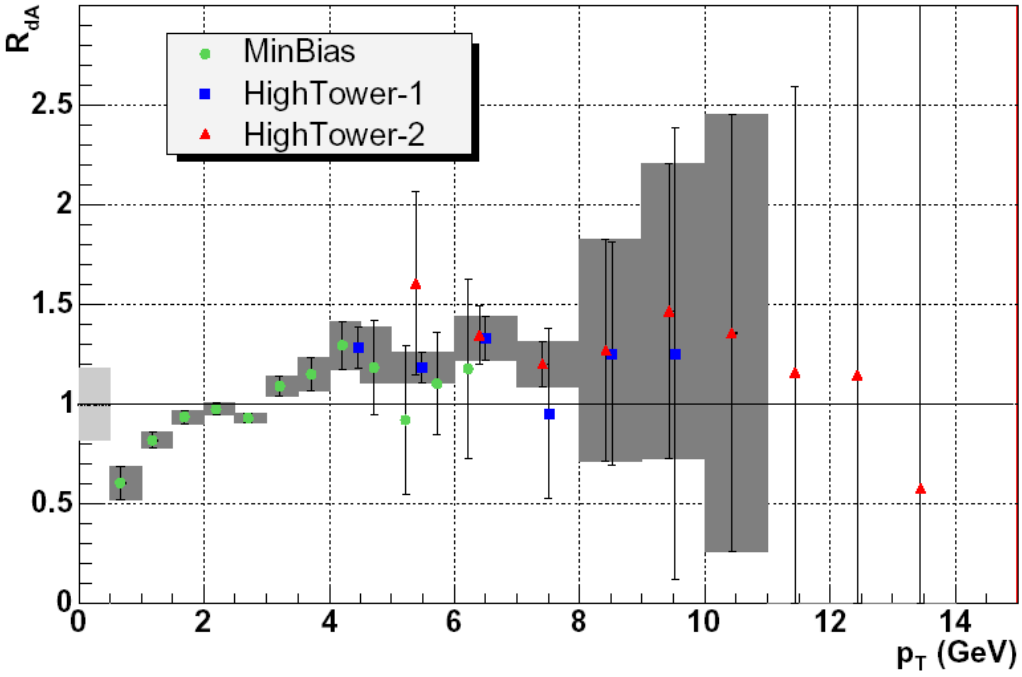

Figure 8.7: R_{dAu} for π^0s is shown for the alternate analysis of STARs *d+Au* data, as given in [Sto05].

8.5 Model Applicability

pQCD is known to provide a calculational framework for high-p_T cross sections in high energy collisions. It is clear that the results obtained for *p+p* collisions do not apply directly to central *Au+Au* collisions. Modifications to pQCD calculations due to the Au nucleus allow initial-state effects to describe observations in central *Au+Au* collisions to various degrees. If these models describe the actual dynamics of the *Au+Au* collisions then it is not necessary to invoke the QGP as an explanation. Thus it is important to study the range of acceptable initial-state effects attributable to the

Au nucleus in order to establish which effects are seen in collisions, and possibly eliminate those that do not require QGP to explain the central *Au+Au* results.

It is also possible that hadronic interactions in the final-state of *Au+Au* collisions may cause the pQCD description to fail. That is, interactions of jet-like hadrons with a hadronic medium created during the collision is an alternate explanation of high-p_T hadron suppression.

The results shown for R_{dAu} are consistent with *p+p* collisions. The low-p_T portion of the R_{dAu} results is consistent with Cronin enhancement, while the high-p_T portion cannot be distinguished from incoherent binary scattering. The latter result is qualitatively different from *Au+Au* collisions and is inconsistent with models that predict effects based solely on modifications to the Au wavefunction. The result is also qualitatively different from models predicting that final-state hadronic interactions may modify the high-p_T hadron spectra.

This dissertation is one of many analyses of *d+Au* collisions at $\sqrt{s_{nn}}$ = 200 GeV. The similar behavior of these collisions to binary-scaled *p+p*, as measured by R_{dAu} is a consistent theme across many such analyses across the experiments at RHIC.

8.6 Recent and Upcoming

RHIC is running *d+Au* collisions in the 2007-2008 run. This run also coincides with a more developed STAR BEMC, so the combination of more recorded collisions and larger reliable portion of the acceptance should result in better statistics. However, the primary physics goals of this run lie in studying the heavy quark contributions, and will thus include possibly large portions of data taken with charm quark based triggers.

To eliminate systematic uncertainty in the analysis, it is possible to use *p*+*p* measurements from STAR data for development of R_{dAu}. The Figure 8.7 is based on STAR-only data. There is not, however, STAR data for R_{AA} for π^0s. This is primarily due to the design of STAR's BEMC as a coarse spatial granularity calorimeter. In *Au*+*Au* central collisions the STAR BEMC reaches occupancy greater than 25% and combinatorics combined with signal degradation have made it very difficult to extract useful π^0 production cross sections.

8.7 Conclusion

This work reflects only a small part of the body of knowledge being generated by STAR and the rest of the detector facilities at RHIC. We have measured the mid-rapidity π^0 production spectrum in *d*+*Au* collisions at $\sqrt{s_{nn}}$ = 200 GeV from 1.25 < p_T < 9 GeV/c with 25% or better systematic uncertainty and an overall scale uncertainty of 15%. The data shown here can extend this range to 14 GeV/c, however the additional systematic uncertainty limits the applicability of the measurements.

Using the measured spectrum we have shown that the nuclear modification factor R_{dAu} for π^0s is similar to that measured in charged-hadron analyses at STAR and PHENIX. π^0 production in *d*+*Au* collisions does not show the suppression of high-p_T hadron production seen in central *Au*+*Au* collisions. This observation shows that π^0 production is not affected by the incoming Au wavefunction. The observation also provides evidence that the suppression in *Au*+*Au* collisions is due to the interaction of high-p_T partons with the dense medium created in the collisions.

RHIC and its detector experiments have produced and observed collisions that behave in partially anticipated and partially unanticipated ways. In devising different conditions for the collisions the results have shown that something interesting is being produced in RHIC central *Au+Au* 200 GeV collisions. Evidence is still being mounted as to the nature of the produced medium, but it is clear that if it is QGP then QGP conditions produce many exciting effects upon particles traversing it and upon the entire collision system as it briefly equilibrates.

APPENDIX A

Acronyms

ADC	Analog-to-Digital Converter
AGS	Alternating Gradient Synchrotron
AtR	AGS to RHIC transfer line
BBC	Beam-Beam Counter
BEMC	Barrel Electromagnetic Calorimeter
BNL	Brookhaven National Laboratory
BRAHMS	Broad RAnge Hadron Magnetic Spectrometers
BSMD	Barrel Shower Maximum Detector (also SMD)
BtA	Booster to AGS transfer line
CERN	European Organization for Nuclear Research
CTB	Central Trigger Barrel
DAQ	Data Acquisition
DGLAP	Dokshitzer-Gribov-Lipatov-Altarelli-Parisi
FTPC	Forward Time-Projection Chamber
GEANT	GEometry ANd Tracking
HIJING	Heavy Ion Jet INteraction Generator
HT	High-Tower (or HT1, HT2 for High-Tower 1 or 2)
IR	Intersection Region
KKP	Kniehl-Kramer-Pötter
LHC	Large Hadron Collider
MB	Minimum Bias
MIP	Minimum-Ionizing Particle
NLO	Next to Leading Order (as in pQCD)
NNLO	Next to Next to Leading Order (as in pQCD)
PHENIX	Pioneering High Energy Nuclear Interaction eXperiment
PHOBOS	(not an acronym – named for Mars' moon)
PMT	Photo-Multiplier Tube
PSF	Prescale Factor
pQCD	Perturbative QCD
QA	Quality Assurance
QCD	Quantum Chromodynamics
QED	Quantum Electrodynamics
QGP	Quark-Gluon Plasma
RCF	RHIC Computing Facility
RF	Radio-Frequency

RHIC	Relativistic Heavy Ion Collider
SMD	Shower Maximum Detector (also BSMD)
SPS	Super Proton Synchrotron
STAR	Solenoidal Tracker at RHIC
SVT	Silicon Vertex Tracker
TCU	Trigger Control Unit
TCD	Trigger Clock Distribution (has other meanings in STAR)
TOF	Time of Flight
TPC	Time Projection Chamber
TtB	Tandem to Booster transfer line
UCLA	University of California, Los Angeles
UPC	Ultra-Peripheral Collision(s)
WLS	Wavelength-Shifting Fiber
ZDC	Zero Degree Calorimeter

APPENDIX B

Experiment Data Book

This appendix is a collection of some physical constants and materials parameters that are important to this work.

AGS Extraction: $\gamma = 10.520480$ (Au and deuteron) [Gar01, DeL01]
RHIC Store: $\gamma = 107.396090$ (Au and deuteron) [Gar01]
STAR Intersection Region: 6 O'clock

Au (+79):
Mass: 183.4331220 (GeV/c^2)
Collision Energy: 100.000000 (GeV/n) [Gar01]
Binding Energy: 8.0 (MeV/n)

d (+1):
Mass: 1.875612762 (GeV/c^2)
Collision Energy: 100.716738 (GeV/n) [Gar01]
Binding Energy: 1.1 (MeV/n)

Pb – BEMC Conversion Material
Critical Energy, E_c: 7.5 MeV [WN02]
Radiation Length, X_0: 0.56 cm

Kuraray SCSN81 – BEMC Scintillator Material
Critical Energy, E_c: 80 MeV [WN02]
Radiation Length, X_0: 42.4 cm

π^0:
Mass: 134.9766 ± 0.0006 MeV [WN02]
2γ Branching Ratio: $98.798 \pm 0.032\%$
Mean Lifetime (τ): $(8.4 \pm 0.6) \times 10^{-17}$ s.

APPENDIX C

Relativistic Kinematics

For relativistic heavy ion collisions, the following kinematic variables are used.

$$p = \left(E, p_x, p_y, p_z\right) \Rightarrow \left(E, p_T, \theta, \phi\right) \Rightarrow \left(E, p_T, \eta, \phi\right) \tag{C.1}$$

Where θ is the angle between the momentum and the beam-line, p_T is the transverse momentum, and η is the pseudorapiditiy, they are defined as follows.

$$\begin{aligned} p_T &= \sqrt{p_x^2 + p_y^2}, \\ \theta &= \tan^{-1}\left(\frac{p_y}{p_x}\right), \\ \phi &= \tan^{-1}\left(\frac{p_T}{p_z}\right), \\ \eta &= -\ln\left(\tan\left(\frac{\theta}{2}\right)\right) \end{aligned} \quad , \tag{C.2}$$

Particles that decay into two photons are observed by using the 4-vectors associated with each photon to construct the invariant mass of the original particle. The mass of the candidate particle is found by determining the invariant mass of the two-photon system as follows (the *c*-subscripts indicate "candidate").

$$\begin{aligned} \overrightarrow{p_C} &= \overrightarrow{p_1} + \overrightarrow{p_2}, \\ E_C &= E_1 + E_2 \\ m_C^2 &= \left|p_1 + p_2\right| = 2E_1E_2 - 2\overrightarrow{p_1} \cdot \overrightarrow{p_2} \\ &= 2E_1E_2\left(1 - \cos\alpha\right) \end{aligned} \tag{C.3}$$

Here α is the opening angle between the two momentum vectors.

APPENDIX D

Shower Development

In this appendix the properties of electromagnetic showers in the BEMC are briefly discussed. The primary goal of this appendix is to provide reference material for evaluating the size of an electromagnetic shower in the BEMC in order to compare it to the size of the BEMC towers and SMD strips.

The transverse development of electromagnetic showers in media are best described by the Molière radius [WN02]:

$$\frac{1}{R_M} = \frac{1}{E_s} \sum \frac{w_j E_{cj}}{X_j}, \qquad \text{(D.1)}$$

where the sum is over the different materials the shower is passing through, $E_s \approx 21$ MeV, w_j is the weight fraction of the given material, X_j is the radiation length of the material, and E_{cj} is Rossi's form of the critical energy for the material. (The standard definition of the critical energy is that it is the energy where the energy loss due to Bremsstrahlung is equal to the energy loss due to ionization. Rossi's form for the critical energy is more appropriate for describing shower development. In that form, the critical energy is given by the energy where $| dE / dx |_{\text{brems}} \approx E / X_0$ [WN02].)

The materials and arrangement for the towers of the BEMC are described in [Bed03]. The detector has 20 layers of Pb and 21 layers of scintillator, with the first layer of scintillator coming before the lead to provide the preshower layer. The SMDs, made of Al, circuit-board, and gas, are about the thickness of two layers of Pb

and scintillator, and have little impact on this calculation. For Pb, E_c is about 7.5 MeV and X_j = 0.56cm. For the scintillator material (Kuraray SCSN81), E_c is about 80 MeV and X_j = 42.4cm. The actual scintillator material is polystyrene with some doping chemicals; but it is essentially just polystyrene. Since the linear thickness of each is about the same, the factor of 100 difference suggests only Pb is important in the shower development. We could add about 1% to the result for R_M from taking all the material as Pb.

The Pb result is R_M = 1.57cm. R_M contains about 90% of the shower energy, while 3.5 R_M contains about 99% of it. 99% of the energy is then contained in a diameter of about 10cm. BEMC towers are roughly 10cm by 10cm. Thus 99% of the energy from an electromagnetic shower will be contained in a region small enough that 4 towers, arranged 2 by 2, will contain it. Further, since the strips in the SMDs are roughly 1.5cm wide, 90% of the energy in an electromagnetic shower will be contained in 2 to 3 strips, allowing identification of the shower position.

APPENDIX E

Opening Angle and Energy Asymmetry Density Distributions

For relativistic decays, the density of decays that can be found within a detector element is critical for selecting the best configurations. Once data is selected, knowledge of the distributions expected of detected particles allows quality control and background reduction. In this appendix we will provide distributions for the density of particle decays as a function of opening angle, α, and energy asymmetry ε.

The parameters α and ε are defined by observed signals. In particular, for our work, π^0-decay photons impinge on the BEMC and deposit energy. The energies and positions of these depositions give the energy-momentum 4-vectors:

$$p_1' = \begin{pmatrix} E_1' \\ p_{1T}' \\ p_{1L}' \end{pmatrix}, p_2' = \begin{pmatrix} E_2' \\ p_{2T}' \\ p_{2L}' \end{pmatrix} \tag{E.1}$$

Where the primes indicate these are measured after a boost to the laboratory frame, and the azimuthal angle has been suppressed (so that only p_T, transverse momentum, is carried). Only two components of the momentum vectors are given, the transverse and the longitudinal. Using these two momenta, α and ε are defined as follows:

$$\varepsilon = \frac{\left|E_1' - E_2'\right|}{E_1' + E_2'}, \alpha = \cos^{-1}\left(\frac{\vec{p}_1' \cdot \vec{p}_2'}{\left|\vec{p}_1'\right|\left|\vec{p}_2'\right|}\right), \tag{E.2}$$

Here the vector symbols indicate regular vector operations on the transverse and longitudinal components of the 4-vectors[1].

The densities of decays at given α and ε can be calculated. The procedure parallels the process of determining either of these parameters for a general decay. That is, we consider a decay in the π^0s reference frame, then determine how a boost modifies the distributions of detected α and ε.

The general case of a decaying π^0 is shown in Figure E.1 in three panel. First the π^0 is moving, it then decays, and the final shows the effect of a relativistic boost. Here the initial π^0 decays into two back-to-back photons that are rotated by an angle θ relative to the direction of motion. Then the photons are boosted to produce the 4-vectors discussed above.

[1] We will refer to these as 4-vectors and assert that if the azimuthal angle is tracked it makes no impact on the calculations. Without the azimuthal angle, the x- and y- components collapse to a simple transverse component.

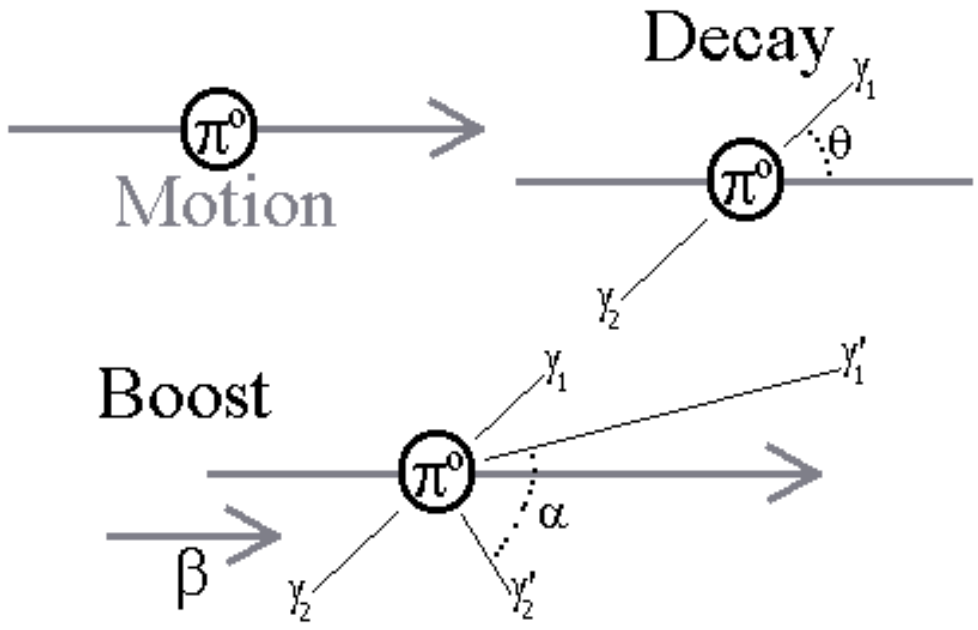

Figure E.1: The general process of π^0 decay is shown in stages (left to right, then bottom). First the π^0 is taken to be in motion. Its decay is then considered, as two photons, γ_1 and γ_2, are produced. The system is then boosted due to the initial π^0 velocity, β.

The unboosted photons are described by the 4-vectors below:

$$p_1 = \frac{m}{2}\begin{pmatrix} 1 \\ \cos\theta \\ \sin\theta \end{pmatrix}, p_1 = \frac{m}{2}\begin{pmatrix} 1 \\ -\cos\theta \\ -\sin\theta \end{pmatrix} \tag{E.3}$$

Following a boost to the inertial frame of the π^0, the final 4-vectors are:

$$p_1{}' = \frac{m}{2}\begin{pmatrix} \gamma+\gamma\beta\cos\theta \\ \gamma\beta+\gamma\cos\theta \\ \sin\theta \end{pmatrix}, p_2{}' = \frac{m}{2}\begin{pmatrix} \gamma-\gamma\beta\cos\theta \\ \gamma\beta-\gamma\cos\theta \\ \sin\theta \end{pmatrix} \tag{E.4}$$

The norms of the momenta given in the 4-vectors are surprisingly simple, and are given below:

$$\left|\vec{p}_1{}'\right|, \left|\vec{p}_2{}'\right| = \frac{m}{2}\gamma\left(1 \pm \beta\cos\theta\right) \tag{E.5}$$

Combining this information we can determine the dependence of the decay density on the parameters α and ε. Specifically we wish to calculate $dN/d\alpha$ and $dN/d\varepsilon$. These are determined by finding the products $dN/d\theta \cdot d\theta/d\alpha$ and $dN/d\theta \cdot d\theta/d\varepsilon$. The density of decays as a function of θ is proportional to the surface area of the portion of a sphere carved at that angle.

A couple useful intermediate forms are handy:

$$\begin{aligned}
\cos\alpha &= 1 - \frac{2}{1+\gamma^2\beta^2\sin^2\theta}, \\
\sin\alpha &= \frac{2\gamma\beta\sin\theta}{1+\gamma^2\beta^2\sin^2\theta}, \\
1-\cos\alpha &= \frac{2}{\gamma^2}\left(1-\beta^2\cos^2\theta\right)^{-1} \\
\sin\theta &= \frac{\sin\alpha}{\gamma\beta(1-\cos\alpha)}
\end{aligned} \qquad \text{(E.6)}$$

We know that the limits for the opening angle occur when the decay is either parallel or perpendicular to the direction of motion. The largest opening angle occurs when $\theta = 0$, which corresponds to $\cos\alpha = -1$, or $\alpha = \pi$ (see E.6, third equation). The smallest opening angle occurs when $\theta = \pi/2$, where $1 - \cos\alpha = 2/\gamma^2$.

The relationships between the relevant variables, then, can be seen in Equations E.7 below.

$$\begin{aligned}
\frac{dN}{d\theta} &= C\sin\theta \\
\frac{d\theta}{d\varepsilon} &= \left(\frac{d\varepsilon}{d\theta}\right)^{-1} = \left(\beta\sin\theta\right)^{-1} \\
\frac{d\theta}{d\alpha} &= \left(\frac{d\alpha}{d\theta}\right)^{-1} = \frac{\gamma\beta\left(1+\gamma^2\beta^2\sin^2\theta\right)}{\cos\theta}
\end{aligned} \quad , \qquad \text{(E.7)}$$

From Equations (E.6) and (E.7) it is straight-forward, but tedious, to show that the densities of interest, expressed in their natural variables, are the following:

$$\frac{dN}{d\varepsilon} = \frac{dN}{d\theta}\frac{d\theta}{d\varepsilon} = C/\beta$$

$$\frac{dN}{d\alpha} = \frac{dN}{d\theta}\frac{d\theta}{d\alpha} = C\gamma^2\beta\sin\alpha\left(\frac{\beta^2}{\left(1-\frac{2}{\gamma^2(1-\cos\alpha)}\right)^{\frac{1}{2}}} - \left(1-\frac{2}{\gamma^2(1-\cos\alpha)}\right)^{\frac{1}{2}}\right), \quad \text{(E.8)}$$

Where the limits of validity are $0 \le \varepsilon \le \beta$, and $\cos^{-1}(1 - 2/\gamma^2) \le \alpha \le \pi$. Note that the small angle approximation of cosine gives the minimum opening angle of $\alpha = 2/\gamma$.

From these densities, it is clear that the density of decays as a function of energy asymmetry is constant. It is also clear that the density of decays as a function of opening angle is singular at the minimum. The equations are used to produce density figures seen in Section 6.1 (Figure 6.1.1).

APPENDIX F

$dy/d\eta$

A small problem arises in analyses based on the STAR detector, related to rapidity. It is quite common for such analyses to arbitrarily change between rapidity, y, and pseudorapidity, η. There is, of course, a difference in using these variables. In this appendix we will give the relationship between these two variables, how they change relative to each other, and the impact of replacing dy with $d\eta$ in calculations.

All relationships between these two variables can be determined from three basic statements.

$$\begin{aligned} y &= -\frac{1}{2}\log\left(\frac{E - p_Z}{E + p_Z}\right), \\ \eta &= -\log\left(\tan\left(\frac{\theta}{2}\right)\right), \\ \cos\theta &= \tanh\eta. \end{aligned} \tag{F.1}$$

It is then straightforward to show the following.

$$\begin{aligned} y &= -\frac{1}{2}\log\left(\frac{\gamma m - p\cos\theta}{\gamma m + p\cos\theta}\right) = -\frac{1}{2}\log\left(\frac{1 - \beta\tanh\eta}{1 + \beta\tanh\eta}\right), \\ \frac{dy}{d\eta} &= \beta\frac{1}{1 + \frac{1}{\gamma^2}\sinh^2\eta} \end{aligned} \tag{F.2}$$

Utilizing Equations F.2, one can show that for the pseudorapidity window used in the analysis (0 to 1), the resulting rapidity window is 99% of this, for π^0s at 1.5 GeV/c (γ = 10). This window expands to 99.7% at γ = 20. Thus, changing from y to η has a

negligible effect on this work, given the other sources of uncertainty. Furthermore, the differential impact at mid-rapidity can be seen to be β. For this work, β is 99.5%c or higher, in all analysis bins.

APPENDIX G

Yield Results

This appendix reports the total yield for the minimum bias, high tower 1, and high tower 2 datasets. The yields were determined using a Gaussian plus polynomial fit, which was then tested using the bin summing method to obtain counts using an alternate method.

This data was obtained by histogramming the invariant mass of two-photon pairs in the 183 runs used for analysis. Event cuts include trigger, $|Z|<60$ cm, and number of BEMC points below 70. The photon candidates must leave signals in both SMD planes, and be free of charged particle contamination, they must also come from regions of the detector determined to be acceptable. The π^0 candidate pairs must have energy asymmetry below 0.5. The extracted yields are presented in Table [G.1].

The normalization of each bin, for determination of per-event yield requires two quantities beyond the detected counts. The first is the appropriate number of events, which is determined by the equations in the text for determining the appropriate number of minimum bias events for each trigger type (see Table [6.2.3]). For minimum bias, this is 7.463×10^6 events, 2.512×10^8 for high tower 1, and 2.083×10^9 for high tower 2. For the calculation of per event yield, the appropriate p_T must be chosen. We choose the p_T to be that where the weighting function is equal to its average on the interval. While this is not explicitly correct for this dataset, it makes the final calculations, including the application of efficiencies much more

straightforward. What we show here, as the per-event yield, is $1/N_{evt}\ 1/2\pi p_T\ d^2N/dp_Td\eta$.

Table G.1: π^0 counts in the standard analysis bins.

Trigger	p_T range (GeV/c)	Bin p_T (GeV/c)	Yield	Statistical Error	Systematic Uncertainty	Per Event Yield
Min Bias	1.0-1.5	1.22	3.18e4	5.9e2	3.7e3	1.11e-3
	1.5-2.0	1.72	1.66e4	2.5e2	1.3e3	4.12e-4
	2.0-2.5	2.23	6.44e3	1.3e2	6.6e2	1.23e-4
	2.5-3.0	2.73	2.68e3	7.6e1	1.6e2	4.19e-5
	3.0-3.5	3.23	1.03e3	4.9e1	1.1e2	1.36e-5
	3.5-4.0	3.73	2.96e2	2.7e1	5.1e1	3.38e-6
	4.0-4.5	4.23	1.43e2	1.9e1	2.0e1	1.44e-6
	4.5-5.0	4.73	6.78e1	1.1e1	1.3e1	6.11e-7
	5.0-5.5	5.23	4.45e1	9.5e0	1.2e1	3.63e-7
	5.5-6.0	5.73	8.06e0	7.6e0	3.8e0	6.00e-8
	6.0-7.0	6.44	7.23e0	5.5e0	3.2e0	2.39e-8
	7.0-8.0	7.45	6.98e0*	6.1e0	7.5e-1	1.14e-8
High Tower 1	4.0-4.5	I4.23	6.58e1	1.5e1	5.1e1	1.97e-8
	4.5-5.0	4.73	2.40e2	2.6e1	6.9e1	6.43e-8
	5.0-5.5	5.23	2.67e2	2.6e1	2.9e1	6.47e-8
	5.5-6.0	5.73	2.44e2	3.0e1	5.0e1	5.40e-8
	6.0-7.0	6.44	4.17e2	6.1e1	8.0e1	4.10e-8
	7.0-8.0	7.45	2.04e2	2.0e1	2.1e1	1.73e-8
	8.0-9.0	8.45	9.44e1	1.5e1	9.8e0	7.08e-9
	9.0-10.0	9.45	5.77e1	1.4e1	8.4e0	3.87e-9
	10.0-11.0	10.45	2.44e1*	1.3e1	1.5e1	8.63e-10
High Tower 2	6.0-7.0	6.44	3.06e1	1.2e1	2.3e1	3.63e-10
	7.0-8.0	7.45	2.35e2	3.0e1	1.1e2	2.41e-9
	8.0-9.0	8.45	3.27e2	2.9e1	7.5e1	2.96e-9
	9.0-10.0	9.45	2.18e2	4.4e1	3.1e1	1.76e-9
	10.0-11.0	10.45	1.12e2	1.8e1	3.2e1	8.19e-10
	11.0-12.0	11.45	6.71e1	5.5e1	3.2e1	4.48e-10
	12.0-13.0	12.45	3.76e1	1.1e1	1.5e1	2.31e-10
	13.0-14.0	13.45	3.00e1*	1.2e1	1.9e1	1.01e-10

*The final bins from all trigger sets were taken from analysis with |Z|<180 cm. The event counts were 1.305e7, 4.306e8, and 3.503e9 for minimum bias, high tower 1, and high tower 2, respectively.

APPENDIX H

Convergence of p_T-Weighting

H.1 Statement of the Problem

When weighting a flat simulation spectrum, a "guess" theory function must be assumed. The "guess" function may not accurately reflect the real production spectrum, and the impact of any discrepancies must be considered.

The "guess" function mixes results from earlier or later (in respect to p_T) in the bin differently, and may incorrectly give weight to portions of the bin where detector efficiency may be greatly changing, so that the simulation may be unstable We look at this situation in detail for two distinct data situations in this appendix.

The first situation for consideration is where the efficiency of the data collection is perfect, or at least constant. Second, we will consider the situation where the efficiency is not constant. We will not cover the situation where nothing is known of the production function. In that case, we suggest an iterative process. First, plot the points at the bin centers. Then use the resulting curve to generate an empirical production distribution. Then use that production distribution as a "theoretical" production distribution and follow the steps discussed here.

It is useful to present the issue as a proposition with related questions. Once the problem is stated, a discussion of solution techniques will be presented in the following sections.

For a particle p with production distribution $f(p_T)$ there are several questions which must be understood in order to appropriately interpret the detection distribution $h(p_T)$. Here $h(p_T)$ is the distribution of particles observed in the analysis. Note that both of these functions are normalized so that they present the production during a single event.

$$\begin{matrix} f(p_Y) \equiv \text{Real Particle Production Distribution} \\ h(p_Y) \equiv \text{Detected Particle Distribution} \end{matrix}, \qquad \text{(H.1)}$$

This sort of analysis is made with focus on a particular p_T-Bin $B=(p_{Ti},p_{Tf})$. The analysis is also done by considering some large number of events, N, over which the data is averaged. Then the total number of detected particles in bin B is $D_B = \int_B N h(p_T) dp_T$ while the number of produced particles is $P_B = \int_B N f(p_T) dp_T$.

We will show here the following. If the detector response is correctly simulated then the process of using the detected spectrum to create a new weighting function will converge to the real production spectrum.

Situation A: The simplest situation is that a constant fraction of all produced particles are detected. I.e. $h(p_T) = Cf(p_T)$. In this case, what is the appropriate efficiency, (ε_B), for detection of particles in bin B? At what p_T should the normalized yield $y_B = D_B / (\varepsilon_B \cdot N \cdot B)$ (where B is the bin size) be plotted?

Situation B: In general, the relationship between $f(p_T)$ and $h(p_T)$ can be extremely complicated. Simple examples are that the detected p_T can be smeared, or shifted, and the fraction of detected particles, even if p_T does not change, may be a function of p_T. In order to investigate the resulting distributions and determine how to interpret the observed data, simulations are used. This is generally more at risk to uncertainty

than situation A above, but it is a more accurate statement of the situation in this analysis.

In this case a theoretical production distribution $g(p_T)$ is assumed. For our analysis, n particles are then simulated with constant density $n/\Delta p_T$. (In general, simulations made using the theoretical distribution $g(p_T)$ are favorable, however, in this case g changes by about 7 orders of magnitude over the p_T-range, and g is not well know and is subject to change after production of simulations.) The detected simulation density is $s(p_T)$. What we want to know in this case is again the efficiency for detecting the particles on B, (ε_B), and the appropriate p_T at which to plot the normalized yield $y_B = D_B/(\varepsilon_B \cdot N \cdot B)$.

H.2 Discussion for Situation A

For this case, in N events, the number of particles produced in bin B is

$$P_B = \int_B N f(p_T) dp_T . \tag{H.2}$$

The number of detected particles in B is

$$\begin{aligned} D_B &= \int_B N h(p_T) d p_T \\ &= \int_B NC f(p_T) d p_T \end{aligned} . \tag{H.3}$$

And since N and C are constant, we have:

$$P_B = N\int_B f(p_T) dp_T ; D_B = NC\int_B f(p_T) dp_T , \tag{H.4}$$

which immediately gives a good value for the efficiency

$$\varepsilon_B = D_B / P_B = C . \tag{H.5}$$

This choice of efficiency allows us to determine the appropriate p_T by examination.

The data-point for bin B, (V_B), then becomes

$$V_B = D_B \Big/ \left(C \cdot N \cdot B\right) = \tfrac{1}{B} \int_B f\left(p_T\right) dp_T = \left\langle f\left(p_T\right) \right\rangle_B, \qquad \text{(H.6)}$$

and the appropriate p_T is then

$$p_{TB} = f^{-1}\left(\left\langle f\left(p_T\right) \right\rangle_B\right). \qquad \text{(H.7)}$$

Thus, in the case of constant efficiency, C, where p_T-modification of detected particles can be ignored, we have the following. $V_B = D_B / \left(C \cdot N \cdot B\right)$, and it should be plotted at $p_{TB} = f^{-1}\left(\left\langle f\left(p_T\right) \right\rangle_B\right)$.

H.3 Discussion for Situation B

The second situation, where the relationship between the production distribution $f(p_T)$ and the detection distribution $h(p_T)$ can be arbitrary, requires consideration of a few alternative approaches. Therefore, although the best answer is relatively simple, it is not clear that it applies to the various ways of considering the problem. Hence this discussion will split at a few points to explore different solutions, but the explorations will ultimately come to the same course of action on each split.

The general case of an arbitrary relationship between $f(p_T)$ and $h(p_T)$ is much more tricky than in discussion A. One of the major risks here is that the real production density $f(p_T)$ is unknown.

To enable analysis a theoretical production distribution $g(p_T)$ must be chosen. Luckily, the overall normalization of $g(p_T)$ cancels out of all results. Unluckily, however, it is difficult to establish that the choice of $g(p_T)$ and the resulting $f(p_T)$ do not, circularly, establish an incorrect production density. That is, the choice of $g(p_T)$ produces a set of efficiencies (ε_{Bi}), one for each bin B_i, and associated p_{TB}'s. These,

in turn provide $f(p_T)$. The validity of the process is established by (1) noting that $g(p_T)$ agrees with $f(p_T)$ or by (2) replacing $g(p_T)$ by $f(p_T)$ and repeating the process till agreement is found. It is not at all obvious if this process will converge to a unique, and therefore correct production density $f(p_T)$.

A shape that agrees with past experience, and generally agrees with theoretical expectations is chosen for $g(p_T)$. Particles are simulated with constant density $n/\Delta p_T$. The simulated particles are then reconstructed and weighted by $g(p_{Ts})$ where p_{Ts} is the simulated p_T of the particle (as opposed to its "reconstructed" p_{Tr}). The resulting density is $s(p_T)$, to which we evaluate the detected particles in B is D_B^s.

$$D_B^s = \int_B s(p_T) dp_T \,, \tag{H.8}$$

What should D_B^s be compared to? Reason suggest that we compare it to what would have happened if all the simulated particles were detected with their original p_Ts.

In this case, the expected measurement matches the simulation, or P_B^s.

$$P_B^s = \int_B n g(p_T) dp_T \,, \tag{H.9}$$

Here n total particles are simulated, but $g(p_T)$ is the distribution for π^0 with this p_T, given an event occurred, so $g(p_T)$ handles the per-event probability a π^0 was created. That is, in one event, $\int_B g(p_T) dp_T = p(\text{particle in B, averaged over n events})$. Therefore $n\int_B g(p_T) dp_T = \langle \#\text{ of particles in n events} \rangle = \int_B n g(p_T) dp_T)$. (This assumes a certain normalization for g which will divide out and does not affect the calculations.) Then the definition of efficiency follows directly

$$\varepsilon_B = \frac{D_B^s}{P_B^s} = \frac{\int_B s(p_T)dp_T}{\int_B ng(p_T)dp_T}. \tag{H.10}$$

Since the number of observed particles is D_B, this means that the resulting yield is

$$V_B = \frac{D_B}{N\varepsilon_B B} = \frac{D_B}{NB}\cdot\frac{P_B^s}{D_B^s}. \tag{H.11}$$

If the simulation's production distribution is accurate and the simulated detector response is right, then some stuff should cancel, because $h(p_T) = Cs(p_T)$, so

$$D_B = \int_B Nh(p_T)dp_T = \int_B NCs(p_T)dp_T = NCD_B^s. \tag{H.12}$$

Then what is *C*? By definition, $h(p_T)$ is the detection distribution for a single event. $s(p_T)$, however, is the production density of reconstructed particles for the entire simulation. In the simulation, *n* events are simulated, so $s(p_T) = nh(p_T)$, and it follows that $C = n$. Thus $D_B = \frac{N}{n}D_B^s$

$$V_B = \frac{\frac{N}{n}D_B^s}{NB}\cdot\frac{P_B^s}{D_B^s} = \frac{P_B^s}{nB} = \langle g(p_T)\rangle_B. \tag{H.13}$$

The appropriate p_T (as in discussion of situation A) is the p_T where $g(p_{TB}) = \langle g(p_T)\rangle_B$.

V_B is plotted at

$$p_{TB} = g^{-1}\left(\langle g(p_T)\rangle_B\right). \tag{H.14}$$

Three questions should be addressed. (1) Does this method reproduce $g(p_T)$ if $f(p_T)$ is not similar to $g(p_T)$? (2) How does this method perform if, e.g. the energies are always 10% too high, and therefore the new detection function

$h(p_T) = h(0.9p_T)$? Finally, (3), where should data that has not been efficiency-corrected be placed?

Question (1) is important to knowing the validity of the method. Certainly, if we select a theoretical production distribution $g(p_T)$ which is wrong, if the method used to position the points does not show this incorrect choice, then we are at risk of having a biased result.

It should be sufficient here to show that if the efficiency is constant then the resulting behavior must match $f(p_T)$. If it matches for the constant efficiency case, then others follow by taking arbitrarily small bin sizes so that the efficiency is essentially constant. Although this may not be practical for some bins, it will establish the validity of the procedure.

To analyze this situation, consider again an arbitrary bin B. By the discussion above, the measured yield will be

$$V_B = \frac{D_B}{NB} \cdot \frac{P_B^s}{D_B^s}, \text{ plotted at } p_{TB} = g^{-1}\left(\langle g(p_T)\rangle_B\right). \tag{H.15}$$

Assume that the efficiency of particle detecton (including smearing and translation effects) is the constant ε. Then $h(p_T) = \varepsilon f(p_T)$ and $s(p_T) = n\varepsilon g(p_T)$. Which gives the following for the detection distributions.

$$\begin{aligned} D_B &= \int_B N\varepsilon f(p_T)dp_T = N\varepsilon B\langle f\rangle_B \\ D_B^s &= \int_B s(p_T)dp_T = \int_B n\varepsilon g(p_T)dp_T = n\varepsilon B\langle g\rangle_B \\ P_B^s &= \int_B ng(p_T)dp_T = nB\langle g\rangle_B \end{aligned} \tag{H.16}$$

Thus we can calculate the expected measured yield.

$$V_B = \frac{D_B}{NB} \cdot \frac{P_B^s}{D_B^s} = \frac{N\varepsilon B\langle f \rangle_B}{NB} \cdot \frac{nB\langle g \rangle_B}{n\varepsilon B\langle g \rangle_B} = \langle f \rangle_B \qquad \text{(H.17)}$$

From this we see that V_B which is plotted at the position where $g(p_T)$ is equal to its average on B is equal to the average of f on the same interval. That is, if $V_B = g(p_{TB})$, then $\langle g \rangle_B = \langle f \rangle_B$, and we have the right function for g. If it does not, however, then we have a new alternate definition for $g(p_{TB})$. In practice, individual values are not changed. Rather, the process is carried out on the entire dataset, after which a new form for g is determined by fitting an expected form to the resulting shapes as a function of p_T.

Question (2) deals with certain types of systematic changes or inaccuracies in the detection spectrum. If there is a change, such as $h(p_T) = h(0.9\,p_T)$, it is important to know how the analysis is impacted. There is, however, an important follow-on question: Is this change carried over to the simulation?

The classic example of an energy-scale uncertainty in an electromagnetic calorimeter is the motivation for this situation. In this case the problem is not duplicated in the simulation. Let us consider first the situation where the simulation does duplicate the problem.

In that case, recall that $V_B = \frac{D_B}{NB} \cdot \frac{P_B^s}{D_B^s}$, which is plotted at $p_{TB} = g^{-1}\left(\langle g(p_T) \rangle_B\right)$.

For our D_Bs here, we use h' and s' ($s'(p_T) = s(0.9\,p_T)$) and we further adopt the position that the function g and the simulation s reproduce f and h, so that $h(p_T) = \frac{1}{n} s(p_T)$. Then

$$\begin{aligned} D_B &= \int_B Nh'(p_T)dp_T = N\int_B h(0.9p_T)dp_T \\ &= \tfrac{N}{n}\int_B s(0.9p_T)dp_T = \tfrac{N}{n}\int_B s'(p_T)dp_T = \tfrac{N}{n}D_B^s \end{aligned} \tag{H.18}$$

So that Equation H.13 holds, and the observed value is

$$\begin{aligned} V_B &= \frac{D_B}{NB}\cdot\frac{P_B^s}{D_B^s} = \frac{1}{nB}P_B^s \\ &= \frac{1}{nB}\int_B ng(p_T)dp_T = \frac{1}{B}\int_B f(p_T)dp_T = \langle f\rangle_B \end{aligned} \tag{H.19}$$

Thus the value and the positioning match and no systematic problems are introduced.

The same is not true when the simulation does not reflect systematic effects in the detector. For such a situation, the simulation density *g* is taken to match the real distribution *f*, but the detected distributions do not match. If we assume to know the type of mismatch (as above, we will use p_T detected = $0.9p_T$) and take *s* and *h* to match, other than this discrepancy, then the following holds. (Taking primes to indicate measurements.)

$$\begin{aligned} D_B &= \int_B Nh'(p_T)dp_T = N\int_B h(0.9p_T)dp_T \\ &= \tfrac{N}{n}\int_B s(0.9p_T)dp_T = \tfrac{N}{n}\int_B s'(0.9p_T)dp_T \\ &= \tfrac{N}{n}\frac{dp_T}{dp'_T}\int_{B'} s'(p'_T)dp'_T = \tfrac{N}{n}\frac{dp_T}{dp'_T}D_{B'}^s \end{aligned} \tag{H.20}$$

Calculations when such a discrepancy occurs require knowledge of the problem, because the modified bin *B'* and the factor dp_T/dp'_T cannot be removed.

Question (3) must be addressed every time new data is introduced. This question asks where to place data points if efficiency is unknown. Without knowing the efficiency all we are considering is a straight relationship between *h* and *f*, the detection and production distributions, with no knowledge of *h*/*f*.

From the discussion of Question (1) we know that if h/f is constant, then the appropriate location is where the theoretical distribution g is equal to its average on the interval, as in Equation H.14.

The answer, however, for this question, is that there is no good place to plot the data alone. For example, if the p_T-bin was 1 to 4 GeV/c and the efficiency was a step function changing from 0 to 1 at p_T = 3 GeV/c, the resulting measurement would be completely unrelated to f and g. Measurements can, however, be plotted at consistent locations (such as the bin-centers, or the positions given in Equation H.14), provided it is clear that the positions were chosen arbitrarily since the data has not been efficiency corrected.

APPENDIX I

Full Cross-Section Analysis

The total cross-section for *d+Au* collisions is given by the standard equation:

$$N_{dAu} = L_{dAu} \cdot \sigma_{dAu}\,, \tag{I.1}$$

Similarly, the differential cross-section for production of π^0s in *d+Au* collisions is:

$$dN_{dAu\to\pi^0+X} = L_{dAu} \cdot d\sigma_{dAu\to\pi^0+X}\,, \tag{I.2}$$

From Equations I.1 and I.2, the Lorentz-invariant production of π^0s in *d+Au* collisions can be determined from the cross section and the number of detected events, normalized through the luminosity as follows.

$$\begin{aligned} E\frac{d^3\sigma_{dAu\to\pi^0+X}}{dp^3} &= E\frac{1}{L_{dAu}}\frac{d^3N_{dAu\to\pi^0+X}}{dp^3} \\ &= E\frac{\sigma_{dAu}}{N_{dAu}}\frac{d^3N_{dAu\to\pi^0+X}}{dp^3} \end{aligned}\,, \tag{I.3}$$

Since $N_{dAu\to\pi^0+X}$ is just a count of π^0s, it is useful to simply refer to it as *N*. Furthermore, the cross section will also be rewritten here to use the standard kinematic variables of high-energy collisions. The formal statement is then the following:

$$\begin{aligned} E\frac{\sigma_{dAu}}{N_{dAu}}\frac{d^3N}{dp^3} &= \sigma_{dAu}\frac{1}{N_{dAu}}\frac{1}{p_T}\frac{d^3N}{dp_T d\eta d\phi} \\ &= \sigma_{dAu}\frac{1}{N_{dAu}}\frac{1}{2\pi}\frac{1}{p_T}\frac{d^2N}{dp_T d\eta} \end{aligned}\,, \tag{I.4}$$

The final form is for azimuthally symmetric situations, and can be further simplified for specific η and p_T ranges. Such a form will be shown shortly, however, we will skip some details here and present the full calculational form used in this work. All relative efficiencies and add-ons will be present for determining the actual production rate of π^0s for a given measured number of π^0s. Measurements apply to given p_T-bins denoted by '*i*', and each bin has an associated p_{Ti} that is the place, on that bin, where calculations and plotting should be done, based on [LW95]. The formula follows (with the cross section excluded since it must be included or removed for comparison, as needed).

$$\frac{1}{N_{dAu}}\frac{1}{2\pi}\frac{1}{p'_{Ti}}\frac{d^2N}{dp_T d\eta}\left(p'_{Ti}\right)=\frac{1}{2\pi}\frac{1}{p'_{Ti}}\frac{1}{\Delta p_{Ti}}\frac{N_i}{N_{MB}}\frac{1}{Eff_i}\frac{1}{B.R.}, \qquad \text{(I.5)}$$
$$\left(Eff_i \equiv n^{Sim}{}_i / N^{Sim}{}_i\right)$$

Each parameter (except Eff_i, which is the ratio of the π^0 detected in the p_T-bin during simulation to those π^0s actually simulated) has associated statistical and systematic uncertainties. Each parameter is listed, along with its typical uncertainties and sources, in Table I.1.

Table I.1: The uncertainty in Equation I.5 due to various parameters.

Parameter	Statistical Uncertainty	Systematic Uncertatiny	Systematic Source	Norm. Only
N_i	<1% to 30%	0-25%	Hardware vs. Software Trigger	
		2-100%	Signal Quality (histograms)	
		1-25%	Sensitivity of count to fit method.	
		5%	Detector Acceptance Consistency	5%
Eff_T [a]		5%	π^0s in untriggered events unknown.	5%
N_{MB}	<0.1%			
P'_{Ti}		Negligible	Finding 1/ p_T for Analysis Bin.	
		10%	Positioning Data Point	10%
$n^{Sim}i$	4-10%	< 2%	Signal Histogram Quality in p_T Range.	
	> 10% (HT1 over 5 GeV/c)	2-10% (larger, but correlated)	Sensitivity to $w(p_T)$ Large portion divides out.	
		2%	TPC Veto Match	2%
		5%	Detector Acceptance Mismatch	5%
		Accounted	Z Mismatch	
		10-3000% (turn on only)	Hardware vs. Software difference.	
$N^{Sim}{}_i$	< 0.75%	< 1%	Counting Method[b]	<1%
		Large, correlated to n	$w(p_T)$ is not exact, divides out though.	
$d\eta$		< 1%	Not using dy	< 1%

[a]This parameter does not appear in Equation I.5. It is the trigger efficiency for the Minimum Bias trigger.

[b]The number of simulated particles is based on counting, but since detected particles do not necessarily come from a region of p_T where particles were simulated, it is not necessarily true that uncertainty in $N^{Sim}{}_i$ represents the uncertainty in the population producing $n^{Sim}{}_i$.

APPENDIX J

Analysis Run List

Table J.1: List of 2003 *d+Au* 200 GeV runs used for analysis.

4040025	4045010	4047040	4055014	4061019	4066056
4041008	4045011	4047044	4055015	4061020	4066057
4041023	4045032	4047046	4055016	4061024	4066058
4041029	4045033	4048002	4055017	4062007	4068004
4041030	4045035	4048004	4055018	4062010	4068024
4041031	4045036	4048005	4056004	4062011	4072057
4041036	4045039	4049016	4056013	4062012	4073005
4041037	4045040	4049020	4056014	4063041	4074041
4041038	4046002	4049021	4056017	4063046	4075009
4041039	4046003	4049022	4056018	4063047	4075012
4041041	4046005	4049023	4056021	4065002	4075013
4041042	4046006	4049025	4056033	4065003	4076015
4041043	4046016	4049026	4060011	4065004	4077023
4042010	4046018	4049028	4060017	4065005	4077028
4042014	4046020	4049029	4060020	4065016	4078007
4042016	4046021	4049030	4060021	4065052	4079008
4042017	4047010	4054003	4060023	4065065	4079009
4043001	4047011	4054012	4060024	4065068	4079010
4043005	4047013	4054014	4060026	4065069	4079030
4043006	4047014	4054015	4060055	4066002	4079037
4044004	4047015	4054016	4060056	4066003	4079038
4044027	4047017	4054022	4060058	4066009	4079057
4044028	4047018	4054041	4060064	4066010	4080003
4044029	4047019	4054056	4060067	4066011	4080025
4044032	4047027	4054057	4060074	4066012	4080026
4044034	4047029	4054060	4060088	4066013	4080027
4044035	4047031	4055002	4060093	4066014	4080033
4044036	4047032	4055005	4060094	4066016	4080034
4045007	4047034	4055007	4061004	4066017	
4045008	4047035	4055008	4061007	4066045	
4045009	4047039	4055010	4061008	4066054	

APPENDIX K

Analysis Acceptance

Due to the time-dependent nature of the data collection, and the large number of channels in the BEMC, the determination of the detector acceptance contains uncertainty. Most of the uncertainty is eliminated by removing bulk sections of the detector where the quality of the recorded data was always low, or fluctuated wildly over the data-taking period. A table of BEMC modules removed from the analysis is given in Table K.1. Additionally, towers of the BEMC, strips of the SMD-η or SMD-ϕ were removed by the application of time-dependent status tables (or indirectly by the application of pedestal or gain tables that effectively removed the signal).

Table K.1: The modules masked out of analysis are listed.

Module#	ϕ - low	ϕ - high
41	-2.98	-2.88
36	-2.46	-2.36
34	-2.25	-2.15
33	-2.15	-2.04
32	-2.04	-1.94
31	-1.94	-1.83
22	-0.99	-0.89
18	-0.58	-0.47
10	0.26	0.37
7	0.58	0.68
5	0.79	0.89
4	0.89	0.99
1	1.20	1.31
46	2.78	2.88
43	3.09	3.19*

*This module straddles π at the 3 o'clock position.

APPENDIX L

STAR Collaboration

B.I. Abelev[10], M.M. Aggarwal[32], Z. Ahammed[47], B.D. Anderson[21], D. Arkhipkin[14], G.S. Averichev[13], Y. Bai[30], J. Balewski[25], O. Barannikova[10], L.S. Barnby[2], J. Baudot[19], S. Baumgart[52], D.R. Beavis[3], R. Bellwied[50], F. Benedosso[30], R.R. Betts[10], S. Bhardwaj[37], A. Bhasin[20], A.K. Bhati[32], H. Bichsel[49], J. Bielcik[12], J. Bielcikova[12], B. Biritz[7], L.C. Bland[3], M. Bombara[2], B.E. Bonner[38], M. Botje[30], J. Bouchet[21], E. Braidot[30], A.V. Brandin[28], S. Bueltmann[3], T.P. Burton[2], M. Bystersky[12], X.Z. Cai[41], H. Caines[52], M. Calderon[6], J. Callner[10], O. Catu[52], D. Cebra[6], R. Cendejas[7], M.C. Cervantes[43], Z. Chajecki[31], P. Chaloupka[12], S. Chattopadhyay[47], H.F. Chen[40], J.H. Chen[41], J.Y. Chen[51], J. Cheng[45], M. Cherney[11], A. Chikanian[52], K.E. Choi[36], W. Christie[3], S.U. Chung[3], R.F. Clarke[43], M.J.M. Codrington[43], J.P. Coffin[19], T.M. Cormier[50], M.R. Cosentino[39], J.G. Cramer[49], H.J. Crawford[5], D. Das[6], S. Dash[16], M. Daugherity[44], M.M. de Moura[39], T.G. Dedovich[13], M. DePhillips[3], A.A. Derevschikov[34], R. Derradi de Souza[8], L. Didenko[3], T. Dietel[15], P. Djawotho[18], S.M. Dogra[20], X. Dong[24], J.L. Drachenberg[43], J.E. Draper[6], F. Du[52], J.C. Dunlop[3], M.R. Dutta Mazumdar[47], W.R. Edwards[24], L.G. Efimov[13], E. Elhalhuli[2], V. Emelianov[28], J. Engelage[5], G. Eppley[38], B. Erazmus[42], M. Estienne[19], L. Eun[33], P. Fachini[3], R. Fatemi[22], J. Fedorisin[13], A. Feng[51], P. Filip[14], E. Finch[52], V. Fine[3], Y. Fisyak[3], C.A. Gagliardi[43], L. Gaillard[2], D.R. Gangadharan[7], M.S. Ganti[47], E. Garcia-Solis[10], V. Ghazikhanian[7], P. Ghosh[47], Y.N. Gorbunov[11], A. Gordon[3], O. Grebenyuk[30], D. Grosnick[46], B. Grube[36], S.M. Guertin[7], K.S.F.F. Guimaraes[39], A. Gupta[20], N. Gupta[20], W. Guryn[3], B. Haag[6], T.J. Hallman[3], A. Hamed[43], J.W. Harris[52], W. He[18], M. Heinz[52], S. Heppelmann[33], B. Hippolyte[19], A. Hirsch[35], A.M. Hoffman[25], G.W. Hoffmann[44], D.J. Hofman[10], R.S. Hollis[10], H.Z. Huang[7], E.W. Hughes[4], T.J. Humanic[31], G. Igo[7], A. Iordanova[10], P. Jacobs[24], W.W. Jacobs[18], P. Jakl[12], F. Jin[41], P.G. Jones[2], E.G. Judd[5], S. Kabana[42], K. Kajimoto[44], K. Kang[45], J. Kapitan[12], M. Kaplan[9], D. Keane[21], A. Kechechyan[13], D. Kettler[49], V.Yu. Khodyrev[34], J. Kiryluk[24], A. Kisiel[31], S.R. Klein[24], A.G. Knospe[52], A. Kocoloski[25], D.D. Koetke[46], T. Kollegger[15], M. Kopytine[21], L. Kotchenda[28], V. Kouchpil[12], P. Kravtsov[28], V.I. Kravtsov[34], K. Krueger[1], C. Kuhn[19], A. Kumar[32], L. Kumar[32], P. Kurnadi[7], M.A.C. Lamont[3], J.M. Landgraf[3], S. Lange[15], S. LaPointe[50], F. Laue[3], J. Lauret[3], A. Lebedev[3], R. Lednicky[14], C-H. Lee[36], M.J. LeVine[3], C. Li[40], Y. Li[45], G. Lin[52], X. Lin[51], S.J. Lindenbaum[29], M.A. Lisa[31], F. Liu[51], H. Liu[40], J. Liu[38], L. Liu[51], T. Ljubicic[3], W.J. Llope[38], R.S. Longacre[3], W.A. Love[3], Y. Lu[40], T. Ludlam[3], D. Lynn[3], G.L. Ma[41], J.G. Ma[7], Y.G. Ma[41], D.P. Mahapatra[16], R. Majka[52],

L.K. Mangotra[20], R. Manweiler[46], S. Margetis[21], C. Markert[44], H.S. Matis[24], Yu.A. Matulenko[34], T.S. McShane[11], A. Meschanin[34], J. Millane[25], M.L. Miller[25], N.G. Minaev[34], S. Mioduszewski[43], A. Mischke[30], J. Mitchell[38], B. Mohanty[47], D.A. Morozov[34], M.G. Munhoz[39], B.K. Nandi[17], C. Nattrass[52], T.K. Nayak[47], J.M. Nelson[2], C. Nepali[21], P.K. Netrakanti[35], M.J. Ng[5], L.V. Nogach[34], S.B. Nurushev[34], G. Odyniec[24], A. Ogawa[3], H. Okada[3], V. Okorokov[28], D. Olson[24], M. Pachr[12], S.K. Pal[47], Y. Panebratsev[13], T. Pawlak[48], T. Peitzmann[30], V. Perevoztchikov[3], C. Perkins[5], W. Peryt[48], S.C. Phatak[16], M. Planinic[53], J. Pluta[48], N. Poljak[53], N. Porile[35], A.M. Poskanzer[24], M. Potekhin[3], B.V.K.S. Potukuchi[20], D. Prindle[49], C. Pruneau[50], N.K. Pruthi[32], J. Putschke[52], I.A. Qattan[18], R. Raniwala[37], S. Raniwala[37], R.L. Ray[44], D. Relyea[4], A. Ridiger[28], H.G. Ritter[24], J.B. Roberts[38], O.V. Rogachevskiy[13], J.L. Romero[6], A. Rose[24], C. Roy[42], L. Ruan[3], M.J. Russcher[30], V. Rykov[21], R. Sahoo[42], S. Sakai[7], I. Sakrejda[24], T. Sakuma[25], S. Salur[52], J. Sandweiss[52], M. Sarsour[43], J. Schambach[44], R.P. Scharenberg[35], N. Schmitz[26], J. Seger[11], I. Selyuzhenkov[18], P. Seyboth[26], A. Shabetai[19], E. Shahaliev[13], M. Shao[40], M. Sharma[50], S.S. Shi[51], X-H. Shi[41], E.P. Sichtermann[24], F. Simon[26], R.N. Singaraju[47], M.J. Skoby[35], N. Smirnov[52], R. Snellings[30], P. Sorensen[3], J. Sowinski[18], H.M. Spinka[1], B. Srivastava[35], A. Stadnik[13], T.D.S. Stanislaus[46], D. Staszak[7], R. Stock[15], M. Strikhanov[28], B. Stringfellow[35], A.A.P. Suaide[39], M.C. Suarez[10], N.L. Subba[21], M. Sumbera[12], X.M. Sun[24], Z. Sun[23], B. Surrow[25], T.J.M. Symons[24], A. Szanto de Toledo[39], J. Takahashi[8], A.H. Tang[3], Z. Tang[40], T. Tarnowsky[35], D. Thein[44], J.H. Thomas[24], J. Tian[41], A.R. Timmins[2], S. Timoshenko[28], M. Tokarev[13], T.A. Trainor[49], V.N. Tram[24], A.L. Trattner[5], S. Trentalange[7], R.E. Tribble[43], O.D. Tsai[7], J. Ulery[35], T. Ullrich[3], D.G. Underwood[1], G. Van Buren[3], N. van der Kolk[30], M. van Leeuwen[30], A.M. Vander Molen[27], R. Varma[17], G.M.S. Vasconcelos[8], I.M. Vasilevski[14], A.N. Vasiliev[34], F. Videbaek[3], S.E. Vigdor[18], Y.P. Viyogi1[6], S. Vokal[13], S.A. Voloshin[50], M. Wada[44], W.T. Waggoner[11], F. Wang[35], G. Wang[7], J.S. Wang[23], Q. Wang[35], X. Wang[45], X.L. Wang[40], Y. Wang[45], J.C. Webb[46], G.D. Westfall[27], C. Whitten Jr.[7], H. Wieman[24], S.W. Wissink[18], R. Witt[52], J. Wu[40], Y. Wu[51], N. Xu[24], Q.H. Xu[24], Z. Xu[3], P. Yepes[38], I-K. Yoo[36], Q. Yue[45], M. Zawisza[48], H. Zbroszczyk[48], W. Zhan[23], H. Zhang[3], S. Zhang[41], W.M. Zhang[21], Y. Zhang[40], Z.P. Zhang[40], Y. Zhao[40], C. Zhong[41], J. Zhou[38], R. Zoulkarneev[14], Y. Zoulkarneeva[14], J.X. Zuo[41],

[1]Argonne National Laboratory, Argonne, Illinois 60439
[2]University of Birmingham, Birmingham, United Kingdom
[3]Brookhaven National Laboratory, Upton, New York 11973
[4]California Institute of Technology, Pasadena, California 91125
[5]University of California, Berkeley, California 94720
[6]University of California, Davis, California 95616
[7]University of California, Los Angeles, California 90095
[8]Universidade Estadual de Campinas, Sao Paulo, Brazil

[9]Carnegie Mellon University, Pittsburgh, Pennsylvania 15213
[10]University of Illinois at Chicago, Chicago, Illinois 60607
[11]Creighton University, Omaha, Nebraska 68178
[12]Nuclear Physics Institute AS CR, 250 68 \v{R}e\v{z}/Prague, Czech Republic
[13]Laboratory for High Energy (JINR), Dubna, Russia
[14]Particle Physics Laboratory (JINR), Dubna, Russia
[15]University of Frankfurt, Frankfurt, Germany
[16]Institute of Physics, Bhubaneswar 751005, India
[17]Indian Institute of Technology, Mumbai, India
[18]Indiana University, Bloomington, Indiana 47408
[19]Institut de Recherches Subatomiques, Strasbourg, France
[20]University of Jammu, Jammu 180001, India
[21]Kent State University, Kent, Ohio 44242
[22]University of Kentucky, Lexington, Kentucky, 40506-0055
[23]Institute of Modern Physics, Lanzhou, China
[24]Lawrence Berkeley National Laboratory, Berkeley, California 94720
[25]Massachusetts Institute of Technology, Cambridge, MA 02139-4307
[26]Max-Planck-Institut für Physik, Munich, Germany
[27]Michigan State University, East Lansing, Michigan 48824
[28]Moscow Engineering Physics Institute, Moscow Russia
[29]City College of New York, New York City, New York 10031
[30]NIKHEF and Utrecht University, Amsterdam, The Netherlands
[31]Ohio State University, Columbus, Ohio 43210
[32]Panjab University, Chandigarh 160014, India
[33]Pennsylvania State University, University Park, Pennsylvania 16802
[34]Institute of High Energy Physics, Protvino, Russia
[35]Purdue University, West Lafayette, Indiana 47907
[36]Pusan National University, Pusan, Republic of Korea
[37]University of Rajasthan, Jaipur 302004, India
[38]Rice University, Houston, Texas 77251
[39]Universidade de Sao Paulo, Sao Paulo, Brazil
[40]University of Science & Technology of China, Hefei 230026, China
[41]Shanghai Institute of Applied Physics, Shanghai 201800, China
[42]SUBATECH, Nantes, France
[43]Texas A&M University, College Station, Texas 77843
[44]University of Texas, Austin, Texas 78712
[45]Tsinghua University, Beijing 100084, China
[46]Valparaiso University, Valparaiso, Indiana 46383
[47]Variable Energy Cyclotron Centre, Kolkata 700064, India
[48]Warsaw University of Technology, Warsaw, Poland
[49]University of Washington, Seattle, Washington 98195
[50]Wayne State University, Detroit, Michigan 48201
[51]Institute of Particle Physics, CCNU (HZNU), Wuhan 430079, China

[52]Yale University, New Haven, Connecticut 06520
[53]University of Zagreb, Zagreb, HR-10002, Croatia

REFERENCES

[Abe88] F. Abe, et al. "Transverse-momentum distributions of chared particles produced in $p^{-}p$ *interactions at* $\sqrt{s}$*=630 and 1800 GeV*", *Phys. Rev. Lett.* **61**:1819-1822, 1988.

[Ack03] K.H. Ackermann, et al. (STAR Collaboration) "STAR detector overview", *Nucl. Instrum. Meth.* **A499**:624-632, 2003.

[Ada03] J. Adams, et al. (STAR Collaboration) "Evidence from d+Au measurements for final-state suppression of high p_T hadrons in Au+Au collisions at RHIC", *Phys. Rev. Lett.* **91**:072304 2003.

[Ada03b] J. Adams, et al. (STAR Collaboration) "Transverse momentum and collision energy dependence of high pT hadron suppression in Au+Au collisions at ultrarelativistic energies", *Phys. Rev. Lett.* **91**:172302, 2003.

[Ada05] J. Adams, et al. (STAR Collaboration) "Pion, kaon, proton and anti-proton transvers momentum distributions from p+p and d+Au collisions at sqrt(snn) = 200 GeV", *Phys. Lett.* **B616**:8-14, 2005.

[Ada05b] J. Adams, et al. (STAR Collaboration) "Experimental and theoretical challenges in the search for the quark-gluon plasma: The STAR Collaboration's critical assessment of the evidence from RHIC collisions", *Nucl. Phys.* **A757**:102-183 2005.

[Ada06] J.Adams, "Identified hadron spectra at large transverse momentum in *p+p* and *p*+Au collisions at $\sqrt{s_{NN}}$ = 200 GeV", nucl-ex/0601033, *Phys. Lett.* **B637**:161-191 2006.

[Adc02] K. Adcox, et al. (PHENIX Collaboration) "Suppression of Hadrons with Large Transvers Momentum in Central *Au+Au* Collisions at *sqrt*[s_{NN}] = 130 *GeV*", *Phys. Rev. Lett.* **88**:022301, 2002.

[Adl01] C. Adler, et al. "The RHIC Zero Degree Calorimeter", *Nucl. Instrum. Meth.* **A470**:488-499, 2001.

[Adl02] C. Adler et al. (STAR Collaboration) "Centrality dependence of high pT hadron suppression in Au+Au collisions at sqrt(sNN)=130 GeV", nucl-ex/0206011, *Phys. Rev. Lett.* **89**:202301 2002.

[Adl03] C. Adler, et al. (STAR Collaboration) "Disappearance of back-to-back high p_T hadron correlations in central Au+Au collisions at $\sqrt{s_{NN}}$ = 200 GeV", nucl-ex/0210033, *Phys. Rev. Lett.* **90**:082302 2003.

[Adl03b] C.Adler, et al. (STAR Collaboration), "The STAR Level-3 trigger system", *Nucl. Instrum. Meth.* **A499**:778-791, 2003.

[Adl03c] S.S. Adler, et al. (PHENIX Collaboration), "Absence of Suppression in Particle Production at Large Transverse Momentum in *sqrt*[s_{NN}]=200 GeV *d*+Au", *Phys. Rev. Lett.* **91**:072303, 2003.

[Adl03d] S.S. Adler et al., (PHENIX Collaboration), "Midrapidity Neutral-Pion Production in Proton-Proton Collisions at *sqrt*[s]", *Phys. Rev. Lett.* **91**:241803, 2003.

[Agg98] M.M. Aggarwal, et al. (WA98 Collaboration), "Centrality Dependence of Neutral Pion Production in 158 A GeV *Pb + Pb* Collisions", *Phys. Rev. Lett.* **81**:4087-4091, 1998; *Erratum-ibid.* **84**:578-579, 2000, nucl-ex/9806004

[Ahr03] L. Ahrens et al. "The RHIC injector accelerator configurations, and performance for the RHIC 2003 Au-d Physics Run", *Proceedings of the 2003 Particle Accelerator Conference*, 2003. IEEE

[Alb90] C. Albajar et al. (UA1 Collaboration) "A study of the general characteristics of proton-antiproton collisions at √s=0.2 to 0.9 TeV", *Nucl. Phys.* **B335**:261-287, 1990.

[Alb98] R. Albrecht, et al. (WA80 Collaboration), "Transverse momentum distributions of neutral pions from nuclear collisions at 200 AGev", nucl-ex/9805007, *Eur. Phys. J.* **C5**:255-267, 1998.

[And03] M. Anderson, et al. "The STAR Time Projection Chamber: A Unique Tool for Studying High Multiplicity Events at RHIC", *Nucl. Instrum. Meth.* **A499**:659-678, 2003.

[AP77] G. Altarelli and G. Parisi, "Asymptotic freedom in parton language", *Nucl. Phys.* **B126**:298-318 1977.

[Arn82] G. Arnison, et al. (UA1 Collaboration) "Transverse momentum spectra for charged particles at the CERN proton anti-proton collider", *Phys. Lett.* **B118**:167, 1982.

[Arn90] M. Arneodo, et al. (EMC-NA28 Collaboration) "Measurements of the nucleon structure function in the range $0.002 < x < 0.17$ and $0.2 < Q^2 < 8$ GeV^2 in deuterium, carbon and calcium", *Nucl. Phys.* **B333**:1-47, 1990.

[Bas04] S. Bass. (Figure from presentation at KFKI by Molnár Levente, Purdue University, 2004)

[Bed03] M. Beddo, et al. "The STAR Barrel Electromagnetic Calorimeter", *Nucl. Instrum. Meth.* **A499**:725-739 2003.

[Berg03] F.Bergsma et al. "The STAR detector Magnet subsystem", *Nucl. Instrum. Meth.* **A499**:633-639, 2003.

[Bie03] F.S. Bieser et al. “The STAR trigger”, *Nucl. Instrum. Meth.* **A499**:766-777 (2003).

[Bjo82] J.D. Bjorken, “Energy Loss of Energetic Partons in Quark-Gluon Plasma: Possible Extinction of High p_T Jets in Hadron-Hadron Collisions” FERMILAB-PUB-82-059-THY, 1982

[Bla06] J. P. Blaizot. “Ultrarelativistic heavy ion collisions: Theoretical Overview”, *J. Phys. Conf. Ser.* **50**:1-7, 2006

[BDG66] D. Boccaletti, V. De Sabbata and C. Gualdi, *Nuovo Cimento* 45A (1966) 513.

[Che03] Y. Chen. *High Transvers Momentum Charged Hadron Production in Au+Au Collisions at the Relativistic Heavy Ion Collider*, PhD Dissertation, University of California-Los Angeles 2003.

[Cho74] A. Chodos, R.L. Jaffe, K. Johnson, C.B. Thorn and V.F. Weisskopf. “New extended model of hadrons”, *Phys. Rev.* **D9**:3472 1974).

[Cho03] B. Choi. *Phi p_perp Inclusive Charged Hadron Distributions in* Au+Au *Collisions at sqrt(s_NN) = 130 GeV at RHIC* , PhD Dissertation, Univerity of Texas-Austin (2003).

[CGS86] J. Cleymans, R.V. Gavai, E. Suhonen. “Quarks and gluons at high temperatures and densities”, *Phys. Rep.* **130**:217 1986

[Col84] P.D.B. Collins and A.D. Martin. *Hadron Interactions*. Adam Hilger, Ltd, Bristol, 1984

[Cor02] M. Cormier et al., STAR Note SN0436 “STAR Barrel Electromagnetic Calorimeter Absolute Calibration Using ‘Minimum Ionizing Particles’ from Collisions at RHIC” Nov. 2001; *Nucl. Instrum Meth.* **A483**:734-746, 2002.

[DeL01] J. DeLong, et al, “Synthesizer Controlled Beam Transfer from the AGS to RHIC”, *Proceedings of the 2001 Particle Accelerator Conference*, IEEE, vol.2, 1523-1525, Chicago, 2001.

[Dok77] Yu.L. Dokshitzer, Sov. Phys. JTEP 46, 641 (1977)

[EKS99] K.J. Eskola, V.J. Kolhinen, and C.A. Salgado. “The scale dependent nuclear effects in parton distributions”, *Eur. Phys. J.* **C9**:61-68, 1999.

[Eng81] J. Engels, F. Karsh, I. Montvay, and H. Satz. “High temperature SU(2) gluon matter of the lattice”, Phys. Lett. **B101**:89-94 1981; “Gauge field thermodynamics for the SU(2) Yang-Mills system”, Nucl. Phys. **B205** [FS 5] (1982) 545.

[Ent03] D. d’Enterria, “High p_T Identified Particles in PHENIX: Data vs. Theory” 19th Winter Workshop on Nuclear Dynamics, Breckenridge, 2003

[Ent03b] D. d'Enterria, "High-p_T π^0 suppression in Au+Au collisions at $\sqrt{s_{NN}}$ = 200 GeV", *Nucl. Phys.* **A715**:749-752, 2003.

[Gar01] C.J. Gardner, et al., "Status and Recent Performance of the Accelerators that Serve as Gold Injector for RHIC", *Proceedings of the 2001 Particle Accelerator Conference*, IEEE, vol.5 3326-3328 Chicago, 2001.

[Gar01b] C.J. Gardner, "Notes on the Delivery of Deuterium and Gold Ions for RHIC", AGSRHIC website: http://www.agsrhichome.bnl.gov/AP/RHIC2003/dAu/deutgold02-KGardner.pdf, 2001.

[GEA] "GEometry ANd Tracking", see http://spi.cern.ch/extsoft/packages.php?pkg=geant4

[GGX03] K. Gallmeister, C. Greiner, and Z.Xu. "Quenching of high p(t) hadron specra by hadronic interactions in heavy ion collisions at RHIC", *Phys. Rev.* ***C*67**:044905 2003.

[GL72] V.N. Gribov and L.N. Lipatov, *Sov. J. Nucl. Phys.* **15**:438, 1972.

[GM70] R. Glauber and G. Matthiae. "High-energy scattering of protons by nuclei". *Nucl. Phys.*, **B21**:135-157 1970

[Han03] H. Hahn, *et al*. "The RHIC design overview", *Nucl. Instrum. Meth.* **A499**:245-263 2003.

[HS57] L. Hulthén and M. Sagawara, *Handbuch der Physik*, Vol 39, Springer-Verlag, Berlin, 1957.

[IK65] D. Ivanenko and D.F. Kurgelaidze. *Astrofizika* **1**:479 1965; *Lett. Nuovo Cimento* **2**:13, 1969.

[ILL74] F. Iachello, W.D. Langer and A. Lande, "Quark-like model of high density matter", *Nucl Phys.* **A219:**612-620, 1974.

[Ito70] N. Itoh, "Hydrostatic Equilibrium of Hypothetical Quark Stars",*Progr. Theor. Phys*. **44**:291-292, 1970.

[Jag03] B. Jager, A. Schafer, M. Stratmann, and W. Vogelsang. "Next-to-leading order QCD corrections to high-p_T pion production in longitudinally polarized p+p collisions", *Phys. Rev.* **D67**:054005, 2003.

[Kar02] F. Karsch. "Lattice QCD at High Temperature and Density", *Lecture Notes in Physics* **583**:209-249 2002.

[KKP00] B.A. Kniehl, G. Kramer, and B. Pötter. "Fragmentation functions for pions, kaons, and protons at next-to-leading order", *Nucl. Phys.* **B582**:514-536, 2000.

[KLN04] D. Kharzeev, E. Levin, and M. Nardi, "QCD saturation and deuteron-nucleus collisions", *Nucl. Phys.* **A730**:448-459, 2004.

[KN01] D. Kharzeev, M. Nardi, "Hadron pproduction in nuclear collisions at RHIC and high-density QCD", *Phys. Lett.* **B507**:121-128, 2001.

[Kok69] J.J.J. Kokkedee. *The Quark Model* (New York, N.Y.), 1969.

[Kot03] L. Kotchenda et al. "STAR TPC Gas System." *Nucl. Instr. Meth.* **A499**: 703-712, 2003.

[KPS81] J. Kuti, J. Polónyi and K. Szlachányi, "Monte Carlo study of SU(2) gauge theory at finite temperature", *Phys. Lett.* **B98:**199-205, 1981.

[Kre00] S. Kretzer. "Fragmentation functions from flavour-inclusive and flavour-tagged e^+e^- annihilations", *Phys. Rev.* **D62**:054001, 2000

[Kun03] G. Kunde, (STAR Collaboration) "High transverse momentum results from the STAR collaboration", *Nucl. Phys.* **A715**:189-198, 2003.

[Lip75] [x]L.N. Lipatov, Sov. J. Nucl. Phys. 20, 95 (1975)

[LR02] J. Letessier and J. Rafelski. *Hadrons and Quark-Gluon Plasma*. Cambridge University Press, Cambridge, UK, first edition, 2002.

[LW95] G.D. Lafferty, T.R. Wyatt, "Where to stick you data points: The treatment of measurements within wide bins", *Nucl. Instrum. Meth.* **A355**:541-547, 1995.

[Mio03] S. Mioduszewski. (PHENIX Collaboration) "High p_T measurements from PHENIX", *Nucl. Phys.* **A715**:199-208, 2003.

[MS81] L.D. McLerran and B. Svetitsky, "A Monte Carrlo study of SU(2) Yang-Mills theory at finite temperature", *Phys. Lett.* **B98**:195-198, 1981;

[MS81b] L.D. McLerran and B. Svetitsky, "Quark liberation at high temperature: A Monte Carlo study of SU(2) guage theory", *Phys. Rev.* **D24:**450-460, 1981.

[Pac66] F. Pacini, "High-energy Astrophysics and a Possible Sub-nuclear Energy Source", *Nature* **209**:389-390, 1966.

[RV01] V.L. Rykov, A.N. Vasiliev, "Comparison of STAR BEMC Responses to Electrons and Penetrating Charged Particles in the Beam-Test-'98", STAR Note SN0433, April 2001.

[Sat03] T. Satogata et al., "COMMISSIONING OF RHIC DEUTERON-GOLD COLLISIONS", *Proceedings of the 2003 Particle Accelerator Conference*, IEEE, 2003.

[Sat05] T. Satogata, "Experience with Asymmetric Hadron Collisions at RHIC", CERN p-A Workshop2005

[Sav98] M.V.Savina, et al. “Global Features of Nucleus-Nucleus Collisions in Ultrarelativistic Domain”, *JINR Rapid Commun.* **91**:65-72, 1998.

[Sto05] A. Stolpovsky. *Neutral Pion Production in p+p and d+Au Collisions at RHIC*, PhD Dissertation, Wayne State University, 2005.

[Sor03] P.R.Sorensen. *Kaon and Lambda Production at Intermediate p_T: Insights into the Hadronization of the Bulk Partonic Matter Created in Au+Au Collisions at RHIC*, PhD Dissertation, Univeristy of California-Los Angeles 2003.

[Un1] Unpublished summary of STAR performance during run 8 was shown. This figure may be included in the STAR Beam Use Request for 2008-2009.

[VG02] I. Vitev, M. Gyulassy. “High-p_T Tomogrraphy of *d*+Au and Au+Au at SPS, RHIC, and LHC”, *Phys. Rev. Lett.* **89**:252301 2002.

[Wan98] X.-N. Wang. “Where Is the Jet Quenching in *Pb*+*Pb* Collisions at 158A GeV?””, *Phys. Rev. Lett.* **81**:2655-2658, 1998.

[Wan00] X.-N. Wang. “Systematic study of high p_T hadron spectra in *pp*, *pA*, and *AA* collisions at ultrarelativistic energies”, *Phys. Rev.* **C61**:064910, 2000

[Wan02] X.-N. Wang. “Monte Carlo models: Quo vadimus?”, *Nucl. Phys.* **A698**:296-305, 2002

[WG91] X.-N. Wang and M.Gyulassy, “HIJING: A Monte Carlo model for multiple jet production in *pp*, *pA*, and *AA* collisions”, *Phys. Rev.* **D44**:3501-3516, 1991;

[WG94] “HIJING 1.0: A Monte Carlo Program for Parton and Particle Production in High Energy Hadronic and Nuclear Collisions”, LBL-34246, nucl-th/9502021, *Comput. Phys. Commun.* **83**:307-344 1994.

[WiMV] *wikipedia*: Mandelstam_variables (http://en.wikipedia.org/wiki/Mandelstam_variables)

[WN02] E.J. Weinberg, D.L. Nordstrom Editors. *Physical Review D*. 2002

[WX07] J. Wu and M. Xu. (STAR Collaboration) “A barrel TOF for STAR at RHIC”, *J. Phys. G*, **34**:S729-S732, 2007.